

Compton Polarimetry for Neutral Weak Form Factor Measurements in ^{208}Pb and ^{48}Ca

Allison Jane Zec

Newport News, VA, USA

B.S. Physics, University of Massachusetts Amherst, 2015

A Dissertation Presented to the Graduate Faculty of the
University of Virginia in Candidacy for the Degree of Doctor of
Philosophy

Department of Physics

University of Virginia

January 2022

Prof. Kent D. Paschke (Advisor)

Prof. Xiaochao Zheng (Committee Member)

Prof. Dustin Keller (Committee Member)

Dr. Dave Gaskell (Committee Member)

Prof. Phil Arras (GSAS Representative)

This work is licensed under the Creative Commons Attribution
Noncommercial 4.0 (CC BY-NC 4.0)

Newport News, VA, USA 2022

Abstract

Atomic nuclei contain a number of protons and neutrons. Most heavy nuclei contain more neutrons than protons in order to remain stable. The nuclear proton distribution can be measured via elastic scattering of charged particles, but the neutron distribution remains poorly constrained. Nuclear structure theory also predicts a “neutron skin” Δr_{np} where the mean radii of neutrons in the nucleus exceeds that of protons. Two experiments were run in 2019 and 2020 to measure the neutron skin in two different nuclei. The first experiment, PREX-II, was designed to measure the neutron skin in ^{208}Pb , while the second experiment, CREX, was designed to measure the neutron skin in ^{48}Ca . Both experiments employed the parity-violating electron scattering (PVES) technique in which longitudinally spin-polarized electrons are scattered off an unpolarized target. The parity-violating asymmetry \mathcal{A}_{PV} is then measured which is the normalized difference of scattering cross section from electrons in alternating positive and negative helicity states. PREX-II performed this experiment with 950 MeV electrons scattered at a 5° angle with $Q^2 = 0.00616 \pm 0.00004 \text{ (GeV/c)}^2$, while CREX used 2182 MeV electrons at the same angle with $Q^2 = 0.0297 \pm 0.0002 \text{ (GeV/c)}^2$.

One of the potentially largest sources of systematic uncertainty for both experiments arises from the measurement precision of the beam polarization \mathcal{P}_e . To accurately measure \mathcal{P}_e a Compton scattering polarimeter was used. The electron beam for the main experiment was passed through a resonant laser optical cavity. The Compton backscattered photons then entered the photon detector where their asymmetry was measured yielding \mathcal{P}_e . The Compton polarimetry data from PREX-II lacked the statistical precision necessary to make a final polarimetry measurement. However, for CREX the Compton polarimetry measurement was $\mathcal{P}_e = (87.115 \pm 0.453)\%$ with negligible contribution from statistical uncertainty.

The measurement of \mathcal{P}_e was then incorporated into both experiments’ calculation of \mathcal{A}_{PV} . Additionally, both experiments used a dynamic beam correction system to correct for any sources of false asymmetry. For PREX-II the asymmetry was $\mathcal{A}_{PV} = 550 \pm 16 \text{ (stat)} \pm \text{ (syst) ppb}$, which corresponds to $\Delta r_{np}^{208} = 0.278 \pm 0.078 \text{ (exp.)} \pm 0.012 \text{ (theo.) fm}$. The CREX asymmetry was $\mathcal{A}_{PV} = 2658.6 \pm 106.1 \text{ (stat)} \pm 39.3 \text{ (syst) ppb}$, although the analysis for Δr_{np}^{48} is not yet complete. The results of these two experiments will have significant implications for the theory of nuclear structure, and even for the nuclear equation of state which governs neutron stars.

*To my friends Aaron Heuer and Tobias Gies whose support kept me sane
all these years, and to my wonderful sister Emma.*

Acknowledgements

I cannot begin to express the full depth of gratitude I have for the number of people who, throughout my years as a student in Virginia, helped me become better researcher and a better person, and without whom this dissertation would not be possible. But I'm going to attempt to begin anyway, out of ample love and respect for my wonderful colleagues.

I would specifically like to thank my adviser Kent Paschke. Your expertise, guidance and mentorship helped me become the scientist I am today. You took a chance in taking me on several years ago and I'm forever grateful for the opportunities I gained because of it. Your mentorship and leadership has left an indelible impression on me as a researcher and as a person that will guide me through the remainder of my life as a physicist.

I would like to thank the members of Comptonia for their role in making this research possible. First I'd like to thank Dave Gaskell, under whose direction I was able to thrive and who made the project of running the Compton polarimeter a successful one. I'd also like to thank Juan Carlos Cornejo, whose generosity with his time and attention rivaled few else in the collaboration and became my primary mentor during those stressful run periods. I would also like to thank my UVA student colleague Amali Premathilake. And I give my thanks to everyone else in Comptonia including Mark, Don, Brian, Ciprian, and Caryn.

I would also like to thank the primary spokespersons of both PREX-II and CREX: Seamus Riordan, Juliette Mammei, Paul Souder, Dustin McNulty, Bob Michaels, Krishna Kumar, Silviu Convrig-Dusa, and Guido Uricioli. Thank you all for your guidance and expertise when we were scrambling to make these experiments actually *work*, and for making them possible to begin with. I'll be following whatever future projects you all have with great interest.

Next, I would like to thank the PREX-II and CREX students who, like myself, were always actively learning and growing as experimental physicists, even during the long nights and owl shifts of running the experiment. In no particular order thank you to Ryan, Cameron, Victoria, Tao, Weibin, Robert, Devi, Iris, Sakib, Zeke, Eric, Siyu, Devika, Yufan, Catherine, Quinn, and Carrington. We were a ragtag band of misfit weirdos, but we were a *proud and happy* ragtag band of misfit weirdos with determination and heart. I could not choose a better more supportive group of colleagues and friends, truly.

I would also like to thank the PREX/CREX postdocs and faculty not already named so thank you to Rakitha, Sanghwa, Ye, Chandan, Hanjie, Nilanga, Paul King, Jinlong, and Dave Armstrong. I wish all of you nothing but the best in all your endeavors. I'd also like to thank the staff of JLab who not only tolerated our incessant questions but actually continued to help us in spite of our extremely specific needs. Thank you to Jay Benesch, Yves Roblin, Alexandre Camsonne, and Ole Hansen. Also thank you to the technical staff of Hall A: Jessie Butler, Heidi Fansler, Jack Segal, Andrew Lumanog, and Ellen Becker.

Turning to the personal side, I would like to give a very special thank you to Aaron Heuer and Tobias Gies. I don't believe I've properly expressed it but your support and your lending me a sympathetic ear all these years has been the continual highlight of each week these past few years. I truly don't believe I would have been able to muddle through all the challenges of this program without your support. Us three are separated by great distance but talking with the both of you makes this world seem all the smaller, and those distances more bearable. And one day, mark my words, there will be a fantastic reunion for the ages, even if we must continue to wait.

I would also like to thank my friend Andréa C. Mason who in a difficult period in my life helped open me up to who I really am, and helped me discover a whole new world within myself that I might have completely ignored otherwise. Thanks to you, I am Allison now, proudly and indisputably. I cannot thank you enough for helping me realize this freedom, and for helping me live more authentically than ever before. I would also like to thank the various members of the trans community who helped me throughout the years who are, I am delighted to say, too numerous to mention. And in return I can only offer my promise that I will be there to fight for that beautiful day when we are understood and accepted as who we are, our care is prioritized and our existence is no longer imperiled by hatred.

Finally I would like to thank my family, my bedrock of support during my academic adventures. I would like to thank my father Joseph, my mother Christine, my aunts Julie, Anne, and Melissa, my uncles Chip and Mark, and my grandparents Jim and Sigrid. I would like to give a special thank you to my sister Emma, who is an incorrigible dork like myself, and is the best sister a gal could ever hope for. And thank you to Rhea for being an excellent friend to our family.

Additionally thank you to my friends Chris and Matt, who I'll always remember fondly.

Contents

| | |
|--|------------|
| Abstract | iv |
| Acknowledgements | vi |
| List of Figures | xii |
| List of Tables | xv |
| 1 Introduction | 1 |
| 1.1 Motivation | 3 |
| 1.2 Theory | 4 |
| 1.2.1 Electroweak Unification | 5 |
| 1.2.2 Electroweak Scattering Amplitude | 7 |
| 1.2.3 Form Factors | 9 |
| 1.2.4 Parity Violation, Asymmetry & Neutron Skin Thickness | 11 |
| 1.3 Nuclear Structure | 15 |
| 1.3.1 Nuclear Equation of State | 17 |
| 1.3.2 ^{208}Pb and Neutron Stars | 17 |
| 1.3.3 The Importance of ^{48}Ca | 19 |
| 2 PREX-II/CREX Overview | 21 |
| 2.1 Parity-Violating Electron Scattering | 21 |
| 2.2 Kinematics | 24 |
| 2.3 Measuring a Small Asymmetry | 26 |
| 2.4 Beam Polarization Effects | 27 |
| 2.4.1 Transverse Polarization | 28 |
| 2.5 Measuring Δr_{np} from Asymmetry | 28 |

| | | |
|----------|--|-----------|
| 3 | PREX-II/CREX Experimental Apparatus | 31 |
| 3.1 | CEBAF Complex | 31 |
| 3.1.1 | Polarized Source | 33 |
| 3.1.2 | Injector | 37 |
| 3.1.3 | Accelerator | 38 |
| 3.2 | Hall A Beamline Features | 38 |
| 3.2.1 | Beam Charge Monitors | 39 |
| 3.2.2 | Beam Position Monitors | 40 |
| 3.2.3 | Beam Modulation Coils | 42 |
| 3.2.4 | Polarimeters | 42 |
| 3.2.5 | Raster | 46 |
| 3.2.6 | Small-Angle Monitors | 47 |
| 3.3 | Feedback | 48 |
| 3.3.1 | Charge Feedback | 48 |
| 3.3.2 | Fast Feedback | 48 |
| 3.4 | Target System | 49 |
| 3.4.1 | PREX-II Targets | 50 |
| 3.4.2 | CREX Target | 51 |
| 3.5 | Radiation Controls | 52 |
| 3.5.1 | Monte Carlo Simulation | 52 |
| 3.5.2 | Collimator | 53 |
| 3.5.3 | Shielding Concept and Design | 55 |
| 3.6 | Spectrometers & Optics | 60 |
| 3.6.1 | Septum Magnet | 60 |
| 3.6.2 | Acceptance Collimator | 60 |
| 3.6.3 | Spectrometer Quads & Dipole | 61 |
| 3.7 | Main Detectors | 63 |
| 3.7.1 | \mathcal{A}_T Detectors | 64 |
| 3.8 | Counting Mode Detectors | 65 |
| 3.8.1 | Drift Chambers | 65 |
| 3.8.2 | S0 & S3 Detectors | 65 |
| 3.9 | Data Acquisition | 66 |
| 3.9.1 | Integrating Mode DAQ | 66 |
| 3.9.2 | Counting Mode DAQ | 68 |
| 3.10 | Slow Controls, EPICS, & CODA | 69 |

| | | |
|----------|--|------------|
| 4 | Compton Polarimetry Principles | 70 |
| 4.1 | Compton Kinematics | 71 |
| 4.2 | Compton Cross Sections & Asymmetry | 74 |
| | 4.2.1 Compton Analyzing Power | 77 |
| | 4.2.2 Compton Radiative Corrections | 79 |
| 4.3 | Hall A Compton Polarimeter | 80 |
| | 4.3.1 Laser System | 81 |
| | 4.3.2 Photon Detector | 85 |
| | 4.3.3 Electron Detector | 90 |
| 4.4 | Compton DAQ | 91 |
| | 4.4.1 Integrating Mode Components | 92 |
| | 4.4.2 Counting Mode Components | 94 |
| | 4.4.3 Pulsar DAQ Control | 102 |
| 4.5 | Compton Analyzer | 107 |
| | | |
| 5 | Compton Polarimetry Data | 109 |
| 5.1 | Beam Monitor Calibrations | 109 |
| 5.2 | Measuring a Compton Asymmetry | 112 |
| | 5.2.1 Cycles & Snails | 112 |
| | 5.2.2 Measured Asymmetries | 115 |
| | 5.2.3 Data Aggregation | 117 |
| 5.3 | Data Quality & Cuts | 118 |
| | 5.3.1 Pedestal Subtraction | 119 |
| | 5.3.2 CycleCut | 122 |
| | 5.3.3 Background Sources and Corrections | 124 |
| 5.4 | Analyzing Power | 125 |
| | 5.4.1 Compton Monte Carlo Simulation | 127 |
| 5.5 | Laser Polarization Measurements | 128 |
| | 5.5.1 NPBS Laser Polarimetry | 129 |
| | 5.5.2 Exit Line Scans | 130 |
| | 5.5.3 Off-100% DOCP Running | 132 |
| 5.6 | Sources of Systematic Uncertainty | 133 |
| | 5.6.1 Photon Cone Offset & Simulation | 134 |
| | 5.6.2 Laser Polarization & Optical Model | 145 |
| | 5.6.3 Detector Corrections | 149 |
| | 5.6.4 Beam Kinematics | 154 |
| 5.7 | CREX Compton Result | 155 |
| | 5.7.1 CREX Møller Result | 161 |

| | | |
|----------|--|------------|
| 5.7.2 | CREX Combined Polarimetry Result | 163 |
| 5.8 | PREX-II Compton Result | 165 |
| 6 | PREX-II/CREX Analysis | 167 |
| 6.1 | Cuts | 168 |
| 6.2 | Asymmetries | 168 |
| 6.2.1 | Helicity-Correlated Beam Properties | 170 |
| 6.2.2 | Regression & Dithering | 171 |
| 6.2.3 | Asymmetry Corrections | 174 |
| 6.3 | Spectrometer Optics & Acceptance | 175 |
| 6.4 | Counting Mode Measurements | 177 |
| 6.4.1 | Detector Alignment & Inelastic Backgrounds | 177 |
| 6.4.2 | Q^2 Measurements | 179 |
| 6.5 | Transverse Asymmetry Measurements | 180 |
| 6.6 | PREX-II/CREX Physics Asymmetry | 182 |
| 7 | Results & Discussion | 185 |
| 7.1 | Form Factors & Skin Thickness | 185 |
| 7.1.1 | PREX-II | 185 |
| 7.1.2 | CREX | 187 |
| 7.2 | Implications | 188 |
| 7.2.1 | PREX-II & Symmetry Energy | 188 |
| 7.2.2 | PREX-II & Neutron Stars | 189 |
| 7.2.3 | CREX Implications for DOM Theories | 190 |
| 7.3 | What Does the Future Hold? | 191 |
| 7.3.1 | MOLLER | 191 |
| 7.3.2 | SoLID | 192 |
| 7.3.3 | P2 & MREX | 194 |
| 7.4 | Summary | 194 |
| A | PREX-II Compton Snailwise Plots | 196 |
| B | CREX Compton Snailwise Plots | 206 |
| | Bibliography | 215 |

List of Figures

| | | |
|------|---|----|
| 1.1 | Nuclei Charge Densities | 2 |
| 1.2 | EM and Weak Scattering Feynman Diagrams | 8 |
| 1.3 | Correlation of asymmetry and neutron skin thickness | 14 |
| 1.4 | Neutron Skin Correlations with Neutron Star Radii | 18 |
| 2.1 | PREX-II/CREX Components Diagram | 23 |
| 2.2 | Cross Sections and Asymmetries vs. Scattering Angle | 25 |
| 2.3 | Asymmetry Sensitivity vs. Scattering Angle | 26 |
| 3.1 | CEBAF 12 GeV Upgrade Schematic | 32 |
| 3.2 | Polarized Source Layout | 33 |
| 3.3 | RTP Pockels Cell Voltages | 34 |
| 3.4 | Pockels Cell Asymmetry Types | 36 |
| 3.5 | Wien Filter Diagram | 37 |
| 3.6 | Hall A Layout | 38 |
| 3.7 | Hall A BCMs | 39 |
| 3.8 | BPM Diagram | 41 |
| 3.9 | Møller Polarimeter Diagram | 44 |
| 3.10 | PREX-II Raster Plots | 47 |
| 3.11 | SAM Diagram | 48 |
| 3.12 | Cold Target Ladder | 49 |
| 3.13 | Lead Target Degradation | 51 |
| 3.14 | Beamline Collimator | 54 |
| 3.15 | Collimator Shielding | 56 |
| 3.16 | PREX-II/CREX Pivot Region | 59 |
| 3.17 | Septum & Acceptance Path | 61 |
| 3.18 | Q1 Collimators | 62 |
| 3.19 | HRS Optical Diagram | 63 |

| | | |
|------|--|-----|
| 3.20 | PREX-II/CREX Detector Package | 64 |
| 3.21 | PREX-II/CREX Helicity Patterns | 67 |
| 4.1 | Feynman Diagrams of Compton scattering | 72 |
| 4.2 | Compton Scattering Angles | 72 |
| 4.3 | Scattering Photon Energy vs Scattering Angle | 74 |
| 4.4 | Compton Cross Section and Analyzing Power | 76 |
| 4.5 | Hall A Compton Polarimeter Layout | 80 |
| 4.6 | Compton Laser System | 81 |
| 4.7 | Compton Laser Electronics | 83 |
| 4.8 | QW1/HW1 DOCP Function | 86 |
| 4.9 | Photon Detector Diagram | 86 |
| 4.10 | Photon Detector Upstream Photo | 87 |
| 4.11 | Photon Detector Photo | 89 |
| 4.12 | Compton Integrating Timing Diagram | 92 |
| 4.13 | Compton DAQ Photon Signals | 93 |
| 4.14 | Compton DAQ Clock Signals | 97 |
| 4.15 | Single Compton Pulse Shape | 98 |
| 4.16 | Compton DAQ Run Scaler Components | 101 |
| 4.17 | Compton DAQ IP Scaler Components | 102 |
| 4.18 | Pulser Timing Diagram | 103 |
| 4.19 | Compton DAQ Map of Pulser Signals | 105 |
| 4.20 | Nonlinearity Gain Thermal Dependence | 107 |
| 5.1 | Compton laser cycle measured quantities | 116 |
| 5.2 | Pedestal Shift Cycle Comparison | 120 |
| 5.3 | CREX Compton Acc0 RMS | 121 |
| 5.4 | Compton Spectrum Comparison | 126 |
| 5.5 | Laser DOCP Test Setup | 129 |
| 5.6 | Laser Exit Line Scan Diagram | 131 |
| 5.7 | Compton MC Fits | 135 |
| 5.8 | PREX Analyzing Power Simulations | 137 |
| 5.9 | PREX-II Analyzing Power Vs Time | 137 |
| 5.10 | CREX Compton Circle Fits | 139 |
| 5.11 | CREX Photon Cone Offset Simulations | 140 |
| 5.12 | CREX Simulation Spectrum Comparison | 141 |
| 5.13 | CREX Photon Cone Offset Estimate with Rudimentary χ^2 Simulation | 144 |

| | | |
|------|---|-----|
| 5.14 | CREX Laser DOCP Solutions | 146 |
| 5.15 | PREX-II Compton DOCP Time Dependence | 147 |
| 5.16 | Compton Nonlinearity Functions | 150 |
| 5.17 | PREX-II PMT Gain Shift | 153 |
| 5.18 | CREX Compton Snailwise Polarization | 156 |
| 5.19 | CREX Compton Piecewise Fit Polarization | 158 |
| 5.20 | CREX Møller Polarization Measurements | 162 |
| 5.21 | CREX Compton-Møller Polarimetry Comparison | 163 |
| 5.22 | CREX Compton-Møller Residuals | 164 |
| 5.23 | PREX-II Compton Moller Comparison | 166 |
| | | |
| 6.1 | Experimental Asymmetry Calculations | 169 |
| 6.2 | BPM Regression Slopes | 172 |
| 6.3 | Beam Modulation Cycle | 173 |
| 6.4 | Sieve Collimators | 176 |
| 6.5 | CREX Acceptance Function | 177 |
| 6.6 | CREX Inelastic Backgrounds | 178 |
| 6.7 | PREX-II/CREX Beam Corrections to Asymmetry | 184 |
| | | |
| 7.1 | ^{208}Pb Weak Charge Density | 187 |
| 7.2 | CREX Form Factors | 188 |
| 7.3 | PREX-II Symmetry Energy | 189 |
| 7.4 | PREX-II Result & Neutron Star Deformability | 190 |
| 7.5 | MOLLER Experimental Setup | 192 |
| 7.6 | SoLID PVDIS Configuration | 193 |

List of Tables

| | | |
|-----|--|-----|
| 2.1 | PVES Experiment Asymmeteries | 22 |
| 2.2 | Neutron Radius Calculation Parameters | 30 |
| 3.1 | Collimator Energy Absorption | 54 |
| 3.2 | HRS Radiation Dose | 57 |
| 3.3 | Collimator Shield Radiation Dose | 58 |
| 3.4 | Simulated Skyshine Neutron Rate | 58 |
| 4.1 | Compton Edge Values | 74 |
| 4.2 | Compton DAQ Discriminator Channels | 100 |
| 5.1 | Compton DAQ BCM/Laser Power Resolution | 111 |
| 5.2 | Compton Data Overview | 118 |
| 5.3 | CycleCut Results | 124 |
| 5.4 | Laser Polarizations for Experimental Running | 133 |
| 5.5 | Compton Laser DOCP Systematics | 149 |
| 5.6 | CREX Compton Polarization Averages | 160 |
| 5.7 | CREX Compton Uncertainty Table | 160 |
| 5.8 | Compton Polarimetry Uncertainty Comparison | 161 |
| 5.9 | CREX Møller Uncertainty Table | 162 |
| 6.1 | PREX-II/CREX Raw Asymmetries | 170 |
| 6.2 | PREX-II/CREX Raw Asymmetries | 170 |
| 6.3 | PREX-II/CREX Raw Asymmetries | 175 |
| 6.4 | CREX Inelastic Contribution | 179 |
| 6.5 | PREX-II/CREX Q^2 Measurements | 180 |
| 6.6 | CREX Transverse Asymmetry Correction | 182 |
| 6.7 | PREX-II/CREX Uncertainty Table | 183 |
| 6.8 | PREX-II/CREX Measured Asymmetries | 184 |

7.1 PREX-II Physical Measurements 186

Chapter 1

Introduction

The inception of nuclear physics as a field of study can be traced to 1911 with the publication of the results of a series of experiments carried out by Ernest Rutherford, Hans Geiger, and Ernest Marsden, which suggested that atoms contained a small dense positively-charged nucleus [1]. This discovery led to the formulation of the Bohr model of the atom [2]. The 1932 discovery of the neutron by James Chadwick [3] revealed that atomic nuclei were composed of two primary nucleons: the positively-charged proton and the electrically neutral neutron.

Contemporaneous with these early developments in nuclear physics was the development of spin quantum mechanics. The Stern-Gerlach experiment, first performed in 1922, demonstrated the quantization of magnetization in magnetism [4], which was later determined by Wolfgang Pauli to be a quantization of spin angular momentum [5]. The spin angular momentum of particles such as protons, neutrons, and electrons was found to be either $+\frac{\hbar}{2}$ or $-\frac{\hbar}{2}$. In 1928, Paul Dirac proposed the mathematical formalism of the spin-dependent interactions of particles with $\pm\frac{1}{2}$ spin [6]. These developments helped modernize the field of quantum theory, and helped motivate further experimental studies of spin-dependent quantum effects.

Early observations of the process of radioactive β -decay suggested that the process involved four spin- $\frac{1}{2}$ particles. In 1956 Lee and Yang theorized that the weak interaction was not invariant under an inversion of spatial coordinates [7]. This was experimentally verified the following year by a team led by Chien Shiung Wu [8]. Thus, the weak nuclear force was shown to not conserve parity. Parity is said to be conserved for any quantity \vec{k} if

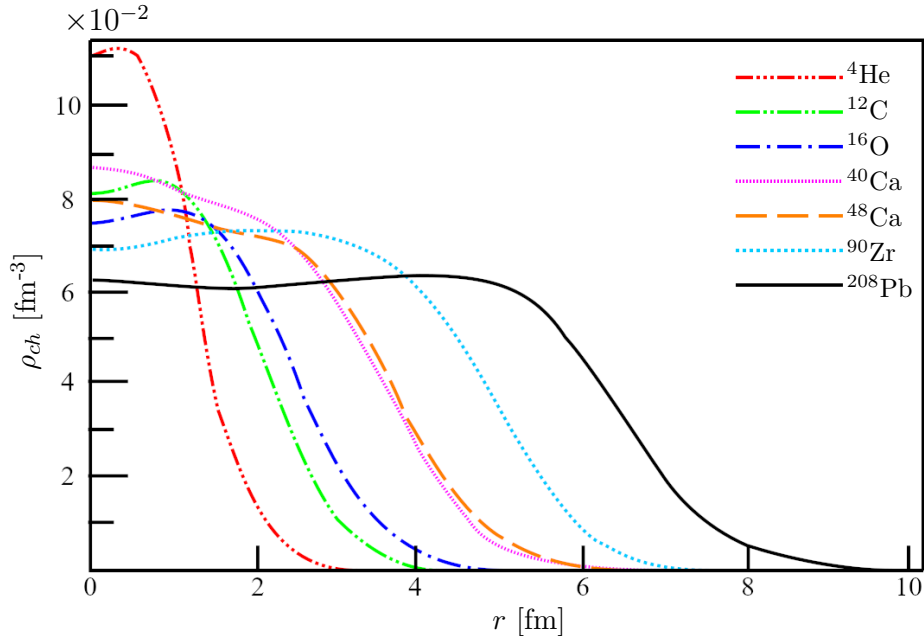


Figure 1.1: Nuclear charge densities plotted as a function of radii for different doubly-closed shell nuclei. Adapted from Foris and Papanicolas [9].

under a parity transformation \mathcal{P} , \vec{k} is invariant:

$$\mathcal{P}(\vec{k}(x, y, z)) = \vec{k}(-x, -y, -z) = \vec{k}(x, y, z). \quad (1.1)$$

While electromagnetic interactions conserve parity, the fact that weak interactions do not opens up possibilities for experimental confirmation of weakly interacting phenomena.

Developments in nuclear physics in the latter half of the 20th century include direct measurements of the electric charge density of nuclei of different sizes. Measurements of the mean charge radius of different nuclei $\sqrt{\langle r_{ch} \rangle^2}$ made using elastic electron-nucleon scattering varied between 1.6 fm (for ${}^4\text{He}$) and 5.5 fm (for ${}^{208}\text{Pb}$) [10]. The mean charge density as a function of nuclear radius can be seen for nuclei of various sizes in Fig. 1.1. While both electromagnetic and weak scattering amplitudes contribute to elastic scattering cross section measurements, in reality the amplitude of weak scattering is suppressed relative to the electromagnetic scattering and thus contributes

very little to these measurements. As a result, early electron-nucleon elastic scattering could reveal a distribution of protons in nuclei, but the neutron, being electrically neutral, would not be sensitive to these experimental techniques, leaving the neutron distribution of nuclei unmapped.

1.1 Motivation

Any atomic nucleus containing Z protons and N neutrons is either stable meaning that the nucleus will continue having Z protons and N neutrons indefinitely, or unstable meaning that the nucleus will undergo a radioactive decay changing the number of protons and neutrons it contains. For stable light nuclei ($Z < 20$), the ratio $\frac{N}{Z}$ is approximately 1. However, as nuclei get heavy the ratio changes increasingly such that $\frac{N}{Z} > 1$ in order to remain stable. Thus, without scattering probes that do not utilize EM effects, the neutron distribution in heavy nuclei cannot be determined despite the fact that in heavy stable nuclei neutrons outnumber protons.

Excess neutrons in heavy nuclei are predicted to form a “neutron skin” where the radii occupied by neutrons in the nucleus extends beyond the radii occupied by protons. The thickness of the neutron skin is then the difference between the mean neutron radius r_n and the mean proton radius r_p

$$\Delta r_{np} = \sqrt{\langle r_n^2 \rangle} - \sqrt{\langle r_p^2 \rangle}. \quad (1.2)$$

Experiments as early as 1980 measured $\Delta r_{np}^{(208)}$ using hadronic scattering techniques [11]. These experiments have since measured $\Delta r_{np}^{(208)}$ through proton scattering, alpha scattering, π^- scattering, and antiprotonic atoms [12]. However, these experimental measurements are inherently limited by systematic uncertainties from QCD, which makes extracting $\Delta r_{np}^{(208)}$ from experimental observables challenging.

Strong and electromagnetic interactions conserve parity, but because weak interactions do not, this nonconservation can be exploited by scattering experiments. Parity violation in electron-nucleon scattering was first observed in 1978, and the result was a major milestone in confirming the Weinberg-Salam model of electroweak unification [13]. Since then the parity-violating electron scattering (PVES) technique has been a remarkable probe of nuclear structure and tests of the standard model.

Weak charge is analogous to electric charge in that weak charge measures a nucleus' coupling to weak interactions. Parity violation in atomic systems and in electron scattering have verified that the proton weak charge is less than that of the neutron. Consequently, scattering techniques that can take advantage of weak interactions can act as probes of neutron density, analogous to how electromagnetic elastic scattering acts as a probe of proton density.

To obtain a precise measurement of Δr_{np} on two key nuclei two experiments employing the parity-violating electron scattering technique were proposed. The first was PREX-II, designed to measure parity violation in electron scattering off ^{208}Pb , while the second CREX was proposed to measure parity violation in ^{48}Ca . A description of the mathematical formalism of the observable quantities in both experiments will be discussed in Sec. 1.2, while a description of the implications of the results of both experiments as well as the importance of these two nuclei will be discussed in Sec. 1.3.

1.2 Theory

Scattering experiments in all their different forms are traditionally one of the most common experimental techniques employed by nuclear and particle physicists. The primary observable in scattering experiments is the cross section σ which measures the likelihood of scattering happening for any given reaction. To calculate the cross section from first principles we must first calculate the matrix element \mathcal{M} for each reaction considered. In the case of electron nucleon scattering the reaction is the elastic scattering of two spin- $\frac{1}{2}$ particles. The propagation of a spin- $\frac{1}{2}$ particle is governed by the Dirac equation¹ which is

$$(i\partial_\mu\gamma^\mu - m)\psi = 0, \quad (1.3)$$

where γ^μ are the covariant gamma matrices, m is the particle mass, and ψ is the particle wave function.²

This equation is solved generally by a wave function of the form

$$\psi = u(p)e^{-ip_\mu x^\mu}, \quad (1.4)$$

¹The calculations in this dissertation will be written in units where $\hbar = c = 1$ and therefore factors of \hbar and c will be omitted from equations.

²This dissertation also uses the Einstein summation notation to shorted sums: $a_\mu b^\mu = \sum_\mu \sum_\nu \eta^{\mu\nu} a_\mu b_\nu$ where $\eta^{\mu\nu}$ is the metric tensor.

where $u(p)$ is a Dirac spinor vector, and $p_\mu x^\mu$ is the inner product of 4-vector position and momentum.

From this it can be shown that the cross section σ for four-particle scattering can be expressed in terms of the scattering amplitude \mathcal{M} as

$$d\sigma = \frac{|\mathcal{M}|^2}{4\sqrt{(p_1 \cdot p_2)^2 - m_1^2 m_2^2}} \left(\frac{d^3 \vec{p}_3}{(2\pi)^3 2E_3} \right) \left(\frac{d^3 \vec{p}_4}{(2\pi)^3 2E_4} \right) \times (2\pi)^4 \delta(p_1 + p_2 - p_3 - p_4), \quad (1.5)$$

where p_1 , and p_2 are the four-momenta of the two initial-state particles, p_3 and p_4 are the four-momenta of the two final-state particles, m and E are the mass and energy respectively of each particle numbered 1-4, and δ is the Dirac delta function, included to account for conservation of energy and momentum [14].

For electron-nucleon scattering we can take the approximation $m_1 \ll m_2$. In this limit if we neglect the effects of nuclear recoil then the cross-section of electron-nucleon scattering becomes

$$\frac{d\sigma}{d\Omega} = \left(\frac{1}{8\pi M} \right)^2 |\mathcal{M}|^2, \quad (1.6)$$

where M is the nucleon mass. The cross section here is calculated with the assumption that the nucleon is a point like particle. In practice the finite size of nucleons and their structure must be taken into account. This correction will be described in Sec. 1.2.3.

For the PREX-II and CREX experiments, the electrons measured were scattered either by EM processes or by the weak processes. Thus the scattering amplitude had two components:

$$|\mathcal{M}|^2 = |\mathcal{M}_{EM} + \mathcal{M}_{weak}|^2. \quad (1.7)$$

These matrix elements then have to be constructed dependent on the kinematics of each of their respective processes.

1.2.1 Electroweak Unification

Knowing the scattering amplitude \mathcal{M} is important to these calculations as it is used in calculating both cross section and reaction rate. The kinematics contained within also must be taken into account while integrating over

the outgoing particle momenta. Constructing the amplitude requires understanding the nature of each interaction, and this can be different for both electromagnetic interactions and weak ones.

While the rules for electromagnetic interactions were codified in the late 1940's [15], the development of the theory of the weak nuclear interaction was still ongoing. The weak force was originally proposed in 1934 as a solution to describe β -decays [16] and, as described above, was developed further in the 1950's when it was shown that the weak force did not conserve parity. The next major development in the weak interaction was the development of a unified theory of the electromagnetic and weak interactions. In 1967 Steven Weinberg proposed a theory of weak interactions which proposed the existence of left- and right-handed Dirac spinors analogous to the ones that are used in quantum electrodynamics [17]:

$$u_L(p) = \frac{1 - \gamma^5}{2}u(p), \quad u_R(p) = \frac{1 + \gamma^5}{2}u(p), \quad (1.8)$$

where γ^5 is the so-called ‘‘fifth’’ gamma matrix defined by:

$$\gamma^5 \equiv i\gamma^0\gamma^1\gamma^2\gamma^3. \quad (1.9)$$

Once the Lagrangian for the interaction is calculated, three vector bosons become apparent. The first is the massless electrically neutral photon. The second is a massive charged boson, the W^\pm . The third is the massive electrically neutral Z^0 boson. Though the W and Z bosons would not be directly detected until later, the masses of the bosons were predicted to be related to each other as

$$M_W = M_Z \cos \theta_w, \quad (1.10)$$

where θ_w is the ‘‘weak mixing angle’’ which must be measured empirically. The mass of the W and Z bosons ends up being what suppresses the strength of the weak interaction relative to the electromagnetic interaction. The propagator for a photon interaction has no mass term and instead leaves the scattering amplitude inversely proportional to momentum transfer q :

$$\mathcal{M}_{EM} \propto \frac{g_e^2}{q^2}. \quad (1.11)$$

Whereas the amplitude of weak scattering is suppressed by the mass of each mediating boson:

$$\mathcal{M}_{weak}^W \propto \frac{g_w^2}{q^2 - M_W^2}, \quad \mathcal{M}_{weak}^Z \propto \frac{g_z^2}{q^2 - M_Z^2}, \quad (1.12)$$

where g_w and g_z are related to the electromagnetic coupling constant as:

$$g_w \propto \frac{g_e}{\sin \theta_w}, \quad g_z \propto \frac{g_e}{\sin \theta_w \cos \theta_w}. \quad (1.13)$$

While the charged weak interaction with W^\pm is not relevant for the measurements of nuclear structure taken in PREX-II and CREX, the weak neutral current interaction mediated by Z^0 is. The Z -boson mass $M_Z \approx 90$ GeV $\gg \sqrt{\langle q^2 \rangle}$ for both PREX-II and CREX kinematics the weak scattering amplitude then becomes

$$\mathcal{M}_{weak} \propto \frac{g_z^2}{M_Z^2}. \quad (1.14)$$

In an energy regime where $q^2 > M_Z^2$ then the relative suppression of weak interactions disappears and the unified “electroweak” interaction can be observed. However, for the kinematics for PREX-II and CREX the mass suppression of the weak interaction is a significant effect, making the relative size of the weak cross section of electron-nucleon elastic scattering small.

1.2.2 Electroweak Scattering Amplitude

To understand the dependence of the specific kinematics of the cross section on the scattering, we must calculate $|\mathcal{M}|^2$. As equation 1.7 demonstrates, the electromagnetic amplitude dominates the full scattering. Therefore the calculation of \mathcal{M}_{EM} yields information about the overall magnitude of the cross section, whereas the calculation of \mathcal{M}_{weak} yields information about the size of the asymmetric effect from parity violation.

First the EM scattering amplitude can be written in the Feynman calculus as

$$\mathcal{M}_{EM} = -\frac{g_e^2}{(p_1 - p_3)^2} [\bar{u}^{(s_3)}(p_3) \gamma^\mu u^{(s_1)}(p_1)] [\bar{u}^{(s_4)}(p_4) \gamma_\mu u^{(s_2)}(p_2)], \quad (1.15)$$

where $p_1 \dots p_4$ are the four-momenta of the incoming and outgoing particles, and $s_1 \dots s_4$ specify the spins of the particles. The particles are labeled in the diagrams shown in Fig. 1.2.

By assuming the mass of the nucleon M is much larger than the mass of the electron m_e , and that the effects of nuclear recoil can be safely neglected, the calculation of both scattering amplitude and cross section can be simplified. This has already been taken into account in equation 1.15 as

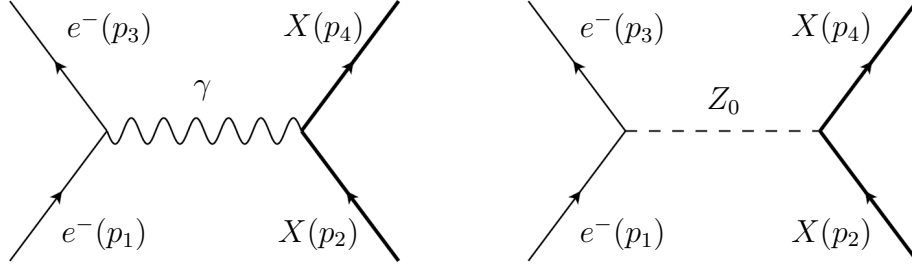


Figure 1.2: Feynman diagrams for electron-nucleon scattering for EM processes (left) and weak processes (right). The nucleon X represents either protons or neutrons.

the integration over momentum transfer causes the factor of q^2 to evaluate as $q^2 = (p_1 + p_2 - p_3 - p_4)^2 = (p_1 - p_3)^2$ because the nucleon is treated as being at rest both before and after scattering. Also, the magnitude of the momentum of the electron is treated as equal before and after scattering $|\vec{p}_1| = |\vec{p}_3|$, with a scattering angle θ as $\vec{p}_1 \cdot \vec{p}_3 = |\vec{p}_1|^2 \cos \theta$. With this in mind the EM scattering cross section is

$$\left(\frac{d\sigma}{d\Omega}\right)_{Mott} = \left(\frac{1}{8\pi(E+M)}\right)^2 |\mathcal{M}_{EM}|^2 = \left(\frac{\alpha M Z}{2E(E+M)\sin^2\frac{\theta}{2}}\right)^2 \cos^2\frac{\theta}{2}, \quad (1.16)$$

where E is the electron energy, Z is the number of protons in the nucleus and $\alpha \approx \frac{1}{137}$ is the fine structure constant. This is the Mott cross section, which models the spin-averaged interaction between one light and one heavy charged particle. Because $|\mathcal{M}_{EM}|^2$ is the leading term in the expansion of equation 1.7 it also serves as an approximation for the overall cross section of elastic electron-nucleon scattering.

The weak interaction amplitude terms then allow the overall cross section to include chiral effects due to the weak interaction's nonconservation of parity. The amplitude of weak scattering can then be written as

$$\mathcal{M}_{weak} = -\frac{g_z^2}{4M_Z^2} [\bar{u}(p_3)\gamma_\mu(c_V^e - c_A^e\gamma^5)u(p_1)][\bar{u}(p_4)\gamma^\mu(c_V^q - c_A^q\gamma^5)u(p_2)], \quad (1.17)$$

where c_V^e and c_V^q are vector coefficients for the electron and quark respectively and c_A^e and c_A^q are the axial vector coefficients for the electron and the quark respectively. While the electron coefficients are known:

$$c_V^e = 2 \sin \theta_w - \frac{1}{2}, \quad c_A^e = -\frac{1}{2}, \quad (1.18)$$

the value of the quark coefficients are dependent on the flavor of the quark in the scattering:

$$c_V^q = \begin{cases} \frac{1}{2} - \frac{4}{3} \sin^2 \theta_w, & \text{if quark is } u \\ -\frac{1}{3} + \frac{2}{3} \sin^2 \theta_w, & \text{if quark is } d \text{ or } s \end{cases}$$

$$c_A^q = \begin{cases} \frac{1}{2}, & \text{if quark is } u \\ -\frac{1}{2}, & \text{if quark is } d \text{ or } s. \end{cases}$$

One important assumption that is made in the calculation of the Mott cross section is that both the electron and nucleon are point-like particles. At the energies required to reach the limit of weak scattering the internal structure of nuclei has an effect on the cross section. The Mott cross section can still be used in the overall cross section, albeit with a correction factor taking into account the internal structure of the nucleus.

1.2.3 Form Factors

To take into account the effect of nuclear density on the scattering we must first consider the electromagnetic effects of scattering off a finite volume of charge. While the amplitude \mathcal{M}_{EM} was calculated for the specific case of electron-nucleon scattering in Sec. 1.2.2, the amplitude can be expressed more generally in terms of a scalar potential as

$$\mathcal{M}_{EM} = \langle \psi_f | V(\vec{r}) | \psi_i \rangle. \quad (1.19)$$

For the electromagnetic component of scattering, the potential is the Coulomb potential for a charge density:

$$V(\vec{r}) = \frac{Ze^2}{4\pi\epsilon_0} \int d^3\vec{r}' \frac{\rho_{ch}(\vec{r}')}{|\vec{r} - \vec{r}'|}, \quad (1.20)$$

where $\rho_{ch}(\vec{r})$ is the electric charge density and e is the electron charge.

The result of this formulation is that the integral of $V(\vec{r})$ can be parameterized into a Fourier transform over the nuclear charge density

$$F_{ch}(q^2) \equiv \int d^3\vec{r}' e^{i\vec{q}\cdot\vec{r}'} \rho_{ch}(\vec{r}'). \quad (1.21)$$

This is the EM charge form factor, which by definition encodes geometric information about nuclear structure. Because what remains in the integral in the inner product in equation 1.19 is the integral over the Coulomb potential the rest of the integration yields the Mott cross section calculated in equation 1.16 [18] which is

$$\frac{d\sigma}{d\Omega} = \left(\frac{d\sigma}{d\Omega} \right)_{Mott} |F_p(q^2)|^2. \quad (1.22)$$

Now we have succeeded in finding the relation between an experimentally observable quantity (scattering cross section) with a quantity containing information about the geometry of the scattering nucleus. However, the formulation above is specifically for the electromagnetic interaction which is insensitive to the neutron. Thus for measuring neutron density and neutron skin we need a similar formulation for the weak interaction.

Weak Charge & The Weak Form Factor

To understand how the measurement of the weak amplitude in electron-nucleon scattering is related to nuclear structure we can add an axial vector term to the potential in equation 1.20 [18] as

$$\hat{V}(\vec{r}) = V(\vec{r}) + \gamma^5 A(\vec{r}), \quad (1.23)$$

where the vector potential term $A(\vec{r})$ is

$$A(\vec{r}) = \frac{G_F}{2^{\frac{3}{2}}} [(1 - 4 \sin^2 \theta_w) Z \rho_p(\vec{r}) - N \rho_n(\vec{r})]. \quad (1.24)$$

G_F is the Fermi constant, $\rho_p(\vec{r})$ is the nuclear proton density and $\rho_n(\vec{r})$ is the nuclear neutron density. While the nuclear charge density and nuclear proton density are interchangeable the effect of nucleons coupling to the weak interactions is more subtle. When integrating the potential in an inner product calculation the integration takes the form of a Fourier transform over the charge density, and this is true when applied to the axial vector

potential term too. Except this time the weak form factor has both proton and neutron components:

$$F_{weak}(Q^2) = \int d^3\vec{r}' e^{i\vec{q}\cdot\vec{r}'} [(1 - 4 \sin^2 \theta_w) Z \rho_p(\vec{r}') - N \rho_n(\vec{r}')] \equiv \int e^{i\vec{q}\cdot\vec{r}'} \rho_{weak}(\vec{r}'), \quad (1.25)$$

where Q^2 is the mean momentum transfer $Q = \sqrt{\langle q^2 \rangle}$. Here we define a density of “weak charge” ρ_{weak} analogous to the electrical charge density ρ_{ch} used in the electromagnetic potential. The empirical value of the weak mixing angle $\sin^2 \theta_w \approx 0.23$ meaning that the overall factor governing the proton component of weak charge is $1 - 4 \sin^2 \theta_w \approx 0.08$. Because the neutron term has no such factor, the neutron density of the nucleus largely determines the weak charge density making this quantity a good proxy for neutron density measurements.

Knowing now that the weak form factor $F_{weak}(Q^2)$ can be used to measure nuclear neutron densities (and ultimately the neutron radius) we need an experimental observable related to this form factor. In addition this observable must be measurable in spite of the weak interaction’s suppression relative to electromagnetic effects at electron energies below the electroweak unification threshold.

1.2.4 Parity Violation, Asymmetry & Neutron Skin Thickness

One of the weak interaction’s defining features is its nonconservation of parity. To measure parity violation experimentally, one aspect of the weak interaction must undergo a parity transformation and the results with and without that transformation can be compared. Any difference in measured scattering rates or cross sections can be attributed to the weak interaction exclusively.

The form of the parity transformation in equation 1.1 can be applied to the electron wavefunction $\psi(\vec{r})$. One constraint of the eigenvalues of the parity operator is that applying two parity transformations should produce the original function [19] which is

$$\mathcal{P}^2(\psi(\vec{r})) = \mathcal{P}(p\psi(-\vec{r})) = p^2\psi(\vec{r}) = \psi(\vec{r}). \quad (1.26)$$

This eigenvalue then is constrained to be $p = \pm 1$ with $+1$ corresponding to parity conservation and -1 corresponding to parity nonconservation. While

the formalism of parity transformation is laid out, we need now to design an experimental system capable of exploiting and observing this parity violation.

One aspect of the scattering that can be transformed by parity is the spin of the incident electron beam³. More accurately, the sign of the relative projection of spin onto the direction of momentum can be reversed under a parity transformation. Particle spin projected onto the direction of momentum is termed “helicity” and can be expressed by

$$h = \vec{s} \cdot \hat{p}, \quad (1.27)$$

where \vec{s} is the spin vector and $\hat{p} = \frac{\vec{p}}{|\vec{p}|}$ is the unit vector of momentum. If the spin of electrons is parallel to the direction of momentum then $h = 1$ and if the direction of spin is anti-parallel to momentum then $h = -1$. If one of these is true then under a parity transformation the sign of helicity is reversed as

$$\mathcal{P}h = \mathcal{P}(\vec{s} \cdot \hat{p}) = \vec{s} \cdot (-\hat{p}). \quad (1.28)$$

This helicity reversal will be apparent in the amplitude (and subsequently the cross section) of weak neutral current scattering as a parity-violating component to the overall scattered power.

Once the cross section for scattering in both helicity states has been measured, the difference between the two corresponds to the parity-violating component from weak scattering. Because the weak scattering amplitude can change with parity by a sign transformation the cross section for both positive and negative helicity states can be expressed by a combination of equations 1.6 and 1.7. Additionally, because higher order terms of \mathcal{M}_{weak} are suppressed by a factor of $\frac{1}{M_Z^2}$ at low energies, only the leading order parity-violating terms need be taken into account with

$$\left(\frac{d\sigma}{d\Omega}\right)_{\pm} \propto |\mathcal{M}_{EM} \pm \mathcal{M}_{weak}|^2 \approx |\mathcal{M}_{EM}|^2 \pm 2\mathcal{M}_{EM}^* \mathcal{M}_{weak}. \quad (1.29)$$

In this convention also “+” is shorthand for the cross section of scattering with right-handed helicity electrons (that is to say electrons where the

³The 1957 Wu experiment also utilized spin to detect parity violation. The experiment measured the rate of beta decay of spin-polarized ⁶⁰Co nuclei for spin polarized in one direction vs spin polarized in the opposite direction. The parity violation effect was observable in the anisotropy of decay rates between different polarizations [8].

directions of spin and momentum are aligned) and “-” is for left-handed helicity electrons (electrons where the directions of spin and momentum are anti-aligned). The explicit definition of this convention is written in Eq. 1.8.

The key observable from this formulation is the parity-violating asymmetry \mathcal{A}_{PV} . The asymmetry is the normalized difference between scattering cross sections in left- or right-handed helicity states. \mathcal{A}_{PV} can be written as

$$\mathcal{A}_{PV} = \frac{\sigma_R - \sigma_L}{\sigma_R + \sigma_L}. \quad (1.30)$$

By definition \mathcal{A}_{PV} can be any dimensionless scalar value between -1 and +1. To show the explicit helicity-dependence of \mathcal{A}_{PV} we can rewrite \mathcal{A}_{PV} in terms of the expansion in equation 1.29 by

$$\mathcal{A}_{PV} \approx \frac{2\mathcal{M}_{EM}^* \mathcal{M}_{weak}}{|\mathcal{M}_{EM}|^2}. \quad (1.31)$$

To relate this back to nuclear geometries, we can again look at the potential in equation 1.23. The key feature of this potential is that once it is placed in the inner product in equation 1.19 the γ^5 factors act in concert with either the right- or left-handed spinors (u_R or u_L) to similarly make the interaction potential helicity-dependent [19] we can show

$$\hat{V}(\vec{r}) = V(\vec{r}) \pm A(\vec{r}). \quad (1.32)$$

We can relate \mathcal{A}_{PV} , the scattering amplitude, the cross sections and the different nuclear form factors by

$$\mathcal{A}_{PV} = -\frac{G_F Q^2}{4\pi\alpha\sqrt{2}} \frac{F_{weak}}{F_{ch}} \quad (1.33)$$

and finally we can express this in terms of the neutron and proton form factors directly as

$$\mathcal{A}_{PV} = \frac{G_F Q^2}{4\pi\alpha\sqrt{2}} \left[4\sin^2\theta_w - 1 + \frac{F_n(Q^2)}{F_p(Q^2)} \right]. \quad (1.34)$$

Then to explicitly state the neutron and proton form factors in terms of nucleon density (as opposed to either electromagnetic or weak charge density) the Fourier transforms required can be written as [18]:

$$F_p(Q^2) = \frac{1}{4\pi} \int d^3\vec{r}' \frac{\sin(\vec{q} \cdot \vec{r}')}{\vec{q} \cdot \vec{r}'} \rho_p(\vec{r}'), \quad F_n(Q^2) = \frac{1}{4\pi} \int d^3\vec{r}' \frac{\sin(\vec{q} \cdot \vec{r}')}{\vec{q} \cdot \vec{r}'} \rho_n(\vec{r}'). \quad (1.35)$$

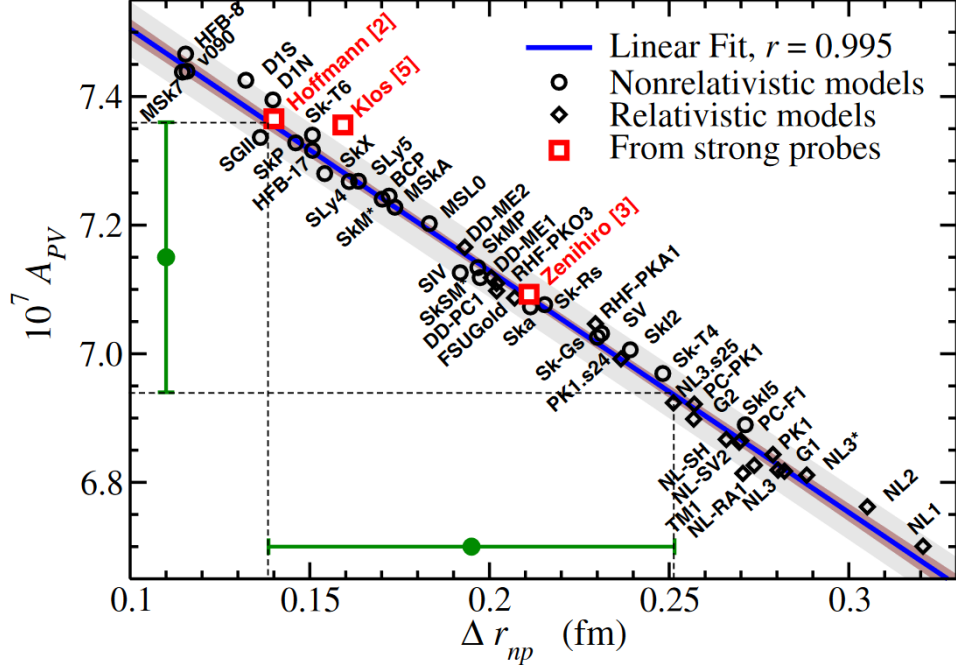


Figure 1.3: Plot showing different theoretical predictions of \mathcal{A}_{PV} correlated with Δr_{np} . While the exact number of neutron skin thickness is not constrained, the models show a high degree of correlation between predicted asymmetry and neutron skin thickness. In red are three reported measurements of Δr_{np} from hadronic probes. In green is a hypothetical measurement of $\mathcal{A}_{PV} = 715$ ppb, with 3% precision and its corresponding neutron skin thickness. Reproduced from Roca-Maza et al. [20].

This demonstrates that \mathcal{A}_{PV} is a powerful technique for isolating weak interaction features in electroweak scattering at energies well below the Z^0 pole. This technique is termed parity-violating electron scattering (PVES) and its history, as well as some notable PVES results will be discussed in Sec. 2.1. However, as far as nuclear structure is concerned, the technique allows for a weak force probe of neutron density which avoids sources of systematic uncertainty inherent to previous neutron density measurements using hadronic probes. While the technical challenges involved in conducting a PVES experiment at high precision will be discussed as the main subject of Ch. 2, PVES just conceptually as a technique presents a tantalizing op-

portunity to make a high-precision measurement of Δr_{np} .

Fig. 1.3 demonstrates that just knowing \mathcal{A}_{PV} is enough to know neutron thickness. Different mean-field models from nuclear theory have a high degree of correlation between the \mathcal{A}_{PV} and Δr_{np} . Even though the exact size of neutron skin thickness is not constrained by these different models, a single \mathcal{A}_{PV} measurement is enough to apply that constraint.

1.3 Nuclear Structure

In order to further motivate the PREX-II and CREX experiments we must address the obvious question: “what utility does an accurate measurement of Δr_{np} have towards nuclear theory?” To answer this we must address the current theory of nuclear structure, as well as its unknowns.

The basic principle of nuclear structure is that every atomic nucleus is composed of a number of protons Z and a number of neutrons N for a nuclear mass number of $A = Z + N$. Nuclei are either stable or unstable as a function of N and Z , with unstable nuclei eventually undergoing a decay process to change the nucleus towards a stable one. The primary determinant of whether a nucleus is stable or not is its binding energy B . Conceptually, binding energy can be thought of as the energy to disassemble a nucleus into its constituent nucleons. More quantitatively, the binding energy arises from the nuclear mass defect, the difference between the sum of the neutron and proton masses individually and the total nuclear mass is

$$B = (Zm_p + Nm_n - m_{nuc})c^2, \quad (1.36)$$

where m_{nuc} is the mass of the nucleus [21]. This number is positive for all nuclei, however as the ratio B/A decreases, the nucleus becomes more likely to become unstable and undergo some form of decay. The formula to predict binding energy from just the nuclear configuration N and Z is the Bethe-Weizsäcker Semi-Emperical Mass formula (SEMF) which is written as:

$$B(N, Z) = a_v A - a_s A^{\frac{2}{3}} - a_c \frac{Z^2}{A^{\frac{1}{3}}} - a_a \frac{(N - Z)^2}{A} + a_p \delta_{NZ}, \quad (1.37)$$

where the five terms are:

1. The volume term with coefficient a_v comes from the total nuclear volume. Since nuclear volume scales with the number of nucleons this term is proportional to A .

2. The surface area term with coefficient a_s represents the fact that neighboring nucleons will interact differently if they're on the surface of the nucleus than if they're near the center. Since for solid shapes surface area scales with volume ^{$\frac{2}{3}$} the surface area term is proportional to $A^{\frac{2}{3}}$.
3. The Coulomb term with coefficient a_c represents the effect of electrostatic repulsion of protons with each other. The Coulombic potential energy of any two positive point charges is proportional to q_1q_2/r where r is the distance between charges. The sum total of potential energy of each proton in the nucleus with every other proton is proportional to Z^2 , while the mean distance between protons in the nucleus can be expressed by the mean charge radius which in this formulation is proportional to $A^{\frac{1}{3}}$.
4. The asymmetry energy term with coefficient a_a is more complex but results from the Pauli exclusion principle. It reflects the fact that fermions (such as protons and neutrons) must occupy higher energy states as more are added to the nucleus. While this term will be justified later, we can for now say that it is proportional to $(N - Z)^2$.
5. The pairing term with coefficient a_p represents the fact that two nucleons in the same quantum state but with opposite spins will “pair” effectively reducing the interaction energy between the two. The term is then proportional to δ_{NZ} .

The SEMF is a powerful tool itself but as the name implies the coefficients for each energy term must be determined empirically, which can be challenging. Specifically, the asymmetry energy term can only be measured on nuclei which have a larger fraction of neutrons than protons. Some of the most common light nuclei (such as ${}^4\text{He}$, ${}^{12}\text{C}$, ${}^{16}\text{O}$, and ${}^{28}\text{Si}$) have $N \simeq Z$ reducing the size of the contributions from asymmetry energy. However, stable heavy nuclei have a neutron excess relative to protons, meaning that a measurement of neutron density in these nuclei can be closely associated with the asymmetry energy term of the SEMF. The heaviest stable nucleus is ${}^{208}\text{Pb}$, which has a significant excess of neutrons relative to protons so the asymmetry result of PREX-II will have significant implications for the asymmetry energy term.

1.3.1 Nuclear Equation of State

While the SEMF makes it clear that binding energy is a function of nucleon interactions, these interactions themselves are dependent on nuclear density. Nuclei are, because of the short range of the strong nuclear interaction, very compact and dense objects, and the interaction between nucleons is both difficult to model and non-trivial.

To understand the dependence of energy on nuclear density we must first consider the density of stable nuclei $\rho = \rho_p + \rho_n$. In particular we look at the energy around the nuclear saturation density ρ_0 . The saturation density of nuclei is estimated by theoretical models to be $\rho_0 \approx 0.15 \text{ fm}^{-3}$ [22]. We can then define the nuclear equation of state (EOS) by an expansion around $\rho = \rho_0$. The expansion yields two non-trivial terms: one representing the energy from a nuclear system with $N = Z$, and one from the neutron-proton asymmetry $\alpha = \frac{\rho_n - \rho_p}{\rho}$

$$\mathcal{E}(\rho, \alpha) = \mathcal{E}(\rho, \alpha = 0) + S(\rho)\alpha^2 + \mathcal{O}(\alpha^4), \quad (1.38)$$

where the first term is the symmetric energy term expanded around $\rho = \rho_0$ as

$$\mathcal{E}(\rho, \alpha = 0) \simeq \mathcal{E}(\rho_0, \alpha = 0) + \frac{1}{2}(\rho - \rho_0)^2 \frac{\partial^2 \mathcal{E}}{\partial \rho^2} \Big|_{\rho=\rho_0} \quad (1.39)$$

and the second term is the ‘‘symmetry energy’’ again, expanded around $\rho = \rho_0$:

$$S(\rho) \simeq S(\rho_0) + L \frac{(\rho - \rho_0)}{3\rho} + \frac{1}{2} K_S \left(\frac{\rho - \rho_0}{3\rho_0} \right)^2, \quad (1.40)$$

where the linear factor is $L = 3\rho_0 \frac{\partial S}{\partial \rho} \Big|_{\rho=\rho_0}$, and the quadratic factor is $K_S = 9\rho_0^2 \frac{\partial^2 S}{\partial \rho^2} \Big|_{\rho=\rho_0}$ [23]. One important detail of this formulation is that for heavy nuclei $\rho \simeq \rho_0$ meaning that nuclei like ^{208}Pb approximates uniform nuclear matter nicely. And also near saturation density the linear factor L is proportional to the nuclear pressure, which again, is a function of nuclear baryon density.

1.3.2 ^{208}Pb and Neutron Stars

At the end of the lifetime of a massive star following a supernova the core of the star can collapse into an extremely dense system of nucleons called a

neutron star. Neutron stars are typically formed after supernovae if the core of the star isn't massive or dense enough to become a black hole. Neutron stars are typically held together by both nuclear forces and gravity against the Fermi pressure that results from many fermions needing to occupy different quantum states. Ultimately the neutron star equation of state is dominated by the pressure near saturation density, which PVES on ^{208}Pb can quantify. Thus, heavy nuclei like ^{208}Pb can function as a terrestrial laboratory to study the physical properties of neutrons stars despite them being approximately 18 orders of magnitude different in size.

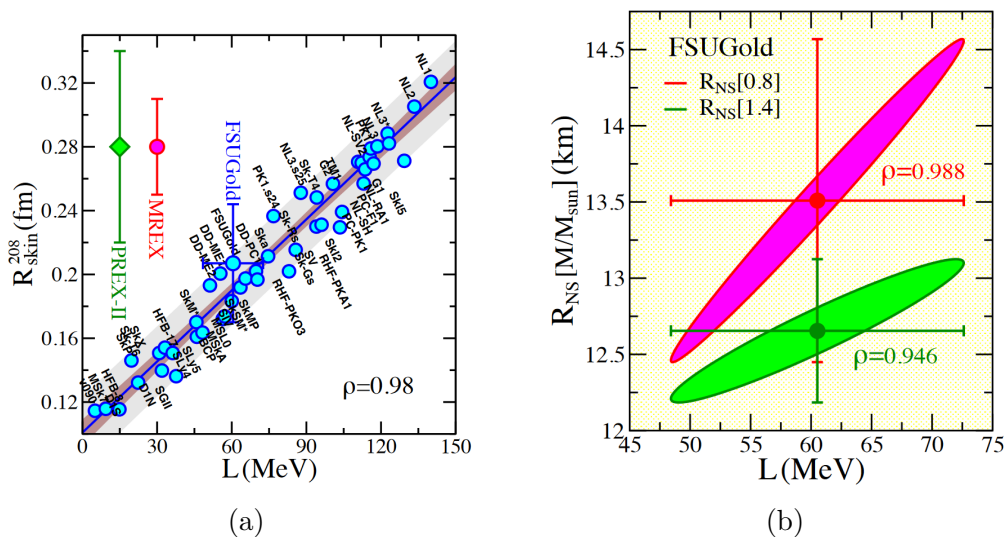


Figure 1.4: *Left:* The correlation between Δr_{np}^{208} and the symmetry energy parameter L for both saturation density as shown with different structure models. Reproduced from Thiel et al. [24]. *Right:* The correlation between L and the radii of neutron stars R_{NS} . Correlation points are compared between neutron stars of different masses from the FSUGold theory model. The correlation is high between both quantities therefore the neutron radius measurement correlates highly with neutron star properties. Reproduced from Thiel et al. [24].

The correlation between Δr_{np}^{208} and neutron star radius R_{NS} is illustrated by the dual plots in Fig. 1.4. The key correlating quantity is the linear factor on the symmetry energy term $L = 3\rho_0 \left. \frac{\partial S}{\partial \rho} \right|_{\rho=\rho_0}$. Because a many-fermion nuclear system is difficult to model from first principles, L can only

be measured as precisely as physical observables of nuclei can. PREX-II, just by virtue of measuring Δr_{np}^{208} , can constrain several physical observables of neutron stars.

Aside from just radius, L is highly correlated with the baryon pressure of pure neutron matter at saturation density:

$$P_N \approx \frac{1}{3}\rho_0 L, \quad (1.41)$$

which again, is a strong approximation of the conditions inside a neutron star [24].

One other property of neutrons stars is their deformability Λ , a measure of the neutron star's ability to form mass quadrupoles under gravitational forces. This deformability is a function of neutron star radius in the form of the neutron star's compactness (i.e., radius per mass)

$$\Lambda \propto \left(\frac{R_{NS}}{M_{NS}} \right)^5, \quad (1.42)$$

where M_{NS} is the neutron star mass [25]. This is particularly relevant to LIGO's 2017 detection of a binary neutron star merger, which set an upper bound on the deformability at 800 [26]. Though the gravitational interferometry used in the LIGO detector and the electron-nucleon scattering used by PREX-II are by all practical means quite different experimental techniques, they nevertheless can constrain the same astrophysical properties of neutron stars.

1.3.3 The Importance of ^{48}Ca

While the PREX-II asymmetry result has very important implications not just for the theory of nuclear structure, but for nuclear astrophysics as well, the implications of the CREX results are more subtle. For one, ^{48}Ca is a neutron-rich nucleus that is much lighter than ^{208}Pb and as a result is governed by a different realm of nuclear theory. For example, heavy nuclei can be modeled using a mean-field approach in the realm of density functional theory. In this treatment individual interactions between nucleons are only used to constrain an overall functional used to parameterize a mean field for the nuclear system [27].

Another approach exists in the computational *ab initio* models which seek to model nuclear behavior from first principles. In this treatment, individual interactions between nucleons are centered and solved for in traditional nonrelativistic quantum mechanics [28]. As nuclei get larger and more nucleons are in the system, the number of interactions between each grows. This means that greater and greater computation power is needed for larger and larger nuclei.

An example of another approach to nuclear modelling is the dispersive optical model (DOM) which constructs a complex non-local potential for the nuclear interaction. The real and imaginary components of the potential are then connected with dispersion relations. The potential can then be used to predict observables from ^{48}Ca scattering [29].

Scattering from ^{48}Ca can then be used to resolve the tensions that arise between various approaches. Especially PVES with ^{48}Ca can measure Δr_{np}^{48} which structure models from all three approaches can predict [30].

Chapter 2

PREX-II/CREX Overview

The experiments PREX-II and CREX were proposed to measure the neutron radius, and consequently neutron skin thickness Δr_{np} . While the physics motivation for these experiments has been laid out as the primary subject of Ch. 1, there are a number of practical concerns that must be addressed in order to run these experiments effectively. This chapter discusses these practical concerns as well as the conceptual design of PVES experiments to measure Δr_{np} .

2.1 Parity-Violating Electron Scattering

While PVES still has novel uses for making high-precision measurements of weak-interaction-correlated phenomena, the experimental technique has a history of over 40 years. In that time, various refinements and improvements have been made to the experimental technique and process in order to achieve progressively higher precision on progressively lower asymmetries.

Table 2.1 contains the measured asymmetries from selected PVES experiments between 1978 and 2018 as well as the precision on current PVES experiment proposals¹. The experiments listed in the table have different purposes, although the same PVES technique was used in each. E122 was run to test different models of the electroweak interaction. Experiments like SAMPLE, A4 and HAPPEX measured the strange quark contribution to

¹It should be noted that PREX-II and CREX results have already been made public, however for the purpose of this dissertation these results will be presented in Ch. 6 after a thorough discussion of the experimental analysis process.

| Experiment | Year | $\mathcal{A}_{PV} \times 10^9$ | $\delta\mathcal{A}_{PV}/\mathcal{A}_{PV}$ | Citation |
|------------|----------|--------------------------------|---|----------|
| E122 | 1978 | 152,000 | 17% | [13] |
| SAMPLE | 2004 | 3,510 | 23% | [31] |
| A4 | 2004 | 5,440 | 11.1% | [32] |
| E158 | 2005 | 131 | 17% | [33] |
| HAPPEX-I | 2006 | 6,720 | 12.8% | [34] |
| HAPPEX-III | 2011 | 23,800 | 3.6% | [35] |
| PREX-I | 2012 | 656 | 9.3% | [36] |
| Qweak | 2018 | 226.5 | 4.1% | [37] |
| PREX-II | Proposal | $\approx 600^*$ | 3%* | [38] |
| CREX | Proposal | $\approx 2,000^*$ | 2.4%* | [39] |
| MOLLER | Future | $\approx 35.6^*$ | 2.0%* | [40] |

Table 2.1: Measured asymmetries of various parity-violating electron scattering experiments throughout history. Measured asymmetries as well as the measurement precision have gotten progressively smaller as the experimental technique gets more refined and experimental technologies improve. The next generation of PVES experiments will be able to measure an asymmetry on the order of 10^{-8} .

*Numbers from proposal only

nucleon form factors. E158 and MOLLER are designed to measure the weak mixing angle θ_w . Qweak measured the weak charge of the proton as well as θ_w . While the overall technique is the same for various PVES experiments, each one has different design requirements (such as scattering kinematics and experimental apparatus design) which makes each experiment unique in execution.

Of particular importance to this dissertation are the PREX-I, PREX-II and CREX experiments, each designed to measure the neutron form factor in either ^{208}Pb or ^{48}Ca . PREX-II specifically was designed to be a continuation of the PREX-I experiment from nine years prior, which sought to measure the same neutron radius. PREX-I required a continuation because the original run period was beset with a number of difficulties during running which limited statistical precision to $\approx 9\%$. PREX-II would increase the precision on this measurement and also on Δr_{np}^{208} in general. The CREX experiment follows much of the same design as the PREX experiments, although it seeks to provide constraints on a different realm of nuclear theory, as was described

in Sec. 1.3.3.

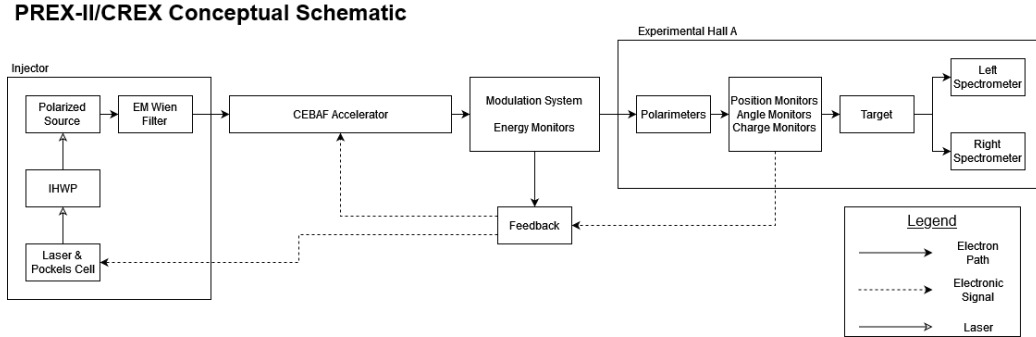


Figure 2.1: A diagram of the layout and interactions of the primary experimental systems of PREX-II and CREX. The electron beam is created at the polarized source, accelerated, and then fed into the experimental hall where it scatters off the target. Several feedback systems are implemented to allow for fast corrections to the beam configuration to minimize false asymmetries.

PVES experiments are often very technically challenging, especially as measured asymmetries and uncertainty requirements get progressively lower. If the electron beam quality is poor or unstable, a number of helicity-correlated asymmetric effects can be produced on target or in the beam itself but are not related to the parity-violating asymmetry \mathcal{A}_{PV} . These are sources of “false asymmetries” and they must be either minimized or corrected² in order to make the highest-precision measurement possible. As a result PVES experiments often employ specialized technological refinements in the polarized source, accelerator, target, and detectors. Fig. 2.1 lays out these systems as they were used for PREX-II and CREX to ensure beam quality high enough to measure \mathcal{A}_{PV} to high precision.

The main practical requirement for running PVES experiments is a longitudinally spin-polarized electron source with the ability to flip between helicity states $h = +1$ and $h = -1$. Additionally the helicity flip rate must be fast enough that slowly changing beam conditions, detector response, electronics gain or noise, etc. are negligible in comparison. For PREX-II and CREX this helicity flip rate has to be on the order of ≈ 100 Hz. This is implemented by a laser and Pockels cell system in the polarized source which controls the

²In the specific case of PREX-II and CREX, both minimization and correction are done.

polarization of the laser, and thus the polarization of the electrons off the source. While this system will be described in more detail in Sec. 3.1.1, for now it will suffice to say that the system is capable of delivering highly spin-polarized electrons to the experiment at a rapid helicity flip rate.

2.2 Kinematics

Once the experimental principle has been laid out then we must address the question “how can we configure the target and scattering mechanics such that the precision we measure on \mathcal{A}_{PV} is maximized?” This is, perhaps unsurprisingly, not a trivial question. There are many factors to consider including the rate of scattering and which scattered electrons from the target make it to the detector, the size of the physics asymmetry measured, and the dependence on the kinematic beam parameters such as beam energy E , momentum transfer q and scattering angle θ .

The primary metric for judging the data quality for different scattering kinematics is the figure of merit (FOM). The FOM is in general

$$FOM = \frac{d\sigma}{d\Omega} \mathcal{A}_{PV}^2 \epsilon^2, \quad (2.1)$$

where $\frac{d\sigma}{d\Omega}$ is the scattering cross section, \mathcal{A}_{PV} is the expected parity-violating asymmetry which is calculated from mean-field theory models, and ϵ is the asymmetry sensitivity [41]. The statistical uncertainty then for asymmetry measurements then goes as $\delta\mathcal{A}_{PV}^{(stat)} \propto (FOM)^{-\frac{1}{2}}$. So as FOM increases so does the precision of the measurement, so kinematics should be selected to maximize FOM.

The scattering cross section is included as it is proportional to scattering rate. Higher rate means a larger electron signal produced in the experiment detectors. The cross section increases for smaller scattering angles for both ^{208}Pb and ^{48}Ca targets, as seen in Fig. 2.2. It should also be noted that cross section similarly increases for lower q values because as $q \rightarrow 0$ then $\theta \rightarrow 0$.

The opposite is true for \mathcal{A}_{PV} , however. At higher values of both θ and q the predicted value of \mathcal{A}_{PV} increases³. Larger asymmetries also increase data

³It should be noted that the \mathcal{A}_{PV} plot in Fig. 2.2 includes Coulomb corrections so the trend in asymmetry is generally increasing but not monotonic.

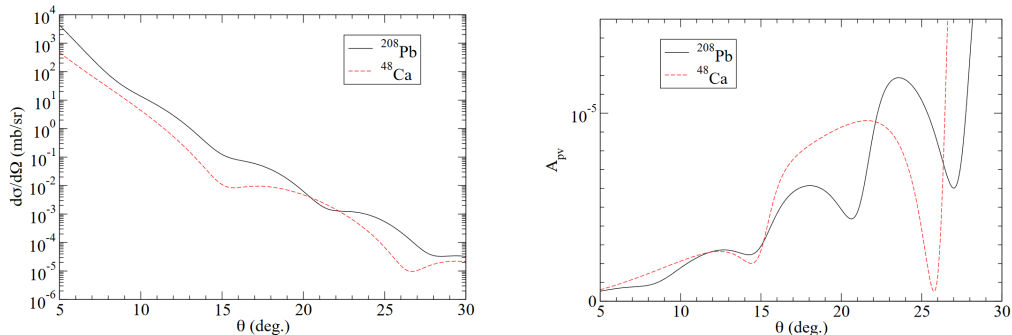


Figure 2.2: *Left:* Cross section dependence on scattering angle for both ^{208}Pb and ^{48}Ca at 855 MeV. *Right:* \mathcal{A}_{PV} dependence on scattering angle for both ^{208}Pb and ^{48}Ca at 855 MeV. Both figures reproduced from Reed et al. [42].

quality by virtue of making the relative size of false asymmetry corrections smaller. The asymmetries can be seen as a function of angle in Fig. 2.2.

The asymmetry sensitivity ϵ is defined by

$$\epsilon \approx \frac{\mathcal{A}_{PV}^{(1)} - \mathcal{A}_{PV}}{\mathcal{A}_{PV}}, \quad (2.2)$$

where \mathcal{A}_{PV} is the predicted parity-violating asymmetry, and $\mathcal{A}_{PV}^{(1)}$ is the predicted parity-violating asymmetry assuming Δr_{np} is increased by 1%. A high difference between \mathcal{A}_{PV} and $\mathcal{A}_{PV}^{(1)}$ indicates that measured asymmetries will have a high resolution in determining Δr_{np} . The plots of sensitivities can be seen in Fig. 2.3.

While the chosen experimental values of E , q , and θ are all related there are additional considerations to be taken into account when optimizing FOM. For example, scattering with high q^2 run the risk of generating inelastic scatters where the nucleus enters an excited state. While the PREX-II and CREX spectrometers are designed to reject inelastics (as will be described in Sec. 3.6) a high rate of inelastic scatters contributes backgrounds to the measurement of \mathcal{A}_{PV} which reduces the FOM [19]. Additionally there are practical considerations for the selection of angle θ which must be taken into account. Steering electrons from accepted elastic events towards the experimental detector package is only feasible for angles above $\approx 3^\circ$. The combination of maximized FOM and practical constraints informs experiment kinematics.

The original PREX-II proposal found FOM was maximized at $\theta_{PREX} = 5^\circ$

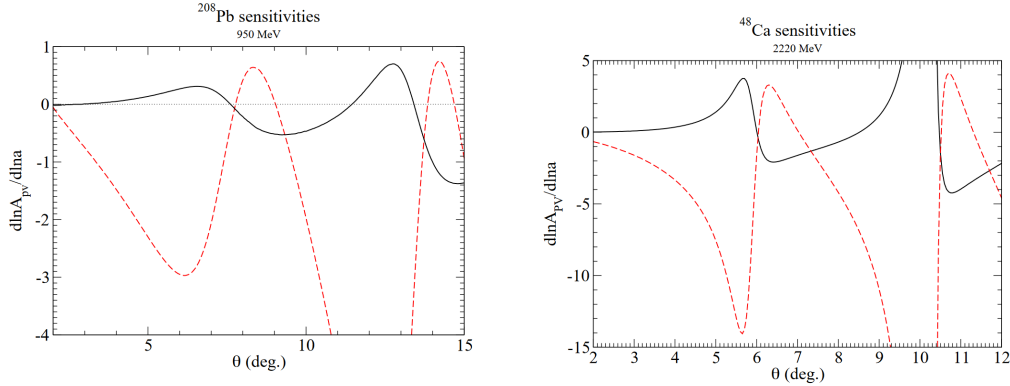


Figure 2.3: Dependence of asymmetry sensitivity ϵ for ²⁰⁸Pb at 950 MeV (*left*) and ⁴⁸Ca at 2220 MeV (*right*). Solid black lines indicate the sensitivity of asymmetry on neutron skin thickness, whereas the red dashed lines indicate the sensitivity of asymmetry on weak charge radius. Both figures reproduced from Reed et al. [42].

and $E_{PREX}=0.95$ GeV [38], while the CREX proposal called for scattering kinematics of $\theta_{CREX} = 4^\circ$ and $E_{CREX}=2.1$ GeV [39]. Midway through the development of both experiments the decision was made to increase θ to 5° for the CREX experiment [43]. The rationale for this decision was to run with the CREX target in the PREX-II target position, thereby easing the installation process for both experiments. The change would not necessitate changes to the design of other experimental hardware.

2.3 Measuring a Small Asymmetry

The predicted parity-violating asymmetries for PREX-II and CREX are on the order of ~ 1 part per million, which means false asymmetries should be tracked and controlled at that level or better. The polarized source was carefully configured to minimize residual helicity-correlations. Also, to control false asymmetries during experimental running, a feedback system to control beam intensity asymmetries was used. The feedback system will be discussed in more detail in Sec. 3.3.

The second method was to measure the false asymmetries during running and subtract them out during analysis. The beam monitors that could be used to send feedback could also measure beam kinematic properties during

each helicity state. Then by correlating observed changes in the measured asymmetries with the output of the beam monitors, false asymmetries can be subtracted. The subtraction takes the form of

$$\mathcal{A}_{meas} = \mathcal{A}_{raw} - \sum_i C_i \Delta x_i \equiv \mathcal{A}_{det} - \mathcal{A}_Q - \sum_i C_i \Delta x_i, \quad (2.3)$$

where \mathcal{A}_{meas} is the corrected asymmetry, \mathcal{A}_{det} is the asymmetry read directly off the detectors, \mathcal{A}_Q is the helicity-correlated asymmetry in the number of electrons deposited on target, Δx_i is the helicity-correlated difference in the kinematic quantity x_i , and C_i are the correlation slopes between \mathcal{A}_{det} and Δx_i [44].

While the subtraction of charge asymmetry is straightforward the details of measuring correlation slopes and the subsequent subtraction will be discussed as a topic of Ch. 6. However, it should still be noted that the combination of feedback and false asymmetry subtraction were used to keep false asymmetries low and to subtract the remainder.

2.4 Beam Polarization Effects

The theory calculations for \mathcal{A}_{PV} assume a perfectly longitudinally spin-polarized beam. In reality, the beam polarization cannot practically be 100% at all times. The beam polarization was monitored either continuously or periodically throughout the running of both the PREX-II and CREX experiments. While the specific design, function, and analysis of these polarimeters will be discussed in Sec. 3.2.4, what matters for the parity-violating asymmetry measurement is that they each can produce a beam polarization \mathcal{P}_e with some uncertainty $\delta\mathcal{P}_e$.

\mathcal{P}_e can be conceptually thought of as the fraction of electrons deposited on target in the correct helicity state. The spin state of the electrons does not affect the EM scattering amplitude, but it does affect the weak scattering amplitude. The weak scattering amplitude for any one helicity state is proportional to the average electron spin polarization. As Eqn. 1.31 demonstrates the the beam polarization is added as a factor of \mathcal{M}_{weak} meaning that the measured asymmetry is proportional to polarization by [45]

$$\mathcal{A}_{PV} = \frac{\mathcal{A}_{meas}}{\mathcal{P}_e}. \quad (2.4)$$

This demonstrates, perhaps quite obviously, that more highly polarized electrons results in a higher measured asymmetry. Thus the configuration in the polarized source and accelerator were configured before both experiments ran to maximize the beam polarization.

2.4.1 Transverse Polarization

Both PREX-II and CREX must be designed with the possibility of electrons with spins polarized transversely to the beam direction contributing to scattering as well. In the case of an electron scattering with its spin exactly normal to the direction of propagation the helicity $h = 0$ for this electron, but also if the spin were completely flipped. This effect produces a source of false asymmetry \mathcal{A}_T which is parity-conserving:

$$\mathcal{A}_T = \frac{\sigma^\uparrow - \sigma^\downarrow}{\sigma^\uparrow + \sigma^\downarrow}, \quad (2.5)$$

where \uparrow and \downarrow denote spins transverse to the direction of electron beam motion [19]:

To correct for this asymmetry the PREX-II and CREX detector package employed two detectors per spectrometer arm to detect scatters from transverse polarized electrons. The kinematics of scattered transverse electrons are dependent on the in-scattering-plane angle θ and the out-of-scattering-plane angle and transverse polarization angle ϕ . The \mathcal{A}_T detectors can then not just measure an asymmetry between transverse polarized states but also can use the optical reconstruction to integrate \mathcal{A}_T as a function of detector geometry. The specific details of the transverse asymmetry measurement and correction will be presented in Sec. 6.5.

2.5 Measuring Δr_{np} from Asymmetry

While the high degree of correlation between measured \mathcal{A}_{PV} and Δr_{np} for both ^{208}Pb and ^{48}Ca is promising, it behooves us to define a more specific formalism for converting asymmetry to neutron skin thickness.

Eqn. 1.33 allows us to relate the measured value of \mathcal{A}_{PV} to the weak charge form factor F_{weak} which as Eqn. 1.25 reminds us, is the Fourier transform of weak charge density $\rho_W(r)$. The functional form of weak charge

density can be given by

$$\rho_W(r) = \frac{\rho_0}{1 + e^{\frac{r-R}{a}}}, \quad (2.6)$$

where ρ_0 is then weak charge normalization factor, R is the weak charge radius parameter, and a is a surface thickness parameter (calculated from mean-field theory models). The weak charge density, when integrated over volume gives the total weak charge

$$Q_W = \int d^3r \rho_W(r) = Zq_p + Nq_n, \quad (2.7)$$

where $q_p = 0.0721$ is the weak charge of the proton and $q_n = -0.9878$ [46].

The mean radius squared of weak charge is then obtained by

$$R_W^2 = \frac{1}{Q_W} \int d^3r r^2 \rho_W(r). \quad (2.8)$$

According to Horowitz et al. [46], the charge radius of any nucleus can be expressed as

$$R_{ch}^2 = R_p^2 + \langle r_p^2 \rangle + \frac{N}{Z} \langle r_n^2 \rangle + \frac{3}{4M^2} + \langle r_{so}^2 \rangle, \quad (2.9)$$

where R_p is the proton radius of the nucleus $\langle r_p^2 \rangle = 0.691 \text{ fm}^2$ [47] is the mean charge radius squared of a single proton, $\langle r_n^2 \rangle = -0.110 \text{ fm}^2$ [48] is the mean charge radius squared of a single neutron, M is nuclear mass, and $\langle r_{so}^2 \rangle$ is the spin-orbit current corrections. It should be noted that the mass term is small and can be neglected.

This illustrates that the overall method of getting the mean charge radius for both electromagnetic and weak charge is to integrate form factors over nuclear volume weighted by charge density. It can be shown in this treatment that the mean neutron radius squared is

$$R_n^2 = \frac{Q_W}{q_n N} R_W^2 - \frac{q_p Z}{q_n N} R_{ch}^2 - \langle r_p^2 \rangle - \frac{Z}{N} \langle r_n^2 \rangle + \frac{Z + N}{q_n N} \langle r_s^2 \rangle, \quad (2.10)$$

where $\langle r_s^2 \rangle = 0.02 \pm 0.04 \text{ fm}^2$ is the mean strangeness radius squared [46].

The parameters used for the calculation of R_p and R_n are shown in table 2.2. To express this explicitly in terms of R_W^2 then for ^{208}Pb the neutron radius becomes

$$R_{n_{208}}^2 = 0.9525 R_{W_{208}}^2 + 0.7875 \text{ fm}^2, \quad (2.11)$$

| Quantity | ²⁰⁸ Pb | ⁴⁸ Ca | Citation |
|----------------------------|------------------------|------------------------|----------|
| Z | 82 | 20 | - |
| N | 126 | 28 | - |
| Q_W | -26.22 | -118.55 | - |
| $\langle r_{so}^2 \rangle$ | -0.028 fm ² | -0.110 fm ² | [46, 49] |
| R_{ch} | 5.503 fm | 3.47 fm | [10] |
| R_p | 5.458 fm | 3.41 fm | - |

Table 2.2: Parameters used in R_n calculation for both PREX-II and CREX targets.

and for ⁴⁸Ca the neutron radius is

$$R_{n48}^2 = 0.2107R_{W48}^2 - 0.0193\text{fm}^2. \quad (2.12)$$

Once then the neutron radius is obtained it, as well as the proton radius R_p can be entered into Eqn. 1.2 to measure Δr_{np} for each nucleus.

Chapter 3

PREX-II/CREX Experimental Apparatus

Both PREX-II and CREX were run at the Thomas Jefferson National Accelerator Facility (JLab for short) in experimental Hall A. PREX-II was run between June and September 2019 while CREX was run in three intervals the first interval in December 2019, the second interval between January and March 2020 and the third interval in August and September 2020¹.

This chapter will describe the physical equipment and control systems used for the PREX-II and CREX experiments. For the purposes of this dissertation the systems are divided up into two categories, the first being the source and accelerator and the second being the Hall A equipment.

3.1 CEBAF Complex

The main feature of JLab is its Continuous Electron Beam Accelerator Facility (CEBAF). CEBAF was originally brought online in 1994 capable of delivering 4 GeV (and subsequently 6 GeV) polarized electrons at beam currents reaching 100 μ A to one of three experimental halls. In 2012, CEBAF received a substantial upgrade, which increased the beam energy to 12 GeV and added a fourth experimental hall [50]. The current CEBAF appara-

¹The interruption between March and August 2020 was not originally planned but was implemented out of caution due to the global COVID-19 pandemic. Accelerator running was not restarted until after pandemic safety protocols and protections were implemented both at JLab and statewide in the US state of Virginia.

tus can deliver up to $200\mu\text{A}$ of beam to all four halls simultaneously while fulfilling different individual experimental requirements for each hall.

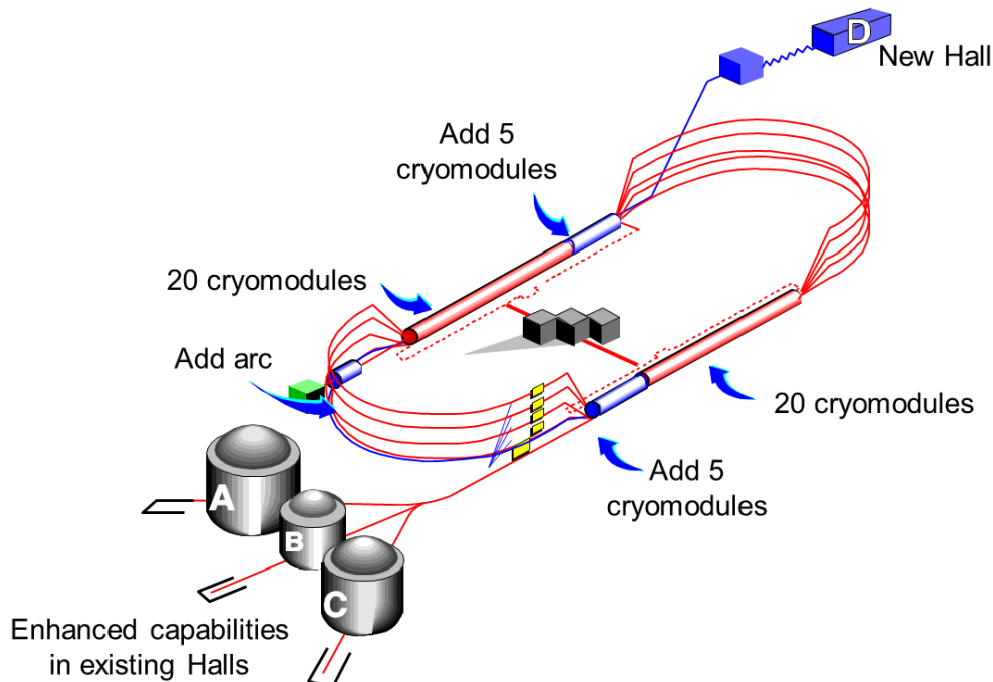


Figure 3.1: A CEBAF complex schematic detailing the components added during the 12 GeV upgrade. The injector can be seen in green on the left-hand side of the picture.

The layout of CEBAF can be seen in Fig. 3.1. The process of delivering the electron beam begins with the injector which contains the source of the beam. Once the beam is generated, the beam is then fed to the north linear accelerator (LINAC). There the beam gains energy by passing through a series of superconducting radio frequency (SRF) cryogenic modules [51]. The module fields operate at radio frequency and are capable of producing beam in continuous wave (CW) excitation. The beam then passes through an arc which steers the beam into the south LINAC. The beam then passes through the west arc where it can continue in the CEBAF system or be deposited into its destination hall before the arc. The beam is fed into a separate parallel arcs in both the east and west arcs for every circulation it makes around the

CEBAF system, for up to 5.5 passes.

Once the beam has made the required number of passes it is fed into Hall A by moving on an arc in a beam switchyard where it continues on a straight path through the experimental hall. The hall then uses the beam for whichever experiment is installed in it. The beam that then passes through the hall is deposited in a beam dump which consists of a series of water-cooled aluminum cylinders in a tank located down a concrete tunnel on the far side of Hall A [52].

3.1.1 Polarized Source

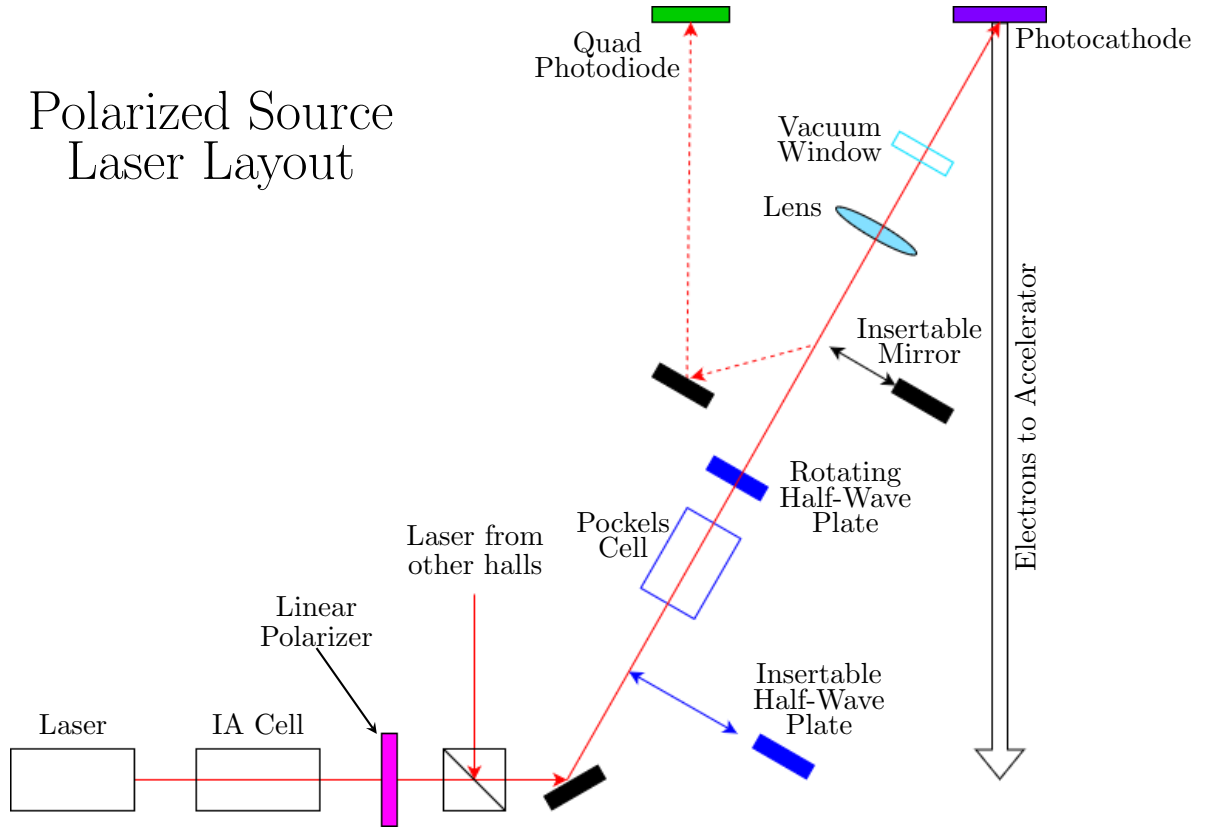


Figure 3.2: Layout of the polarized source showing the path of the source laser through the Pockels cell and half-wave plates and onto the GaAs photocathode. Adapted from [53] and [54].

The main principle behind the source of the electron beam is that by directing circularly polarized light onto a gallium arsenide (GaAs) photocathode, whereby the photoelectric effect produces the polarized electrons that form the electron beam in the accelerator. The laser intensity can be controlled remotely and could create different beam currents on request (up to a maximum value).

The partial layout of the injector laser table configuration can be seen in Fig. 3.2. Laser light pulsed at RF-frequency with wavelength $\lambda = 780$ nm is passed through an Intensity Attenuator (IA) cell, and continued through a linear polarizer. The laser is then combined with the laser light for halls B, C, and D such that the total laser light that will eventually land on the photocathode produces the correct amount of electrons for all four experimental halls. The laser is also passed through several optical elements which control the direction of polarization.

RTP Pockels Cell

One core feature of PVES experiments is the ability to measure scattered signal in opposite beam helicity states, as described in Sec. 1.2.4. This is accomplished by, at the beam source, quickly flipping helicity state. This allows the experiment to make many independent measurements of \mathcal{A}_{PV} during running.

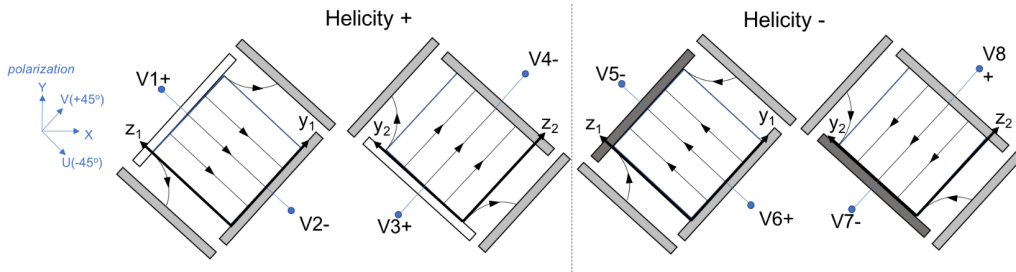


Figure 3.3: Schematic drawing of the two RTP crystals and the voltages applied for positive (left) and negative (right) helicity states. The two voltage states V1 through V4 and V5 through V8 are alternated rapidly to alternate between helicities. Optical axes U and V are labeled on the diagram. Reproduced from [55].

The mechanism for fast helicity-flipping is a Pockels cell which can convert

the linearly polarized laser light to either left- or right-handed circularly polarized light by applying different voltages. The assembly of the Pockels cell as well as the tests and calibration were carried out by experimental collaborators from the University of Virginia. At the core of the Pockels cell are two piezoelectric crystals of Rubidium Titanyl Phosphate (RTP) to which high voltage is applied to achieve the optical properties necessary to produce circularly polarized light. The high voltage is then alternated at the helicity flip rate, which changes the birefringence of the RTP cells to produce circularly polarized light in opposite directions. A diagram of the voltages applied to the RTP cells can be seen in Fig. 3.3.

During helicity flipping, time must be allotted out of every helicity period to allow for the RTP crystals to settle into a final state. This time is referred to as t_{settle} , and it is separated from the rest of the helicity period where the RTP crystal was stable which was designated as t_{stable} . RTP was specifically chosen for PREX-II and CREX due to its low settle time roughly $t_{settle} \approx 90 \mu\text{s}$. Thus the remaining stable time of the helicity period is $t_{stable} = 10^6/120\mu\text{s} - 90\mu\text{s} \approx 8243\mu\text{s}$ [53].

To analyze the laser polarization as it entered the beam line, a linear polarizer and mirror could be inserted into the laser between the rotating half-wave plate (RHWP) and the focusing lens. The light was then reflected onto a series of photodiodes. By adjusting the setting of the RHWP with the analyzer and measuring the photodiode response the laser polarization parameters could be obtained. This procedure was done for intermittent tests of laser quality while the electron beam was not running.

The Pockels cell is potentially a source of false asymmetries if the laser configuration exiting the Pockels cell is helicity-correlated. If there is a residual degree of linear polarization in the laser after the Pockels cell this can create intensity asymmetries on the photocathode. If there is a polarization gradient either asymmetries of laser position or laser spot size can result. These asymmetries can be seen visualized in Fig. 3.4. Several steps are taken to reduce the effect of these asymmetries. One such step was to optimize laser spot sizes on the Pockels cell which reduced the effect of crystal nonuniformity on the outgoing laser. Another such step was to adjust the laser entrance angle to minimize the effect of refraction and birefringence. The two-crystal setup also helped reduce systematics arising from nonuniform effects in any one crystal [55].

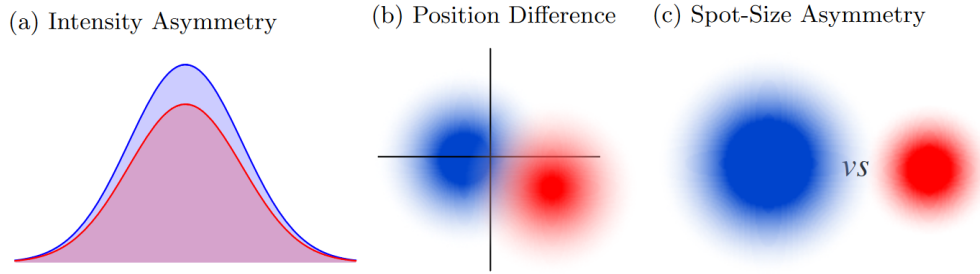


Figure 3.4: Asymmetries arising from the first three moments of the laser spot. The intensity asymmetry (where the laser intensity changes with helicity state), the position asymmetry (where the laser position is different in different helicity states) and the spot size asymmetry (where the laser beam size changes with helicity state). These asymmetries result from there being a polarization gradient across the RTP material or a birefringence. Reproduced from [53, 55].

Insertable Half-Wave Plate

Along the laser line in the injector, there is an additional half-wave plate which can be remotely inserted or retracted (IHWP for short). When the IHWP was inserted the direction of laser polarization entering and exiting the Pockels cell was reversed relative to when it was retracted. This was one of two methods of slow helicity-reversals which were used to isolate and identify any helicity-correlated contamination. The IHWP state would be flipped by experimenters on timescales ranging from 8 hours to 1 day. Ultimately the decision of whether or not to flip was made if the statistical precision of the current IHWP period matched the previous ones. This control allowed for similar statistical weights in each IHWP sample.

The other form of slow helicity reversal, changing the electromagnetic wien filter, will be discussed in Sec. 3.1.2.

Photocathode

After the laser passes through the polarizers, Pockels cell and HWPs, the laser is passed through a lens which focuses the beam. The laser then passes through a vacuum window into the vacuum chamber in which the photocathode sits. The photocathode is primarily composed of GaAs, a semiconducting material with a band gap of about 1.4–1.6 eV. The laser light then is enough

to excite electrons in GaAs up to the conduction band where they are ejected from the material by the photoelectric effect, and accelerated towards the anode [56]. This whole setup forms the electron gun which begins the electron propagation to the accelerator.

3.1.2 Injector

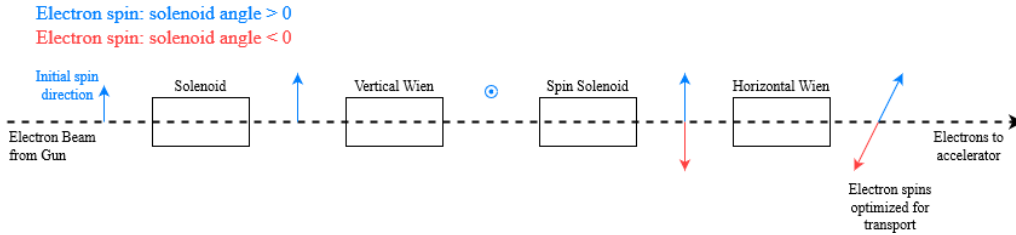


Figure 3.5: A diagram of the double Wien filter in the injector. Electron spins are progressively changed using electromagnetic fields until they are aligned for the accelerator. The spin solenoid angle can be changed to flip spins either to the left or to the right of the beam line. Changing this angle is what changes the Wien filter direction. Adapted from [54, 57].

The electrons off the gun must then have their spins aligned such that after passing through the accelerator and entering Hall A the electron beam is maximally longitudinally polarized. To do this a double Wien filter is placed along the injector beamline. The Wien filter consists of, in order, a focusing solenoid, a vertical Wien field, a spin solenoid, and a horizontal Wien field. The fields precess the electron spins according to the field angles of each component. Importantly, the spin solenoid field precesses the spins in opposite directions depending on the sign of the solenoid angle. A diagram of the Wien filter can be seen in Fig. 3.5.

The spin solenoid angle could be changed during experimental running to flip electron spins in the opposite direction from the previous angle setting. This, after the IHWP flipping, was the second method of slow helicity-reversals. By reversing the Wien angle the electrons entering Hall A would have the opposite sign relative to the Pockels cell voltages in the other Wien period. Flipping this angle was not a trivial process and could only be conducted once every few weeks, for no more than four flips per experiment.

Additionally the injector beamline had numerous position and current monitors to monitor beam quality at the source.

3.1.3 Accelerator

JLab's CEBAF accelerator is composed of two parallel LINACs (north and south) and two steering arcs (east and west). With each pass of the electron beam in the LINACs the electrons gain energy. For PREX-II and CREX purposes however, electrons passing through each LINAC once was sufficient to meet the beam energy requirements of both experiments.

Once electrons reach the desired energy for each hall they can be extracted from the accelerator loop by a series of RF-extractor magnets. The beam is then steered by a series of magnets along an arc leading into experimental Hall A.

3.2 Hall A Beamline Features

Experimental Hall A at JLab is cylindrical with a radius of ≈ 26.8 m, and a height of between 16 m at the edge and 24 m at the center. The beamline is mounted 3.05 m above the floor. The floor, wall, and roof of the hall are made of concrete.

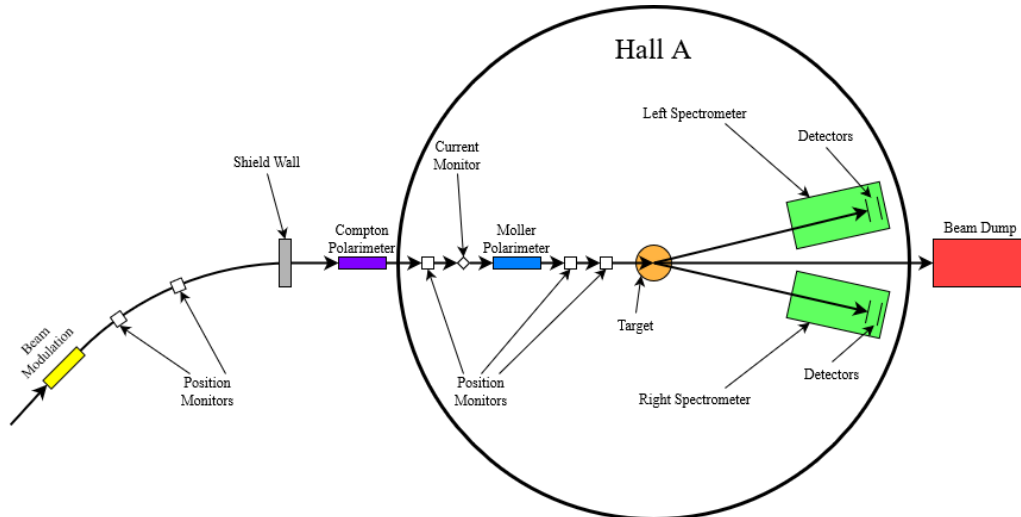


Figure 3.6: Top-down view of the layout of Hall A with important components labeled. Distances and lengths not to scale. Adapted from [19].

On the upstream end of the hall is a narrow alcove in which the Compton polarimeter and other important beamline elements are placed. The Hall

An alcove is separated from the arc in the beam switchyard by a retractable concrete shield wall. The wall was left in place for the entirety of PREX-II and CREX running as well as during the time in between the experiments. At the downstream end of the hall is the high-power beam dump. The beam dump serves to contain power from the exhaust beam as well as very low angle scattered electrons along the primary beamline.

Fig. 3.6 shows the Hall A configuration as seen from above. The figure also contains a number of important experimental components labeled.

3.2.1 Beam Charge Monitors

PREX-II and CREX employed a series of Beam Charge Monitors (BCMs) along the primary beamline to track not just how much current was being delivered to the hall but also if there were any helicity-correlated charge asymmetries. There were three components to the BCM setup: a magnetically-shielded parametric current transformer called the “Unser” and two resonant RF-cavities on each side of the Unser, upstream (US) and downstream (DS). The schematic cross section of the Hall A BCMs can be seen in Fig. 3.7.

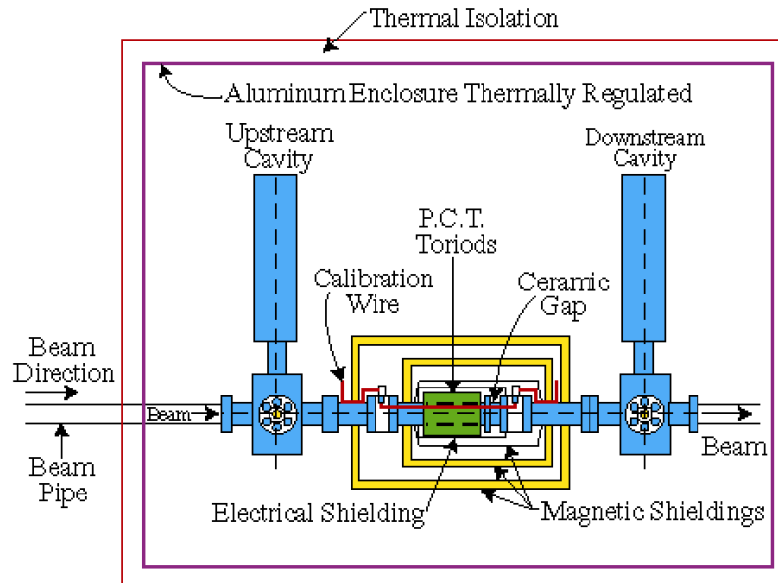


Figure 3.7: Diagram of the Hall A BCMs. BCMs are approximately 25 m upstream of the target. Reproduced from [58].

For stable operations the Unser was electrically, magnetically, and thermally isolated from surrounding fields. Once the beam passed through the Unser a response was generated in a calibration wire proportional to the beam current² [59]. The output voltage of the Unser was then recorded and beam current calculated from it. Data from the Unser was not used during regular experimental running, as the Unser output would drift even after just a few minutes of beam running. Instead, the Unser was used periodically to calibrate the current response of the RF-cavity current monitors on either side of it.

Like the Unser, the US and DS BCMs read out a voltage dependent on the magnitude of the beam current passing through them. Unlike the Unser however, the US and DS BCMs function by using resonant RF cavities. The response function—though highly linear over the region of interest—required calibration. The output of the BCMs was fed to an amplifier and then into a 1 MHz RMS-to-DC converter. The analog converter output was read by a voltmeter, while three copies of the same output were digitized into three channels with $\times 1$, $\times 3$ and $\times 10$ amplification. These US and DS BCMs, when properly calibrated, provided a continuous current monitor for each helicity period in both experiments.

3.2.2 Beam Position Monitors

A number of beam position monitors (BPMs) were placed along the Hall A beamline to track the beam position and direction along the beamline. BPMs were placed frequently after beam steering magnets, quads and other focusing beam elements. A diagram of a typical BPM can be seen in Fig. 3.8. The BPMs consisted of four wire antennae running parallel to the beamline placed diagonally on each of the four corners of the beamline. When beam is passed through the BPM the beam induces current in the antennae depending on the beam position.

The beam current-independent beam position in each direction can be computed from the signals for each of the four wires X_p , X_m , Y_p , and Y_m :

$$x_{rot} = C \frac{X_p - X_m}{X_p + X_m}, \quad y_{rot} = C \frac{Y_p - Y_m}{Y_p + Y_m}, \quad (3.1)$$

where $C = 18.76$ mm is a calibration constant [54]. To convert the rotated positions to the normal hall coordinates the positions must be rotated around

²The Unser voltage response was 4 mV per μ A of beam current.

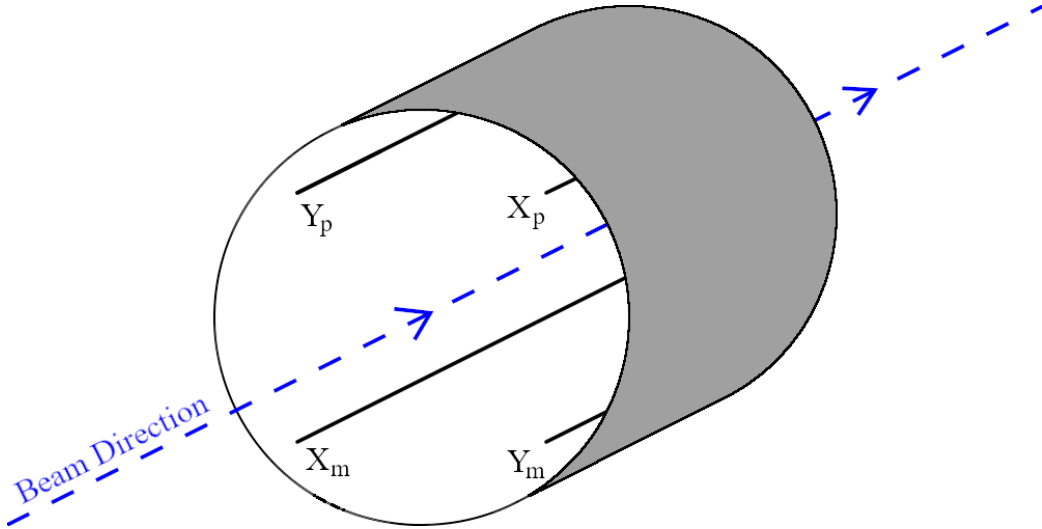


Figure 3.8: An isometric diagram of a typical stripline BPM like the kinds used in PREX-II and CREX. The four wires run parallel to the beamline and are read externally from the BPM. Adapted from [59].

the beam direction by $\theta = 45^\circ$:

$$\begin{bmatrix} x \\ y \end{bmatrix} = \begin{bmatrix} \cos \theta & -\sin \theta \\ \sin \theta & \cos \theta \end{bmatrix} \begin{bmatrix} x_{rot} \\ y_{rot} \end{bmatrix}. \quad (3.2)$$

The BPMs enabled several key experimental processes. The first of these was to lock of the beam position into place by feeding back BPM information to corresponding steering magnets. The BPM positions could as well be read out by experiment electronics to get position information for each helicity period. Finally, the BPM information from all along the beamline was fed back to the accelerator and injector to minimize sources of beam noise. This feedback system will be described in Sec. 3.3.

For PREX-II and CREX there were six key BPMs used to track helicity-correlated position differences. Three of these were in Hall A: bpm4E which was on the beamline 1.642 m upstream of the target, bpm4A which was 5.725 m upstream of the target, and bpm1 between the Hall A BCM and the Møller . The other three, bpm11, bpm12, and bpm16 were on the arc leading into Hall A. All six of these beam monitors provided a continuous measurement of the beam x and y positions at the monitor.

The drawback with this design of BPM was that the signal from the

BPM would be unreliable below 0.5 μA . Typical running for both PREX-II and CREX operated well above this threshold so this was not an issue for asymmetry measurements. However counting mode measurements, including raster checks (described in Sec. 3.2.5) and Q^2 measurements (described in Sec. 3.6) needed to be conducted at very low current in order to maintain acceptable rates for the spectrometer detector package. To lock the beam position into place three alternate BPMs using the RF-cavity model like the US and DS BCMs. These BPMs were not used beyond this function and were not factored into the parity analysis [60].

3.2.3 Beam Modulation Coils

Both PREX-II and CREX employed a beam modulation system (otherwise known as “dithering”) which introduced artificial beam motion. This process was used in conjunction with correlation slope regression calculations described in Sec. 6.2.2 to correct false asymmetries.

The beam modulation is comprised of six magnetic coils (3 for modulating trajectory in the X-direction and 3 for modulating in the y-direction.) These coils were placed on the beamline arc leading into Hall A after the switchyard separation with halls B and C. In addition, the beam energy modulation was done with an energy vernier on the south LINAC. During beam modulation cycles the coils would activate and modulate the beam position and angle with a frequency of 15 Hz and an amplitude of $\approx 100 \mu\text{m}$. BPMs along the beamline would then record the small changes in beam position and angle in order to correlate the modulation with changes in the uncorrected asymmetry [61].

A beam modulation cycle was run once every ten minutes during typical PREX-II and CREX experimental running. Each cycle would pause fast feedback trajectory control processes for approximately one minute per cycle.

3.2.4 Polarimeters

PREX-II and CREX employed three separate systems for conducting beam polarimetry measurements. Two of the systems, the Møller and Compton polarimeters sat in Hall A while the third, the Mott polarimeter, was on the injector beamline. While these beam polarimetry measurements were expected to have consistency with each other, the physical mechanisms behind each subsystem varied greatly. As a result, each polarimeter was run at

different times from the other in different beam configurations.

Mott Polarimeter

The Mott polarimeter is located in the 5 MeV section of the injector beam line between the Wien filter and the entrance to the north LINAC. To measure the magnitude of polarization the horizontal Wien field is scanned to maximize transverse polarization onto the polarimeter target. Electrons then scatter off of one of either gold, silver, or copper targets. Light from the scattering is read by four scintillator detectors placed orthogonally to each other. The asymmetry from the scattering is then compared to a theoretical analyzing power to calculate polarization [62].

The Mott polarimeter analyzes the electron beam polarization before the beam reaches the accelerator, meaning that the polarization was independent of any accelerator components or spin-precession. However, the specific conditions of Mott polarimetry running limited the usefulness of Mott measurements for the experimental polarimetry data. Firstly, the Mott polarimeter was run with a perfectly transverse electron beam which would have a different spin-polarization direction than the longitudinally-polarized beam entering Hall A. Secondly, Mott polarimetry measurements are invasive and cannot be run in parallel either with Hall A running or indeed, running from any other hall.

Thus the usefulness of the Mott measurements is primarily to determine the Wien configuration which produced the highest degree of polarization. The absolute degree of polarization measured by the Mott was not used for PREX-II/CREX \mathcal{P}_e measurements³.

Compton Polarimeter

The first of the two polarimeters in hall A is the Compton polarimeter. During Compton operations the electron beam is diverted about 30 centimeters below the primary beamline in a magnetic chicane into a resonant optical cavity in which a circularly polarized green laser is locked in a resonant wave. The beam then passes through the laser resulting in Compton scattered photons received by a photon detector. This signal is then used to calculate an asymmetry in the photon detector which is proportional to electron beam

³However it could be used as a cross-check for polarization measurements from the Møller and Compton polarimeters.

polarization \mathcal{P}_e . The remainder of the electron beam is then diverted out of the cavity & chicane and continues along into Hall A. This meant that unlike the Mott or Møller polarimeters the Compton could be run in parallel with the main experiment with a minimal effect on beam. Any asymmetries induced on the beam by Compton running are negligible for the main experiment.

The Compton polarimeter and its associated data is the core subject of this dissertation and will be discussed in great detail elsewhere. The theory and practical setup of the Compton polarimeter will be discussed in chapter 4 and the data and analysis from the Compton will be discussed in chapter 5.

Møller Polarimeter

The Møller polarimeter is the second polarimeter system within Hall A located along the beamline between the raster coils and the target BPMs. The primary function of the Møller is to scatter the polarized electron beam off a spin-polarized target and measure the helicity-correlated asymmetry in the scattered electrons.

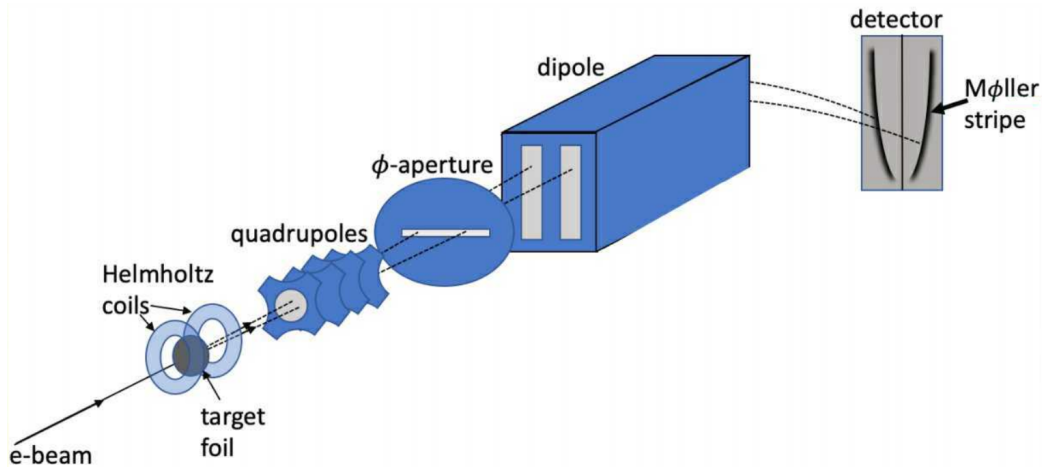


Figure 3.9: Diagram of the Møller polarimeter including the target, the Møller quads, the Møller dipole and the detector array with the acceptance. Reproduced from [63].

During Møller running the electron beam is scattered off an iron foil tar-

get. The Møller target is placed inside a solenoidal magnetic field, generated by superconducting Helmholtz coils around the target. The magnet is also maintained via a cryogenic line at a temperature of 4 K. The strong B-field magnetically saturates the target, polarizing the atomic electrons. At the target elastic Møller scattering off the atomic electrons then occurs and the scattering cross section contains a spin- and helicity-dependence.

The scattered electrons are then passed through four quadrupole magnets to focus the Møller electrons on their path to the detectors. After passing through an aperture the Møller -scattered electrons are then steered by a dipole magnet down off the primary beamline towards the detector array. The detector system consists of both left and right arrays consisting of two blocks of four PMTs each (for a total of 8 PMTs).

The Møller measures the helicity-correlated scattering asymmetry

$$\mathcal{A}_{mol} = \frac{\left(\frac{d\sigma}{d\Omega}\right)_{\uparrow\uparrow} - \left(\frac{d\sigma}{d\Omega}\right)_{\uparrow\downarrow}}{\left(\frac{d\sigma}{d\Omega}\right)_{\uparrow\uparrow} + \left(\frac{d\sigma}{d\Omega}\right)_{\uparrow\downarrow}} = \mathcal{P}_e \mathcal{P}_f \langle \mathcal{A}_{zz} \rangle, \quad (3.3)$$

where $\left(\frac{d\sigma}{d\Omega}\right)_{\uparrow\uparrow}$ is the cross section when the beam and target spins are aligned, $\left(\frac{d\sigma}{d\Omega}\right)_{\uparrow\downarrow}$ is the cross section when the beam and target spins are anti-aligned, \mathcal{P}_f is the degree of target polarization and $\langle \mathcal{A}_{zz} \rangle$ is the integrated theoretical analyzing power of the Møller measurement which is calculated through simulation [64].

For PREX-II and CREX running the Møller analyzing power was $\langle \mathcal{A}_{zz} \rangle \approx 0.75$ and the foil polarization was $\mathcal{P}_f \approx 0.08$. At 100% beam polarization this meant measured Møller asymmetries would be as high as 6%. Thus, high statistical precision could be achieved with even short Møller running time. The limiting source of systematic uncertainty for the Møller measurement was the foil polarization itself, which was limited by both constraints from theory and nonuniformities in the target. The second leading source of systematic uncertainty for the Møller came from the extrapolation from low-current to high current. The Møller target could only accept beam current up to 3 μA while PREX-II and CREX were run at 70 μA and 150 μA respectively. The heating of the photocathode at high current could in principle affect polarization and as such the Møller data must be corrected for high-current running.

Because of the low current requirements and need for a spin-polarized target insertion the Møller polarimeter cannot be run in parallel with the main experiment. In order to conduct a Møller measurement several hours

of setup are needed to enter the Møller run configuration and to return to normal running in addition to the time needed to actually take the measurements. In total a single Møller measurement could take between 8 and 16 hours depending on the number of systematic tests that are needed to be performed. So during PREX-II and CREX Møller measurements were typically taken once every other week. During the first few months of PREX-II when it was not clear the Compton would run at all during the experiment, Møller measurements were taken weekly.

3.2.5 Raster

For both PREX-II and CREX the intrinsic beam size is on the order of 100 μm when it entered the hall. If a beam with this spot size were to be delivered directly on either the ^{208}Pb or ^{48}Ca targets the high thermal density would be too high to be dissipated and the target would be damaged. Thus a system was required to distribute the beam profile over the target.

This system was the beam “raster.” The raster consists of a set of magnetic coils placed along the beamline upstream of the target between the charge monitors and the Møller polarimeter. While active, the raster coils modulate the beam steering at high frequency such that when it arrives at the target its profile is on the order of 1 mm. If the raster is too large then the spectrometer optical calibration becomes difficult, but if the raster is too small then the target is at risk of being damaged by high beam intensity. The optimum raster size for each target was computed using thermal simulations before the experiment began.

The size of the raster is verified using the counting mode scintillator detectors (described in Sec. 3.8). The raster current is measured as a function of time in order to find detector rates for each rastered position on the target. The raster size is determined by running the rastered beam on a carbon target with a 2 mm hole in the center. As shown in Fig. 3.10 the hole would be visible on the raster map, and the size of the hole could be compared to the size of the raster.

In addition to raster size the intrinsic beam spot size before the raster must be optimized. Small spot sizes could still damage the target (even while rastered) and large spot sizes would be susceptible to noise from beam position differences or halo. The spot size is checked by passing an array of conductive wires through the beam, which is referred to as a “harp scan.” Both the raster checks and harp scans are invasive, and are only performed

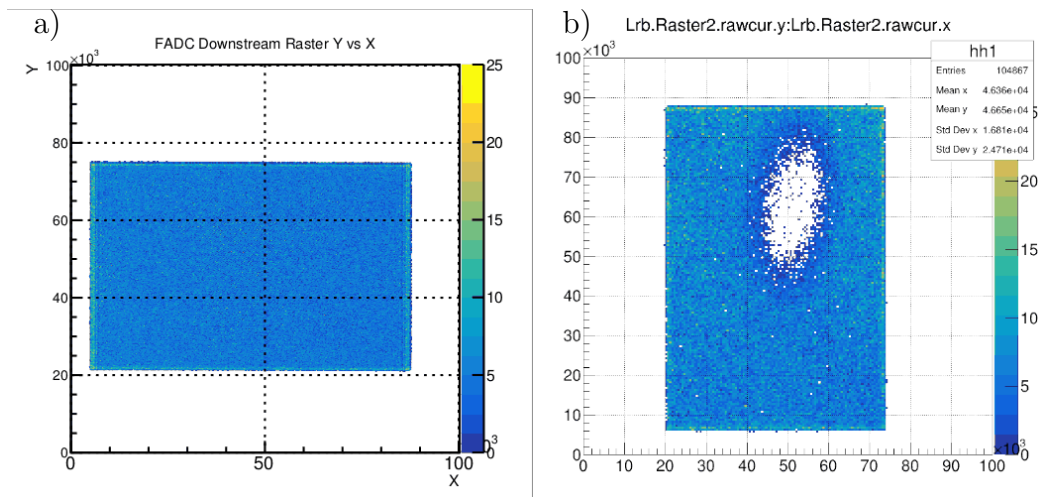


Figure 3.10: a) Raster map on a ^{208}Pb target. b) Raster map on the carbon hole target. Both plots use uncalibrated raster units. To perform the calibration the size of the hole is compared to the size of the raster. In this case the raster is found to be 5.3 mm in the horizontal and 3.9 mm in the vertical.

at low current and without ^{208}Pb or ^{48}Ca targets in the path of the beam.

3.2.6 Small-Angle Monitors

The primary beam monitors downstream of the target are an array of eight small-angle monitors (SAMs). The SAMs are placed about 7 m downstream of the target in the beamline at 45° angles to each other. The layout of the SAMs can be seen in Fig. 3.11. The SAMs consist of a small piece of fused quartz attached to the end of a light guide which leads to a PMT at the end of each SAM. PMTs and the light guide geometry are chosen to produce accurate detector signal at high light yield and rate.

The SAMs record the energy from very low angle scatters which carried zero asymmetry at low Q^2 . The SAMs are also sensitive to changes in beam position, angle, energy and quality on the target. The SAMs also provide a way to check the health of the target, and to identify false asymmetries. The SAMs saw higher rate during PREX-II than during CREX due to the wider scattering cone produced at lower energies [19].

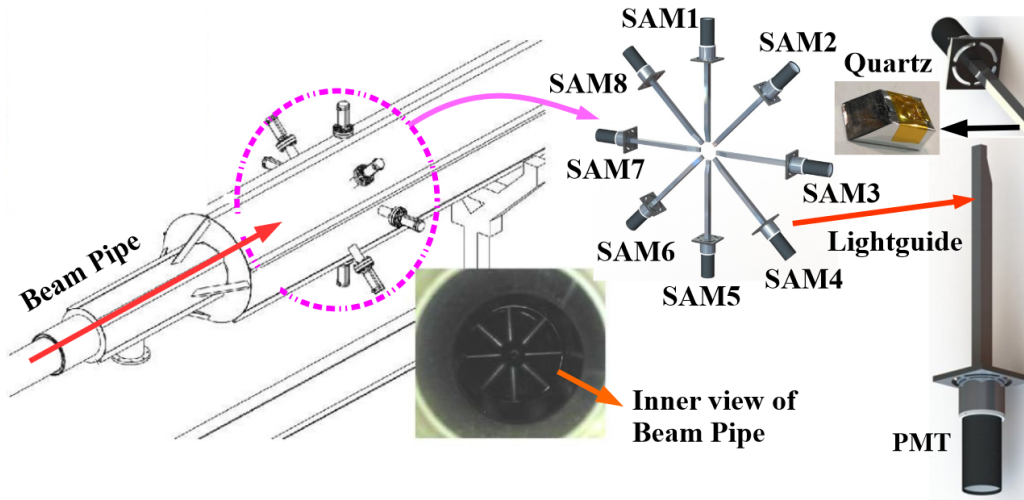


Figure 3.11: Diagram of the SAMs in the downstream beamline. Reproduced from [19].

3.3 Feedback

To minimize false asymmetries in the beam, two systems of feedback were used to maintain high beam quality. There are two feedback systems that were run independently: charge feedback and fast feedback.

3.3.1 Charge Feedback

The charge feedback system measures the charge asymmetry \mathcal{A}_Q and feeds back that asymmetry to the Pockels cell. There the Pockels cell voltage is automatically adjusted to drive the charge asymmetry down. The charge feedback is run any time beam was in the hall, but is usually restricted to high enough current to be accepted as normal running. Charge feedback was run for the entire duration of normal running for both experiments.

3.3.2 Fast Feedback

The second system of feedback was fast feedback, which monitored asymmetries from position and energy in Hall A and sent those feedback signals to the accelerator RF cavities. The feedback is done to suppress beam noise

resulting from power line harmonics (which occur in multiples of 60 Hz) [65]. Establishing fast feedback requires several BPMs along the Hall A beamline to achieve a stable calibration, so it requires comparably more time and fine-tuning to run than charge feedback. If the fast feedback calibration took too long to achieve stability then either experiment could be run without it.

3.4 Target System

Both the PREX-II and CREX targets were sealed inside an aluminum scattering chamber. All targets were arranged on two copper “ladders” which could be inserted into the beamline or retracted, centering the beamline on any one target. The primary ladder (the “cold” ladder) contained ten ^{208}Pb targets, one ^{48}Ca target, one ^{40}Ca target, three natural Pb targets, one carbon foil target, and one carbon foil target with a 2 mm diameter hole drilled in. This ladder can be seen with the targets labelled in Fig. 3.12. This ladder was cooled by liquid helium and during normal running the ladder temperature would be between 17 K and 26 K.

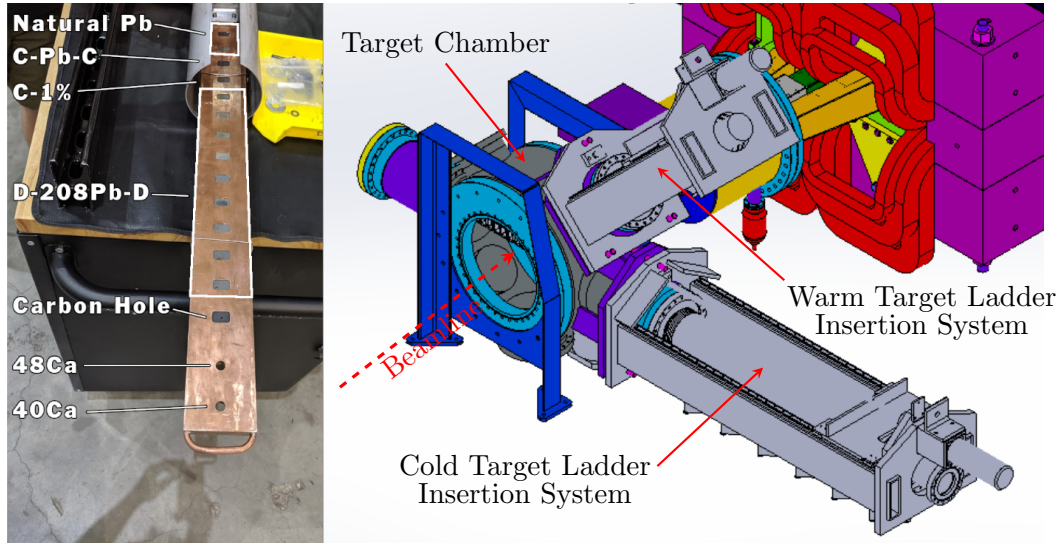


Figure 3.12: *Left:* A picture of the cold target ladder before installation in PREX-II. The targets are labelled. Note that the calcium targets had not been inserted in the ladder yet when this photo was taken. *Right:* CAD visualization of the PREX-II/CREX target chamber.

The second ladder (the “warm” ladder) contained five targets which were used for optics calibration. This ladder contained one natural Pb target, one tungsten target (which was not used), one carbon foil target, one carbon hole target, and one cell of water. This ladder was maintained at room temperature. The warm ladder was oriented at a 45° angle relative to the cold ladder in the target chamber.

3.4.1 PREX-II Targets

The primary targets used for PREX-II are the ten ^{208}Pb foil targets. Each foil is ≈ 0.5 mm thick and 90-95% isotopically pure. Nine of the ten foils are sandwiched by thin foils of diamond (0.25 mm thick) on both the upstream and downstream ends of each target, with the last target foil sandwiched by graphite foils. Diamond has a high thermal conductivity and helped dissipate the power deposited by the beam.

As more beam is deposited on each target foil, the diamond eventually degrades and the ^{208}Pb target underneath would be damaged. This was to be expected as the approximate lifetime of the targets in beam was measured in PREX-I. Degraded or nonuniform ^{208}Pb targets would result in excess noise in the detector and increased radiation in the hall. This motivated the inclusion of ten separate ^{208}Pb foils, so that there would always be a fresh target to switch out with any damaged targets⁴. Degradation is measured using the raster map technique described in Sec. 3.2.5. An example of both a uniform and degraded target raster map can be seen in Fig. 3.13.

The contribution to the asymmetry from scattering off of carbon in the diamond foils is predicted using an optical simulation. The carbon correction to the asymmetry is

$$\mathcal{A}_{phys} = \frac{\frac{\mathcal{A}_{corr}}{\mathcal{P}_e} - \mathcal{A}_C f_C}{1 - f_C}, \quad (3.4)$$

where \mathcal{A}_C is the asymmetry from carbon, and f_C is the background fraction of carbon events. In the limit that $\frac{\mathcal{A}_{corr}}{\mathcal{P}_e} \simeq \mathcal{A}_C$ (like in PREX-II) then the correction factor approaches 1.

Of the nine diamond-encased ^{208}Pb targets seven were used throughout experimental running and the graphite-backed ^{208}Pb target was not used at all.

⁴PREX-I by comparison had three production targets, all of which saw some amount of beam.

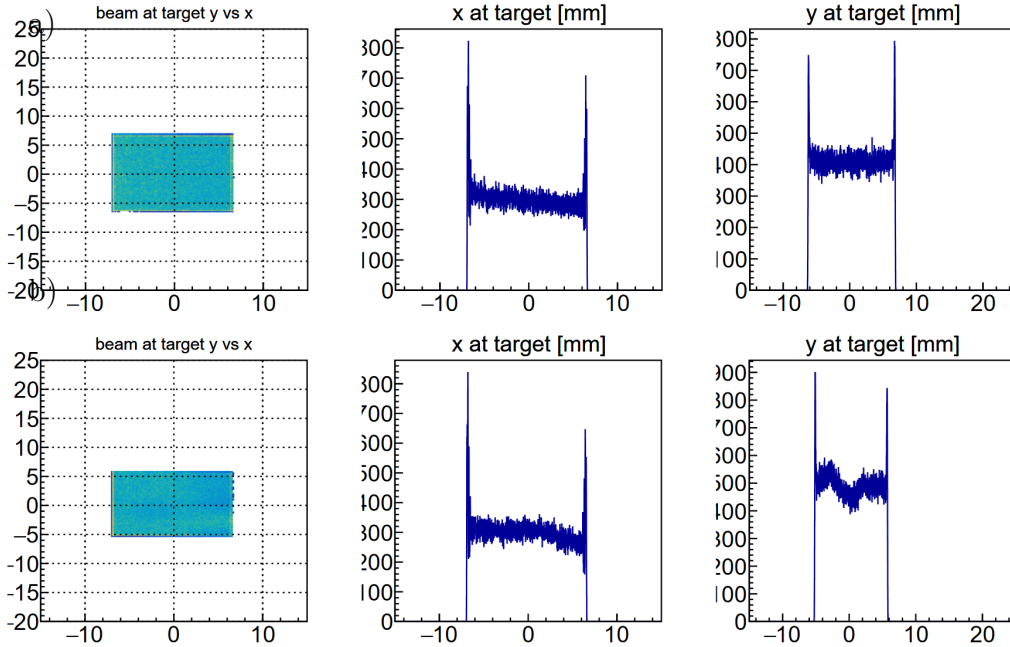


Figure 3.13: a) Raster map on one of the ^{208}Pb targets when it was fresh. b) The same target after a week of PREX-II running. Note in the bottom plots nonuniformities have formed, indicating the diamond has degraded and the target has been damaged. After the data shown in the bottom plots was taken, a new ^{208}Pb target was commissioned and then used for the rest of experimental running.

3.4.2 CREX Target

The CREX target is a single 6 mm thick piece of 95% pure isotopic ^{48}Ca . Calcium already has a high thermal conductivity and therefore diamond backing was not needed. Calcium also experiences oxidation when exposed to air, so the target is kept in mineral oil when not under vacuum. The target does not experience beam-based degradation in standard operation unlike the ^{208}Pb targets.

On January 18th, 2020 there was a beam mis-steering incident which resulted in the destruction of the original ^{48}Ca target. The remainder of the experiment was conducted using an alternate ^{48}Ca target which had been constructed for earlier tests. The replacement target had minor surface oxidation, which was removed at the cost of a small bit of target thickness.

The rest of the experiment was conducted with this target without incident.

3.5 Radiation Controls

One of the primary complications which limited the statistical precision of PREX-I was the occurrence of radiological damage to experimental equipment. For example, the electronics on the High-Resolution Spectrometer (HRS) platforms contain optocouplers which are particularly sensitive to damage by neutron radiation. Additionally, the beam pipe leading to the dump that was during PREX-I sealed by an elastomer O-ring which degraded under a high radiation load. The radiological hazards are partly due to the design of the experiment which required high-luminosity, high- Z targets.

In order to safely run the two experiments, steps towards radiological mitigation had to be taken. There were several categories of radiological hazards which had to be controlled in different ways. Firstly, ionizing radiation on any of the Hall A electronics needed to be significantly reduced from PREX-I levels.

Secondly, controls were implemented to ensure that PREX-II complied with JLab's regulations concerning environmental radiation. The specific hazard to control were high-energy neutrons which could escape through the hall roof and enter the ambient environment (so-called "skyshine" radiation). JLab measured this radiation by placing radiation dosimeters on the fence along the perimeter of the CEBAF complex. Shielding to regulate the energy of neutrons heading towards the Hall A roof, was needed to control the amount of skyshine radiation detected at the JLab site boundary.

The experimental radiation load was estimated before experimental running through simulations of experimental running with the simulated Hall A geometry. Estimated radiation in different areas of Hall A could be extracted from the simulation.

3.5.1 Monte Carlo Simulation

The principle of a Monte Carlo (MC) simulation is to simulate particle scatters in software by randomly selecting the incident particle's kinematics from random variable distributions. For PREX-II and CREX the primary scattering to be simulated was the incident electron on each experimental target. This MC was implemented through a particle physics simulation toolkit,

GEANT4. The PREX-II and CREX implementation of GEANT4 not only specified the beam electron’s kinematics, but also could simulate the scaled geometry of Hall A equipment including beamline components, the HRSs, the beam dump, and the hall walls and roof [66].

The MC simulates each particle resulting from the scattering and tracked its propagation through the simulated hall geometry. Particles are only recorded upon reaching a geometrical element designated as a “sensitive detector.” Once reaching a detector, the particle’s information is recorded including its type, position, momentum, energy, and the position of the particle’s origin. This simulated process could be repeated millions of times to achieve a high statistical precision on the measured radiation load.

3.5.2 Collimator

The combination of having a 1 GeV beam plus a high-luminosity target means that the forward scattering cone (i.e., scatters that have very low θ) is comparably wide relative to scatters at higher energy. This means a significant portion of scatters will have a scattering angle too large to reach the dump, but too narrow an angle to reach the HRSs. To prevent these scatters from doing damage to hall equipment, a collimator was installed approximately 80 cm downstream from the target. The design of the collimator and its jacket can be seen in Fig. 3.14.

The collimator is made out of a copper-tungsten alloy and is aligned with the central beam axis. The collimator is 10 centimeters in diameter and 10.5 centimeters in length. The collimator central bore is widened as the beam moves downstream with a widening angle of 0.78° from the target. The collimator absorbs low-angle scatters from the target and ensures that the only scatters making their way down the beampipe are less than 0.78° scattering angle, thus protecting Hall A components downstream of the target. The collimator is fit inside a tungsten jacket which held the collimator mount and absorbed higher-angle scatters than the collimator face.

The collimator is included in the MC simulation. The simulated energy absorption on the collimator face is measured by the difference between the total particle energy incident on the upstream collimator face and the total outgoing particle energy downstream of the collimator. The results from the simulation can be seen in table 3.1.

The collimator is expected to absorb just over 2.5 kW during normal

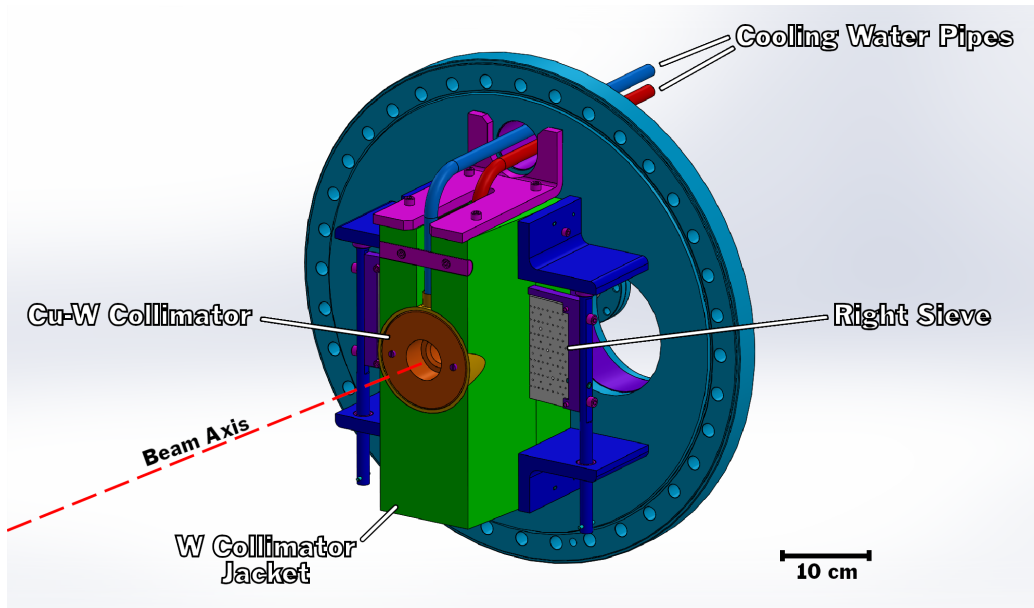


Figure 3.14: A CAD model of the contents of the PREX-II/CREX collimator chamber. Included are the collimator, the collimator jacket, the cooling water system, and the insertable sieves.

| Quantity | PREX-II | CREX |
|--|--------------------|--------------------|
| Power per Current [$\text{W } \mu\text{A}^{-1}$] | 36.22 | 5.96 |
| Power [kW] | 2.536 | 0.893 |
| Total Energy [J] | 6.13×10^9 | 2.78×10^9 |

Table 3.1: The collimator power deposition for each experiment, derived from simulation. PREX-II deposits significantly more power on the collimator face than CREX due to the lower beam energy widening the angle distribution of scatters.

PREX-II operations⁵. To handle this thermal load the collimator is fitted with a water-coolant system. Cool water is piped into the collimator assembly, and would follow a spiral groove along the outside of the collimator where it would get pumped into an exit pipe, where it could be cooled outside the hall and recirculated into the assembly. This added another design constraint

⁵It was decided before the last few days of PREX-II to increase beam current to 85 μA , which would deposit 3.1 kW on the collimator face.

to the collimator where the power deposition had to be low enough that the water would not boil before entering the exit line. The water temperature in both the entrance and exit lines were monitored to make sure the water stayed below boiling.

3.5.3 Shielding Concept and Design

Neutrons and electrons not intercepted by the collimator have the potential to create hazards for electronic components in Hall A. Radiation shielding placed around the areas where most of the beam power is deposited controls this effect. The MC measured the radiation load on the HRS platforms as a metric for radiation deposited in Hall A. Additionally, the MC tracks the radiation absorption by radiation shielding to verify that the total radiation load is within manufacturer-recommended limits.

Collimator Shielding

The target and collimator collectively absorb the most energy of components in Hall A, and thus are the main region of concern for radiological hazards. If not controlled, radiation from this region has the potential to cause damage to hall equipment or components. Additionally, thermal energy neutrons from the target region could in principle be absorbed by Hall A electronics and produce single event upsets (SEUs) which would interrupt the function of the electronics resulting in software crashes elsewhere.

To prevent this a layer of shielding is added to the target and collimator region. The shields between the target and collimator were made of high-density polyethylene (HDPE) with a five percent boron content. The shields are approximately 90 centimeters tall and wide, and about 65 centimeters long. The shields are fitted around the target beamline and the collimator housing such that the scattered beam passes through the center of the shields. The shields can be seen visualized in Fig. 3.15.

The concept behind the HDPE shields is that neutrons produced by the collimator and target enter the shielding and lose energy due to nuclear recoils with the hydrogen in the HDPE. After the neutrons lose energy, they are absorbed by the boron content, which has a high neutron absorption cross section at low energies [67]. This shielding then mitigates both the electronics damage and SEU risk with one mechanism.

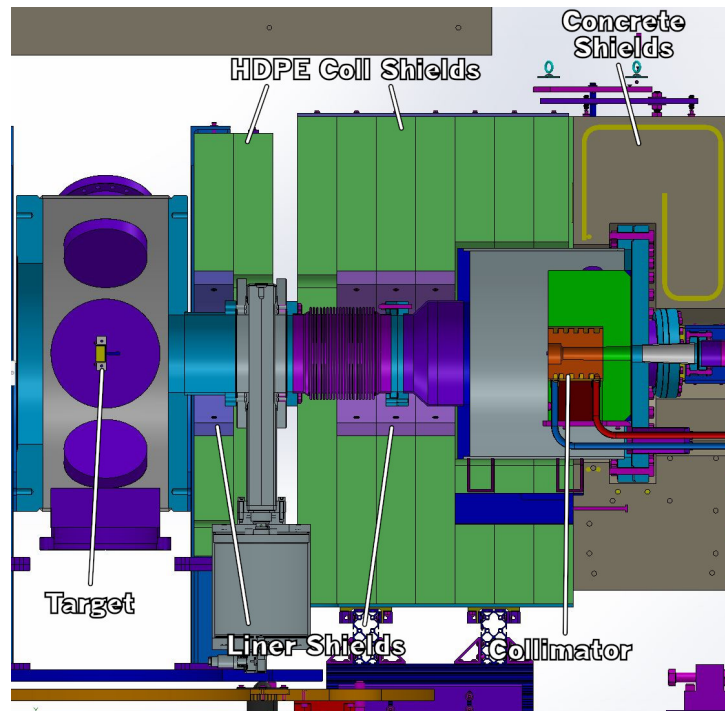


Figure 3.15: A cross sectional CAD visualization of the collimator shields as seen from the right side of the beam, with the cross sectional plane at the beam axis. The visualization covers about 1.3 meters of beamline from left to right. Components are labeled.

Downstream of the collimator is covered by concrete shields without any boron content. These high density shields are in place to reduce ionizing particle energy that otherwise proceeds to the HRS platform. The advantage of using concrete shields in this region is concrete's high radiation hardness relative to plastic.

The effectiveness of the collimator shielding is measured by the total dose per area on the simulated HRS platforms. Because the dose is partially from neutrons and partially from electrons, the full dose is measured in a total 1 MeV neutron equivalent n_{eq} per surface area. The results from the MC can be seen in table 3.2. The MC shows the collimator design markedly reduced the expected dose on the HRS platforms from PREX-I, which did not have beam collimation or shielding.

The HDPE shields need additional considerations due to the radiation

Units of 1 MeV n_{eq}/cm^2

| Particle Type | PREX-1 | PREX-II | CREX |
|--------------------------|--|--|-------------------------------------|
| n | 3.9×10^{10} | 4.6×10^9 | 1.5×10^9 |
| e | 3.4×10^{10} | 8.5×10^9 | 1.9×10^9 |
| Total | 7.3×10^{10} | 1.3×10^{10} | 3.5×10^9 |
| Ratio with PREX-I | 1.00 | 0.18 | 0.05 |

Table 3.2: Integrated dose on the HRS platform per surface area for PREX-I, PREX-II and CREX. Dose is expressed in 1 MeV neutron equivalent. All values calculated from the same Monte Carlo simulation with different experimental geometries and beam energies.

tolerance of HDPE plastic. Manufacturer recommendations suggest that borated HDPE is radiation-safe up to 1 MGy of dose [68]. Above this limit it would be possible for the HDPE shields to degrade and produce HDPE dust which is a contamination hazard. In order to proceed, the MC would have to demonstrate that for the full PREX-II and CREX run period combined, the shields receive less than 1 MGy. This is complicated by the fact that the MC shows that the energy absorption of the HDPE shields is not uniform across the shield volume. Simulations indicate the HDPE shields absorb the most dose in the region closest to the beamline.

To lower the local dose on the collimator shields, the shields are designed to allow for a 2.5 centimeter-thick hollow cylinder of aluminum to be placed around the beamline between the beamline and the shield. The aluminum “liner” shield stops low-energy electromagnetic radiation, lowering the local dose on the HDPE shields enough to prevent degradation. With the liner in the MC the dose is then measured on a section of the shields 1 cm thick nearest the beamline which is expected to receive the highest dose of any part of the shield.

The results of the MC including the full shield geometry show that with the Aluminum liner in place the shield dose was reduced below the 1 MGy threshold for even the highest radiation parts, as is summarized in table 3.3.

Skyshine Shielding

In order to prevent skyshine radiation a shield had to be placed between the target/collimator region and the hall roof. The main source of skyshine is known to be high energy neutrons (>30 MeV) incident on the hall roof.

| Experiment | Quantity | Whole Shield | 1 cm Section |
|-------------------------|---|--------------|--------------|
| PREX-II | Power Deposited [W] | 7.08 | 0.23 |
| | Power Density [$\mu\text{W}/\text{cm}^3$] | 18.8 | 96.4 |
| | Dose [kGy] | 46.9 | 241 |
| CREX | Power Deposited [W] | 3.47 | 0.16 |
| | Power Density [$\mu\text{W}/\text{cm}^3$] | 9.22 | 69.6 |
| | Dose [kGy] | 29.6 | 223 |
| Total Dose [kGy] | | 76.5 | 464 |

Table 3.3: Radiation dose on both the full collimator shield and the 1 centimeter radial section nearest the beamline including the 2.5 cm-thick Aluminum liner shield. Totals are for the total run time of each experiment. All numbers computed from Monte Carlo simulation data.

Skyshine is simulated before experimental running by integrating the total neutron flux for the run time of both experiments. The MC simulated skyshine radiation and it is measured by integrating the total neutron flux for the run time of both experiments.

Two skyshine shields are installed above the target and collimator as seen in Fig. 3.16. Both skyshine blocks are made of concrete, and extended for about 60 cm on the left and right side of the target beamline. The two blocks collectively extend 3.3 meters along the beamline. The length and width of the blocks are designed to block as many neutrons from either the target or the collimator from the hall roof as possible.

| | PREX-I | PREX-II | CREX |
|---|--------|---------|------|
| n's >30 MeV flux [$\text{cm}^{-2} \times 10^8$] | 7.60 | 4.92 | 6.31 |
| Ratio with PREX-I | 1.00 | 0.65 | 0.83 |

Table 3.4: Simulated skyshine neutron rate on the Hall A roof for multiple experiments.

The rate of neutrons with energy >30 MeV on the Hall A roof is simulated with the PREX-I, PREX-II and CREX experimental configurations. The results of these simulations can be seen in table 3.4. The results show that both PREX-II and CREX generate a neutron flux at a similar magnitude to PREX-I when integrated over the full experimental run times of all three experiments. Site boundary dosimetry data from 2010 revealed that PREX-

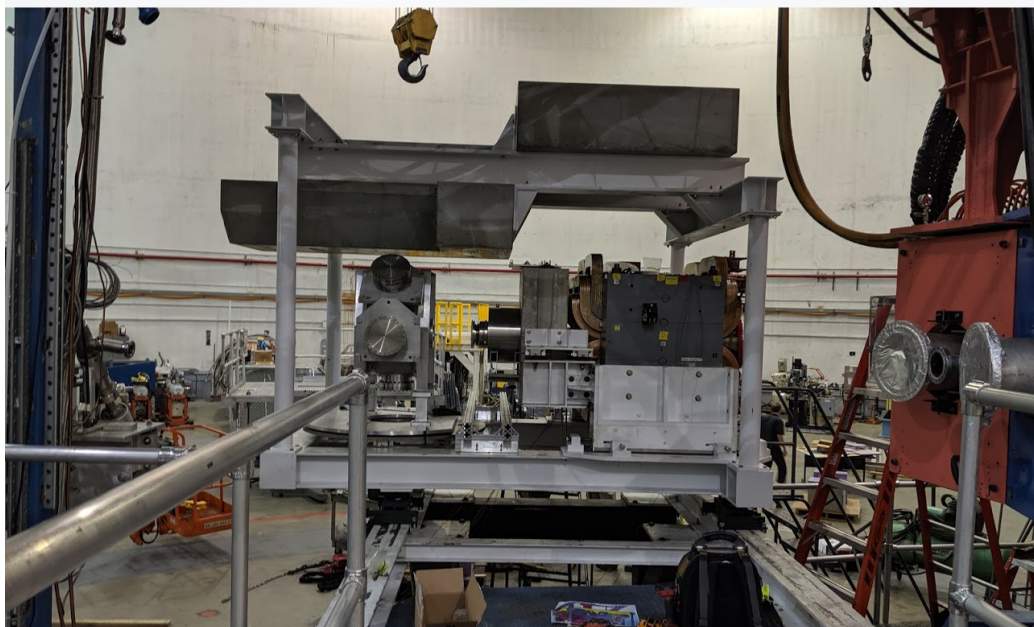
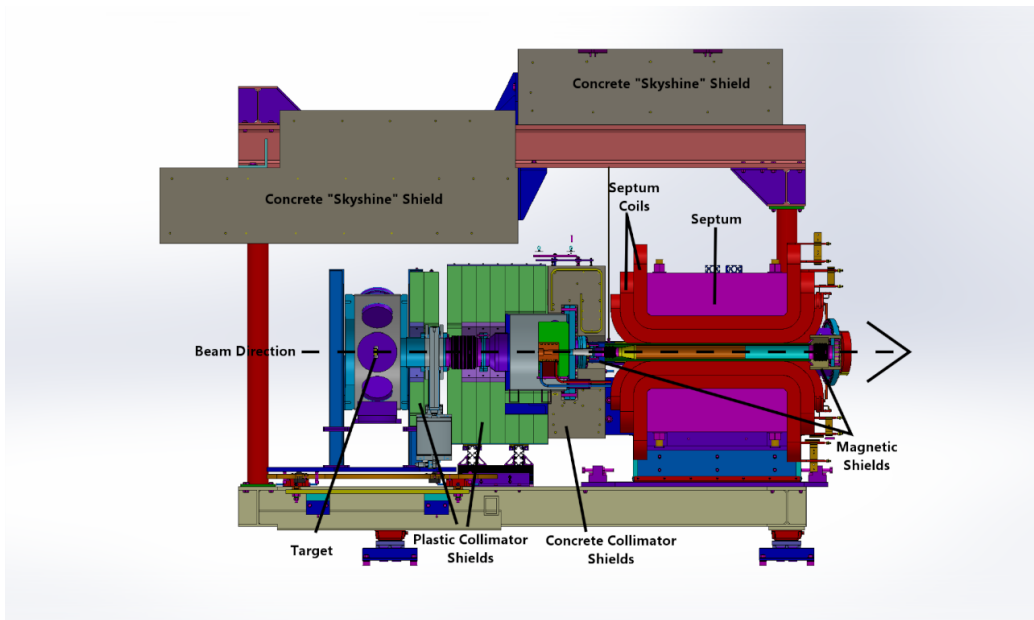


Figure 3.16: *Top*: Cross sectional CAD view of the PREX-II/CREX target region as seen from the right side of the beam. *bottom*: The same view, but taken during the experimental install. The skyshine shields can be seen as two blocks of concrete mounted above the target and beamline.

I produced significantly less dose than the JLab administrative limit, thus demonstrating that PREX-II and CREX are similarly safe to run.

3.6 Spectrometers & Optics

To transport the scattered electrons to the detector, a series of magnets are run at the proper strength to focus the electron acceptance onto the detector plane. These magnets form the septum and spectrometers, and are tuned to maximize detector rate before experimental running. Also, an electron “acceptance” had to be defined to maximize figure-of-merit (FOM). The calculation of FOM is discussed in Sec. 2.2. The acceptance also had to be measured during experimental running to define the measured \mathcal{A}_{PV} .

3.6.1 Septum Magnet

The PREX-II and CREX proposals called for a central acceptance scattering angle of 5° . However, due to the physical constraints of equipment, the minimum angle the spectrometers can be rotated to with respect to the beamline is 12.5° . To direct the scattered 5° electrons to the spectrometer axis, a septum magnet is placed downstream of the collimator.

The magnetic septum has twelve coils mounted inside an iron yoke which generates magnetic fields such that scattered electrons on either side of the beamline are steered to the spectrometer axes. The septum design can be seen in Fig. 3.17. An optical simulation is used to measure the deflection of the scattered electrons through the septum, which informs the design of the vacuum vessels through the septum. The septum also limits the inner and outer angles of the acceptance by needing to steer the acceptance out of the way of the coils.

3.6.2 Acceptance Collimator

At the end of the septum two additional collimators are installed, one on the left spectrometer, and one on the right spectrometer. The collimators are placed at the entrance of the first quadrupole magnet (Q1) on each spectrometer. The Q1 collimators are made of lead and are designed based on the optimal shape of the acceptance. Both collimators have the same dimensions

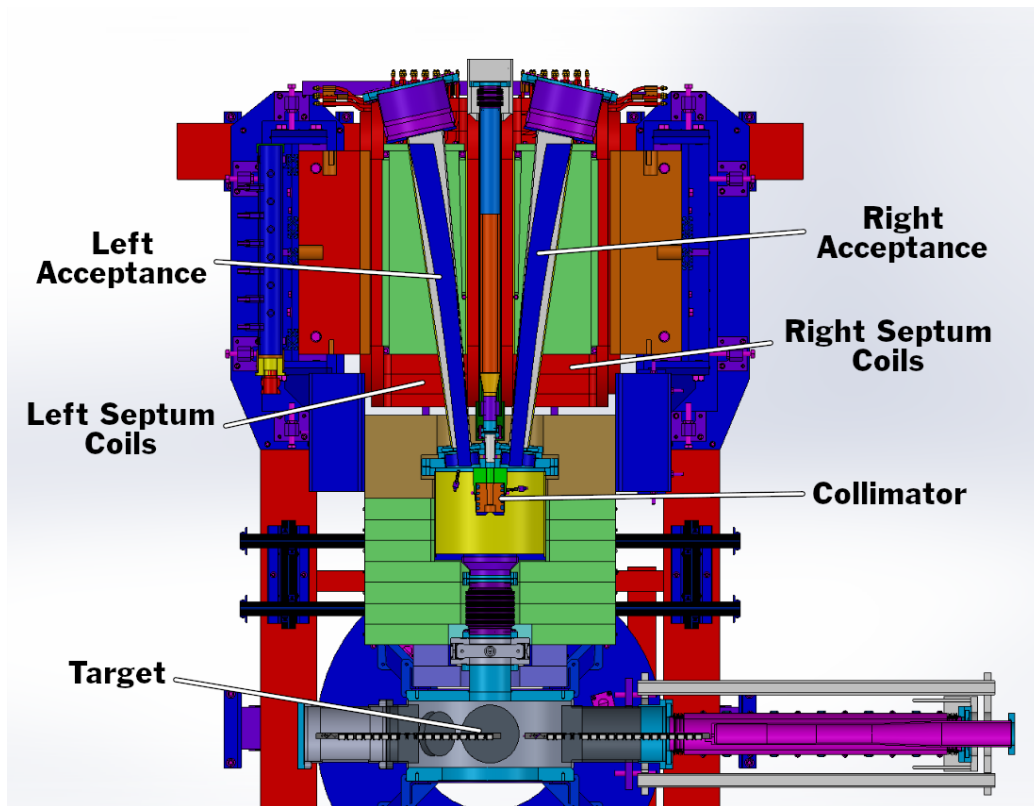


Figure 3.17: A cross sectional CAD rendering of the septum as seen from above the beamline. The acceptance path is drawn in blue on the left and right sides of the septum magnets.

in the inner cut, but were placed in opposite orientations on opposite sides of the beamline. The Q1 collimators can be seen in Fig. 3.18.

3.6.3 Spectrometer Quads & Dipole

A diagram of the HRS magnets can be seen in Fig. 3.19. The two Hall A HRSs are positioned symmetrically on opposite sides of the beamline with each spectrometer axis at an angle of 12.5° to the beamline. Once leaving the septum and passing through the Q1 collimators, both the left and right scattered electrons pass through two quadrupole magnets (Q1 and Q2) which focus the electrons. The electrons then enter the dipole magnets on each arm which deflect the accepted electrons above the beamline to a 45° angle. In-

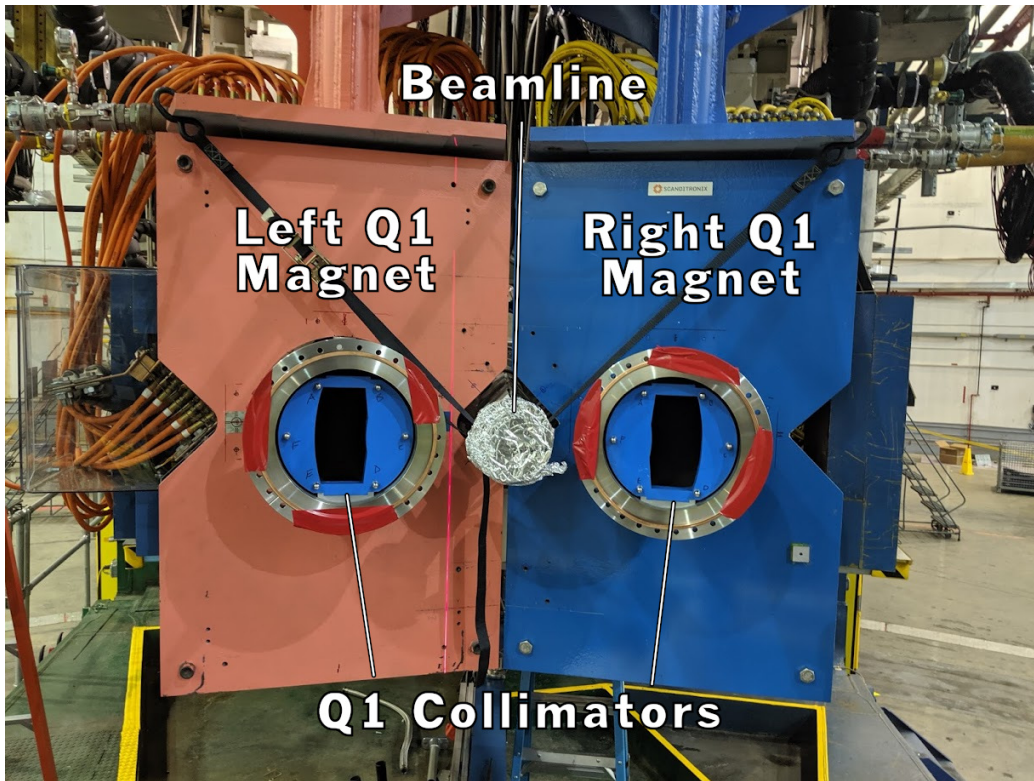


Figure 3.18: Both Q1 collimators as seen during the PREX-II installation. The primary beamline facing downstream can be seen in between the Q1 magnets. Adapted from [19].

elastic scatters (which enter the HRSs with lower energy than their elastic counterparts) are steered on a tighter arc than elastic scatters, providing a clean separation between the two. After leaving the dipole the acceptance passes through one more quadrupole magnet (Q3) before entering the detector package.

The correct currents for each of the four spectrometer magnets on each arm are determined by analyzing detector tracks of accepted electrons for different current configurations. The detector tracks are mapped back to target scattering angles θ and ϕ by calibrating the detector optics for each arm [70]. For both PREX-II and CREX a spectrometer configuration is used for both arms which focus elastics onto the detector plane while providing a physical separation from the lowest lying inelastic level.

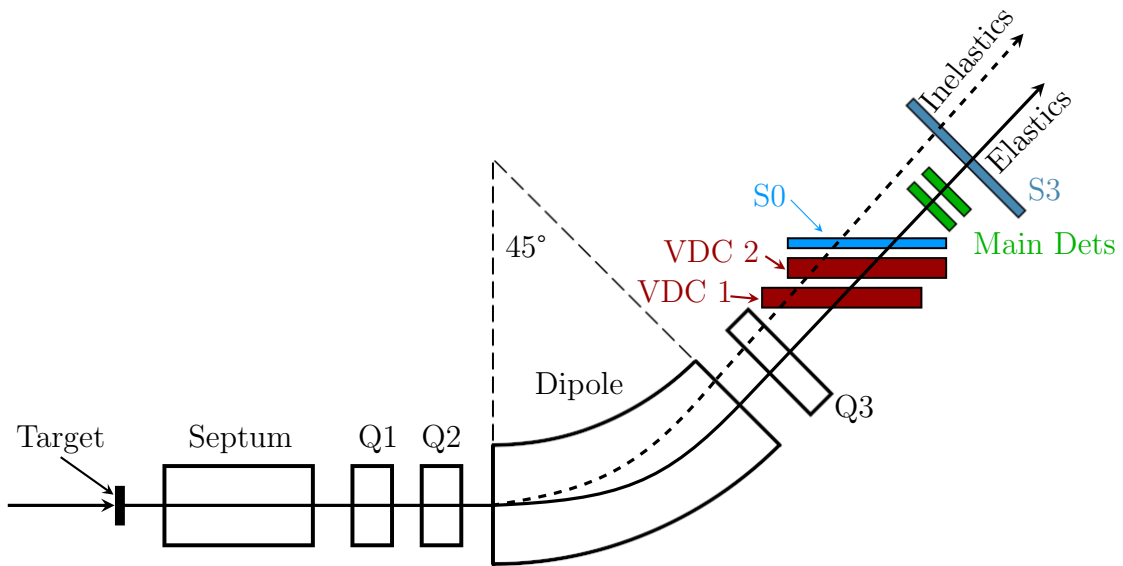


Figure 3.19: A diagram of the HRS optics and electron acceptance seen from the right side of the beamline. The septum and the four primary spectrometer magnets as well as the relative positions of the detector package can be seen. Positions, sizes, and angles not to scale. Adapted from [19, 69].

3.7 Main Detectors

All PREX-II and CREX detectors sat atop the spectrometer arms inside concrete huts. The detector huts had mechanical doors which could be opened for detector access, or closed for experimental running. Both the main detectors and the counting mode detectors are placed inside each hut on each arm.

Both PREX-II and CREX had four main detectors, with two in each spectrometer arm. The two detectors in each arm are placed one upstream and one downstream, with the detectors normal to the path of the electrons. The detectors are each a single piece of fused quartz with an area of $16 \text{ cm} \times 3.5 \text{ cm}$ and thickness of 0.5 cm . A photomultiplier tube (PMT) was attached to each detector which would detect the Čerenkov light of scattered electrons in the quartz.

The main detectors can be realigned during experimental running, which is needed to account for changes to the detector optics. Detector alignment

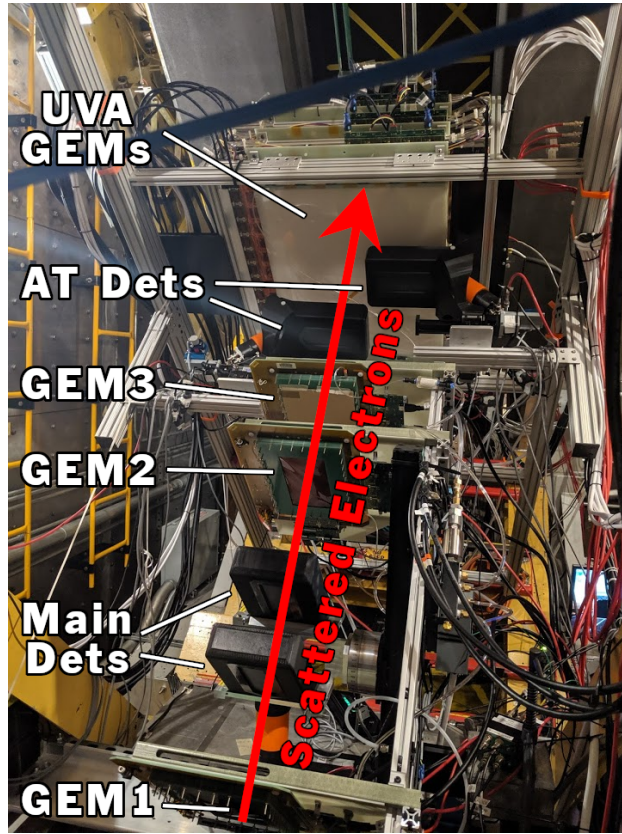


Figure 3.20: The detector package used during PREX-II and CREX with main detectors labeled. Counting mode detectors S0 and S3 are just out of frame above and below the photo respectively.

is done using the tracking vertical drift chambers (VDCs)⁶ [19].

3.7.1 \mathcal{A}_T Detectors

Two additional quartz detectors are placed approximately 1 meter downstream of the main detectors in each spectrometer arm. These “ \mathcal{A}_T ” detectors are aligned with the main detector package to maximize sensitivity to the vertical scattering component. Because scattering from the horizontal transverse-polarized beam component dominates in these regions, the \mathcal{A}_T

⁶As a cross-check for high-rate tracking PREX-II and CREX also use several gaseous electron multiplier (GEM) detectors.

detectors are used to calculate the horizontal transverse polarization correction $\mathcal{A}_T\mathcal{P}_H$ [70]. The correction for the vertical transverse-polarized beam component $\mathcal{A}_T\mathcal{P}_V$ is taken from the main detectors.

3.8 Counting Mode Detectors

While the main detectors produce the measurement of \mathcal{A}_{PV} , they cannot measure individual particle tracks which are used to reconstruct the scattering kinematics on target. To obtain particle tracks a series of detectors are used periodically throughout running for detector alignment, Q^2 measurements, and raster checks. These detectors are usually only run with very low current on the target otherwise measured rates in the counting detectors become unmanageable.

3.8.1 Drift Chambers

Included as part of the standard Hall A detector package are two vertical drift chambers (VDCs) in both spectrometer arms. Each VDC is positioned just below each detector hut with one VDC being approximately 50 cm downstream of the other. The gas in the VDCs is a mixture of argon, ethane and alcohol vapor. Each VDC also has several planar grids of thin high-voltage signal wires. Charged particles passing through the VDCs ionize the gas which is detected as an electrical signal in the wire grids. The position of the ionization track in the corresponding VDC are used to identify the position and angle of incoming electrons, which were then used to reconstruct the electron scattering kinematics [59].

3.8.2 S0 & S3 Detectors

The PREX-II and CREX counting detector package also includes two BICRON 408 plastic counting scintillators in each detector hut. The first detector dubbed “S0” is placed between the second VDC and the main detectors in each arm. The second detector, which consists of an array of scintillators, dubbed “S3” is placed downstream of the entire detector package. These two scintillators cover a wide area of the acceptance each with an area of 170 cm \times 25 cm. The S0 scintillator has multiple PMTs placed on different ends of the physical scintillator material. During PREX-II only one S3 scintillator

was used, but two additional scintillators were used for CREX. These detectors are used to gauge rate at low current and for checks of the size of the raster.

3.9 Data Acquisition

PREX-II and CREX had two different data acquisition systems (DAQs) run independently at different times. The first DAQ, the integrating DAQ measured \mathcal{A}_{PV} and helicity-correlated beam quantities such as \mathcal{A}_Q and other measures of beam asymmetries. The second DAQ, the counting DAQ, measured detector rates and was used whenever a measurement requiring particle tracks of kinematic reconstruction was needed.

3.9.1 Integrating Mode DAQ

PREX-II and CREX operate at very high scattering rates, so individual electron events happen too fast to record individually. Instead, for measurements of \mathcal{A}_{PV} , many parity experiments, such as PREX-II and CREX, use an integrating technique for data acquisition (DAQ). The principle of this technique is to integrate the measured Čerenkov light from acceptance electrons in the detectors over pedestal for the stable time t_{stable} of each helicity period. \mathcal{A}_{PV} is then calculated using the light-weighted integrated helicity-period sums rather than individual electron counts.

This system is implemented by a series of interconnected electronic modules placed in either the injector, Hall A or in the counting house⁷. The first of these was a helicity control board (HCB) in the injector which generates a binary signal matching the helicity state. Helicities are generated in patterns where one of two helicity sequences are chosen at a 30 Hz pattern frequency. These patterns either contain four helicity periods (quartet) or eight helicity periods (octet). For both modes there are only two helicity patterns that could be used. For quartet running the pattern, expressed in terms of helicity sign is either + - - + or - + + - while for octet running the two patterns are + - - + - + + - or - + + - + - - +, where here “+” and “-” refer to the sign of the voltages applied to the Pockels cell. Each pattern is selected pseudorandomly, and helicities are generated in the sequence in

⁷Which is the name of the experimental control room.

each selected pattern [71]. A timing diagram of these periods, including the RTP cell settle time can be seen in Fig. 3.21.

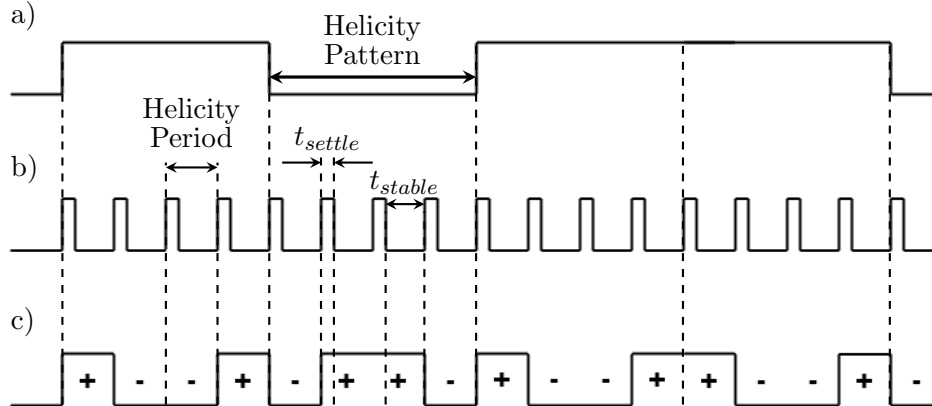


Figure 3.21: Quartet helicity pattern timing used for both PREX-II and CREX showing the a) pattern signal, b) Macro-Pulse Signal (MPS) and c) helicity sign. There are four helicities per pattern in one of two patterns. Which pattern is used is selected pseudorandomly. Each helicity period is divided into two times: the settling time t_{settle} and the stable time t_{stable} . Note that for octet helicity patterns the patterns are different.

The helicity pattern system limited possible false asymmetries or noise. Commercial electricity in the United States is delivered at 60 Hz AC and thus the helicity flip rate is a multiple of 60 Hz for both experiments. PREX-II was initially run at 120 Hz quartet pattern mode, though halfway through running it was changed to 240 Hz octet mode which further suppressed noise and therefore increased statistical precision on \mathcal{A}_{PV} . CREX was run entirely at 120 Hz quartet mode.

The HCB does not send the helicity signal directly to the Hall A DAQs but instead delays the signal by two patterns to minimize the effects of helicity-correlated noise in the electronics. The delayed helicity signal would then be sent to a HAPPEX timing board (HAPT B). The HAPT B is triggered by the Macro Pulse Signal (MPS). MPS triggers at the start of t_{stable} in each helicity period and end at the beginning of the next helicity-period's t_{settle} . The HAPT B's start signal is generated upon starting a new t_{stable} though the stop signal is generated a pre-programmed amount of time after start

[72, 73]. DAQ integration only happens during t_{stable} in order to eliminate effects from the helicity transition.

The start of t_{stable} from HAPT B is distributed to the ADCs which integrated the quartz detector signals over the t_{stable} period. During the t_{settle} period in each subsequent helicity-state, the integrated ADC signals are read out of the electronics and pushed to a software data stream that is saved at the end of the run. In addition to the HAPT B and ADC chain the integrating DAQ also includes different modules for beamline components such as voltage-to-frequency converters (V2Fs), and counting scalers.

The DAQs are remotely controlled, and at the end of every DAQ run a data file is generated from the DAQ electronics. The experimental DAQ systems are run through software called the CEBAF Online Data Acquisition (CODA). Through CODA DAQs are stopped and started by experimenters. At each start CODA initializes the DAQ system and begin recording data. At each stop CODA stops data recording, finalizes the raw data file and moves it to experimenter computer systems. DAQs are stopped and started regularly with each period of continuous data recording being a “run.” During PREX-II and CREX typical runs are between 30 minutes and 90 minutes long with few exceptions.

To read the data file which CODA produces and extract the quantities needed to do a full analysis a software analyzer was developed for PREX-II and CREX. This analyzer (dubbed “JAPAN” for Just Another Parity ANalyzer) is developed from previous parity analyzers used on the PREX-I and QWeak experiments.

3.9.2 Counting Mode DAQ

The two counting DAQs were located one in each detector hut. The S0 and S3 signals were amplified before being fed into a discriminator which registered a pulse whenever the scintillator PMT signal exceeded the channel threshold. A total of five signals were combined in different logical combinations to measure different trigger rates. During running S0 trigger signals were used more frequently owing to the S0 scintillators closer position to the VDCs.

The VDC and GEM signals were read by the same DAQ in parallel configurations. The signals from all detectors were sent through different discriminator channels with different thresholds to count individual tracks.

The counting DAQ analyzer was developed for Hall A experiments generally, and was a separate analysis process from the one in JAPAN.

3.10 Slow Controls, EPICS, & CODA

While running PREX-II and CREX, experimenters require a real-time information system to monitor the apparatus. For this a system of “slow controls” are used. The system which collects experimental information and reports it is the Experimental Physics and Industrial Control System (EPICS). EPICS was developed at Argonne National Laboratory and is implemented at JLab for most accelerator and experimental systems. EPICS works by polling a series of servers called Input/Output Controllers (IOCs) for desired signals or DAQ measurements. The results of the polls (which are conducted on average once per second though some systems are polled slightly faster or slower) the readback is updated system-wide and visible on all JLab computer systems and even remotely over the internet.

PREX-II and CREX use EPICS to track relevant beam quantities and spectrometer and detector information. EPICS gives experimenters real-time information on critical experimental quantities including but not limited to the beam position and angle, beam charge deposited on target, spectrometer magnet currents, raster currents, target temperature, energy resolution, and beamline vacuum strength. EPICS also provides the ability to control experimental hardware remotely though the critical systems that could be controlled this way are too numerous to list here.

Chapter 4

Compton Polarimetry Principles

The Hall A Compton polarimeter uses backscattered Compton photons to measure beam polarization. Since its commissioning in 1999, the Compton polarimeter has been used in a number of Hall A experiments that require additional beam polarization measurements besides the Møller polarimeter (described in Sec. 3.2.4). The Compton polarimeter works by passing green laser light into a high-finesse Fabry-Pérot resonant cavity which amplifies the laser light. First, the primary electron beam is diverted downwards by dipole magnets in a magnetic “chicane” separate from the primary beamline. At the center of the chicane the electron beam is then passed through the laser in the cavity, which creates a high rate of backscattered Compton photons. The physics of Compton scattering for beam polarimetry is discussed in Sec. 4.1 and Sec. 4.2. The laser system that produces high optical power and rate is discussed in Sec. 4.3.1. The backscattered Compton photons impinge on a photon detector consisting primarily of a scintillating crystal, and a photomultiplier tube. The photon detector system is discussed in Sec. 4.3.2. Nominally, Compton scattered electrons, having lost a small fraction of their energy, will be bent by the downstream chicane dipole magnets up into an electron detector system which itself can make Compton asymmetry measurements. There is a discussion of the electron detector systems in Sec. 4.3.3, however it will be brief as only data from the photon detector was used in the primary experiment.

There are two principal methods for calculating a scattering asymmetry from Compton-scattered photons, which can be used to extract the beam

polarization \mathcal{P}_e . The first is an integrating method that integrates the full backscattered photon energy received in the photon detector per helicity period. The asymmetry is then calculated from the energy measured per helicity pattern. The second method instead counts the the number Compton photon pulses per helicity period and calculates the asymmetry of these pulse counts. The first method is discussed in Sec. 5.2 and the hardware that reads this measurement is discussed in Sec. 4.4.1. The hardware components used in the counting mode measurement are discussed in Sec. 4.4.2, however the Compton counting mode asymmetry calculation is not discussed as only the integrating mode asymmetries were used for PREX-II and CREX.

The Compton photon analysis also relied on the results of a GEANT4-based Monte Carlo simulation to calculating the analyzing power for our measurement. The analyzing power is discussed in Sec. 5.4, and the simulation parameters are discussed in Sec. 5.4.1. The method for calculating Compton analyzing power varies between the two asymmetry calculation methods—for the former the energy-weighted average is calculated over the entire Compton spectrum, while for the latter, a rate-averaged analyzing power is calculated over the range of the Compton spectrum that lies above the discrimination threshold.

Additionally the Compton photon detector analyzer, which converts the raw data written by our DAQ into a human-readable form will be discussed in Sec. 4.5.

4.1 Compton Kinematics

Compton scattering is the process of an electron and photon scattering off each other in the reaction $e^- \gamma \rightarrow e^- \gamma$ as seen in Fig. 4.1. The effect was first observed in 1923 by Arthur Holly Compton and was a significant development for physicists' understanding of the photon as a particle in relativistic quantum mechanics [74]. In the near century since, Compton scattering has found diverse applications including astrophysics, materials science and nuclear medicine [75, 76, 77].

The geometry of Compton scattering as it pertains to the Hall A Compton polarimeter can be seen in the lab frame of reference in Fig. 4.2. The beam of polarized electrons enters the cavity with energy E and momentum p where m_e is the electron mass $0.511 \text{ MeV}/c^2$. The electron beam passes through the resonant laser with $\lambda = 532 \text{ nm}$ and photon energy $k = 2.33 \text{ eV}$. The

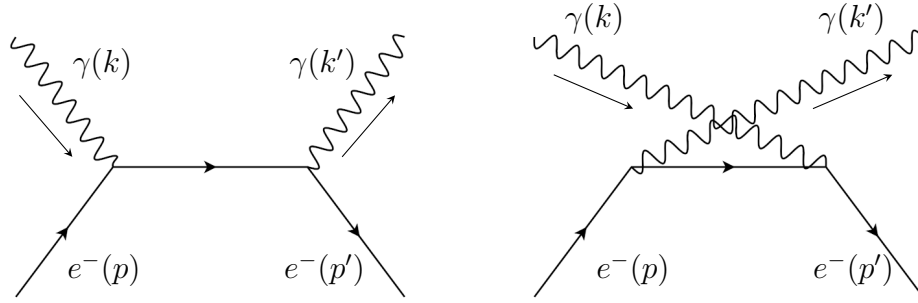


Figure 4.1: *Left*: Feynman diagram for Compton scattering at the tree level with labeled momenta. *Right*: Tree-level crossing diagram for Compton scattering.

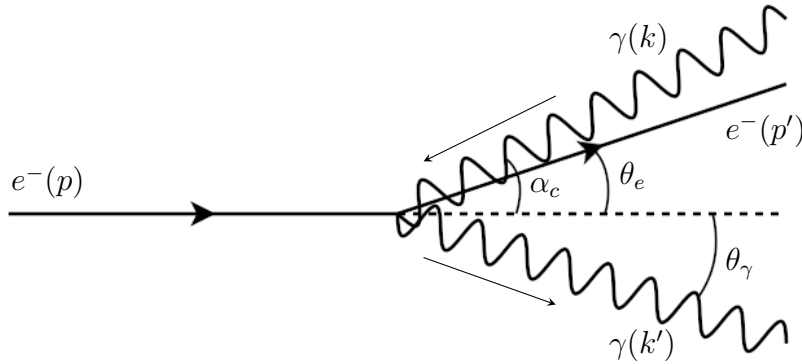


Figure 4.2: Diagram showing the relevant Compton angles for kinematics. Angles in Fig. are exaggerated, and not to scale.

limitations of our setup also means the photon beam must pass the electron beam at a slight crossing angle $\alpha_c \approx 23$ mrad. After scattering occurs the scattered photon leaves the interaction point at in-plane angle θ_γ and energy k' while the electron leaves with in-plane angle θ_e and outgoing energy E' . The initial and final state of the electron and photon can be described by the four-vectors

$$p^\mu = (E, 0, 0, p), \quad (4.1)$$

$$k^\mu = (k, -k \sin(\alpha_c), 0, -k \cos(\alpha_c)), \quad (4.2)$$

$$p'^\mu = (E', p' \sin(\theta_e), 0, p' \cos(\theta_e)), \quad (4.3)$$

$$k'^\mu = (k', k' \sin(\theta_\gamma), 0, k' \cos(\theta_\gamma)). \quad (4.4)$$

For a two-body scattering the conservation of momentum holds that only the in-plane scattering angle θ_γ needs to be accounted for.

By applying both conservation of energy and conservation of momentum we derive the energy for the outgoing photon as

$$k' = \frac{E + p \cos \alpha_c}{E + k(1 + \cos(\alpha_c - \theta_\gamma)) - p \cos \theta_\gamma}. \quad (4.5)$$

We then, because α_c is small, treat it as zero, without significant loss of accuracy. Understanding that $p = \sqrt{E^2 - m_e^2}$ find the photon energy in terms of our initial beam kinematic quantities [78]

$$k' = \frac{4kaE^2}{m_e^2 + a\theta_\gamma^2 E^2}, \quad (4.6)$$

where a is a dimensionless kinematic variable

$$a \equiv \frac{1}{1 + \frac{4kE}{m_e^2}}. \quad (4.7)$$

Of note is the dependence of outgoing photon energy on the value of the photon scattering angle θ_γ . As θ_γ increases, the energy of the Compton scattered photon decreases. Consequently, the highest value of backscattered photon energy k'_{max} can be found when $\theta_\gamma = 0$

$$k'_{max} = \frac{4kaE^2}{m_e^2}. \quad (4.8)$$

This represents the ‘‘Compton edge’’ energy and corresponds to a Compton photon being backscattered a full 180°. Table 4.1 contains the calculated Compton edge values for both experiments. Plots of the backscattered photon energy as a function of θ_γ are shown in Fig. 4.3 for both PREX-II and CREX. Because of the higher beam energy for the CREX experiment, the CREX Compton edge energy is approximately 5 times higher.

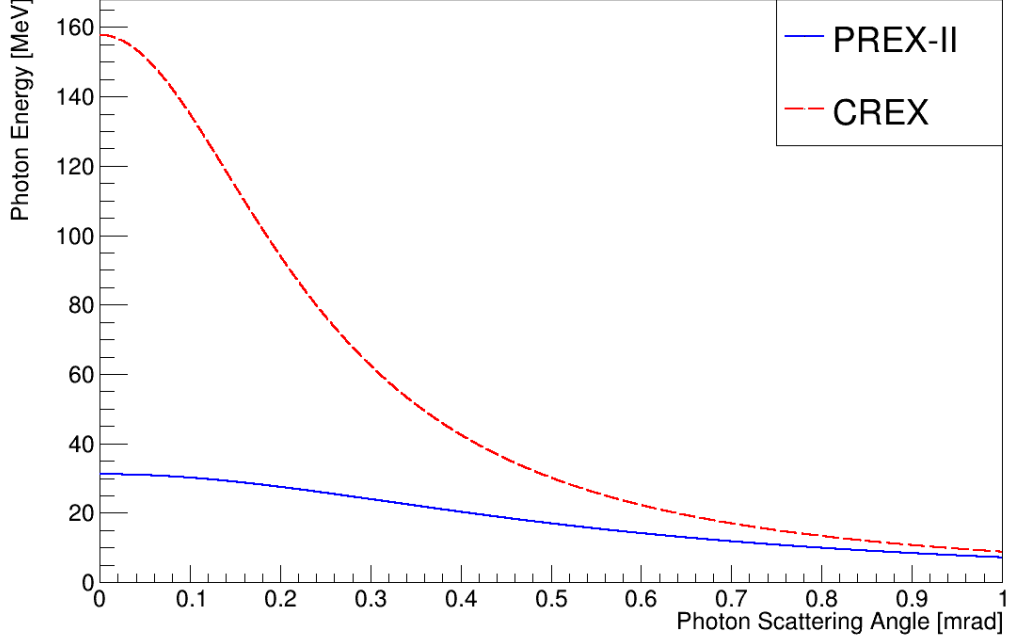


Figure 4.3: Compton photon energy plotted vs scattering angle for both experiments. The Compton edge energy is reached when $\theta_\gamma = 0$, and the Compton photon is completely backscattered.

| Experiment | Beam Energy [MeV] | Compton Edge Energy [MeV] |
|------------|-------------------|---------------------------|
| PREX-II | 950 | 31.2 |
| CREX | 2182.5 | 157.7 |

Table 4.1: Table of Compton edge values for both PREX-II and CREX.

4.2 Compton Cross Sections & Asymmetry

If we assume crossing angle α_c is small, then we can write the unpolarized Compton differential cross section as

$$\frac{d^2\sigma_0}{d\rho d\phi} = r_0^2 a \left[\frac{\rho^2(1-a)^2}{1-\rho(1-a)} + 1 + \left(\frac{1-\rho(1+a)}{1-\rho(1-a)} \right)^2 \right], \quad (4.9)$$

where $r_0 = \alpha\hbar c/mc^2 = 2.817 \times 10^{-13}$ cm is the classical electron radius, $\rho = k'/k'_{max}$ is the fraction of Compton edge energy and a is the kinematic factor defined in Eqn. 4.7 [78].

We then have to take into account the dependence on the Compton differential cross section on the electron and photon polarization. The laser system will be discussed in more detail in Sec. 4.3.1 but relevant to this discussion is the laser polarization is determined by a series of waveplates on the laser table that can be adjusted until we have 100% circular polarization in the cavity.

Similarly, the CEBAF accelerator delivers a longitudinally spin-polarized electron beam into the hall, which flips helicity state by a pseudo-random pattern. This system is described in more detail in Sec. 3.1.1.

To properly modify $d\sigma_0/d\rho$ to account for beam polarization we must include terms dependent on both the beam longitudinal polarization and the beam transverse polarization. The cross section resulting from longitudinally polarized electrons [79] is

$$\frac{d^2\sigma_l}{d\rho d\phi} = ar_0^2(1 - \rho(1 + a)) \left[1 - \frac{1}{(1 - \rho(1 - a))^2} \right], \quad (4.10)$$

and similarly the cross section from transversely polarized electrons is

$$\frac{d^2\sigma_t}{d\rho d\phi} = ar_0^2\rho(1 - a) \frac{\sqrt{4a\rho(1 - \rho)}}{1 - \rho(1 - a)}. \quad (4.11)$$

The complete differential cross section can be written as:

$$\frac{d^2\sigma}{d\rho d\phi} = \frac{d^2\sigma_0}{d\rho d\phi} \mp \mathcal{P}_\gamma \mathcal{P}_e \left(\cos(\psi) \frac{d^2\sigma_l}{d\rho d\phi} + \sin(\psi) \cos(\phi) \frac{d^2\sigma_t}{d\rho d\phi} \right), \quad (4.12)$$

where \mathcal{P}_γ is the laser degree of circular polarization (DOCP), \mathcal{P}_e is the electron beam polarization, ϕ is the out-of-plane scattering angle, and ψ is the angle of the direction of the electron spin with respect to the beam propagation axis \hat{z} . The sign of the polarized cross section terms is determined by whether the laser polarization and electron beam polarization are parallel or antiparallel.

Because the out-of-plane scattering angle ϕ only contributes in the transverse asymmetry term, we can integrate over ϕ to remove that term from our cross section measurement. The differential cross section becomes

$$\frac{d\sigma}{d\rho} = \frac{d\sigma_0}{d\rho} \mp \mathcal{P}_\gamma \mathcal{P}_e \cos(\psi) \frac{d\sigma_l}{d\rho}. \quad (4.13)$$

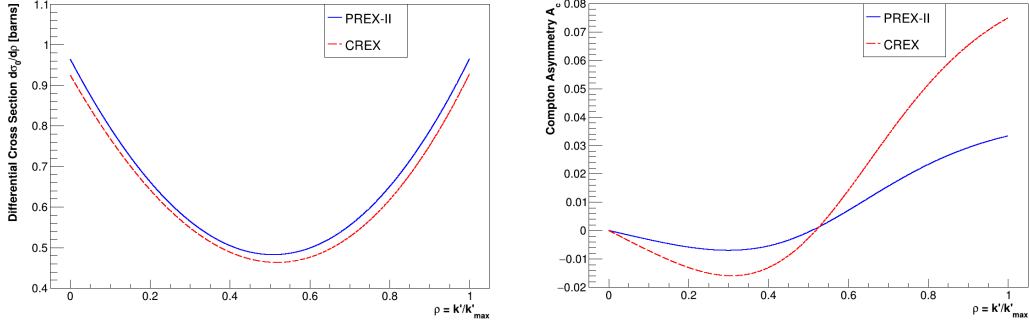


Figure 4.4: The unpolarized Compton cross section $\frac{d\sigma}{d\rho}$ (left) and theoretical analyzing power \mathcal{A}_c (right) both plotted as a function of backscattered photon energy.

Measurement of the beam polarization is then contingent on our ability to measure the difference between the Compton-scattered signal in each electron helicity state. For this purpose it is convenient to define the experimental Compton asymmetry as

$$\mathcal{A}_{exp} \equiv \frac{(d\sigma/d\rho)^+ - (d\sigma/d\rho)^-}{(d\sigma/d\rho)^+ + (d\sigma/d\rho)^-} = \mathcal{P}_e \mathcal{P}_\gamma \cos(\psi) \mathcal{A}_c, \quad (4.14)$$

where the Compton scattering analyzing power \mathcal{A}_c is

$$\mathcal{A}_c \equiv \frac{d\sigma_l/d\rho}{d\sigma_0/d\rho}. \quad (4.15)$$

We can compute the analyzing power in the limit that $\rho = 1$ or equivalently $k' = k'_{max}$. The limiting values are most easily calculated in the cross sections

$$\frac{d\sigma_0}{d\rho}(\rho = 1) = (2\pi r_0 a) \frac{1 + a^2}{a}, \quad (4.16)$$

$$\frac{d\sigma_l}{d\rho}(\rho = 1) = (2\pi r_0 a) \frac{1 - a^2}{a}, \quad (4.17)$$

$$\mathcal{A}_c^{max} = \mathcal{A}_c(\rho = 1) \equiv \frac{(1 - a)(1 + a)}{1 + a^2}. \quad (4.18)$$

The expression for A_{exp} then still retains a dependence on the angle ψ which measures the transverse component of the electron spin. The experimental asymmetry is maximized when $\psi = 0$, (i.e., when the electron spin is purely longitudinal). The asymmetry goes to zero when $\psi = \pi/2$, meaning that if the beam is perfectly transverse then we should measure zero asymmetry. PREX-II and CREX were both set up to have a purely longitudinal beam, so we can safely make the approximation $\cos \psi \simeq 1$.

4.2.1 Compton Analyzing Power

We then calculate the experimental analyzing power which would be our measured Compton asymmetry if we had 100% polarized beam and 100% circularly polarized laser light. The difference between the theoretical analyzing power and the experimental analyzing power is that the experimental analyzing power corrects for measured detector effects such as nonlinearity. The exact calculation of analyzing power depends on if the asymmetry measurement made is via energy-weighted integration or rate-averaged integration [78].

Compton Counting Asymmetry Measurement

If individual Compton scattering events can be measured then a Compton counting measurement can be performed. In this technique the asymmetry of the number of Compton events is calculated. This can be done one of two ways.

The first way is simply to calculate the asymmetry of all events measured over the entire Compton energy range. This Compton energy range lies between the lower threshold energy ρ_{min} and the Compton edge energy $\rho_{max} = 1$. The number of Compton pulses for each helicity state is

$$N_{\pm} = \mathcal{L} \int_{\rho_{min}}^1 d\rho \epsilon(\rho) \frac{d\sigma}{d\rho} (1 \pm \mathcal{P}_e \mathcal{P}_\gamma \mathcal{A}_l), \quad (4.19)$$

where \mathcal{L} is the integrated Compton scattering luminosity, and $\epsilon(\rho)$ is the detector response function. The asymmetry of this measurement is

$$\mathcal{A}_{exp} = \frac{N_+ - N_-}{N_+ + N_-} = \mathcal{P}_e \mathcal{P}_\gamma \langle \mathcal{A}_l \rangle, \quad (4.20)$$

where $\langle \mathcal{A}_l \rangle$ is the experimental analyzing power for this measurement

$$\langle \mathcal{A}_l \rangle = \frac{\int_{\rho_{min}}^1 d\rho \epsilon(\rho) \frac{d\sigma}{d\rho} \mathcal{A}_c(\rho)}{\int_{\rho_{min}}^1 d\rho \epsilon(\rho) \frac{d\sigma}{d\rho}}. \quad (4.21)$$

If the Compton detector has the ability to discriminate pulses based on scattered photon energy then the Compton asymmetry can be measured as function of energy. In this technique the Compton energy range is divided up into N_b bins and the scattering rate is integrated over each bin i by

$$n_{\pm} = \mathcal{L} \int_{\rho_i}^{\rho_{i+1}} d\rho \epsilon(\rho) \frac{d\sigma}{d\rho} (1 \pm \mathcal{P}_e \mathcal{P}_\gamma \mathcal{A}_c(\rho)), \quad (4.22)$$

where ρ_i and ρ_{i+1} are the energy thresholds for bin i and bin $i+1$ respectively. The experimental for asymmetry for each bin is

$$\mathcal{A}_{exp}^{(i)} = \frac{n_+^{(i)} - n_-^{(i)}}{n_+^{(i)} + n_-^{(i)}} = \mathcal{P}_e^{(i)} \mathcal{P}_\gamma \langle \mathcal{A}_c^{(i)} \rangle, \quad (4.23)$$

where $\mathcal{P}_e^{(i)}$ is the mean polarization for each bin i and $\langle \mathcal{A}_c^{(i)} \rangle$ is the average theoretical analyzing power for each bin. If N_b is large enough then we can approximate the analyzing power with the analyzing power at the center of each bin [80]. The mean polarization is then taken from the weighted mean of the bin asymmetries $\mathcal{A}_{exp}^{(i)}$.

Both of these techniques have an arbitrarily small threshold ρ_{min} at the lower end of the Compton energy range. In principle this energy threshold can be arbitrarily small. In practice, practical Compton detection systems may potentially identify pulses arising from low-energy backgrounds and electronics noise. So for practical measurements ρ_{min} is a small positive fraction of the Compton edge. The system that makes this measurement will be discussed in Sec. 4.4.2.

Compton Integrating Asymmetry Measurement

Another method to measure the asymmetry is to measure the total scattered energy in each helicity state and compute the asymmetry from that. This technique does not require individual pulses to be measured, instead requiring that the total deposited energy be integrated for each MPS.

In this technique we measure the “energy-weighted” mean signal

$$S_{\pm} = \mathcal{L} \int_{\rho_{min}}^1 d\rho Y(\rho) \epsilon(\rho) \frac{d\sigma}{d\rho} (1 \pm \mathcal{P}_e \mathcal{P}_\gamma \mathcal{A}_c(\rho)), \quad (4.24)$$

where $Y(\rho)$ is the mean detector signal in each helicity state [78]. For this technique the asymmetry analyzing power also uses the mean detector signal

$$\langle \mathcal{A}_l \rangle = \frac{\int_{\rho_{min}}^1 d\rho Y(\rho) \epsilon(\rho) \frac{d\sigma}{d\rho} \mathcal{A}_c(\rho)}{\int_{\rho_{min}}^1 d\rho Y(\rho) \epsilon(\rho) \frac{d\sigma}{d\rho}}. \quad (4.25)$$

This integrating measurement was the asymmetry measurement technique used for PREX-II and CREX, chosen over counting due to the poor resolution of individual detector pulses at low Compton energies, like those in PREX-II and CREX. For this also $\rho_{min} = 0$, as the backgrounds are assumed to be equal in each helicity state.

Ultimately, the experimental asymmetry for all measurements is

$$\mathcal{A}_{exp} = \mathcal{P}_\gamma \mathcal{P}_e \langle \mathcal{A}_l \rangle, \quad (4.26)$$

where the experimental analyzing power $\langle \mathcal{A}_l \rangle$ is computed differently for each asymmetry measurement technique.

4.2.2 Compton Radiative Corrections

The primary correction to the analyzing power was that of radiative corrections (i.e., the asymmetry contribution from 1-loop Compton scattering diagrams.) At JLab energies we can use an approximation provided by Denner and Dittmaier [81] that uses only corrections that are first-order in β :

$$\mathcal{A}_l = \mathcal{A}_{Born} (1 + \Delta \mathcal{A}), \quad (4.27)$$

$$\Delta \mathcal{A} = \frac{\alpha}{\pi} \frac{3 \cos \theta_\gamma^{CM} - 1}{4(\beta + \cos \theta_\gamma^{CM})}, \quad (4.28)$$

where $\beta = k'^{CM}/E'^{CM}$, and θ_γ^{CM} is the photon scattering angle measured in the center of mass. The correction would make the analyzing power larger, which in turn would be a negative correction on measured polarization.

4.3 Hall A Compton Polarimeter

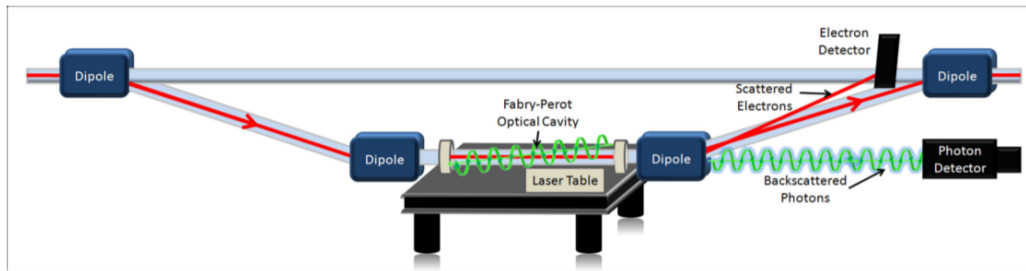


Figure 4.5: The layout of the Hall A Compton polarimeter. Distances and angles not to scale. Beam enters from the left, is diverted down in a magnetic chicane where it scatters off green laser light. The beam is then steered towards the main experiment. The Compton-scattered photons proceed to the main detector downstream. Figure courtesy of Don Jones.

The Compton polarimeter has three key subsystems, two of which were extensively used during PREX-II and CREX. The first important subsystem is the laser system which included not only the laser and amplifier itself, but the optics on the table leading up to the cavity, the cavity itself, photodiodes to measure transmitted and reflected laser power and the locking electronics that relied on the signals from these photodiodes. The laser and associated components will be discussed in Sec. 4.3.1.

The second subsystem is the Compton photon detector which primarily consisted of a scintillating crystal and a photomultiplier tube. The experimental measurement of Compton asymmetry and beam polarization came exclusively from this detector. The physical detector will be discussed in Sec. 4.3.2 while the data acquisition system for the photon detector will be discussed in Sec. 4.4.

The final main subsystem is the electron detector which consisted of 4 planes of ~ 100 strips of silicon which could read pulses from Compton scattered electrons diverted out of the part of the beam. This subsystem will be discussed in Sec. 4.3.3. This detector was not used at all during PREX-II and was only used for diagnostic measurements during CREX so no data from the electron detector will be presented as it did not contribute to our overall polarimetry measurement.

4.3.1 Laser System

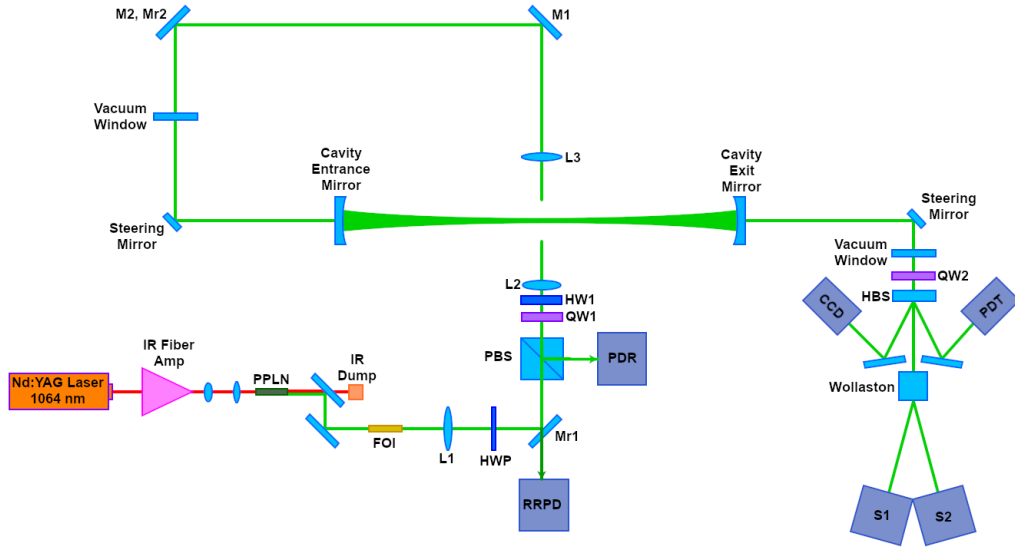


Figure 4.6: Compton laser table system with the primary components labeled. Figure courtesy of Abdurahim Rakhman with minor alterations [82].

The primary laser component is a narrow-linewidth Nd:YAG IR laser ($\lambda = 1064 \text{ nm}$), which can output up to 250 mW power. The laser is coupled via optical fiber to an IPG Photonics YAR-LP-SF yttrium-doped 10 W fiber amplifier which can output up to 10 W laser light from the initial seed. The fiber output of the amplifier is focused and fed into a Periodically Poled Lithium Niobate (PPLN) crystal which frequency-doubles the IR laser light to green ($\lambda_g = 532 \text{ nm}$). The PPLN is placed in a temperature-controlled housing behind a Faraday optical isolator (FOI) which protects the laser emission components from back-reflected light. The optical components on the laser table are illustrated in Fig. 4.6.

The green laser passes through a stationary half-wave plate which optimizes the laser polarization for transport on the laser table. The green laser passes through a polarizing beam splitter (PBS), which is also used to polarize the reflected laser before it reaches the retro-reflected photodiode (RRPD). The laser then goes through a quarter-wave plate and a half-wave plate (abbreviated QW1 and HW1 respectively). The combination of the QW1 and HW1 determines the laser polarization state of the laser that gets

fed into the cavity, and each wave plate can be rotated remotely. The laser also passes through several lenses to optimize the beam waist at the Compton interaction point (CIP), as well as a vacuum window [83].

The laser is then directed through a series of partially-transmitting mirrors into the Fabry-Pérot cavity which is sealed under vacuum, and through which the electron beam passes. Between the QW1/HW1 and the Compton interaction point there are numerous sources of birefringence that mean the DOCP as measured on the table is different from the DOCP as measured in the cavity. For example, the cavity mirror birefringence contributes to depolarization of the laser. The polarization of the laser could not be directly measured at the CIP with the cavity mirrors in place so measurements of the polarization along the cavity entrance line, plus the effects of birefringent elements before the cavity could be used to indirectly measure CIP DOCP.

In order to “lock” the cavity onto a resonance the Pound-Drever-Hall technique is used. The core principle of the Pound-Drever-Hall technique is to generate an error signal based on the frequency sidebands added to the primary laser harmonic. The error signal is then fed back to the laser which adjusts the output for frequency stabilization. For most of PREX-II and CREX running the laser was quickly locked and unlocked regularly. A schematic of the locking electronics can be seen detailed in Fig. 4.7.

Many aspects of the laser system are controlled remotely either manually or by automated programs through the laser’s slow control program. The power output of the fiber amplifier, the position of the QW1 and HW1, and the precise angle of the mirrors on the laser table are controlled through the laser’s slow controls. Notably, the laser locking system is also activated or deactivated through an automated script, which allows our photon detector periodic measurements of both Compton scattered signal and background. This system of “laser cycling” is a key component of the Compton data set for both experiments.

Polarization & Stokes Parameters

As Eqn. 4.26 demonstrates, the Compton experimental asymmetry must be normalized by both analyzing power $\langle \mathcal{A}_l \rangle$ and laser DOCP \mathcal{P}_γ in order to accurately reflect the measured beam polarization. While $\langle \mathcal{A}_l \rangle$ can be derived from simulation, \mathcal{P}_γ must be measured directly in our physical setup.

The monochromatic plane wave can be written as

$$\mathbf{E}(z, t) = (E_{x0}e^{i\phi_x}\hat{x} + E_{y0}e^{i\phi_y}\hat{y})e^{i(\mathbf{k}\cdot\mathbf{x}-\omega t)}, \quad (4.29)$$

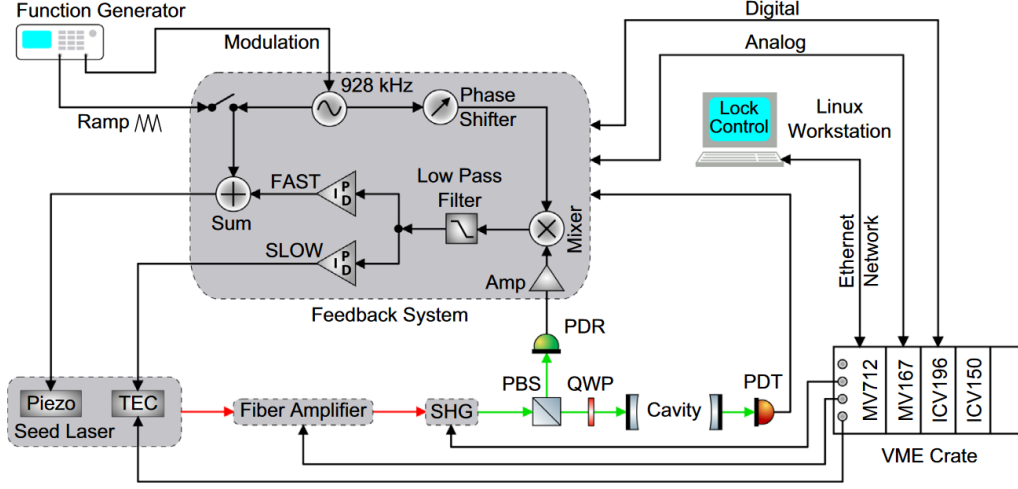


Figure 4.7: The electronics for locking the laser in the cavity onto resonance. The retro-reflected photodiode (RRPD) is read and their signals mixed to determine the phase offset of the laser necessary to maintain a lock. Reproduced from Rakhman et al. [83].

where E_{x0} and E_{y0} are the real-valued amplitudes of the electric field, \hat{x} and \hat{y} are unit vectors orthogonal to each other and to the direction of propagation, and ϕ_x and ϕ_y are the relative phases of the two orthogonal components [84]. We can then rewrite this in terms of complex amplitudes E_x and E_y [85]:

$$\mathbf{E} = \begin{pmatrix} E_x \\ E_y \end{pmatrix} = \begin{pmatrix} E_{x0}e^{i\phi_x} \\ E_{y0}e^{i\phi_y} \end{pmatrix}. \quad (4.30)$$

In this basis the Stokes parameters can be written as

$$s_0 = E_x E_x^* + E_y E_y^*, \quad (4.31)$$

$$s_1 = E_x E_x^* - E_y E_y^*, \quad (4.32)$$

$$s_2 = E_x E_y^* + E_y E_x^*, \quad (4.33)$$

$$s_3 = i(E_x E_y^* - E_y E_x^*). \quad (4.34)$$

The Stokes parameters also contain information about laser polarization. While the total polarization of the laser can be written as $\mathcal{P}_\gamma^{TOT} = \sqrt{(s_1^2 + s_2^2 + s_3^2)}/s_0$ only s_1 and s_2 pertain to the linear part of polarization and only s_3 pertains to the circular part. Thus we can measure the degree of linear polarization (DOLP) and DOCP separately as

$$\mathcal{P}_\gamma^L = \frac{\sqrt{s_1^2 + s_2^2}}{s_0}, \quad (4.35)$$

$$\mathcal{P}_\gamma^C = \mathcal{P}_\gamma = \frac{s_3}{s_0}. \quad (4.36)$$

The polarization is defined such that for 100% left-handed circular polarization $\mathcal{P}_\gamma = 1$ and for 100% right-handed circular polarization $\mathcal{P}_\gamma = -1.0$.

Entrance Function & Cavity Birefringence

In the Jones vector treatment of polarization we can treat any arbitrary optical element that modifies the direction of light polarization as a two-by-two matrix M . Optical reversibility states that light in an optical system will follow the same path if direction is reversed, which means that the parameters for the change in polarization through each element will have their signs reversed. For general transformation M the reverse transformation is its transpose [86]:

$$M_{rev} = M^T. \quad (4.37)$$

Reversibility is important for Compton laser DOCP measurements as the RRPD can be used to characterize the laser polarization. The RRPD receives the reflected laser light from the cavity mirror while the cavity is not locked. If the laser polarization at the cavity is completely circular then the reflected laser polarization will be orthogonal to the incident laser polarization at the PBS. In this case the PBS will extinct the reflected light and the RRPD will receive no signal.

This fact is exploited to build the laser “entrance function” which describes the laser polarization at each element along the entrance line, between the PBS and the cavity entrance mirror. The function is obtained by scanning many different combinations of QW1 and HW1 angles and measuring the response in the RRPD. These scans were done with the cavity open to air. The function is fit using a set of parameters characterizing the QW1 and HW1 to give entrance DOCP for each waveplate angle [87].

Next, we account for the birefringence of the cavity mirrors and the cavity entrance vacuum windows, which can be caused by the vacuum pressure differential. This is done by closing the laser cavity and locking the cavity at different QW1/HW1 angles. The range of QW1/HW1 angles is limited by the fact that the cavity polarization must be near-circular in order to cleanly lock the laser. The polarization of light transmitted through the second cavity mirror can be characterized to find the cavity mirror birefringence. The transformation applied to the entrance function to account for the cavity mirror birefringence is of the same form as a generic birefringent optical element

$$M_{cavity}(\eta, \delta, \theta) = R(\eta)P(\delta)R(\theta), \quad (4.38)$$

where $R(\theta)$ is a rotation of the polarization by angle θ , $R(\eta)$ is a rotation of coordinates by angle η , and $P(\delta)$ is a phase shift by angle δ , [83]. These are determined from fits of the Stokes parameters of the reflected laser. Between PREX-II and CREX the cavity mirrors were changed, so the measurement of cavity birefringence was done separately for each experiment.

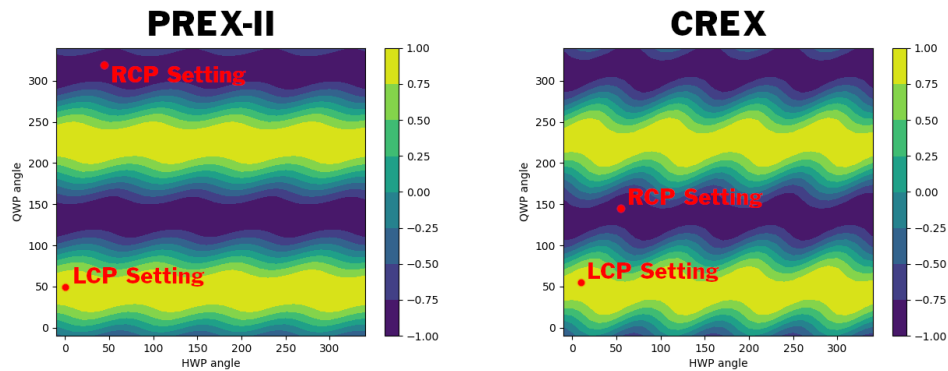
Finally, a second entrance function is fit when the cavity is under vacuum, as opposed to the first entrance function, which is measured with the cavity open. The parameterization of this entrance function is done the same way as with the cavity open.

With both the birefringence parameterization and the entrance function with the cavity under vacuum we can construct an optical model of the CIP DOCP for arbitrary QW1/HW1 angles. The results of this function are shown in Fig. 4.8. The maximum value of DOCP was then chosen before each experiment ran to maximize \mathcal{P}_γ during the experiments.

4.3.2 Photon Detector

The Compton photon detector sits approximately 6 meters downstream from the Compton interaction point. While the primary beam is bent by the third downstream dipole magnet in the chicane out of the path of the photon detector, the backscattered Compton photons themselves will continue on a straight path towards the detector. The detector sits just in front of the final Compton dipole magnet about 21.5 centimeters below the primary beamline.

Before arriving at the photon detector the primary photon beam must first pass through a lead collimator 6 cm long and 2 cm in inner diameter. The collimator serves to reduce background from non-Compton processes.



(a) CIP laser DOCP value as a function of QW1 and HW1 angle with data taken before PREX-II. Left Circular Polarization (LCP) and Right Circular Polarization (RCP) angles are labeled. (b) CIP laser DOCP value as a function of QW1 and HW1 angle with data taken after the cavity mirrors had been changed.

Figure 4.8: CIP laser DOCP value as a function of QW1 and HW1 angle for PREX-II (left) and CREX (right). The chosen values for left circular polarization (LCP) and right circular polarization (RCP) are labeled on each plot.

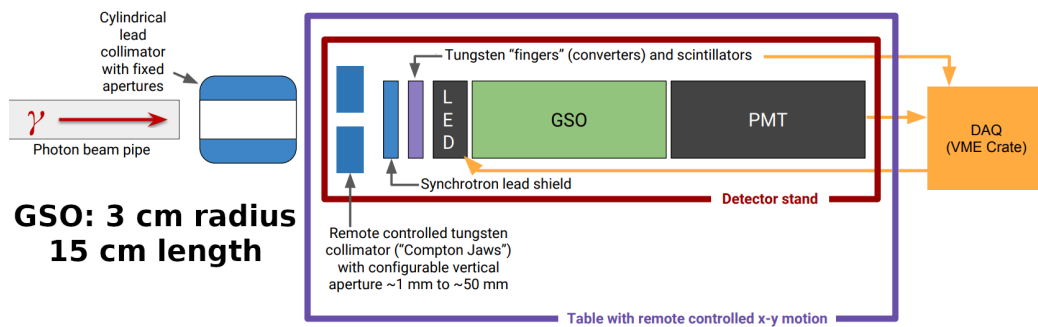


Figure 4.9: Compton photon detector layout as seen from beam-right. Component shapes and sizes not to scale.

The collimator's position relative to the Compton interaction point is fixed, unlike the detector itself. Mounted on the photon detector table behind the photon collimator is a secondary "jaws" collimator consisting of two pieces of tungsten metal that could be moved vertically to narrow the photon acceptance. The jaws collimator was not used during either PREX-II or

CREX beyond diagnostic measurements.

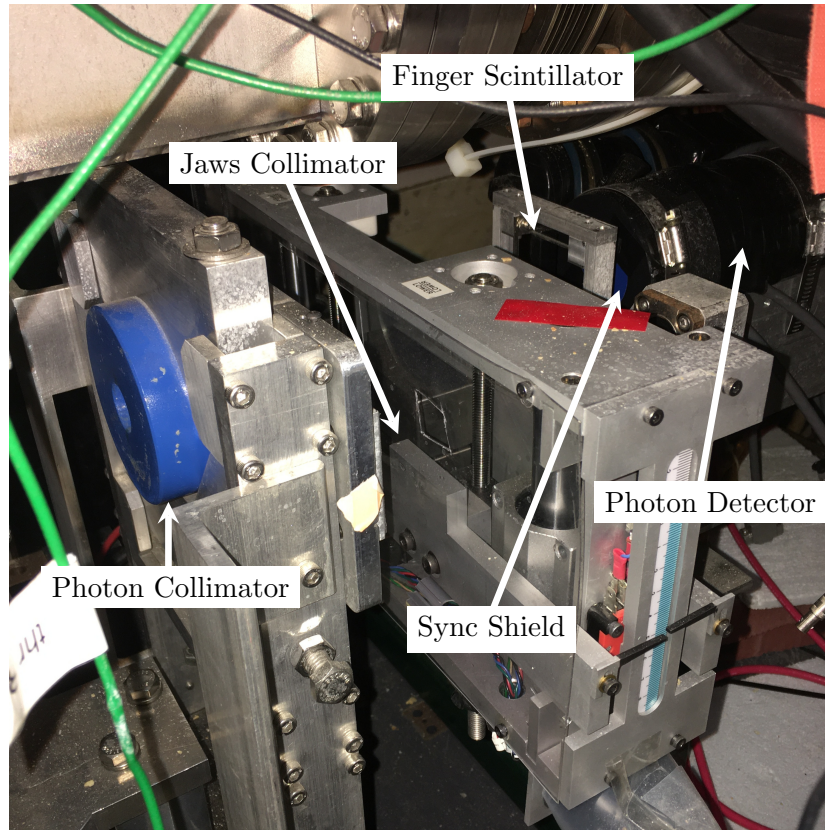


Figure 4.10: Photo of upstream photon detector components as they were arranged during CREX running.

To reduce the contribution of synchrotron light from the electron beam from adding to the background of the photon detector a small circular lead shield is affixed to the front of the photon detector housing. The shield is only 250 μm thick, which was sufficient at PREX-II and CREX energies to block synchrotron light at these beam energies.

Also upstream of the photon detector are two tungsten “fingers,” each of 2 mm diameter mounted perpendicularly to each other. The vertical finger is mounted 2 cm to the left of the central axis of the photon detector and the horizontal finger is mounted 2 cm above the central axis. Just behind the fingers are two small scintillators, each about 8 cm long, 1 cm wide, and

1 cm thick. These scintillators are each attached to photomultiplier tubes separate from the primary photon detector. The fingers, their scintillators, and the photon detector are all mounted onto the same table which had the ability to move horizontally or vertically by remote control. By moving the table such that each finger is placed in the center of the photon beam, the backscattered photons would themselves scatter in the tungsten fingers and produce a high rate in the scintillators behind the fingers. By finding the table position for each finger that yielded maximum rate, we could identify the center of the photon beam to align the central axis of the photon detector to it. The collimator, synchrotron shield, and fingers can be seen in Fig. 4.10.

The primary scintillator for the Compton photon detector is a cerium-doped gadolinium orthosilicate ($\text{Gd}_2\text{SiO}_5:\text{Ce}$, “GSO”) crystal approximately 15 cm long and 6 cm in diameter. GSO was chosen as the scintillator for the Compton polarimeter due to its high light yield at low energies, producing up to $\approx 10,000$ photons per Compton photon [88]. GSO photon pulses have a fast decay time of ≈ 56 ns making it possible to support high rate in the detector [89]. The Hall A Compton photon detector was also already tested at both JLab and the HI γ S facility and shown remarkable agreement with simulation contributing to low systematic uncertainty on the experimental analyzing power $\langle \mathcal{A}_l \rangle$ [90].

One of the primary challenges with using a GSO scintillator is the high thermal neutron capture rate of Gadolinium. In particular ^{157}Gd has the highest thermal neutron capture cross section of any stable element (254,000 barns at 0.025 eV neutron energy) [91]. This is a problem for experiments with heavy-element isotopic targets (like the ones used for both PREX-II and CREX) because of thermal neutrons created from the target. These neutrons get captured in the gadolinium of GSO producing high backgrounds for our detector. During analysis we frequently measure these backgrounds and subtract them, but this produced a number of limitations on measuring our systematic uncertainties which will be discussed more in sections 5.3.3 and 5.6.1. This effect was far more pronounced during PREX-II running than for CREX running.

An RCA BURLE 8575 12-stage end-window photomultiplier tube (PMT) was placed flush up against the downstream end of the GSO crystal and acted as the primary photon detector. PREX-II and CREX each had their own PMTs used for running though both were the same make and model. The PMT voltage was calibrated for both experiments such that a single Compton-edge photon pulse would have a height of 1,200 raw ADC units

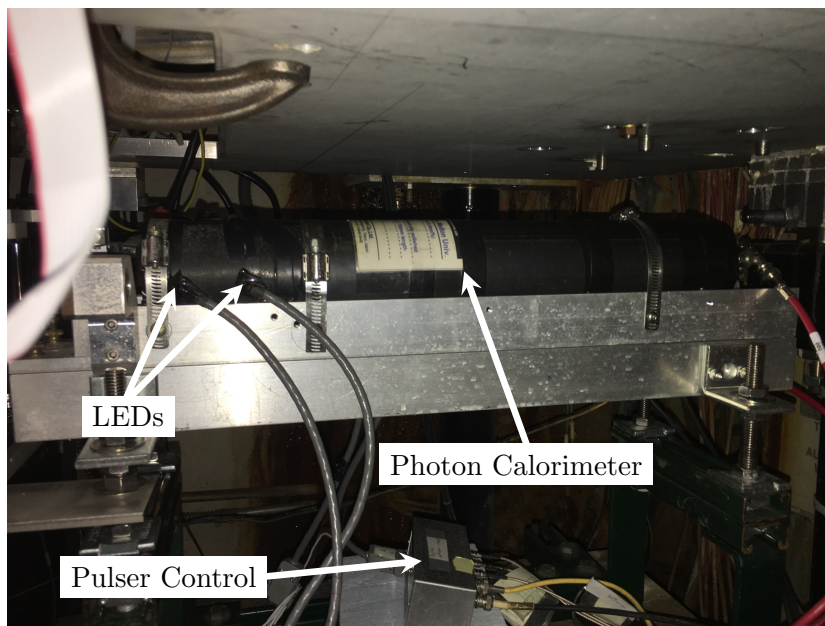


Figure 4.11: Photo of the photon detector as it looked during PREX-II running. LED and pulser components are labeled. The “photon calorimeter” houses both the GSO crystal and PMT/base combo.

(which will be discussed more in Sec. 4.4.1). Both PMTs also used customized base electronics to create a resistance chain between PMT dynodes. The photon detector assembly can be seen in Fig. 4.11.

For CREX running the PMT high voltage was produced by a LeCroy Series 1450 modular high voltage system with individual cards producing up to 3 kV per channel with a <1 V resolution. The PMT voltage could be changed via remote control, allowing us to dynamically change PMT voltage as required during experimental running. For PREX-II we found the LeCroy source could not provide the voltage we required as it would exceed the card’s trip current (2.5 mA). Instead the PREX-II PMT high voltage was supplied by an Ortec 556 3 kV power supply mounted on a rack in Hall A. The Ortec high voltage module had a readback resolution of 10 V. In order to control the high voltage remotely we enabled the Ortec module’s “external” control and connected to it the output from a Tenma 72-2690 30V DC digital power supply, which was placed outside Hall A and connected to the high voltage supply with a long patch panel cable routed into the hall. The

Tenma DC power supply had a resolution of 0.01 V. By changing the output voltage of the low voltage power supply we would proportionally change the output voltage of the high voltage module without needing access to the hall, allowing us to dynamically change PMT high voltage during experimental running (albeit with slightly lower resolution than what we could measure with CREX).

4.3.3 Electron Detector

In addition to the photon detector, the Compton polarimeter also has a detector for measuring Compton-scattered electrons. The detector is placed above the primary beamline on the chicane between the third and fourth chicane dipole magnets. The detector consists of four planes of 192 silicon microstrips each. Compton scattered electrons (which leave the laser cavity with lower energy than primary beam electrons) will be bent by the third chicane dipole out of the path of the primary beam into the electron detector which sits above the beam. The Compton edge for Compton-scattered electrons E'_{min} corresponds to the minimum electron energy and relates to the photon Compton edge k'_{max} as

$$E'_{min} = E - k'_{max}. \quad (4.39)$$

The kinematic expression for electron deflection above the primary beamline by a dipole magnet is

$$\Delta y = ecBx_{det} \left(\frac{1}{E'_{min}} - \frac{1}{E} \right), \quad (4.40)$$

where e is the electron charge, B is the field integral of the dipole magnet (0.129 T·m for PREX-II and 0.291 T·m for CREX), and x_{det} is the beamline distance between the dipole magnet center and the electron detector (4.453 m) [80]. These Compton edge electrons were diverted furthest from the beam of all the Compton-scattered electrons. The information from the detector is fed to the electron detector DAQ which calculates an asymmetry through electron counts per microstrip and in each plane.

The electron detector was not used at all during PREX-II because of the low separation between the Compton-scattered electrons and the primary beam. The electron detector was used for diagnostic measurements during CREX but was not used for the main polarimetry measurement.

4.4 Compton DAQ

The Hall A Compton polarimeter photon detector data acquisition system “DAQ” can simultaneously perform two different types of asymmetry measurements from the photon detector signal and beamline monitor signals: an integrating-mode measurement, and a counting-mode measurement. Although for PREX-II and CREX only the integrating-mode asymmetry was used for polarimetry data, the electronics and modules necessary for the counting-mode measurements were critical for quantifying our sources of systematic uncertainty, and for applying cuts in the data analysis, so both DAQ components will be discussed.

The physical photon DAQ is placed inside Hall A and could only be accessed during pauses in experimental running. The DAQ sits on the floor of the hall, ≈ 15 m on beam-right and ≈ 20 m upstream of the target. The DAQ is divided up into several crates onto which modular electronics could be added or removed. The Compton DAQ fits primarily into three crates: two of them with the Nuclear Instrumentation Module (NIM) format and the others with the VMEbus (Versa Module Europa) format, the latter of which contains our Compton Read-Out Controller (ROC). The modules used for making asymmetry measurements, auxiliary detector counters, and DAQ timing equipment are primarily mounted on the VME ROC while the NIM crates mostly contain electronics for digital logic, signal format conversation, and pulse discriminators. The DAQ programs are run through a computer running the CEBAF Online Data Acquisition system (CODA) on a machine running Linux CentOS 7 in the MATE environment.

The Hall A Compton polarimeter DAQ is separate from both the primary Hall A DAQ systems and the parity DAQ which was used to measure main experimental asymmetry. The photon DAQ is also separate to, and functionally independent from, the Compton electron detector DAQ, which is mounted in the same racks as the photon detector DAQ. This meant the Compton photon detector had its own instance of CODA which could be started and stopped independently of any other DAQ system. Similarly, the Compton photon detector has its own analysis software to turn the raw output data files constructed by CODA and the VME ROC into the ROOT tree format for analysis. This analyzer system will be discussed further in Sec. 4.5.

4.4.1 Integrating Mode Components

A series of DAQ electronics implemented the asymmetry measurement technique referenced in Sec. 4.2.1. Of particular note are the electronics modules which performed the integration and the DAQ integration timing system.

Helicity Trigger

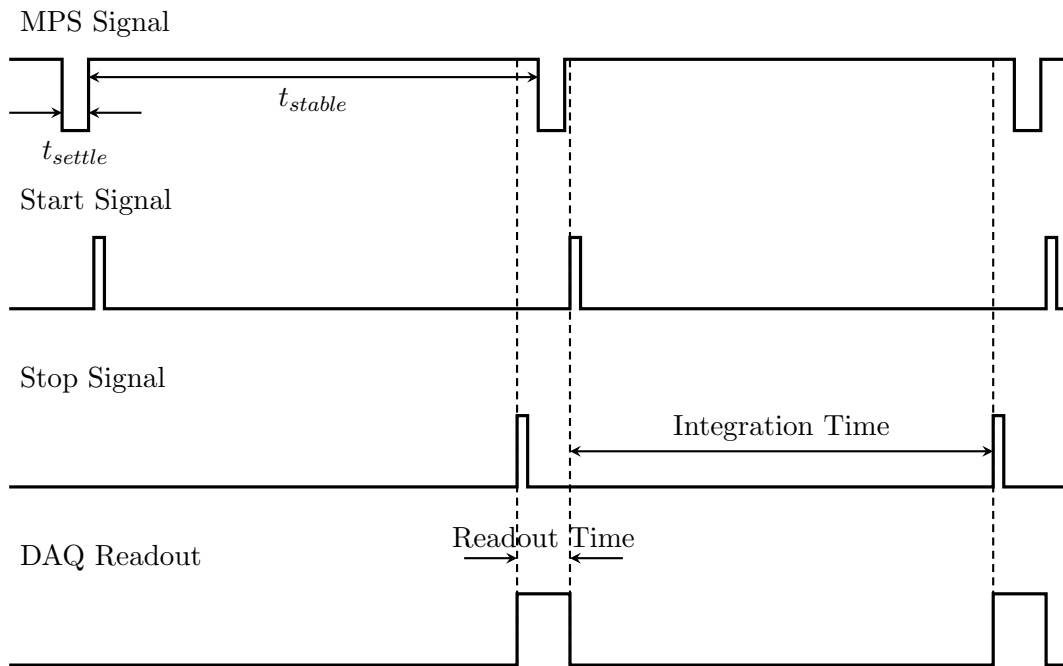


Figure 4.12: Compton integrating mode timing diagram showing the sequence of two MPS's. The helicity for each MPS is chosen from a pattern which is chosen pseudorandomly. Times and pulse sizes shown not to scale.

The Compton DAQ module which performs the integration is a modified Struck SIS3320 8-channel 12-bit 5 volt flash ADC (fADC) with a sampling rate of 200 MHz¹. To correctly time the module's integration and readout times such that they correspond to individual helicity periods and are equal

¹The physical layout of the fADC channels will be discussed in Sec. 4.4.1.

times in each period, a trigger system is implemented to send timing signals to the electronics.

The Compton DAQ helicity trigger used the same principle described in Sec. 3.9.1. A delayed helicity signal sent to the Compton DAQ would trigger a HAPT B to send out signals to the fADC to start and stop integration. The helicity signal timing matched both the integrating DAQ and the Compton DAQ however the HAPT B's in each DAQ were programmed independently to account for detector-specific effects. The specific timing used for the Compton DAQ, including the electronic readout time can be seen in Fig. 4.12.

Integrated Photon Signal

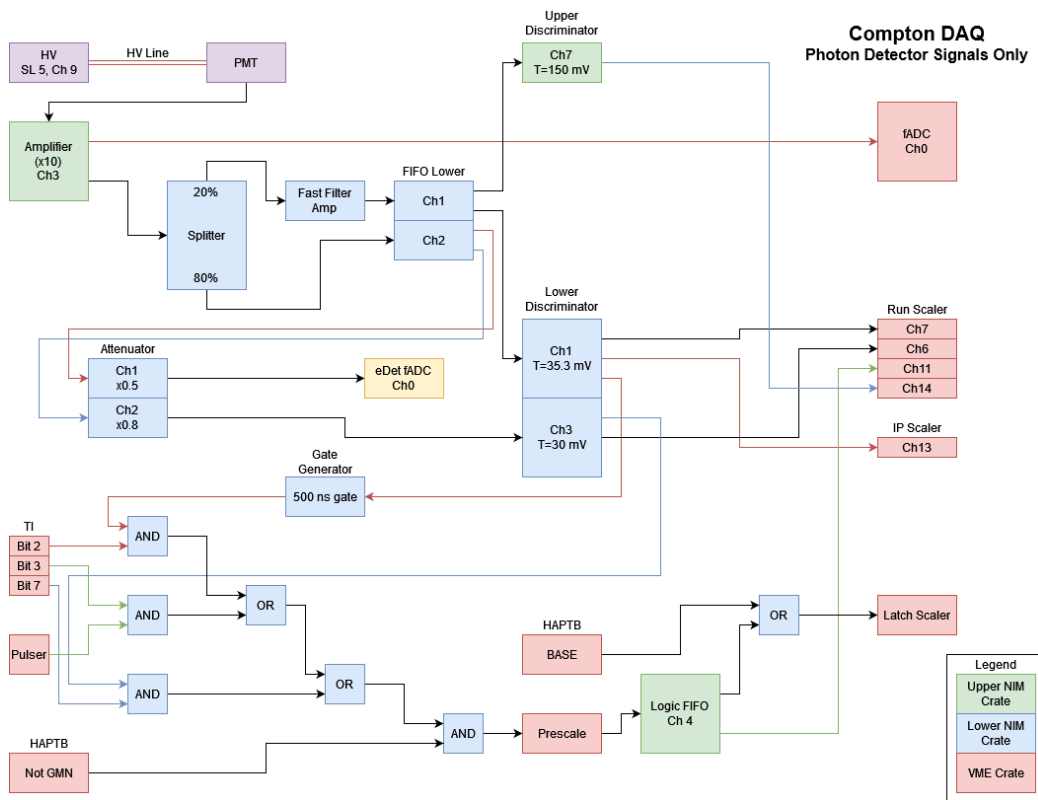


Figure 4.13: A DAQ map of the photon detector signal. Colors of arrows are only for ease of readability.

The fADC referenced in the previous section in normal Compton running has one active channel, which contains the signal from the PMT. Before it reaches the fADC the PMT signal is passed through a LeCroy 612A 12-channel PMT amplifier which amplifies the PMT signal by a factor of 10. During integrating mode the fADC counts every sample it takes from the amplified PMT signal at a frequency of 200 MHz. During the readout period the fADC sums up the samples taken during the previous integration period and the sum is pushed to the data stream as “Acc0.” During analysis the MPS sums are mapped onto their correct helicity state, which makes it possible to use these sums to calculate an asymmetry. The connections supporting the Compton photon detector signal can be seen in Fig. 4.13.

The fADC reads from 0 to 4096 in each sample, and saturates at 5 V and above². fADC sample measurements are reported in the number of channels each sample exceeded pedestal, in “raw ADC units (RAU).” The Compton edge from the PMT in both experiments is calibrated to, at the normal gain used for experimental running, correspond to a peak height of 1.25 V out of the PMT amplifier, which means that Compton edge pulses would have a height of 1024 RAU reported. This limit is sufficiently below the saturation threshold that even with nonzero pileup, Compton scatters are unlikely to saturate the fADC.

Once the integrating period for each MPS ends, the fADC sums up each sample in the period reporting the result in “summed raw ADC units (sRAU).” During analysis the effect of electronic pedestal must be taken into account at a 120 Hz helicity flip rate, the fADC takes ≈ 1.6 million samples per MPS meaning a small mismeasurement in pedestal can become large when multiplied per each sample. Fortunately, as will be explained in Sec. 5.3.1, because of signal background-subtraction the final asymmetry measurement is immune to any sufficiently slow changes in pedestal.

4.4.2 Counting Mode Components

The key to building a DAQ to make the counting measurements described in Sec. 4.2.1 is to build a mixed-trigger system where counting per helicity period is triggered by the MPS signal but individual pulse integrating is triggered by the pulse itself. While for PREX-II and CREX the counting mode

²In actuality the PMT outputted negative voltage so really the fADC reads from 0 V to -5 V and saturated for voltages less than -5.

asymmetries were not used to calculate \mathcal{P}_e the counting mode components were nonetheless indispensable for characterizing systematic uncertainties.

Pulse Trigger & Prescale

In addition to the amplified PMT signal going to the fADC, another copy of the PMT signal is sent to a splitter, a crate-mounted voltage divider that divided the input signal up in an 80%:20% ratio. From the splitter the 20% output is fed into an Ortec 579 fast filter amplifier (FFA) with $\times 0.9$ gain. The amplifier acts primarily as a signal shaper, which creates a more smooth shape while preserving the integral \times gain. The shaper helps prevent sudden transient spikes in PMT voltage output from causing double-triggers.

The output of the FFA is then connected to the input of a LeCroy 623B 8-channel octal discriminator. The discriminator has a programmable threshold for each independent channel, which if an input exceeds, will output a short NIM pulse to register a pulse. The discriminator threshold is programmable only by physically adjusting the measured threshold on the front panel of the module. Because this module was in the photon DAQ lower NIM crate, the threshold can only be changed with access to the hall which is only possible during long pauses in experimental running. In addition, the discriminator threshold cannot be adjusted lower than 30 mV for any channel. This voltage is a small fraction of the Compton edge: $(0.03 \text{ V}) / (0.9 \times 0.2 \times 1.25 \text{ V}) \approx 15.7\%$ which left plenty of dynamic range of energy for the PMT signal. Additionally there is an alternative pulse trigger that can be used instead of the regular pulse trigger. The alternate trigger has the same threshold as the regular trigger, but used the 80% PMT signal, meaning the relative height of Compton edge pulses to threshold is 4 times higher.

The discriminator output is then added to the input chain of a series of transistor logic gates in multiple identical Phillips Scientific model 758 8-channel octal logic units, which perform either AND or OR operations on NIM signals. The PMT signal is fed through AND gates with the output of the HAPTBS such that the HAPTBS bit b_{GMN} would be 1 during the integrating period and 0 any time else. In effect this logic circuit only returns 1 if the discriminator fired a pulse from the photon detector and the fADC is in integrating mode.

In principle the photon DAQ is able to read out the integrated sums of each pulse recorded during t_{stable} . In practice the DAQ is limited by readout time. Each recorded pulse requires 2 μs of fADC readout time. This is in

addition to the 87.2 μs needed to perform the integration of fADC samples, and the ≈ 20 μs needed for the HAPT B to produce a “start” signal response. In addition, 25 μs is added to readout time to account for electrical line noise if the experiment decided to run with the helicity window synchronized with the electrical line AC signal. Too many pulses cause the readout time to start before the end of the integration period. During Compton running a designated maximum number of pulses per helicity window to read is specified via configuration file, after which the fADC would not record any more pulse sums. The maximum was determined before experimental running to be $n_{max} = 10$ pulses per helicity window. This added an addition 20 μs to the photon DAQ readout time bringing the total readout time to ≈ 150 μs .

For normal photon detector rates on the order of 100 kHz, the number of pulses received in a single integrating window far exceeds the limit n_{max} , meaning that for every integration window the allotment of accepted pulses would be exhausted long before the integration period would be over. This creates a potential problem in that recorded pulses from each MPS would be localized in time around the beginning of each integration period, introducing potential time-dependent effects to the pulse sums. To preserve time non-locality, the Compton DAQ uses a VME prescale module, which counts a number of pulses and fires a signal once every n_{pre} counts. In practice, n_{pre} could be adjusted from run to run based on the average photon detector rate. The ideal value of n_{pre} is then

$$n_{pre} = \left\lceil \frac{1}{n_{max}} \frac{f_{PMT}}{f_{hel}} \right\rceil, \quad (4.41)$$

where f_{PMT} is the rate of photon detector pulses and f_{hel} is the helicity flip rate. With the prescale, it is possible to space out accepted photon pulses throughout the MPS integration period.

The output of the trigger logic circuit is fed to the prescale module which fires one pulse every n_{pre} triggers. The output of prescale is then fed to a Struck SIS3801 latching scaler. The latching scaler also receives input from an external 40 MHz pulse clock module, which is mounted in the VME crate. The latching scaler would count clock pulses and upon receiving a photon detector signal from the prescale, record the clock pulse number coincident with the signal. Because the 40 MHz clock also had output to the fADC, the fADC read the latching scaler’s saved clock pulses to map a triggered pulse to an fADC sample to identify samples to sum up. A DAQ map of modules which receive clock pulses can be seen in Fig. 4.14.

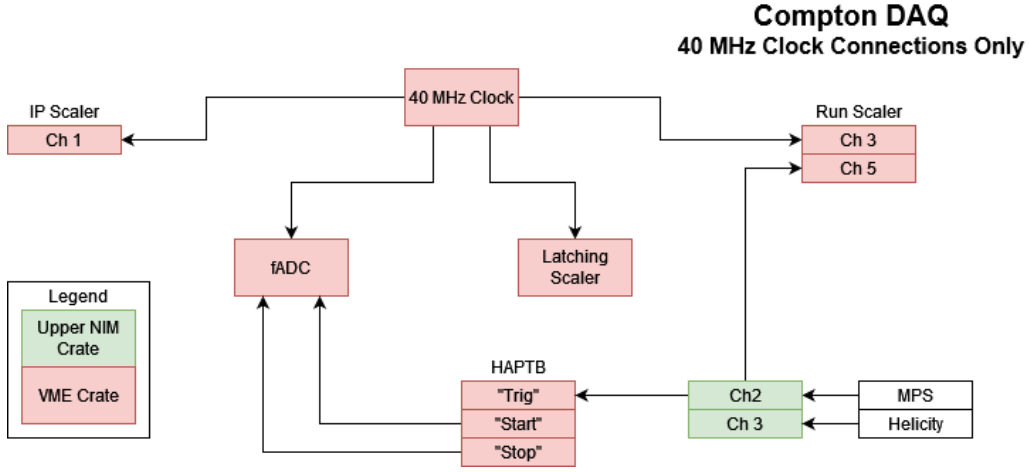


Figure 4.14: A DAQ map of the modules that receive an external 40 MHz clock pulse from our VME crate.

For each accepted pulse a sum over pedestal was calculated during analysis. Each pulse sum is 300 samples long, which at 200 MHz is equivalent to a 1.5 μ s window. For each pulse a number of samples n_1 are selected from the beginning and a number of samples n_2 are selected from the end of each window to determine the pedestal. The triggering pulse is timed so the trigger-crossing would be several samples after the end of the first pedestal window. The measured pedestal is determined by the average of the average sample value for each pedestal period

$$p = \frac{1}{2} \left[\frac{1}{n_1} \left(\sum_{i=0}^{n_1} s_i \right) + \frac{1}{n_2} \left(\sum_{i=N_s-n_2}^{N_s} s_i \right) \right], \quad (4.42)$$

where p is the measured pedestal, $N_s = 300$ is the number of samples per sum window, and s_i is the RAU value of the fADC readout for sample i . The remaining samples outside the sum window are used to compute the pulse sum which is

$$s = \sum_{i=n_1}^{N_s-n_2} p - s_i. \quad (4.43)$$

For most of PREX-II and CREX running the pedestal sample values were set to $n_1 = 40$ and $n_2 = 40$. However halfway through the CREX run the values were changed to $n_1 = 90$ and $n_2 = 150$ because of concerns that the

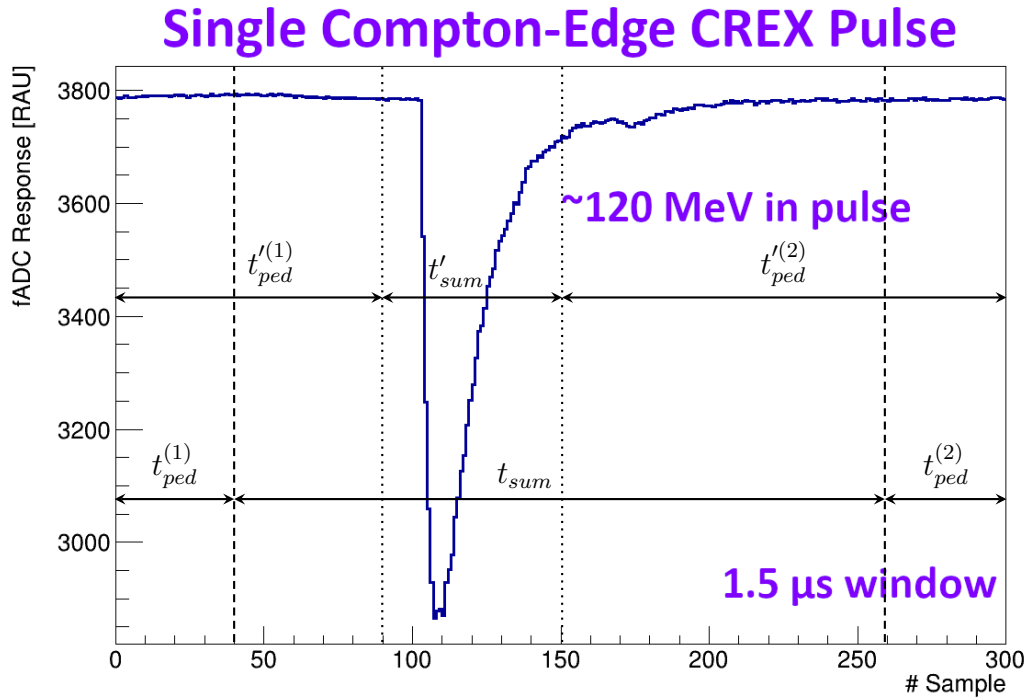


Figure 4.15: Example of a single photon pulse with Compton-edge energy from CREX showing the sampling ranges for each sum in the window. $t_{ped}^{(1)}$ is the first pedestal window, t_{sum} is the sum window and $t_{ped}^{(2)}$ is the second pedestal window. The bounds for the same periods after the change during CREX running are also labelled above. For this $t_{ped}^{(1)}$ is the first pedestal window, t_{sum} is the sum window and $t_{ped}^{(2)}$ is the second pedestal window.

extended sum window was allowing for a large number of pileup pulses in the sum region. The change to shrink the sum window lowered the probability of pileup pulses being included in the primary sum in exchange for increased probability of pileup pulses landing in either pedestal window. Pedestal window values were recorded in the photon detector analysis allowing for post-analysis cuts on pedestal value to be applied.

Auxiliary Detectors

In addition to the PMT for the photon detector, several other detectors are used for both beamline monitoring and detector positioning. There are four beamline scintillating detectors placed on the laser table: two upstream of the cavity and two downstream. The rate in the laser table “background” detectors is the primary indicator of the health of the electron beam in the chicane. Additionally, the detectors measured any potential damage to laser electronics which are in the hall during experimental running. Though the rates in these background detectors could not always be controlled, keeping the rates suitably minimized is a beam quality requirement of the experimental programs. As an indicator of beam quality, the measured rates in the background detectors are also a useful metric to make data cuts on, as discussed in Sec. 5.2.3.

The two upstream background detectors are placed approximately 80 cm upstream from the Compton interaction point, placed just to the left and right of the beam pipe. The two downstream detectors are placed approximately 80 cm downstream from the Compton interaction point, placed just above and below of the beam pipe. The energy thresholds and response of these detectors are not calibrated, so the rate comparison between different detectors is not used.

As already described in Sec. 4.3.2 the two perpendicular finger scintillators are also read by the photon DAQ. The primary function of these detectors was to find the maximum rate as a function of photon detector table position so as to locate the center of the photon beam. While the vertical finger signal is an appropriate size, the horizontal finger signal is not large enough to trigger the discriminator except in special cases. To fix this, the horizontal finger signal is routed through the $\times 10$ gain PMT amplifier before being sent to the discriminator. The horizontal signal is placed in a channel on the opposite side of the amplifier from the main PMT signal to minimize cross-talk between the two detectors.

Discriminators and Scalers

In total, nine discriminator channels are used over two different discriminator modules of identical model. Four channels are reserved for each of the laser table detectors, two channels are reserved for each finger scintillator. The last three channels are reserved for the photon detector signals of different

size and at different thresholds. Table 4.2 contains the threshold information for each discriminator channel.

| Discriminator | Channel | Input | Threshold [mV] |
|----------------------|----------------|----------------|---------------------------|
| Lower | 1 | PMT FFA | 35.3 |
| Lower | 2 | Horiz. Finger | 30 |
| Lower | 3 | PMT 80% | 30 |
| Lower | 4 | Top DS Scint | 100 |
| Lower | 5 | Left US Scint | 71.1 |
| Lower | 6 | Vert. Finger | 30 |
| Lower | 7 | Lower DS Scint | 113 |
| Upper | 5 | Right US Scint | 75.3 |
| Upper | 7 | PMT FFA | 150.4 |

Table 4.2: Discriminator channels, inputs and threshold values for each occupied discriminator channel during PREX-II/CREX running.

The discriminator outputs go to (in addition to the outputs specifically enumerated in previous sections) scaler modules used for counting pulse inputs. The modules used are two Caen V560E 32-bit 16-channel VME scalers with a maximum input frequency of 100 MHz. The first of the two scalers dubbed the “integrating period (IP)” scaler has its channel counts reset once at the start of every integrating period. The second scaler dubbed the “run” scaler has its counts reset at the start of every new CODA run. The DAQ map of all run scaler inputs is shown in Fig. 4.16 and the map of all IP scaler inputs is shown in Fig. 4.17.

Of particular interest are the Hall A beamline component signals fed to the photon DAQ. To dynamically track the beam position in the laser cavity, the information for two BPMs is fed to the photon DAQ: one ≈ 1 m upstream of the Compton interaction point and one ≈ 1 m downstream of the Compton interaction point. The two BPMs are stripline BPMs, whose functionality was described in Sec. 3.2.2. Eight channels are required to track both BPMs (four wires per BPM times two BPMs). These channels are then fed through a V-F module converting them into pulse signals with frequency proportional to input voltage. These are then fed to the IP scaler which recorded the counts to be calibrated later. The same module path is used for the laser power photodiode signal and the primary Hall A BCM

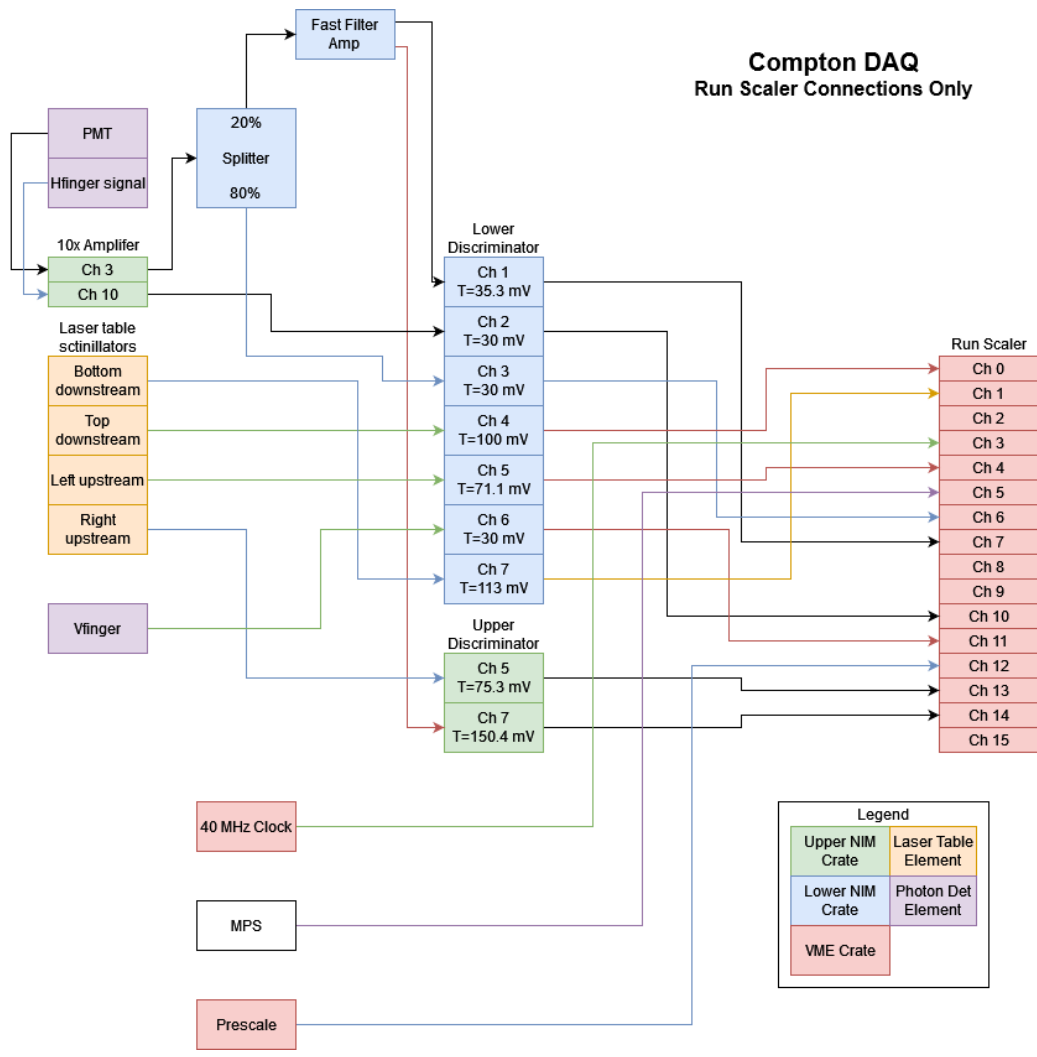


Figure 4.16: All components connected to the Compton run scaler module. The module is reset at the start of each new run.

(whose functionality is discussed in Sec. 3.2.1. The process for calibrating the signals from these monitors to their original values is described in Sec. 5.1.

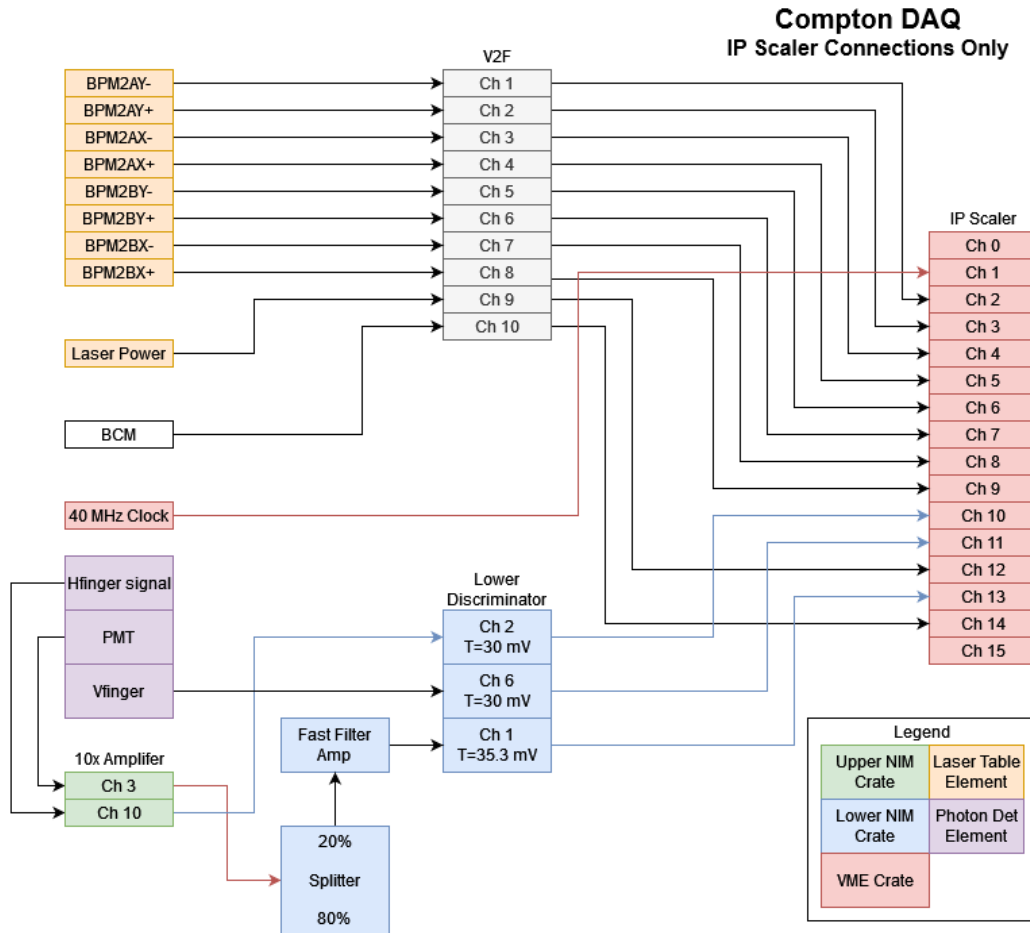


Figure 4.17: All components connected to the Compton integrating period (IP) scaler module. This module is reset at the start of each new MPS.

4.4.3 Pulser DAQ Control

As part of the Compton upgrade in the early 2010s that allowed for high precision polarimetry during HAPPEX-III and PREX-I, a new electronics system was designed in order to automate detector characterization bench tests. This “LED pulser” system was built to automatically control two LED’s positioned at the front of the photon detector that could characterize the photon detector nonlinearity *in situ*.

The photon detector has a nonlinearity where the detector yield as a

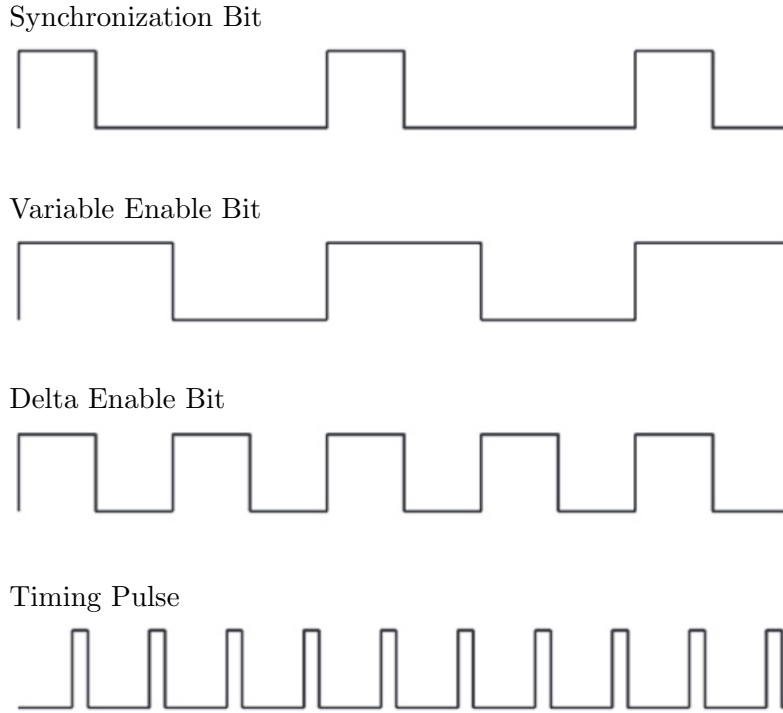


Figure 4.18: Pulser electronics timing diagram showing the pulser enable bits and timing bits for each LED. Adapted from [92].

function of photon light intensity $Y(I)$, has small nonlinear terms modifying the measured yield by

$$Y(I) = I + c_1 I^2 + c_2 I^3 + c_3 I^4 + \dots + c_n I^{n+1}, \quad (4.44)$$

where $c_1 \dots c_n$ are dimensionless coefficients for a polynomial of arbitrary degree n . In a perfectly linear system then $c_1 = c_2 = c_3 = \dots = c_n = 0$ but in a nonlinear system, measuring these coefficients will characterize the nonlinearity.

To measure the coefficients we employ two LEDs, dubbed “variable” and “delta,” flashed for short intervals in sequence at 1 kHz. The sequence of flashing is shown in Fig. 4.18 and shows the sequence as

1. Delta + Variable flash simultaneously

2. Variable flashes alone
3. Delta flashes alone
4. Both LED's off

repeated. For each iteration of the sequence the variable LED is programmed to decrease in brightness while the the delta LED stays at a constant brightness throughout. We then compute the difference between the variable + delta flash and the variable alone flash $Y(V + \Delta) - Y(V)$ and plot it vs the variable alone yield $Y(V)$. For a perfectly linear system the plot will have a slope of zero, but for a nonlinear system this “finite difference” of PMT yield will change as function of $Y(V)$.

To characterize the nonlinearity we then fit this function with an polynomial of arbitrary degree and find that the fit parameters are the coefficients $c_1, c_2 \dots c_m$ where m is the polynomial degree of the fit function. For PREX-II and CREX nonlinearity studies polynomial fits of degree $m = 3$ were sufficient for obtaining nonlinearity measurements with a high degree of accuracy. Once the coefficients are obtained then we can modify the PMT response function to express the nonlinear components only by

$$\frac{Y(I)}{I} - 1 = c_1 I + c_2 I^2 + c_3 I^3 + \dots + c_m I^m. \quad (4.45)$$

The integral of this function from $I = 0$ until when I produces a PMT yield matching the Compton edge brightness will give us the yield correction for nonlinearity.

Pulser Electronics

The pulser control system originates in the Compton DAQ with a Caen VME 2-channel programmable gate generator. By feeding the end of the first gate generator channel into the start of the second channel and vice-versa, the gate generator ends up generating a pulse signal at the programmed frequency for each gate generator. The board is programmed to emit a 1 kHz pulse, which became the input to the pulser electronics system. The first component of this system creates (from the 1 kHz signal input) the timing and pulse signals for each linearity LED. This system is dubbed the “mini-Megan” (so named in honor of a previous Hall A Compton student Megan Friend.) The mini-Megan generates the enable pulses for both LEDs.

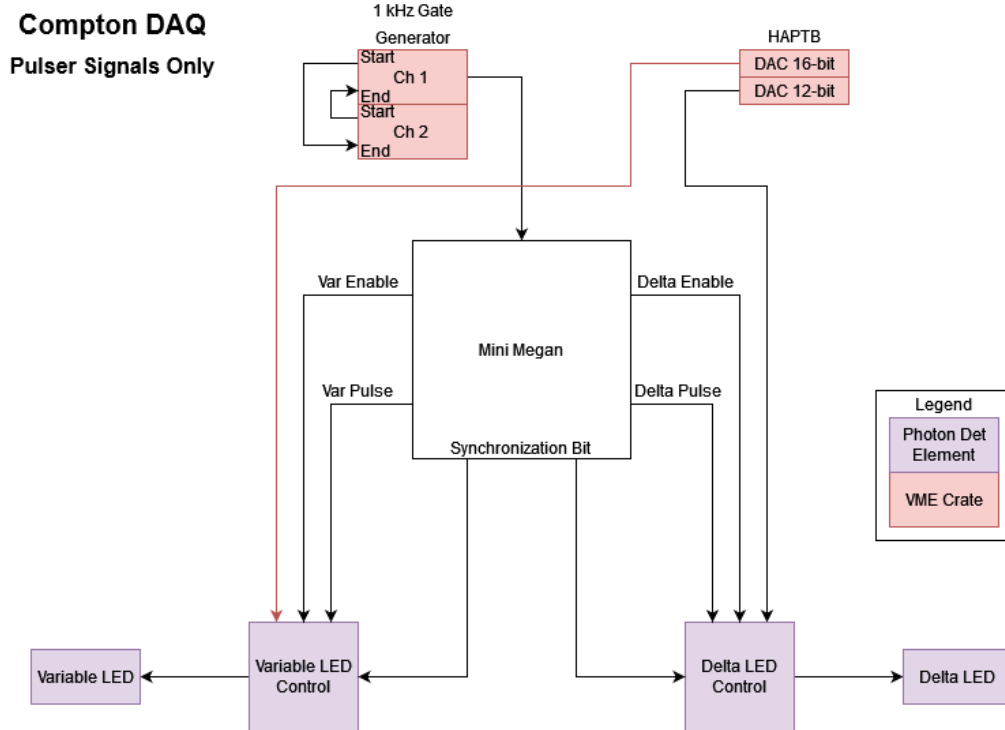


Figure 4.19: Compton DAQ map of pulser signals. The “Mini-Megan” control box sat atop the lower NIM crate on the photon DAQ.

The delta LED is enabled at a 500 Hz frequency while the variable LED is enabled at 250 Hz frequency. The result is that one full pulser cycle over all four states has a frequency of 250 Hz. The signal to pulse the LEDs is generated at 1 kHz, and each pulse was only a few μs long. Additionally, the mini-Megan generates a “synchronization bit” to synchronize the LED flashes from different controllers.

To control the brightness of the LEDs the pulser system uses the DAC outputs of the HAPT B. The delta LED uses the 12-bit DAC output and was not changed during linearity measurements. The variable LED uses the 16-bit DAC output and can be changed programmatically through the CODA DAQ control during linearity measurement.

The enable bits, LED pulse timing, DAC outputs and synchronization bits are sent to the pulser drivers which sit on the photon detector table. There are two drivers, one for each LED, and the corresponding signals are

sent to each. The drivers used the timing signals and DAC brightness setting to produce the actual LED flash inside the photon detector housing. Each LED driver is electrically insulated from the photon detector table. A map of LED pulser DAQ signals can be seen in Fig. 4.19.

The pulser is enabled and disabled against the two PMT trigger options (the normal PMT trigger, and the alternate low-threshold trigger.) For each CODA run one of these three options could be selected by setting one of three bits: b_1 for the regular trigger, b_2 for the alternate trigger and b_3 for the pulser. All three triggers are then be used in a single logic system for triggers with the prescale value similarly changes for linearity runs compared to Compton data runs.

Pulser Systematics

There are two key systematic effects that must be taken into account in order to produce correct nonlinearity measurements. The first of these is the electrical cross-talk between flashing LED's producing a different LED signal than intended. The placement of the LEDs and the LED drivers allows for the current from one circuit to induce currents in the other. To measure the contribution of this effect to nonlinearity running we use a third LED dubbed "dark delta." The dark delta uses the same electronics as the regular delta LED and is placed close to the delta LED wire however, the dark delta LED is placed outside the photon detector housing. Running with the dark delta LED instead of the regular delta LED allows us to mimic the electrical effects of the delta LED without contributing any delta light to the photon detector. In this case, the finite difference function $Y(V + \Delta_{DARK}) - Y(V)$ shows the effect of the delta cross-talk on the variable and the fit function parameters of this function can be subtracted out to account for cross-talk effects.

The second of these systematic effects is the thermal effects on the PMT resulting from the sequence of the pulser. The variable LED is varied by the pulser system starting at a brightness roughly corresponding to $2 \times$ Compton edge decreasing incrementally to zero with every pulser cycle, after which the pulser sets the variable LED to its initial brightness and continues the cycle. Bench tests with the pulser system revealed that when the variable LED changes from its dimmest setting to its brightest setting the PMT gain changes noticeably for the first few pulser settings of the subsequent cycle. We surmised this was due to the PMT cooling off when receiving dim LED

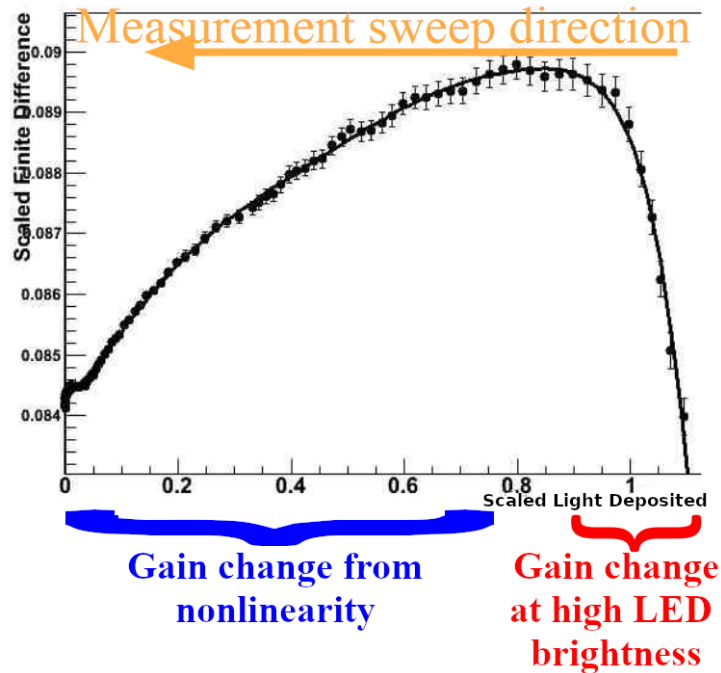


Figure 4.20: Photon detector nonlinearity plot showing the finite difference function $Y(V + \Delta) - Y(V)$. PMT yield is scaled such that a yield of 1 equals the Compton edge. At around the Compton edge a large change in PMT gain can be seen as the tube warms up. the effect disappears when measurements are taken under load.

pulses, only to heat up again and needing to re-thermalize when receiving brighter LED pulses. To fix this we add a fourth LED, “load” which was supplied with a small DC voltage to run at a constant low brightness. This LED could be tuned such that the PMT response from it matches the experimental signal size for both PREX-II and CREX. This LED keeps the PMT under a low brightness load at all times, thus negating the thermal changes from the variable cycle starting over.

4.5 Compton Analyzer

The CODA run control software at the end of every CODA run outputs a single software data file containing the records contents of the ROC including

the fADC Acc0 and pulse sums and the outputs of all scalers. Additionally, while CODA runs are active the run controller runs an EPICS logger script that pulls data from EPICS every time the EPICS data was updated. The resulting file as generated by CODA is not human-readable, requiring a software suite to translate the raw output into a ROOT tree format, which is more convenient for analysis.

For the Hall A photon DAQ this software suite is called “CompMon” (short for “Compton Monitor”) and has been used and developed extensively before PREX-II and CREX ran. The output data file was formatted as a series of CODA “events” which contain ROC readout information for each MPS. The critical calculations handled by CompMon are the calculation of pedestal and pulse sums, the pedestal-subtraction of accumulators, and the summing of accumulators based on helicity state in the helicity pattern.

The format of the output of CompMon has several recorded data tables encoded in files for the ROOT data analysis suite [93]. These files internally follow a ROOT tree structure. The tables from which Compton data taken are:

- **mpswise:** Records accumulator and scaler data per MPS.
- **multipletwise:** Records accumulators summed separately for positive and negative helicity states in each helicity pattern. Compton asymmetries were calculated from data in this tree. Multiplets were either quartets or octets depending on what was running at the time that data was collected.
- **triggerwise:** Records the sums and pedestals for each accepted Compton pulse, maps them to their constituent MPS and multiplet.
- **epicswise:** Records the data grabbed from EPICS with each new EPICS event (≈ 1 per second).

CompMon is run after the completion of each CODA run, producing Compton polarimetry data during experimental running. CompMon is also paired with an external analysis suite which will be discussed in Ch. 5.

Chapter 5

Compton Polarimetry Data

Compton polarimetry data are analyzed both during and after experimental running. For PREX-II the Compton polarimeter only ran during the final half of the experiment, owing to hardware failures with the laser system that kept the device offline during June and July of 2019. For CREX, the Compton polarimeter ran consistently for nearly the entire experiment, only missing early data taken in December 2019 and January 2020, and a few days of experimental running in late September 2020. The main goal of polarimetry running during these experiments is to achieve an overall uncertainty $\delta\mathcal{P}_e/\mathcal{P}_e$ of $<1\%$. To accomplish this the analysis software suite has to be improved with new additions with experimental precision and up-to-the-minute diagnostics in mind.

In addition, the Compton analysis also relies on the analyzing power calculations carried out by a GEANT4-based Monte Carlo simulation of the Compton photon detector. A description of the simulation is in Sec. 5.4.1. The focus of this chapter is the important calculations carried out by the new analysis suite and Monte Carlo, as well as the overall polarimetry results for both experiments.

5.1 Beam Monitor Calibrations

Like the main experiment DAQ the Compton DAQ has to keep track of BPM and BCM data during experimental running. Unlike the parity DAQ, the Compton tracks these signals through a series of V2F converters which converts the raw wire signal into pulses with frequency proportional to the

voltage of the original signal. The pulses are then fed to the IP scaler (described in Sec. 4.4.2) which counts pulses per MPS (defined in Sec. 3.9.1). The raw value that the ROC (described in section 4.4) reports then from the IP scaler is in counts, not in voltage. This means that to get the actual BPM positions, beam current, and laser power (so that they could be used in calculations) the numbers are calibrated to meaningful units.

There are four components fed through the V2F converters before they are read by the IP scaler. The first two are the two Compton BPMs, 2A and 2B. 2A is located on the laser table, just 58 cm upstream of the CIP, while 2B is 58 cm downstream of the CIP. The BPM readouts are critical for tracking the beam position and angle in the cavity, and keeping the electron beam locked on the laser at the CIP. The third component fed into the V2Fs is the Hall A BCM 4A, which tracks the electron beam current in the hall. The final component in the V2Fs is the Compton laser transmitted photodiode (described in section 4.3.1), which is indicative of the laser power in the cavity.

Each channel is calibrated against the same component data as reported in EPICS. Measurements of the uncalibrated BCM signal at multiple beam current setpoints are needed to calibrate the beam current properly. This is to measure the BCM pedestal value β_{BCM} as well as the gain constant α_{BCM} . This is possible because of periodic calibration runs taken during both experiments where the beam current was deliberately incrementally lowered several times. The calibrated BCM value can then be calculated with

$$I_{beam} = \alpha_{BCM} f_{clock} \frac{n_{BCM}}{n_{clock}} - \beta_{BCM}, \quad (5.1)$$

where $f_{clock} = 40$ MHz is the clock frequency, n_{BCM} is the number of BCM V2F pulses counted over the MPS, and n_{clock} is the number of clock pulses counted in the MPS. The EPICS BCM calibration comes from a standard accelerator calibration procedure, based on invasive monitors capable of directly collecting beam charge (“Faraday cups.”)

The process for calibrating the laser cavity power vs. EPICS ($\alpha_{cav}, \beta_{cav}$) is the same. In this case the EPICS calibration of the RPD is based on the laser table power meter measurements.

Calibrating the BPMs is a slightly more involved process. The important beam position parameters as far as the Compton photon analysis are concerned were the beam x-position and beam y-position. However, the DAQ read in the four BPM wires, which by themselves need to be transformed

into usable coordinates. The geometry and function of the stripline BPM wires is described in Sec. 3.2.2. The wire signals from BPMs 2A and 2B are recorded in the photon DAQ IP scaler after being converted by the V2F modules. The BPM coordinate position for each direction can be calculated for each BPM separately as

$$x_{rot} = s \frac{(x_+ - x_+^{(0)}) - \alpha_{BPM}(x_- - x_-^{(0)})}{(x_+ - x_+^{(0)}) + \alpha_{BPM}(x_- - x_-^{(0)})}, \quad (5.2)$$

where x_+ and x_- are the raw IP scaler counts for BPM wires x+ and x- respectively, $x_+^{(0)}$ and $x_-^{(0)}$ are the pedestal values for the two wires respectively, α_{BPM} is a calibration constant applied by the analysis configuration file, and s is the BPM sensitivity measured before the experiments began. The value of the sensitivity is the same value for both Compton BPMs. The calculation of the rotated y-position is of the same form, except using the measured and pedestal value of of the BPM y wires.

Once beam positions x_{rot} and y_{rot} in BPM coordinates are defined, the coordinates are rotated into lab coordinates as

$$\begin{bmatrix} x \\ y \end{bmatrix} = \begin{bmatrix} \cos \theta & -\sin \theta \\ \sin \theta & \cos \theta \end{bmatrix} \begin{bmatrix} x_{rot} \\ y_{rot} \end{bmatrix} - \begin{bmatrix} \beta_x \\ \beta_y \end{bmatrix}, \quad (5.3)$$

where β_x and β_y are the zero position values for the x- and y-coordinate respectively, set in configuration files. For the Hall A BCMs the value of θ is 45° . Like the BCM and laser power, the BPM coordinate data is calibrated by setting $\alpha_{BPM} = 1$, $\beta_x = 0$ and $\beta_y = 0$ and then calculating the calibration constants necessary to match the BPM positions to the EPICS readback. The EPICS readback is itself calibrated using electronic gain and the known geometry of the BPM. It is confirmed using beam steering measurements, ultimately benchmarked to to invasive beam-intercepting “harp monitors.”

| Experiment | Las. Pow. Res. [W] | BCM Res [μA] |
|-------------------|---------------------------|------------------------------------|
| PREX-II | 16 | 0.06 |
| CREX | 26 | 0.04 |

Table 5.1: The photon DAQ bit resolution for the laser power and BCM measurement.

One feature of the V2F setup is that, because the IP scaler could only count integer numbers of pulses per MPS, there is a measurably finite “bit”

resolution for each of the channels which were fed through the V2F. This, in general, did not affect the Compton photon analysis because no instantaneous charge or laser power normalization is needed. The charge and laser power factor into the analysis to determine data which had been taken with or without beam and with or without the laser unlocked, and for general diagnostic purposes. In general the effect of the bit resolution in the Compton BPM data is not significant for the analysis. Nevertheless the BCM and laser power resolutions in the photon DAQ are recorded and are shown in table 5.1. The BPM position resolutions in the DAQ are fine enough to not need consideration regardless of whether they are used or not.

5.2 Measuring a Compton Asymmetry

The ultimate asymmetry calculation for the experimental polarimetry is contingent on being able to measure uncorrected asymmetries on shorter timescales first. To calculate these asymmetries during experimental running a software analysis suite is built to calculate and aggregate the output of the CompMon analyzer. Additionally, the analysis suite was built to include diagnostic information from the detector, including pulse sums and shapes. The software that collected and analyzed this information will be discussed in the following sections.

5.2.1 Cycles & Snails

Measuring a Compton photon integrating mode asymmetry (as will be shown in Sec. 5.2.2) is contingent on being able to precisely and accurately subtract signal backgrounds produced by the beam. Running the electron beam, even with the laser off and no Compton scatters, produces a level of signal in the photon detector. The background signal in the photon detector potentially changes over the course of several minutes owing to changes in the beam configuration and quality, meaning that slow intermittent background measurements do not suffice to measure the correct asymmetry.

To remedy this issue the Compton automates a “laser cycling” system to measure both background and Compton signal at regular intervals. By polling EPICS every few seconds, the laser cycling system detects the power in the cavity and determines whether the cavity is locked or unlocked. If the cavity is unlocked after a certain period of time the laser cycling system

engages the cavity locking electronics automatically, as well as makes small tweaks to the laser setup to allow for easier and faster locking. Once the cavity locks and is made stable, the laser locking system waits another period of time, then disengages the lock and starts the cycle all over again. The laser cycling system used for both PREX-II and CREX is programmed to engage and maintain a lock for 60 seconds and then leave it unlocked for 30 seconds. The process of unlocking the cavity is instantaneous, but achieving a locked cavity takes a few seconds (sometimes even longer) and so the laser-unlocked periods are often longer than the 30 seconds prescribed. Also, occasionally the laser loses its lock before the full 60 seconds has elapsed, in which case the laser cycling system continues with the next laser-unlocked period as if the lock had lasted the full 60 seconds.

The effect of the laser cycling system is that background measurements are taken on a timescale much faster than the beam backgrounds change. While the laser is unlocked, the photon detector reads only backgrounds from non-Compton scatters which make subtracting the backgrounds a simpler operation. A challenge in using this system with the photon analysis is that neither the laser-locked or laser-unlocked periods are necessarily the same duration due to beam trips or laser locking difficulties. Thus, identifying complete cycles correctly in the analysis is not trivial. The photon data analysis is modified to include a method to better identify good cycles from MPS and multiplet trees as described in Sec. 4.5.

Below is a pseudocode description of the process of finding laser cycles in analyzed MPS and multiplet data from the photon DAQ:

1. Iterate over all multiplets in the CODA run, tracking multiplet laser state.
2. Upon encountering a multiplet with a different laser state than the one before it, record the MPS number of the change and store it as a laser period with the starting and ending MPSs and laser state
3. If the laser period has less than 3 seconds worth of multiplets with beam on and dithering inactive then remove it from the list
4. Iterate over all remaining laser periods
 - (a) If the laser periods before and after a removed laser period are the same laser state, then merge them into a single period.

5. If a period of laser-on has a period of laser-off before and a period of laser-off after it, form it into a candidate laser cycle
6. Verify that:
 - (a) The laser cycle has an off-on-off pattern
 - (b) All laser periods have at least three seconds worth of beam-on data
 - (c) The first laser-off period and the laser-on period are separated by no more than ten seconds
 - (d) The laser-on period and the second laser-off period are separated by no more than ten seconds
7. If all the above are true, mark the laser cycle with its first and last MPS of all the laser periods and record it.

Once a laser cycle is verified, and shown to pass the cuts described in Sec. 5.2.3, the laser cycle forms the fundamental unit of the Compton asymmetry measurement. The laser cycle frequency turns out to be an excellent choice as the timescale over which the size of Compton signal or background changes is typically much longer than the scale of ≈ 2 minutes. The changes in background are slow enough that using the average of detector yields from both laser-off periods for background subtraction is sufficient to accurately correct for background.

Slugs & Snails

As discussed in 3.1.2, the main experiment requires that periodically, a insertable half-wave plate (IHWP) is inserted into the laser in the polarized source before it reached the photocathode. This flipping is necessary in order to cancel systematics resulting from the direction of laser polarizations [53]. The IHWP is flipped once after every few hours of beam on target. The IHWP being inserted reverses the direction of laser polarization on the source, relative to the voltage of the Pockels cell, which reverses the sign of the recorded asymmetry and the beam polarization. Thus, measurements of the beam polarization are averaged separately for cycles and runs taken in one single IHWP state.

In the standard nomenclature of the PVES measurement these IHWP time periods are called “slugs.” Because the Compton polarimetry data

employs similar (albeit not exactly the same) divisions, these periods for Compton data are colloquially known as “snails” (in keeping with an assumed gastropod theme). The polarization measurements made during cycles are then averaged for each IHWP state to form snailwise polarizations and (after correcting for polarization sign-reversals) the snail polarizations are averaged to produce an average polarization for each experiment.

5.2.2 Measured Asymmetries

The CompMon analyzer in tandem with the new photon detector analysis suite calculates Compton photon asymmetries from the multiplet information in every cycle. The measured yields from the photon detector are first divided up by helicity and by laser state: S_{ON}^+ and S_{ON}^- for laser-on data and S_{OFF}^+ and S_{OFF}^- for laser-off data. The important helicity multiplet variables are then the helicity-correlated differences and sums for each laser state with

$$D_{ON} = S_{ON}^+ - S_{ON}^-, \quad (5.4)$$

$$D_{OFF} = S_{OFF}^+ - S_{OFF}^-, \quad (5.5)$$

$$Y_{ON} = S_{ON}^+ + S_{ON}^-, \quad (5.6)$$

$$Y_{OFF} = S_{OFF}^+ + S_{OFF}^-, \quad (5.7)$$

where in this formulation, the values S_{OFF}^+ and S_{OFF}^- are averaged over both laser-off periods in a cycle.

The asymmetry in this formulation can be written for both laser-on and laser-off periods as

$$\mathcal{A}_{ON} = \frac{D_{ON}}{Y_{ON} - \langle Y_{OFF} \rangle}, \quad (5.8)$$

$$\mathcal{A}_{OFF} = \frac{D_{OFF}}{\langle Y_{ON} \rangle - \langle Y_{OFF} \rangle}. \quad (5.9)$$

It is necessary to use this averaging over Y_{OFF} periods because there are periods when the background noise is comparable to the separation between ON and OFF signals leading to large tails in the asymmetry distribution.

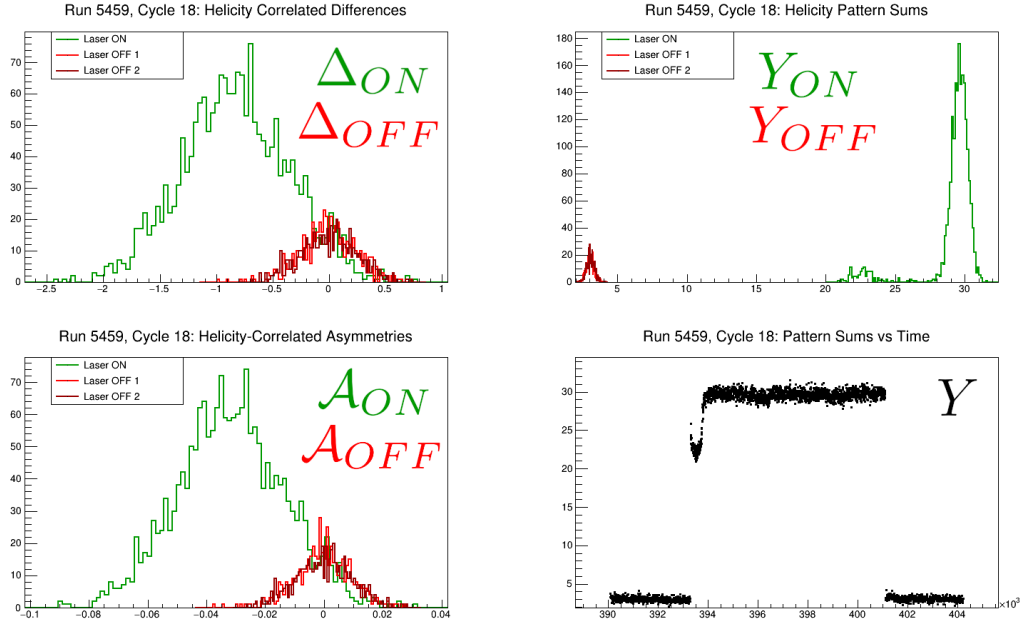


Figure 5.1: Compton multiplet histograms for each quantity needed to measure a doubly-background subtracted asymmetry as measured in a typical CREX laser cycle (divided up by laser period within that cycle). On the top left are helicity correlated differences of photon detector signal, while on the top right are the photon detector sums of each helicity sign. On the bottom right is a histogram of the derived asymmetries. The bottom left graph shows the timescale of the laser cycle, plotting the photon detector multiplet yield vs time.

Fig. 5.1 illustrates the distributions of the quantities in Eqns. 5.4 through 5.1 during a typical CREX laser cycle.

In principle, the laser-off asymmetry \mathcal{A}_{OFF} should be zero, since there are no Compton scatters to produce an asymmetry. In reality, such beam properties such as helicity-correlated halo can potentially cause \mathcal{A}_{OFF} to be nonzero and produce a false asymmetry in the Compton photon detector measurement. However, the magnitude and behavior of the false asymmetry is such that it can be subtracted from the laser-on asymmetry measurement to produce the experimental asymmetry. And with the help of Eqn. 4.26,

we relate this quantity to beam polarization as

$$\mathcal{A}_{exp} = \langle \mathcal{A}_{ON} \rangle - \langle \mathcal{A}_{OFF} \rangle = \mathcal{P}_e \mathcal{P}_\gamma \langle \mathcal{A}_l \rangle. \quad (5.10)$$

Because the CompMon analyzer produces values for helicity-correlated difference and sums, but not for asymmetry the statistical error for asymmetry is most easily calculated by error propagation on the helicity-correlated multiplet values with

$$\delta \mathcal{A}_{exp} = \left[\langle \mathcal{A}_{ON} \rangle^2 \left(\frac{\delta D_{ON}}{\langle D_{ON} \rangle} \right)^2 + \langle \mathcal{A}_{OFF} \rangle^2 \left(\frac{\delta D_{OFF}}{\langle D_{OFF} \rangle} \right)^2 + \left[\langle \mathcal{A}_{ON} \rangle^2 + \langle \mathcal{A}_{OFF} \rangle^2 \right] \frac{\delta Y_{ON}^2 + \delta Y_{OFF}^2}{[\langle Y_{ON} \rangle - \langle Y_{OFF} \rangle]^2} \right]^{\frac{1}{2}}, \quad (5.11)$$

where δD_{ON} , δD_{OFF} , δY_{ON} , and δY_{OFF} are the statistical uncertainties for each associated multiplet variable.

We can see that the factors that might increase statistical uncertainty are high uncertainty on the helicity-correlated difference measurements, high background asymmetry, and a low signal-to-background ratio. These factors all have to be controlled as much as possible to minimize statistical uncertainty in the Compton polarimeter's goal of achieving an overall uncertainty $\delta \mathcal{P}_e / \mathcal{P}_e < 1\%$.

5.2.3 Data Aggregation

Cycles are collected in each CODA run, which are stopped and started periodically. After asymmetries and polarizations are calculated for each cycle, every cycle in a snail (that is to say, one continuous period of running in between IHWP changes) is averaged to produce a snail polarization value, weighted by the inverse square of each cycle asymmetry uncertainty as

$$\langle \mathcal{A}_{exp}^{(s)} \rangle = \frac{\sum_i w_i \langle \mathcal{A}_{exp}^{(c)} \rangle_i}{\sum_i w_i}, \quad (5.12)$$

where

$$w_i = \frac{1}{(\delta \mathcal{A}_{exp}^{(c)})_i^2}, \quad (5.13)$$

and $\langle \mathcal{A}_{exp}^{(c)} \rangle_i$, and $(\delta \mathcal{A}_{exp}^{(c)})_i$ is the cyclewise average asymmetry and asymmetry uncertainty for cycle i . In this formulation the combined statistical uncertainty can be expressed as the inverse sum of the weights:

$$(\delta \mathcal{A}_{exp}^{(s)})^2 = \frac{1}{\sum_i \frac{1}{(\delta \mathcal{A}_{exp}^{(c)})^2}}. \quad (5.14)$$

In addition to the asymmetry data, the photon aggregation records information from the fADC and scalers for each laser cycle. From the fADC, the photon analysis records the average PMT signal size for each helicity state S^+ and S^- , and the multiplet differences and sums for each laser state in the cycle: $D_{ON/OFF}$, $Y_{ON/OFF}$. From the scalers the photon analysis records the positions and helicity-correlated position differences in BPMs 2A and 2B, the calibrated laser power and beam current readouts, the photon main detector rate, and the rates in the six background detectors.

5.3 Data Quality & Cuts

While the PREX-II experiment ran from June to September 2019, the Compton polarimeter was inactive in June and July due to a malfunctioning laser amplifier. As such, the Compton running during PREX-II only covered $\approx 47\%$ of all experimental data taken on a lead target. By contrast, CREX Compton running was more reliable, directly covering $\approx 97.6\%$ of all main experimental running.

| Quantity | PREX-II | CREX |
|--|---------|-------|
| $\langle Y_{ON} \rangle - \langle Y_{OFF} \rangle$ [RAU] | 6.56 | 23.54 |
| Signal/Background Ratio | 0.460 | 6.047 |
| I_{beam} [μA] | 73.11 | 147.3 |
| Laser Power [kW] | 1.986 | 2.205 |
| PhDet Rate/ I_{beam} (Las On) [Hz/ μA] | 4910 | 1425 |
| PhDet Rate/ I_{beam} (Las Off) [Hz/ μA] | 4280 | 245.6 |
| Laser Det DS 1 [Hz/ μA] | 30.1 | 20.89 |
| Laser Det DS 2 [Hz/ μA] | 35.0 | 25.27 |

Table 5.2: Summary of non-helicity-correlated photon data from both experiments.

One of the primary differences between the two experiments' Compton photon detector data quality is the presence of far higher backgrounds during PREX-II running than during CREX running, due to an increased load from thermal neutrons. PREX-II's lower beam energy and wider scattering angle meant that more energy is deposited onto the collimator, producing thermal neutrons which are absorbed in the GSO photon detector due to Gadolinium's high absorption cross section for thermal neutrons[91]. For the purpose of overall photon data quality the result of this effect is that the PREX-II Compton data have a much lower signal-to-background ratio than the CREX Compton data, as quantified in table 5.2.

5.3.1 Pedestal Subtraction

Pulse sums and Acc0 are measured in raw ADC units, and are measured relative to the fADC electronic pedestal. While individual photon triggers have their own inbuilt mechanism for calculating pedestal in the 1.5 μ s pulse time window, the pedestal for Acc0 is measured manually. This is done by taking an average of the fADC response during periods of no electron beam. Once calibrated and subtracted from each sample, any nonzero beam-off fADC signal would be due solely to pedestal mismeasurement. Consequently, the data are reanalyzed, with the beam-off signal added to the pedestal to produce the correct Acc0 size in the data.

In the case that photon data were taken with an incorrect pedestal the effect is seen in the helicity-correlated photon detector yield as $S_{ON}^+ \rightarrow S_{ON}^+ + p$ and $S_{ON}^- \rightarrow S_{ON}^- + p$ where p is the magnitude of the pedestal mismeasurement (and the same effect on S_{OFF}^+ and S_{OFF}^- .) In this formulation the helicity pattern yields change:

$$Y_{ON} \rightarrow Y_{ON} + 2p, \quad Y_{OFF} \rightarrow Y_{OFF} + 2p. \quad (5.15)$$

But because the asymmetry is normalized to $\langle Y_{ON} \rangle - \langle Y_{OFF} \rangle$, then as long as the pedestal is stable during the period of measurement then the pedestal term subtracts out in the asymmetry calculation and does not affect the polarization measurement.

There are however, periods during the running of both PREX-II and CREX periods when the pedestal in the fADC appears to change instantaneously by irregular amounts. This "pedestal shifting" problem was first noticed in the first few weeks of the CREX run period. The pedestal shifts

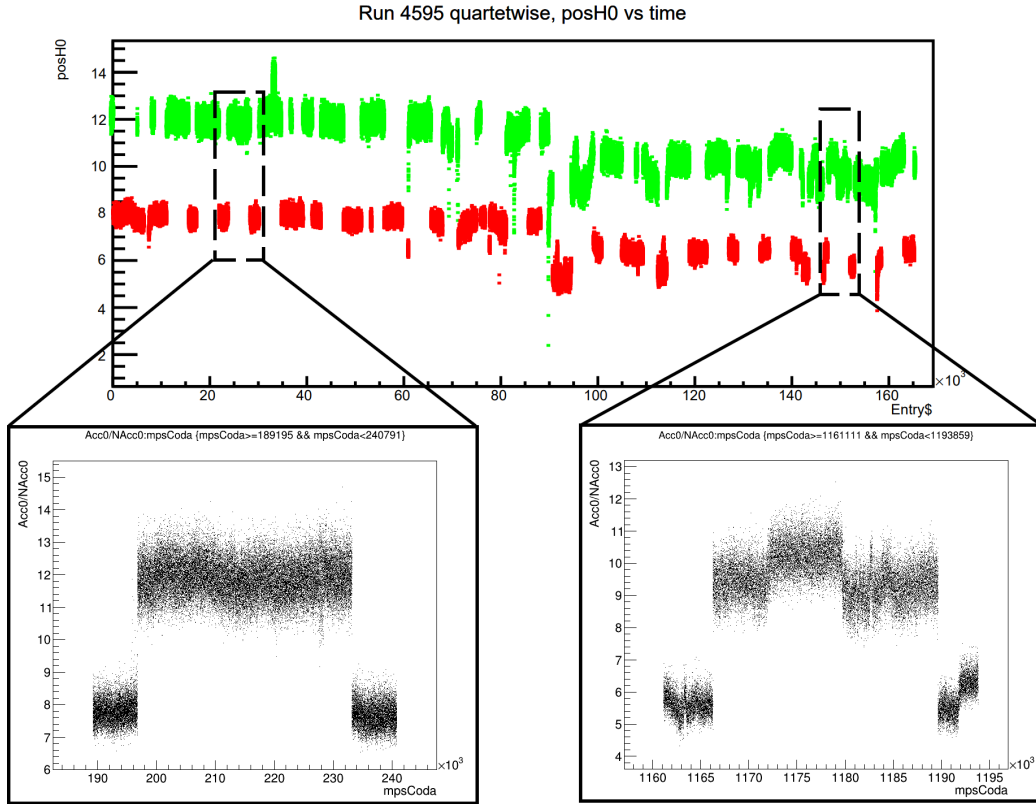


Figure 5.2: Example of a Compton run from PREX-II which had numerous pedestal shifts. In the laser cycle seen on the left, the photon detector signal is mostly stable. In the cycle on the right there are multiple instances where the signal size for both laser states appears to change instantaneously. Looking for these jumps in signal was how we identified pedestal shifts.

can be identified, as Fig. 5.2 shows, by looking for instantaneous shifts in the recorded Acc0, occurring regardless of laser state or beam state. The problem was eventually traced to a signal attenuator box connected between the $10\times$ PMT amplifier and the fADC. After the box was removed, no such shifts were observed in the fADC data. The box was in place during all of PREX-II experimental running and for the part of the first CREX run period until its removal. The inclusion of the attenuator box introduces the potential for rapid pedestal shifts during laser cycles which can affect the asymmetry measurement.

CREX Acc0 (Las Off) RMS by Cycle

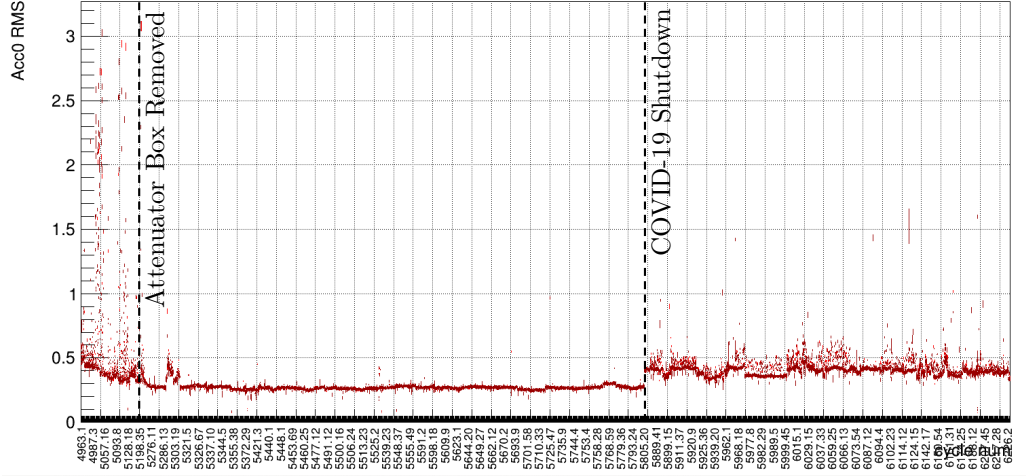


Figure 5.3: Laser-off Acc0 RMS plotted vs time for the CREX experimental run. The effect of pedestal shifts can be seen in the period before the attenuator box was removed.

The first proposed solution to this problem was to implement a dynamic pedestal tracking algorithm for Acc0. To do this, the calculated pedestals are taken from the photon trigger data and averaged over intervals of several seconds in order to produce a pedestal average. It became clear however, that due to the potential of photon pulses from earlier events existing in the pedestal sum region, the pedestal measurement was rate-dependent. No combination of threshold cuts could remove the rate dependence and so the dynamic correction was not applied.

Instead, the decision was made to isolate cycles which had identifiable pedestal shifts in them. To identify pedestal shifts, the RMS of the Acc0 is used as a metric. For stable cycles, the Acc0 RMS is approximately equal from cycle to cycle, as shown in Fig. 5.3. However, during periods of pedestal shifting, the recorded Acc0 contains much higher variation over the course of one cycle, having a higher RMS. We then define a threshold which cuts the cycle if the Acc0 RMS for any period in the cycle is too large. This threshold needs to be implemented dynamically because the Acc0 RMS is also dependent on beam quality and configuration, which can potentially change at longer intervals throughout the run.

5.3.2 CycleCut

In order to cut poor-quality or high-background data, a new cutting concept is implemented to cut laser cycles at analysis-time based on several criteria. This system is called “CycleCut” and the output of the cutting software is stored as a numerical flag along with the rest of the cycle data. Development of CycleCut was borne of the RMS cut discussed in Sec. 5.3.1, and the RMS cut created is implemented as one component of CycleCut.

In addition to the RMS cut, the other components of CycleCut are:

- **Signal size cut:** The Compton photon signal is defined as the fADC Acc0 measurement for laser-on periods minus Acc0 during laser-off periods. If the signal above background is low, then it increases the chance that the asymmetry is poorly normalized. To prevent this, all cycles with laser-on Acc0 less than 0.7 RAU greater than laser-off Acc0 are cut.
- **Double difference cut:** When performing the subtraction in Eqn. 5.10, the measurement of \mathcal{A}_{OFF} is taken during both laser-off periods in a laser cycle. In order for the subtraction of \mathcal{A}_{OFF} to be valid for the entire laser-on period, \mathcal{A}_{OFF} must not vary (or at least, must be varying on a timescale much longer than a laser cycle). For this cut the values of background asymmetry for each laser-off period in a cycle (that is $\mathcal{A}_{OFF}^{(1)}$ and $\mathcal{A}_{OFF}^{(2)}$) are subtracted to define a “double-difference” value, and then normalized to the propagated uncertainty of both asymmetry measurements as

$$\mathcal{A}_{DD} = \frac{\mathcal{A}_{OFF}^{(1)} - \mathcal{A}_{OFF}^{(2)}}{\sqrt{(\delta\mathcal{A}_{OFF}^{(1)})^2 + (\delta\mathcal{A}_{OFF}^{(2)})^2}}. \quad (5.16)$$

If the value of \mathcal{A}_{DD} is greater than 3 for any laser cycle, then the cycle is cut.

- **Asymmetry uncertainty cut:** The overall data quality for any laser cycle is in general reflected in the statistical precision of the primary asymmetry measurement. Low precision can be indicative of beam instability, beam misalignment with the laser target, or low cycle statistics. Because these cycles end up having virtually no contribution to the asymmetry average, they can be safely removed to negate any residual correlations with beam properties. PREX-II asymmetries are cut

if $\delta\mathcal{A}_{exp}$ for any cycle is greater than 5 parts per thousand. For CREX, the analyzing power is higher so cycles are cut if $\delta\mathcal{A}_{exp}$ for any cycle is greater than 11 parts per thousand.

- **Background rate cut:** Another key indicator of the beam quality are four background detectors mounted on the laser table. Ostensibly the rate from these detectors is used to measure and limit the radiation dose on the Compton lasers and power supplies. In practice, the background rates drift and change throughout experimental running, and have to be regularly readjusted by accelerator operators. For the purposes of the photon data the upstream background detectors are recorded, as these detectors measure lower rate, but are more susceptible to beam configuration changes. For PREX-II a cycle is cut if the rate in upstream detector 1 during the cycle is higher than 192 Hz, or if the rate in upstream detector 2 is greater than 672 Hz. This cut is not applied for CREX as no well-defined limits on the background rates were ever specified.
- **Charge asymmetry cut:** In order to control the helicity-correlated beam-charge asymmetry, the main experiment ran a feedback program to make rapid adjustments to the charge off the polarized source during running (which is discussed in Sec. 3.3.) Though the overall charge asymmetry for production running is well below the Compton asymmetry value, brief periods of high charge asymmetry could affect the Compton measurement by depositing a different amount of Compton photon energy on the detector in different helicity periods. A cycle is cut if the measured charge asymmetry in the photon DAQ for any period in a laser cycle is measurably nonzero, which for this analysis means cutting the cycle if $|\mathcal{A}_{charge}|/\delta\mathcal{A}_{charge} > 3$. For the large majority PREX-II and CREX Compton laser periods $|\mathcal{A}_{charge}| < 10$ ppm measured in the Compton DAQ with $\langle\mathcal{A}_{charge}\rangle \approx 0.05$ ppm. Also, $\langle\delta\mathcal{A}_{charge}\rangle \approx 5$ ppm for both experiments.

The results of CycleCut can be seen in table 5.3. The CycleCut, after tuning the cut parameters and thresholds, cuts 16.2% of PREX-II cycles and 4.8% of CREX cycles. This has a negligible effect on the statistical uncertainty as many of the cut cycles had very little contribution to the asymmetry average while simultaneously removing systematic effects due to instability and backgrounds.

| Cut | PREX-II | CREX |
|-----------------------|----------------|--------------|
| <i>Total Cycles</i> | <i>2867</i> | <i>15232</i> |
| RMS cut | 236 | 354 |
| Signal size cut | 77 | 11 |
| Double difference cut | 65 | 78 |
| Asym. error cut | 11 | 34 |
| Background cut | 45 | 0 |
| Charge asym. cut | 31 | 257 |
| Cycles Left | 2402 | 14498 |

Table 5.3: The results of CycleCut once applied to the full Compton data set for both experiments. Note that the cycles are included in the counts above only if they haven't already been flagged by a previous cut. (i.e., the numbers in the ‘‘Double difference cut’’ row are cycles which haven't already been flagged by the RMS cut and the signal size cut.)

5.3.3 Background Sources and Corrections

The Compton background is divided up into two categories. The first of these categories is signal background. Signal background is measured as the photon detector yield while the electron beam is running, but the laser is unlocked. In that circumstance, none of the detector signal is from Compton scattering, and all of it is from beam-associated radiation. This background is subtracted out in the initial asymmetry calculation in equations 5.8 and 5.9.

The second category of background is the asymmetric background. These backgrounds contribute a false asymmetry to the Compton measurement, and are found by observing a helicity-correlated asymmetry during laser-off periods. The primary suspected cause of these asymmetric backgrounds is helicity-correlated beam halo. Beam halo describes an effect where electrons pass down the beamline outside the primary beam spot (which is ≈ 200 μm in diameter). These electrons are steered into the path of the physical beamline by entering the fields of dipole and quadrupole magnets off-axis. If the amount or spatial distribution of beam halo entering Hall A is helicity-correlated it can produce backgrounds in the photon detector which are also helicity-correlated. Beam halo was ultimately never positively identified as the cause of asymmetric backgrounds because conducting measurements of beam halo with the Hall A equipment is prohibitively difficult. However,

beam halo is suspected to cause asymmetric background because of its identification in Compton data during the Qweak experiment, which ran in Jefferson Lab hall C several years prior[72]. Once measured, the asymmetric backgrounds are subtracted out directly from the measured Compton asymmetry.

Regardless of the cause of backgrounds, the solution for measuring and subtracting them is to use the measurements of PMT signal during the laser-off periods of each laser cycle. By doing cycle-by-cycle background subtractions instead of subtracting them out with a global average, we are able to account for slow drifts in any background source over the experimental run.

The difference between PREX-II and CREX signal backgrounds can be seen in Fig. 5.4. While the neutron background from the CREX target has a narrow energy range (only extending to $\approx 8\%$ of the Compton edge) the PREX-II background peak extends out to $\approx 35\%$ of the Compton edge. Additionally the relative rate of background compared to Compton signal is smaller for CREX data than for PREX-II data. Correctly subtracting high backgrounds for low Compton energies is prohibitively difficult, meaning that background-subtracted Compton spectra from experimental data cannot be used to normalize the background subtraction for the accumulator data. Thus, asymmetry and background data from Compton spectra are not used for the Compton asymmetry measurement, but are used as a general diagnostic tool.

5.4 Analyzing Power

In principle the theoretical analyzing power $\langle \mathcal{A}_c \rangle$ is calculated from kinematic variables as prescribed in Eqn. 4.25. In practice, effects from the finite size of the Compton detector, the photon collimator, the response of the GSO crystal, and the nonlinearity of the PMT mean that the analytic calculation of $\langle \mathcal{A}_c \rangle$ is insufficient for high-precision polarimetry. To remedy this problem, a GEANT4-based Monte Carlo simulation is used for the Compton polarimeter, which calculates the analyzing power, from simulated Compton scattered photons received in the detector.

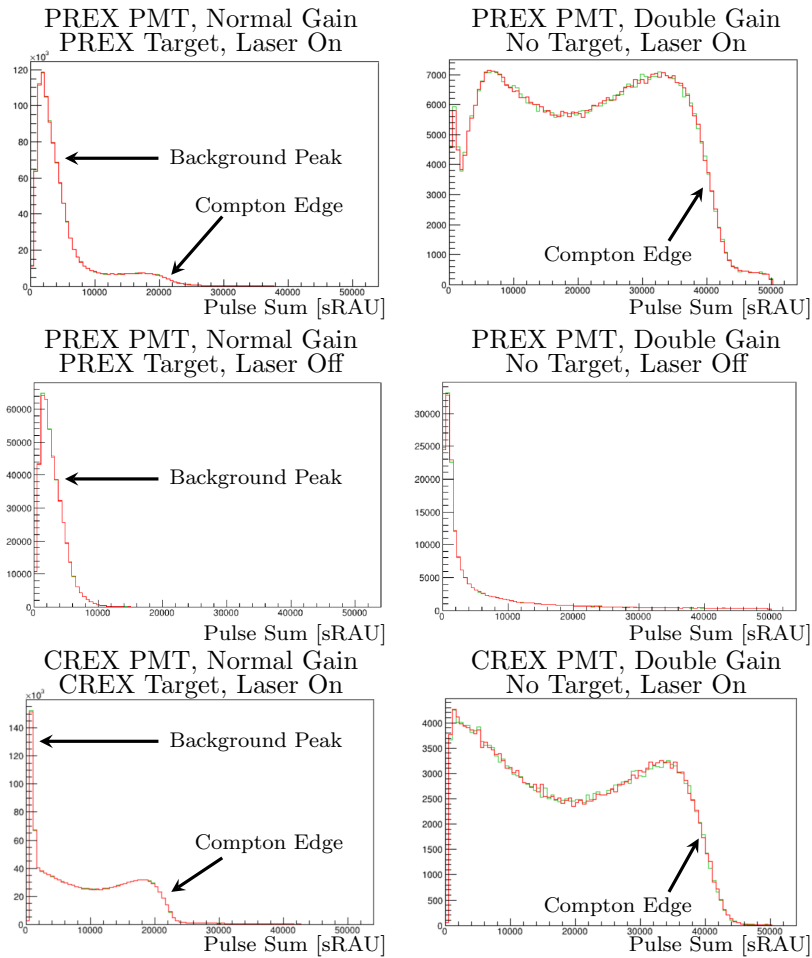


Figure 5.4: PREX-II and CREX Compton spectra showing the difference between target-in and target-out configurations for both experiments. Note the relative size of the Compton spectrum to the background peak caused by neutrons scattering backwards from the target and collimator. Without the target, the photon beam offset and the discriminator threshold are the dominant effects on the spectrum.

5.4.1 Compton Monte Carlo Simulation

The principle of a Monte Carlo (MC) simulation is to simulate individual particle scattering and detection by randomly selecting the particle's kinematics from random variable distributions. In particular, the Compton MC selects its scattered Compton photon energy randomly, following the distribution created by the functional form of the scattering cross section $d\sigma/d\rho$. This form can be seen in Eqn. 4.9.

While analyzing power as defined in Eqn. 4.25 uses integration to calculate a weighted average of asymmetry, the Compton MC does not perform analytic computations. Instead the analyzing power can be calculated numerically with

$$\langle \mathcal{A}_l \rangle = \frac{\sum_i Y(\rho_i) \epsilon(\rho_i) \mathcal{A}_l(\rho_i)}{\sum_i Y(\rho_i) \epsilon(\rho_i)}, \quad (5.17)$$

where as before, \mathcal{A}_c is the theoretical analyzing power, $\epsilon(\rho)$ is the detector response, and ρ_i is the photon energy fraction k'/k'_{max} for energy range i .

To generate a primary Compton scattered photon the simulation first picks a value of ρ using the cross section $d\sigma/d\rho$ as a distribution. The other kinematic variables such as a , defined in Eqn. 4.7, and scattering angle θ_γ are then calculated from ρ . The out-of-plane scattering angle ϕ is selected via a flat random distribution between 0 and 2π .

The primary photon is then sent into simulated volumes representing photon detector components. Once scattered, Compton photons pass down a 5-meter stainless steel beam pipe under vacuum and then out through a stainless steel window towards the photon detector. After passing through about 30 cm of air, the photons then must pass through the lead collimator, tungsten fingers, and synchrotron shield. Inside the photon detector the MC contains volumes representing the GSO crystal, the reflective foil wrap surrounding the GSO, the PMT glass and cathode, and the optical grease which affixed the PMT to the crystal face. The MC tracks the progression of the Compton photon down its scattered path through a series of iterative steps on its track. Once inside a volume the simulation either computes the probability of scattering and performs it, or registers a particle hit on a detector in which energy is deposited. Upon registering a hit, the MC saves information about the particle location, time, momentum, kinetic energy, particle ID and vertex before applying physical particle creation processes [94].

The MC also had the ability to simulate the optical properties of GSO

to create a cascade of photons in the material. The MC was programmed with the scintillation and optical properties of GSO to produce the correct photon energy after each optical hit. In addition the simulation included the reflective, absorption and refractive properties of the mylar foil surrounding the GSO, the optical grease in front of the PMT and the silicate glass window on the PMT.

Ultimately, the MC simulation produced an output containing hits in two primary detectors: the GSO crystal and the PMT cathode. Once the PMT cathode hits are registered, the asymmetry calculation must be modified with the real properties of the PMT. From the simulation a realistic detector response function is generated calculating an average signal size as a function of ρ accounting for geometry and light yield collection.

5.5 Laser Polarization Measurements

As stated in Sec. 4.3.1, the primary difficulty in obtaining an accurate determination of the degree of circular polarization (DOCP) of the laser \mathcal{P}_γ , is that due to the configuration of the laser cavity, the DOCP cannot be directly measured inside the cavity. Instead, an optical model is devised in order to characterize the polarization transfer function between the initial laser polarization and the polarization inside the cavity. The formalism is described in Sec. 4.3.1, however the specific measurements of laser polarization parameters will be presented here.

Because there are a number of different parameters that must be empirically measured in order to construct an optical model, several measurements and tests are carried out on the laser before and during the running of both experiments. The first test is the measurement of laser polarization on the entrance line to the cavity by constructing an entrance function with cavity birefringence terms. This test is described in Sec. 4.3.1. Secondly the slow axis of the quarter wave-plate along the exit line is periodically rotated and measure the light yield in two different detectors that could each measure each directional component of linearly polarized light. This helps quantify the time-dependence of laser DOCP. Finally, electron beam polarization measurements are taken during experimental running with the cavity-DOCP tuned off-100% and the effect on the measured asymmetries. This test is only analyzed with parameters obtained from the former two.

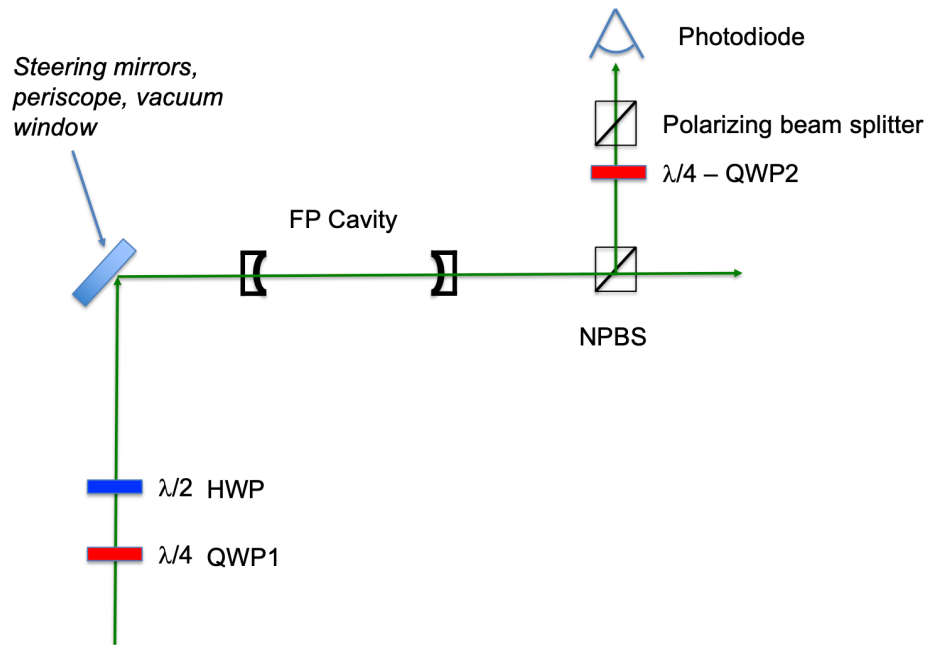


Figure 5.5: A diagram of the hardware setup used to measure laser DOCP on the table. Of interest are the low-loss cavity mirrors, non-polarizing beam splitter (NPBS) which directs the laser towards the photodiode, the QW2 on the laser exit line, and the photodiode which measured reflected laser power.

5.5.1 NPBS Laser Polarimetry

The important components used in making a laser DOCP measurement can be seen in Fig. 5.5. In a dedicated configuration with the cavity open to air a diagnostic station is added after the second cavity mirror. Space limitations prevented this to be placed in line. For this reason a non-polarizing beam splitter is used to direct light at a 90° angle where a diagnostic station is placed. The NPBS could (as advertised) reflect 50% of incident light and transmit the other 50%. The reflected laser light then passes through a quarter-wave plate (QW2) which is rotated during measurements¹, on to a polarizer and a photodiode which measures laser power transmitted through the optical elements.

¹Note that this is not the same QWP on the entrance line to the cavity and was rotated to control the cavity laser DOCP. Hence the entrance line QWP will be referred to as “the QW1” and the exit line QWP will be referred to as “the QW2.”

The measurement principle is the combination of the QW2 and the polarizer. The QW2's main function is to convert circularly polarized light into linearly polarized light and vice versa. The polarization on the exit line is measured by rotating the QW2 and measuring the photodiode response. The fit of the polarization vs QW2 angle gives the Stokes parameters s_0 , s_1 , s_2 , and s_3 .

While the NPBS is advertised as having a $<0.1\%$ difference between reflected and transmitted polarized light, the real NPBS has a non-negligible effect on the polarization. Thus the NPBS is characterized and added to the overall transfer function of optical elements downstream of the cavity for any measurement taken during the NPBS tests. To characterize the NPBS laser light with a variety of polarization states is sent through the NPBS and then measured using the same QWP/linear polarizer technique described above. The extinction ratio of light through the QW2 as a function of the angle of the axis of the QW2 is indicative of the light polarization direction after the NPBS. The NPBS effect on the polarization is parameterized by a Jones matrix for a general birefringent element which is composed of a rotation, a phase shift, and another rotation as

$$M_{NPBS} = R(\eta)P(\delta)R(\theta), \quad (5.18)$$

where R is a general rotation matrix, P is a general shift matrix and η , δ , and θ are empirically determined angles.

5.5.2 Exit Line Scans

To monitor the laser polarization in the cavity, the exit line components are used though without the benefit of the NPBS. These measurements use the laser hardware along the cavity exit line including some optical elements used in the NPBS tests. The components along the laser exit line are illustrated in Fig. 5.6. The first component is the QW2 which, like before is to convert circularly polarized laser light to linear. After the QW2, the laser is sent into a Wollaston prism which separates light into two separate beams with orthogonal polarization directions. Each beam is then sent into two integrating sphere powermeters, labeled S1, and S2.

The principle of the measurement is that as the QW2 is rotated, so too will the direction of linear polarization of light entering the Wollaston prism. The detectors S1 and S2 will then register a change of intensity that is a

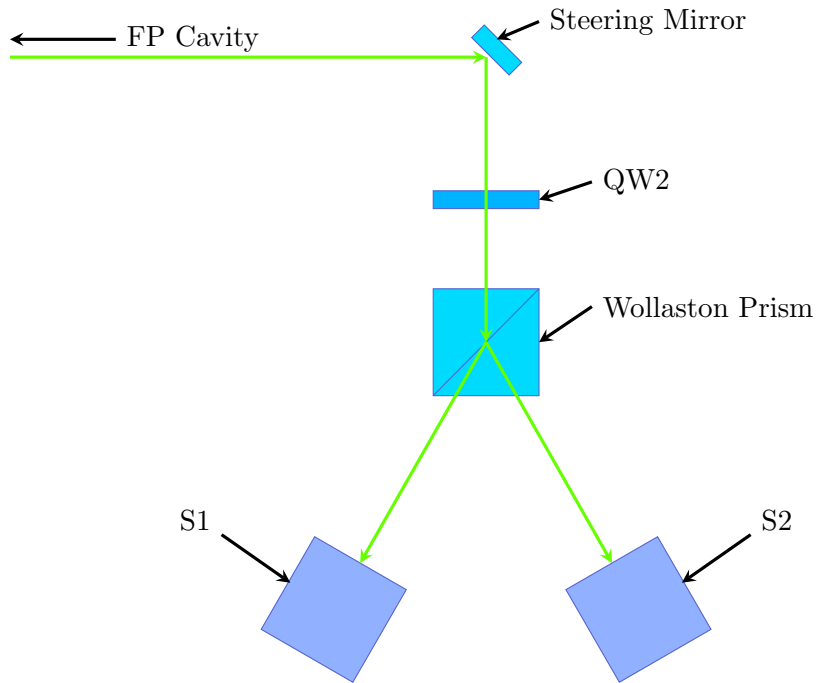


Figure 5.6: A diagram of the laser on the exit line from the cavity. The laser is passed through the QW2 then into the Wollaston prism which separates laser polarization based on direction and sends it into two integrating detectors: S1 and S2. Adapted from Rakhman et al. [83].

function of the QW2 angle which defines the laser polarization state entering the QW2. Periodically, with the laser cavity under vacuum, the QW2 is fully rotated in an “exit line scan” and the S1 and S2 light intensities are measured. The S1 and S2 intensities are then fit as a function of QW2 angle and the Stokes parameters are extracted from the fits [95].

These measurements help characterize the time-dependence of the laser cavity DOCP. These exit line scans are performed during the experimental run period via remote control. The exit line scans also do not affect the laser DOCP in the cavity. The degree of variation in the exit line scan fits over time helps set an upper bound on the variation of DOCP.

5.5.3 Off-100% DOCP Running

The NPBS tests and the entrance scans determine the polarization at the CIP. The exit line data is also used throughout the running of both experiments as a relative measurement of DOCP in the cavity.

As expressed in Eqn. 4.26, the experimental Compton asymmetry must be normalized by the cavity DOCP \mathcal{P}_γ . During normal running the laser DOCP is $\mathcal{P}_\gamma \simeq 1.0$ in order to maximize the measured asymmetry and minimize the size of the laser correction. But for brief periods during both experiments, the cavity entrance line QWP and HWP angles are changed to deliberately run with $\mathcal{P}_\gamma < 1.0$. Without applying a correction to the measured Compton asymmetry, it would be lower than the asymmetry measured in run periods taken around the same time. If the statistical uncertainty on the asymmetry is lower than the size of the laser polarization correction then the uncorrected asymmetry data can be used as a cross-check of the laser polarization model.

While in principle the laser DOCP in the cavity is chosen arbitrarily with each QWP and HWP setting, in practice the degree to which cavity DOCP could be changed is limited. As described in Sec. 4.3.1, the cavity used a laser locking technique which used as a metric for locking the reflected light from the cavity. If the laser DOCP on the table is tuned too far away from either $\mathcal{P}_\gamma = 1.0$ or $\mathcal{P}_\gamma = -1.0$ then too much light is sent back to the laser, which can possibly damage the fiber amplifier. The challenge then becomes to find laser DOCP configurations that are sufficiently lower than 100% DOCP to measure in the asymmetries, but close enough to 100% that the amount of back-reflected light is minimized.

Fortunately, because of the high statistical precision for PREX-II Compton running and even higher statistical precision in CREX Compton running, there are a range of QWP/HWP angle configurations that produce less than 100% DOCP in the cavity. These configurations are listed in table 5.4. The majority of each experimental run is taken at the configuration which produced the highest cavity DOCP (specified in the italicized rows in table 5.4), and the alternate configurations are only run for short times, as the statistics from those measurements was sufficient to constrain the cavity optical model. While 15.5% of PREX-II Compton statistics are taken with low DOCP, only 4.3% of the CREX run is taken with low DOCP.

After the asymmetry of the low DOCP running is obtained, it is used to verify the optical model parameters, and obtain the estimated values of \mathcal{P}_γ .

| Experiment | QWP Angle | HWP Angle | Predicted \mathcal{P}_γ |
|------------|--------------|--------------|--------------------------------|
| PREX-II | <i>49.2°</i> | <i>0.2°</i> | <i>0.9999</i> |
| | 49.2° | 15.2° | 0.9980 |
| | 49.2° | 31.2° | 0.9595 |
| | 47.7° | 19.1° | 0.9887 |
| CREX | <i>39.3°</i> | <i>63.5°</i> | <i>0.9974</i> |
| | 39.3° | 73.0° | 0.9945 |
| | 39.3° | 56.0° | 0.9901 |
| | 50.5° | 27.4° | 0.9974 |
| | 43.5° | 63.5° | 0.9933 |
| | 37.0° | 63.5° | 0.9918 |

Table 5.4: Various QWP/HWP settings used during PREX-II and CREX to cross-check the laser DOCP model. Italicized rows indicate the “normal” settings that most of the experiments were run at. Uncertainties on \mathcal{P}_γ are omitted but were all below 0.5% relative.

With the estimated \mathcal{P}_γ the photon analysis is re-run with the low DOCP run periods correctly normalized making the asymmetries again usable for beam polarimetry. The optical model used to find the mean values of DOCP for each run period is discussed in section 5.6.2.

5.6 Sources of Systematic Uncertainty

The majority of time spent on Compton analysis after the experimental running was dedicated to accurately quantifying sources of systematic uncertainty not handled by cuts. Both PREX-II and CREX offer a high degree of statistical precision to allow us to engage in systematic studies similar to studies done for previous Compton polarimeter measurements. With increased precision, new studies of the behavior of known sources of Compton systematics can be undertaken.

The systematic uncertainties arise from the limitations of the Compton equipment and running conditions. There are known systematic uncertainties resulting from the beam energy and position, the photon detector properties, and the laser system. Each systematic affects one of the three experimentally measured quantities in Eqn. 4.26: the laser polarization \mathcal{P}_γ , the mean analyzing power $\langle \mathcal{A}_l \rangle$, and the experimental asymmetry \mathcal{A}_{exp} . The goal of

this section is to explain the source of each systematic error quantity, how it is monitored using experimental data, how it is eventually measured, and how it affects the measurement of beam polarization \mathcal{P}_e .

5.6.1 Photon Cone Offset & Simulation

Because the MC simulation discussed in Sec. 5.4.1 takes into account the geometry of the Compton photon detector space, effects arising from that geometry can be quantified. The most notable of these is the photon beam offset from the Compton collimator axis. The scattered photon beam is in the shape of a cone with its vertex at the CIP and its axis along the direction of propagation of Compton edge photons at $\theta_\gamma = 0$. Because $|\vec{p}_e|^2 \gg |\vec{k}|^2$ the direction of the backscattered photon propagation is mostly determined by the direction of the incoming electron beam. The Compton beam setup allows for beam motion within the cavity which, as long as the beam intercepts the laser, is not visible in the Compton rates. A small movement of the beam in one of the Compton BPMs can cause the center of the photon beam relative to the center of the collimator to be shifted. The nominal calculation for the offset of the photon cone from the collimator axis in BPM coordinates is

$$\Delta d = \sqrt{\left(\frac{\Delta z_{PhDet}}{\Delta z_{BPM}}(x_{2B} - x_{2A}) + x_{2A}\right)^2 + \left(\frac{\Delta z_{PhDet}}{\Delta z_{BPM}}(y_{2B} - y_{2A}) + y_{2A}\right)^2}, \quad (5.19)$$

where x_{2A} , x_{2B} , y_{2A} , and y_{2B} are the x- and y-coordinates from BPMs 2A and 2B, $\Delta z_{PhDet} = 6$ m is the distance between the CIP and the photon detector and $\Delta z_{BPM} = 1$ m is the distance between the two BPMs.

Photon-cone offset affects the analyzing power by changing the distribution of Compton photon energy that reaches the photon detector. At low beam energies (like those used for PREX-II and CREX), the scattered photon cone has a wider distribution of θ_γ . At the PREX-II energy (950 MeV) a Compton photon with $k' = k_{max}/2$ is scattered at $\theta_\gamma = 547$ μ rad, whereas at the CREX energy (2183 MeV) it is scattered at $\theta_\gamma = 243$ μ rad.² At low beam energies the interception between the photon beam and collimator is much larger, hence the effect of an asymmetry in the beam results in an

²A hypothetical experiment running at 11 GeV beam energy would scatter the photon at $\theta_\gamma = 55$ μ rad, for reference.

asymmetry in photon cone interception by the collimator. Thus it becomes important to quantify the photon cone offset's effect on the analyzing power calculation.

PREX-II Photon Cone Offset

First, the PREX-II analyzing power is calculated for different photon cone offset amounts via simulation. The simulations revealed that the effect of photon cone offset is most pronounced on the low energy shape of the Compton spectra. For regular PREX-II running, this is problematic because the spectrum is dominated by energy from thermal neutrons below 30% of the Compton edge. The spectrum of the thermal neutron background completely dilutes any effect from photon cone offset during regular PREX-II running.

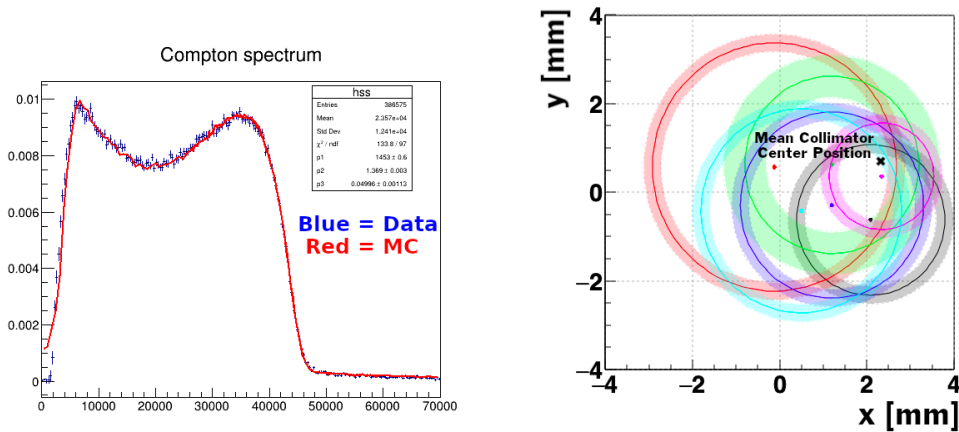


Figure 5.7: *Left:* A single PREX-II spectrum run with the best fit from a simulation with 1.5 mm photon cone offset. *Right:* A circle plot with six PREX-II spectrum runs. The centroid of each circle is the projected collimator position from the BPM data. The circle radii are the photon cone offset of each run matched to simulation. The color band in each circle represents the estimated uncertainty.

To counter this, the Hall A Compton is run periodically for short periods with the target out to get a reasonable measurement of spectrum. These “spectrum runs” typically only need to run for 15 minutes in order to acquire the necessary statistics to have a complete spectrum. Also, these spectrum

runs run with the detector high voltage set to double the PMT gain of the regular experiment in order to increase detector resolution over threshold. The PREX spectra can be seen in the top row of Fig. 5.4, illustrating the large qualitative difference between the target-in and target-out spectra.

Once a spectrum is obtained, the spectrum is fit by spectra from the MC with different photon cone offsets. The offset of the Compton running is then ascertained by finding the MC spectrum which best fits the data and extracting the offset that produced that spectrum in simulation. The best fit is chosen as the one that had the lowest χ^2 -test value.³ A typical MC spectrum fit to data from a spectrum run can be seen in Fig. 5.7.

After the PREX-II experimental run, offsets determined from the spectrum runs are fit to find the overall relative offset between the BPM projection and the center of the collimator. In principle, the photon cone offsets and the projected positions of the photon beam should form a map of the collimator face, where the intersections of all offsets give the approximate location of the collimator center in projected BPM coordinates. The map can be seen in Fig. 5.7. The mean of the offset circles are computed to find the average collimator center position.

The PREX-II asymmetry data is then re-analyzed with the fitted collimator center position included. With the runwise BPM information and a map from BPM coordinates to collimator coordinates provided by the spectrum runs, the photon cone offset is mapped for the entire PREX-II Compton data. Once the offset is calculated, it is then be used to modify the analyzing power based on simulations taken with that offset. Though the simulations are taken at discrete offset values, the average analyzing power is taken from a polynomial fit applied to the simulated analyzing powers as seen in Fig. 5.8.

The analyzing power increases monotonically as a function of photon cone offset, as seen in Fig. 5.8. In principle, periods of high offset in any direction will measure a higher asymmetry than when the photon beam is well-aligned with the collimator. A dynamic analyzing power correction keeps the measured beam polarization correctly normalized as long as the pointing direction towards the collimator face (as measured in the BPMs) is allowed to change.

³In this formulation $\chi^2 = \sum_i (s_i^{(MC)} - s_i^{(Data)})^2 / (\delta s_i^{(Data)})$ where $s_i^{(MC)}$ is the MC fit value for energy bin i , and $s_i^{(Data)}$ and $\delta s_i^{(Data)}$ are the data value and error of each energy bin, respectively. The lowest value of χ^2 represents the best fit.

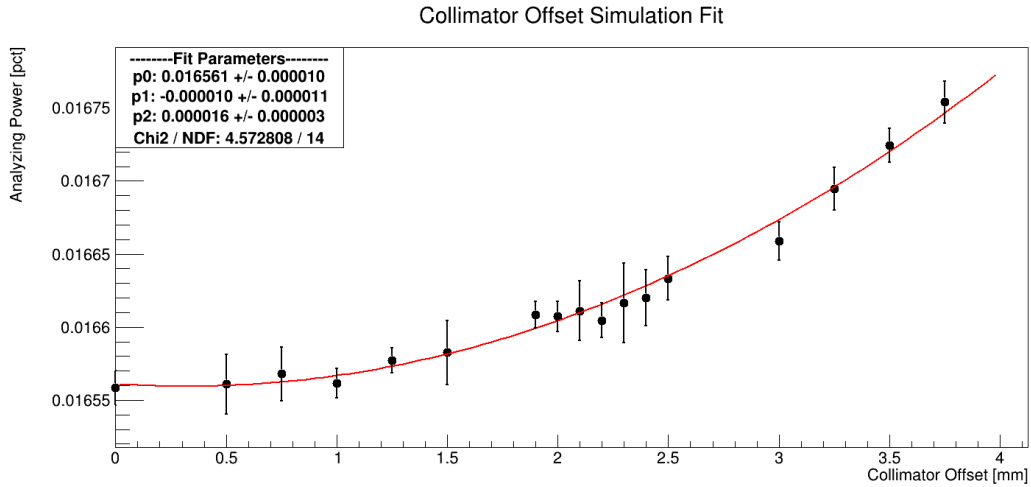


Figure 5.8: Analyzing powers calculated from simulation as a function of simulated photon cone offset from photon beam for PREX-II.

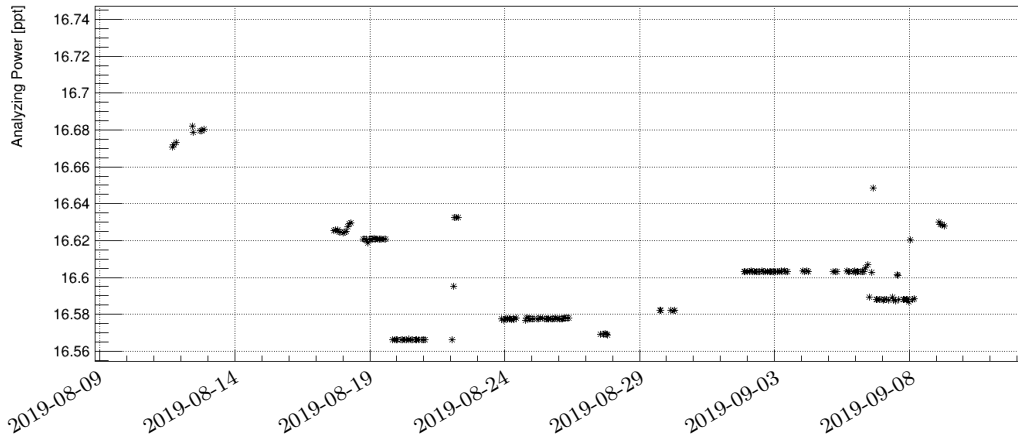


Figure 5.9: PREX-II analyzing power vs time. The run can be divided into periods where the beam position in the chicane was mostly constant, which resulted in analyzing power for these periods also being constant.

During experimental running there are periods of consistent running where few adjustments are made to the beam and the beam position in the chicane (and with it the photon cone offset and analyzing power) stays approximately constant. However, after periods of beam activity where readjustments are

made, the beam often comes back into the chicane in a different position than it had been previously. This sort of behavior, of long stretches of stable analyzing power followed by a sudden change during downtime can be seen in Fig. 5.9.

To estimate the uncertainty in the analyzing power measurement, we first attempt to estimate the uncertainty in the photon cone offset. The BPM resolution is quoted as $\delta x = \delta y = 0.1$ mm. With this in mind the average analyzing power is calculated as a weighted average of analyzing power calculations for each cycle where the weights are calculated from the Compton asymmetries for each cycle i by

$$w_i = \frac{1}{(\delta \mathcal{A}_{exp})^2}, \quad (5.20)$$

and the weighted average is

$$\langle \mathcal{A}_l \rangle = \frac{\sum_i w_i \langle \mathcal{A}_l \rangle_i}{\sum_i w_i}, \quad (5.21)$$

where $\langle \mathcal{A}_l \rangle_i$ is the analyzing power calculated from the offset for cycle i .

The uncertainty on the analyzing power for each cycle ($\delta \langle \mathcal{A}_l \rangle_i$) is then calculated from the uncertainty on the photon cone offset ($\delta \Delta d$). The analyzing power uncertainty is worked out from the analyzing power fit as a function of offset ($\mathcal{A}_l(\Delta d)$), which can be seen in Fig. 5.8. The uncertainty on the analyzing power is calculated as the difference between the analyzing power mean and the analyzing power calculated with one standard error added to the offset with

$$\delta \langle \mathcal{A}_l \rangle_i = (\mathcal{A}_l)_i(\Delta c_i + \delta \Delta c_i) - (\mathcal{A}_l)_i(\Delta c_i). \quad (5.22)$$

With the analyzing power uncertainty in hand, the overall analyzing power uncertainty comes from error propagation of the weighted average as

$$\delta \langle \mathcal{A}_l \rangle = \frac{\sqrt{\sum_i w_i^2 (\delta \langle \mathcal{A}_l \rangle_i)^2}}{\sum_i w_i}. \quad (5.23)$$

The average analyzing power and uncertainty then for PREX-II is (16.599 ± 0.008) ppt or 0.05% relative uncertainty for the entire PREX-II analyzing power measurement.

CREX Photon Cone Offset

Initially the CREX photon cone offset studies followed the same procedure as was done for PREX-II. There are several spectrum runs taken throughout the CREX run period, both before and after the COVID-19 shutdown. The spectrum run circle plot can be seen in Fig. 5.10. While the circle fits do produce an average collimator central position, the presence of some notable outlier runs which did not have the offset within 1 mm of the average gives us doubt as to whether this method is going to be effective for the CREX data.

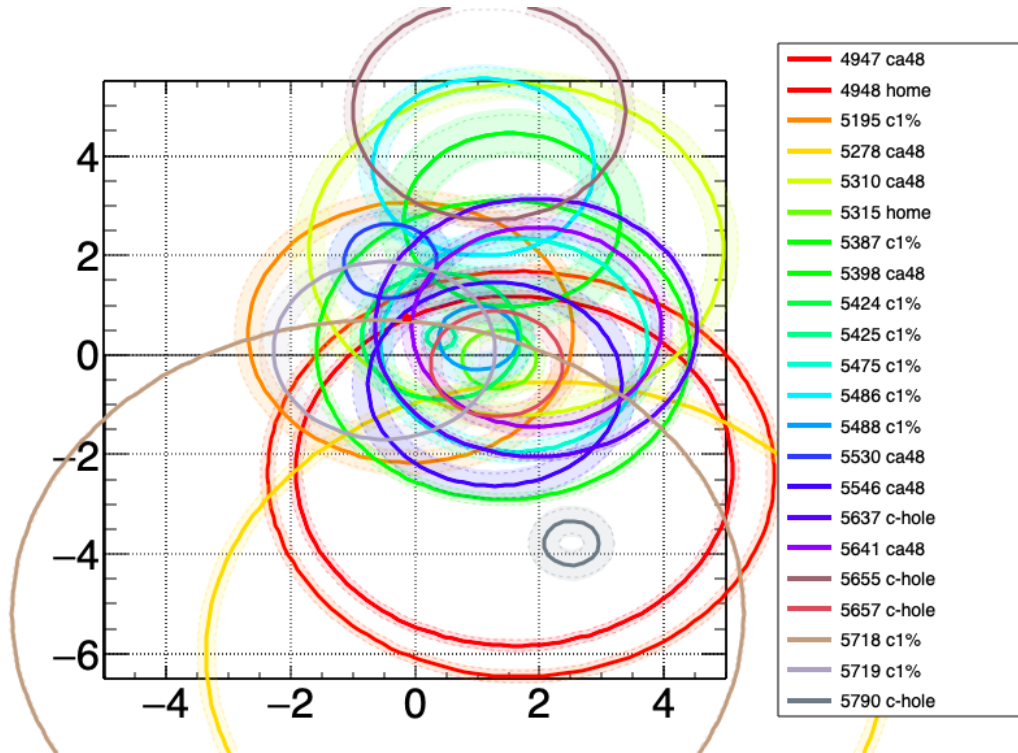


Figure 5.10: Circle plots for all CREX spectrum runs. Plot is produced in the same style as Fig. 5.10.

Due to constraints from the main experiment, the CREX beam pointing direction has a larger range of natural position drifts than during PREX-II. This, alongside the longer experimental run duration, increases the probability that small portions of the run are taken at high photon cone offset. After

analysis of the offset from the mean center position, the data suggested that the offset for the main Compton polarimetry data is, in certain periods, as high as 7 mm off the collimator center.

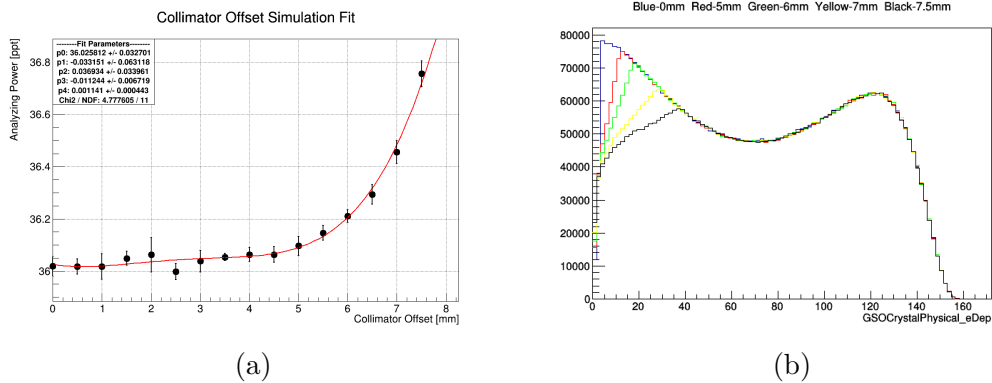


Figure 5.11: *Left*: Simulated CREX analyzing power as a function of photon cone offset. The analyzing power is well behaved until the offset reaches 5 mm, and then the analyzing power increases rapidly. *Right*: Simulated CREX spectra with offsets ranging between 6 mm and 7.5 mm. A no-offset spectrum is also included for comparison. The effect of the offset is most notable at low energies, with increasing threshold for greater offsets.

At 7 mm photon cone offset the effects of a changing analyzing power are pronounced. As seen in Fig. 5.11a, the change in analyzing power as a function of offset is negligible until the offset reaches about 5 mm when the difference between the offset and non-offset analyzing powers is 0.28% relative. At 6 mm the relative difference is 0.53%, at 7 mm the relative difference is 1.22%, and at 7.5 mm the relative difference is 2.05%. Typically CREX snails report asymmetries to 0.1% statistical precision, meaning that even a 0.5% change in measured asymmetry would be immediately noticeable and could be correlated to changes in the beam pointing angle in the chicane. There are no indications in the CREX data set that polarization changes of that size are even occurring, much less that they can be correlated to beam position changes.

Additionally, running with large photon cone offset produces increasingly large effects on the shape and integral of the Compton spectrum. The effect of large offsets on the CREX spectrum can be seen in Fig. 5.11b. With larger offset the relative rate of low energy Compton events decreases. A

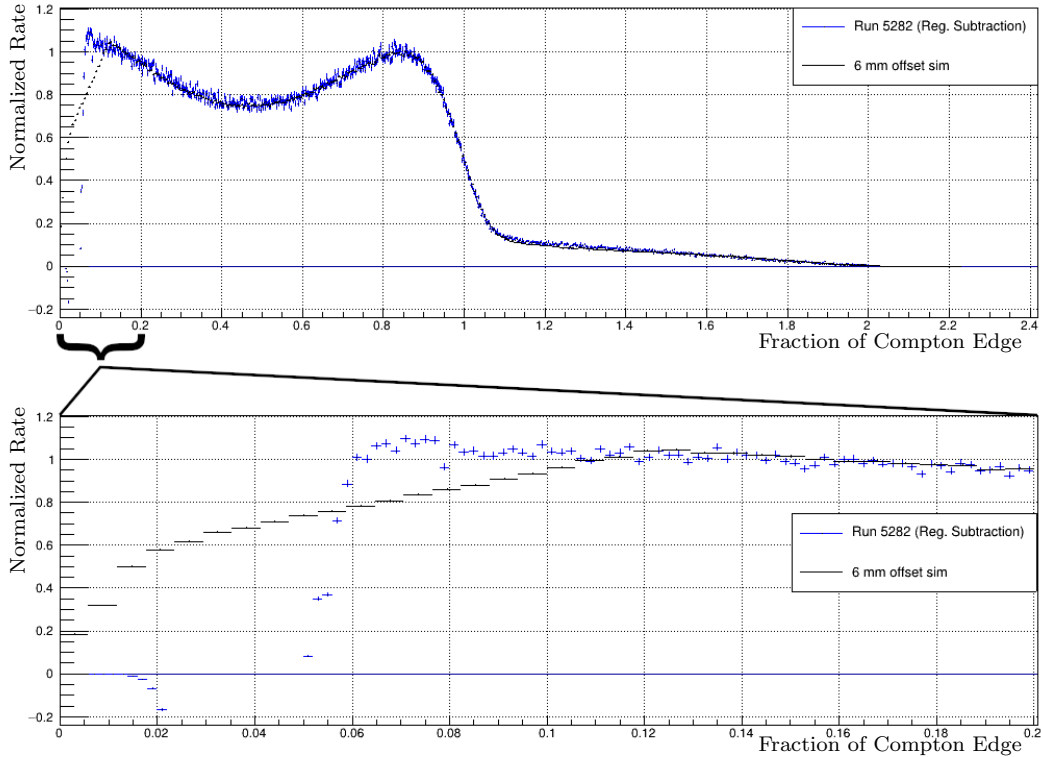


Figure 5.12: A comparison between the background-subtracted spectrum from a CREX Compton run which was predicted to have a 6 mm photon offset, and the normalized spectrum from an MC simulation with a 6 mm offset. Note that between 6% and 11% of the Compton edge, there is significant disagreement between the spectra shapes, suggesting the data spectrum has an offset less than 6 mm.

5 mm offset distorts the spectrum up to 8.7% of the Compton edge, while a 7.5 mm offset distorts the spectrum up to 25% of the Compton edge. The background peak from the CREX target affects the CREX production spectrum up to 10% of the Compton edge, above which the background contribution to the overall spectrum is negligible. This means that even without any background subtraction an offset of 7 mm or above should be immediately visible in the spectrum during normal CREX running. The spectrum was actively monitored by experimenters, and no such observations were made during the run period.

To further verify the correctness of the predicted photon cone offset, the CREX Compton data spectra are used to hunt for periods with high offset. One period that is predicted, using the spectrum run fit method of having an offset above 6 mm is run 5282. The beam positions during this one run match those taken from a spectrum run taken the previous day that measured a 6 mm offset. If the predicted offset is accurate then we should be able to see distortion in the Compton spectrum up to about 12% of the Compton edge. By finely calibrating the background subtraction the Compton spectrum behavior can be recovered down to as low as 7% of the Compton edge, meaning there is a small energy window in which the background subtraction would reveal distortion in the spectrum consistent with a 6 mm offset. It should be noted that background subtraction on a spectrum with the calcium target in is difficult to normalize below about 6% of the Compton edge. Above this energy the effect from normalization errors is small compared to the spectrum size, so 6% of the Compton edge is quoted as the minimum energy at which the background-subtracted spectrum is accurate. The background-subtracted spectrum from run 5282, as well as the spectrum of a 6 mm offset simulation can be seen in Fig. 5.12. A close look at the low energy region shows that the spectrum from data does not show the same distortion as the simulated spectrum, effectively ruling out the possibility that this run is taken with a 6 mm offset.

With a method to get a background-subtracted spectrum down to low energies, we are able to check other spectra throughout the experiment to verify that at no point can we find evidence that the photon cone offset is ever higher than 6 mm, despite the fact that the spectrum run fitting method suggested that is the case several times throughout the CREX experiment. To resolve this contradiction, a new method needs to be devised in order to limit the systematic uncertainty from the offset.

The new method begins by hypothesizing that a reasonable model of variability in photon cone offset would produce excessive statistical noise if the average offset were significant in analyzing power. This statistical noise is quantified with a χ^2 fit test for measured asymmetries of each laser cycle in a snail, and then again on the average asymmetries for each snail over the CREX run. The basic form of the χ^2 calculation is

$$\chi^2 = \sum_i^N \frac{(\mathcal{A}_{exp_i} - \langle \mathcal{A}_{exp} \rangle)^2}{(\delta \langle \mathcal{A}_{exp} \rangle_i)^2}, \quad (5.24)$$

where the sum over i can be taken over asymmetries in N cycles in a snail. This same formulation is also used to define a χ^2 using N snails over the experimental run, in that case with $\delta\mathcal{A}_i$ from the uncertainty of each snail.

If snail asymmetries are normally distributed over the mean, then χ^2 should be about the number of degrees of freedom $\chi^2 \simeq N - 1$. The first analysis of the CREX run (without an analyzing power correction) found $\chi_{exp}^2/(N - 1) = 1.3$. For individual snails the χ^2 average is much closer to 1, suggesting that any changes in the analyzing power have a time dependence that is not immediately observable over a few hours, but can be seen in the entire run data set. A statistical test is then used to see whether this increase in χ^2 is consistent with the expected distribution of collimator offset, and also if the average analyzing power could be changed by uncertainty in the offset without noticeable changes in χ^2 .

The new cross-check involved first taking the photon cone offset distribution from the CREX data and assuming the distribution is wrong by an overall factor R . Different values of R are then applied to the offset distribution, and then offset positions are selected from the modified distribution⁴. The randomly selected offsets are then treated as offsets per each run or cycle and turned into an average analyzing power representing those cycles or runs. The asymmetries calculated from this analyzing power could then be aggregated to produce simulated χ^2 for different degrees of statistics.

The results of such a simulation with $R = 1.1$ can be seen in Fig. 5.13. The simulation tracks χ^2 on two timescales: the first generated 10 simulated cycles (and associated asymmetries with a randomly selected photon cone offset) per snail and calculates the χ^2 per these simulated snails. The simulation then groups 100 snails together to form a “trial” (i.e., a simulated experimental run) and calculates χ^2 from snail asymmetry averages. The $R = 1.1$ and 10 cycles per snail simulation is particularly interesting because it is able to reproduce the overall snail χ^2 value from the CREX Compton data $\chi^2/(N - 1) = 1.3$. the simulation suggests then that an average uncertainty of 0.2% on the analyzing power is enough to explain the excess χ^2 for the entire CREX run.

There are two aspects of the main CREX Compton data the simulation must take into account for it to have predictive power for actual Compton data. The first of these is the rate of change of beam position in the chicane. If the beam pointing direction is unstable enough that there are measurable

⁴Simulations with different R and also with different time periods were considered.

changes in photon cone offset over the course of one CODA run then the χ^2 per snail is much larger than if the change is imperceptible on the time scale of a CODA run⁵. The time dependence of the offset is tracked through the CREX run which reveals that the offset could change measurably over the course of a single day, or if there was an interlude in running in which the beam has to be reconfigured to run through the chicane again. Thus, we conclude that it is appropriate to use the offset distribution from the run as a random distribution, as it does model the variance in offset for snails.

The second aspect that must be accounted for is the amount of simulated cycles to use per snail. If the number of cycles in a snail is high, then the snail asymmetry calculation is less susceptible to individual cycles with high photon cone offset decreasing the polarization average. Thus we observe, if the simulation is run with 100 simulated cycles per snail the snail χ^2 does not change measurably from statistics. However, we felt confident using a small number of cycles per snail, consistent with the model that changes in collimator offset take place on an hour timescale rather than a few minute

⁵For CREX each CODA run was approximately 2 hours, and 10-50 good cycles.

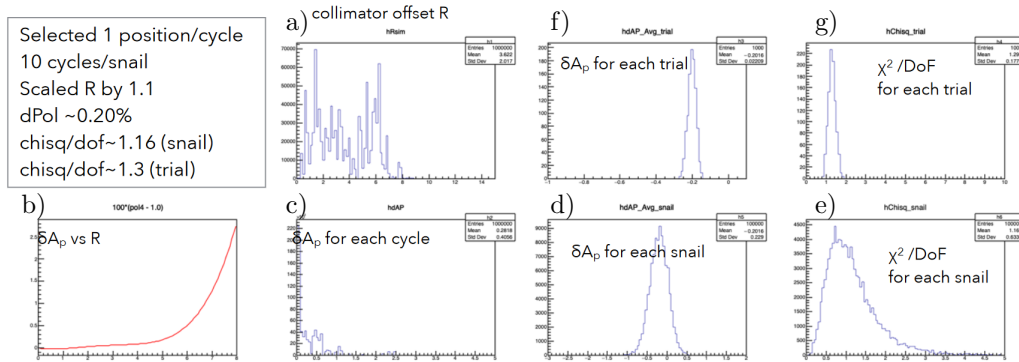


Figure 5.13: Plots from a rudimentary simulation which measured the change in analyzing power by randomly selecting photon cone offsets to determine a the change in asymmetry in snails and cycles. Plots are, as labeled: a) the offset distribution used, b) analyzing power as a function of offset (from Fig. 5.13), c) distribution of cycle analyzing power change from offset, d) change in asymmetry from offset per snail of 10 cycles, e) χ^2 distribution of snails, f) change in asymmetry from offset in the entire trial of 100 snails, g) χ^2 distribution of trials.

timescale. While offset is liable to change with each new beam tune, the offset during running is comparably stable from cycle to cycle. Thus the offset random distribution used in the simulation is appropriate for modeling run-to-run changes in analyzing power. And because there are fewer CODA runs in each snail, a smaller number of statistics per snail is valid.

The result of this study is that because a 0.20% uncertainty on the analyzing power is sufficient to explain the statistical instability seen in the CREX Compton data, we can assign 0.20% as the uncertainty on the CREX analyzing power.

5.6.2 Laser Polarization & Optical Model

Now with laser polarization data from the different tests performed for both experiments (which are discussed in Sec. 4.3.1 and Sec. 5.5), the entrance function, birefringence, and time-dependence of the laser DOCP are measured for different QWP and HWP settings. For the entrance function, the contribution to the uncertainty on the cavity DOCP from the optical properties of the entrance line components is less than 0.1% relative, so for the PREX-II DOCP measurement an uncertainty of 0.1% from fit parameters is applied.

For CREX running this uncertainty formulation is more complicated. The entrance function measured for CREX has two solutions, resulting in two possible solutions for the cavity birefringence. The two solutions can be seen in Fig. 5.14. The χ^2 values for each solution are approximately equal, meaning the fits from each solution matched the polarimetry data equally well. In principle enough experimental running at <100% DOCP would have produced a number of data points for the fits that could have constrained the fits further, however the amount of <100% DOCP running the Compton was able to perform was limited by time. As a result two values for “nominal” DOCP (that is to say the DOCP the majority of the CREX was run at) exist: $0.9999 \pm 0.03\%$ from solution 1 or $0.9974 \pm 0.26\%$ from solution 2. With no clear way to distinguish between the validity of either solution, both are incorporated into the DOCP calculation. The decision was made to combine the uncertainty range from solution 1 and solution 2 for each QWP/HWP setting, and to use the median value of that range to as the cavity DOCP. Thus for CREX the uncertainty from fit parameters is determined to be 0.26% relative for nominal DOCP running.

The data from the scans of the exit line DOCP help constrain the time-

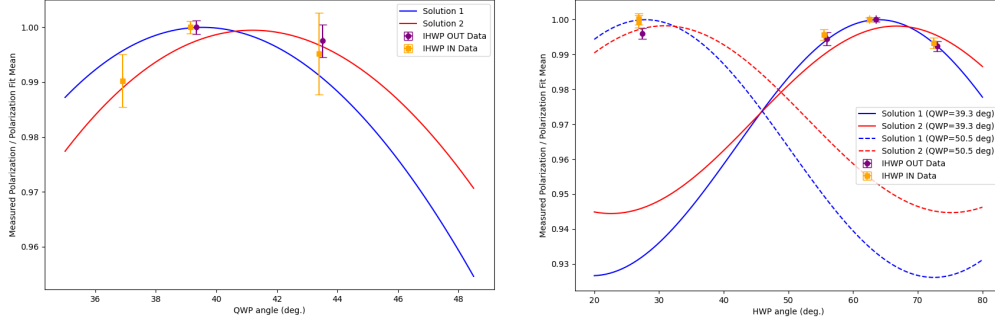


Figure 5.14: Both solutions of the CREX laser DOCP model. The plots on the left plot the measured beam polarization vs QWP angle with HWP angle fixed at 65° , and the plots on the right plot the measured beam polarization vs the HWP angle with QWP angle held at either 39.3° or 50.5° . The points on the plot are taken from the CREX Compton photon data, and represent the average polarization measured at each wave plate setting. The plotted curves are from the parameterized entrance function.

dependence of cavity DOCP in both experiments. Once the parameters of the transfer function are fitted, the time-dependence of cavity DOCP is linked to the time-dependence of exit line DOCP. The calculated Stokes parameters on the exit line are used to infer the birefringence parameters of the cavity, of which there were three: two polarization rotation angles θ and η and a phase difference δ . In addition the birefringence parameters of the cavity are used in an optical model to correlate the size of the power reflected back to the cavity when locked to the cavity DOCP. By solving for both cavity DOCP and exit line DOCP as a function of these angles and reflected power, then it can be directly translated into a cavity DOCP measurement. And most importantly, we can use the variation in exit line DOCP measurement directly then to track, through the cavity birefringence parameters, the change in cavity DOCP as a function of time.

The optical model solution for different values of the cavity phase offset parameter δ for PREX-II is shown in Fig. 5.15. For PREX-II data, this measurement is complicated by the observation that for most of the exit line DOCP recorded during experimental running, the cavity DOCP function is double-valued⁶. In order to distinguish laser polarizations the reflected power

⁶e.g., if the exit line polarization is recorded as 0.97, this could, according to the model,

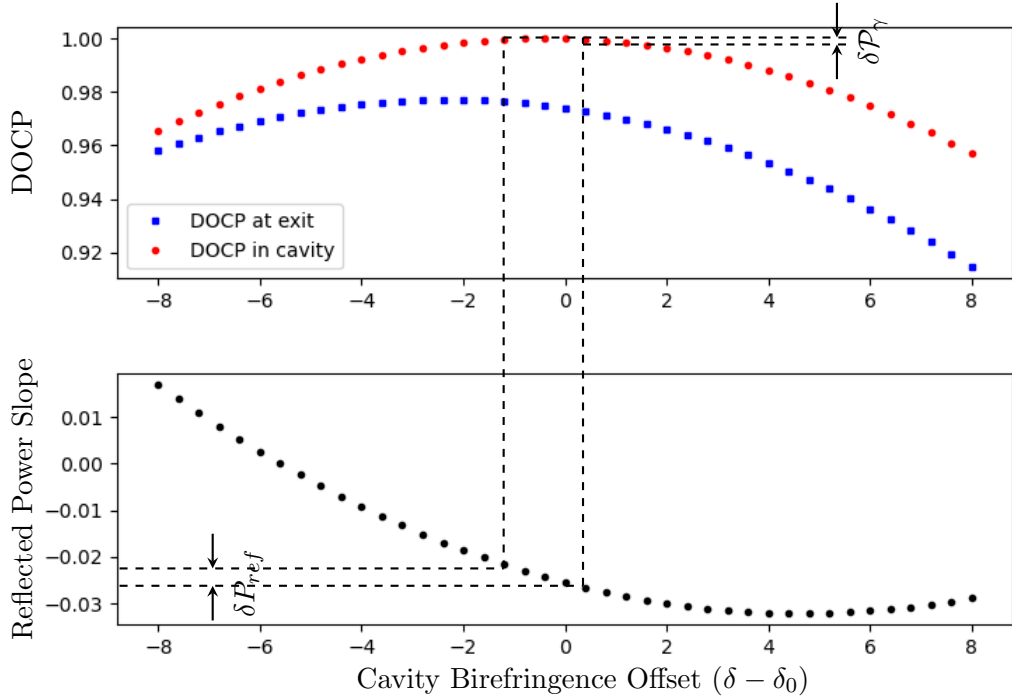


Figure 5.15: A visualization of the measurement of the cavity DOCP uncertainty for PREX-II data. Uncertainty is first gauged by looking at the range of values of the reflected power normalized to cavity power δP_{ref} . This range can then, through the phase offset cavity parameter be mapped onto a range of laser polarizations from which we extract $\delta \mathcal{P}_\gamma$.

measurement is used. The slope of the reflected power as a function of locked cavity power is tracked throughout all PREX-II and a range of slopes have been observed. Because the slope to δ function is single-valued over the range of slopes observed, it is used to find a range of cavity DOCP over the course of the experiment. It should also be noted that while the reflected power function becomes double-valued at high values of the offset $\delta - \delta_0$ these are excluded because there were no observations that the exit line DOCP had ever been low enough to suggest these values were part of the run conditions. The result is a contribution to the uncertainty $\delta \mathcal{P}_\gamma$ of 0.12%.

The functions of DOCP (in both the cavity and exit line) for the rotation

have $\delta - \delta_0 \approx -5.5$ or $\delta - \delta_0 \approx 1.0$. Without a way of distinguishing the two states the cavity DOCP uncertainty could be on the order of 2%.

angles η and θ are also used. The value of the reflected power slope in these cases is not necessary to constrain the DOCP function of exit line DOCP as the function is single-valued for the range of interest for PREX-II. The DOCP as a function of θ suggests an uncertainty on $\delta\mathcal{P}_\gamma$ of 0.03% while the DOCP does not depend on the variation of the angle η at all. Thus, the contribution to the uncertainty $\delta\mathcal{P}_\gamma$ from time-dependent effects in PREX-II is limited to 0.12% at most.

For CREX the primary complication with the estimation of uncertainty contribution from time-dependent effects is from having two solutions for the cavity optical model. However, as before, the uncertainty is estimated from the full uncertainty range of both solutions combined. Additionally, the cavity DOCP uncertainty over the observed range of exit line DOCP is negligible for the first solution, meaning that the second solution determines the uncertainty. It was found that the exit line DOCP varied by no more than 0.1% throughout CREX, which translates to an uncertainty contribution to $\delta\mathcal{P}_\gamma$ of 0.05%.

To estimate the uncertainty on the cavity polarization model itself (after all uncertainties on parameters are quantified and included) residuals are calculated between the cavity polarization model and the measurements of DOCP taken with the cavity open. Because the DOCP measurement grows more sensitive the further away from 100% the measurements are taken, the residuals themselves are a function of the cavity DOCP. To limit this consideration, the residuals for the PREX-II model are only considered with DOCP >0.98 because the vast majority of PREX-II running was taken with DOCP above this threshold. For CREX running, because all laser polarization settings were above 0.99 DOCP, 0.99 was the residuals threshold. For both experiments the largest residuals of any open-cavity measurement are just above 0.3% contribution to $\delta\mathcal{P}_\gamma$.

Finally, the effect of birefringence of the cavity mirrors is taken into account. While the transfer function takes into account the polarization direction change due to the cavity mirrors, the depolarizing effect of the mirror substrate itself (which the laser would have to pass through to enter and exit the cavity) factors into the cavity DOCP measurement. Fortunately, measurements of the cavity mirror substrate birefringence were conducted for the PREX-I and are reported in Rakhman et al. [83] to contribute $<0.1\%$ to $\delta\mathcal{P}_\gamma$.

The total uncertainties on the laser DOCP for each experiment are reported in table 5.4. It should be noted that because the mean value of laser

| Source | Experiment | |
|-------------------------|--------------|--------------|
| | PREX-II | CREX |
| Fit Parameters | 0.10% | 0.26% |
| Time Dependence | 0.12% | 0.05% |
| Substrate Birefringence | 0.10% | 0.10% |
| Model Residuals | 0.33% | 0.34% |
| Total | 0.38% | 0.44% |

Table 5.5: Sources of systematic error for the laser DOCP \mathcal{P}_γ and their relative values.

DOCP is not constant for all run periods in both experiments, all measured asymmetries are normalized to the laser DOCP based on the QWP and HWP settings it was taken with. However, because the laser DOCP provides no statistical uncertainty on the measurement, the uncertainty is applied globally to the run-averaged asymmetry, which will be discussed in Sec. 5.7.

5.6.3 Detector Corrections

During experimental running the photon detector is powered from a high voltage source which can be toggled on and off remotely⁷. PREX-II and CREX used different PMTs and bases which are operated at different voltages. The correct voltage at which to run each PMT are determined at the start of each experimental run, and are not changed for either experiment. The chosen PMT voltages are sufficient to produce a measurable signal above background in both experiments for the entire experimental run.

The choice of PMT voltage is important as the two primary sources of uncertainty in the Compton photon detector—the PMT nonlinearity and the gain shift—are dependent on the PMT gain. Running with as few different voltages as possible simplifies the corrections needed for each experiment and shortens the time necessary to measure them. Both the measurements of nonlinearity and gain shift used the *in situ* LED pulser system are described in Sec. 4.4.3. A description of the two major systematic effects arising from the photon detector are provided in this section as well as the measurements of their contribution to both the PREX-II and CREX systematic uncertainty.

⁷As described in Sec. 4.3.2, the high voltage systems used during PREX-II and CREX are different, however the effect of the voltage control was overall the same.

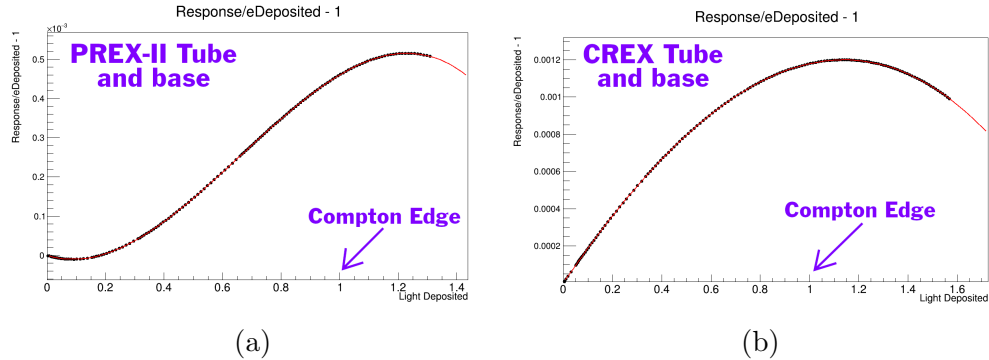


Figure 5.16: The nonlinearity functions for (a) PREX-II and (b) CREX plotted as a function of light deposited I (scaled such that the Compton edge gives $I = 1$).

Nonlinearity

The detector nonlinearity function $\epsilon(\rho) = \frac{Y(I)}{I}$ can be found defined in full in Eqn. 4.45. Determining the nonlinearity function requires measuring the polynomial fit coefficients $c_1 \dots c_m$ for all LED brightness settings I covering the detector response range observed in experimental running.

The exact function of the pulser system is described in detail in Sec. 4.4.3. The pulser works by flashing two LEDs in a 250 Hz sequence. One LED, the “variable” with brightness V , slowly decreases in brightness with each sequence before resetting to a pre-programmed maximum brightness again, while the second LED, the “delta” with brightness Δ , shines at the same brightness throughout running. Once enough detector statistics are gathered, the detector response as a function of both delta and variable brightness minus the variable brightness (i.e., $Y(V + \Delta) - Y(V)$) is plotted and fit. From this fit the coefficients $c_1 \dots c_m$ for an m -degree polynomial fit are extracted. Electronic cross-talk is accounted for by running with a “dark delta” LED to isolate the effects of running the delta electronics. Thermal effects are controlled for by using a “load” LED which mimicked the size of the experimental Compton signal by shining at a very low but constant brightness.

The nonlinearity function $\epsilon(\rho)$ can conceptually be thought of as the deviation of the integral of a pulse of energy ρ from the expected proportional PMT response. For a perfectly linear system $\epsilon(\rho) = 1$. With nonlinear systems, the nonlinearity is expressed in terms of the fit coefficients $c_1 \dots c_m$

as

$$\epsilon(\rho) = 1 + c_1\rho + c_2\rho^2 + \dots + c_m\rho^m, \quad (5.25)$$

where for both PREX-II and CREX a polynomial fit degree of $m = 3$ was sufficient to accurately characterize the nonlinearity for the entire Compton energy range.

The nonlinearity measurements are corrected for the effect of electrical cross-talk during the experiment. The information to create this correction is gathered during the dark delta linearity tests. In this test, the delta electrical signal is sent to an LED on the outside of photon detector, which could mimic the electrical signal of the delta LED without depositing light on the detector. In these tests then ideally $Y(V + \Delta) = Y(V)$ because the only the variable LED is depositing any light on the detector. In practice, the cross-talk from the delta LED signal can change the response of the variable LED meaning that any observed deviation of $Y(V + \Delta) - Y(V)$ from zero is due to cross-talk. Thus fitting the dark delta PMT response function with a polynomial of sufficient degree gives the correction factors which can be applied to the two-LED PMT response function before fitting.

The nonlinearity functions for both experiments can be seen in Fig. 5.16. With parameters of the nonlinearity function, the corrected analyzing power (originally defined in Eqn. 4.25) is applied by specifying the detector response function as

$$\langle \mathcal{A}_l \rangle \simeq \frac{\int_0^1 d\rho \mathcal{A}_c \rho (1 + c_1\rho + c_2\rho^2 + c_3\rho^3) \frac{d\sigma}{d\rho}}{\int_0^1 d\rho \rho (1 + c_1\rho + c_2\rho^2 + c_3\rho^3) \frac{d\sigma}{d\rho}}. \quad (5.26)$$

The nonlinearity-corrected analyzing power is then calculated and compared to the analyzing power without nonlinearity correction which is obtained by performing the above integration with $c_1 = c_2 = c_3 = 0$. For the PREX-II PMT, this correction is 0.08% of the analyzing power while for CREX it is 0.02%. Neither of these are leading sources of uncertainty for either experiment which is to be expected as PMTs are specifically chosen for each experiment based on low nonlinearity in the correct energy region.

Gain Shift

Early nonlinearity tests with the PREX-II PMT taken in Hall A with and without the load LED active indicate that the PMT gain might be itself dependent on the incident light intensity of the PMT. The evidence for this effect is that while both the pulser and the beam were running, the delta

LED appears to have a lower pulse integral while the laser is locked than while it is unlocked. This is despite the fact that for each experiment the delta LED brightness is never changed. This “gain shift,” if confirmed, affects the background subtraction which was part of the Compton asymmetry calculation.

The primary parameter to describe gain shift is the relative change in pulse size α with

$$\alpha = \frac{\Delta_{ON} - \Delta_{OFF}}{\Delta_{ON}}, \quad (5.27)$$

where Δ_{ON} is the integrated pulse size of the delta LED with laser on, and Δ_{OFF} is the same but for laser off. The corrected asymmetry can then be written as

$$\langle \mathcal{A}_{corr} \rangle = \frac{\langle \mathcal{A}_{exp} \rangle + \alpha f D_{OFF}}{1 + \alpha f Y_{OFF}}, \quad (5.28)$$

where f is defined as

$$f \equiv \frac{1}{Y_{ON} - Y_{OFF}}. \quad (5.29)$$

A gain shift test was conducted on the PREX-II tube after the PREX-II experimental run. The procedure for the test is:

1. With the PMT and powered with the same HV supply and voltage used during the experiment, increase the load LED until the PMT response is roughly equivalent to the laser-on signal size.
2. Activate the pulser system and flash both LEDs at a constant brightness. The selected brightness for each LED may be arbitrary.
3. Record the Compton PMT signal for each LED pulse. While recording alternately flip the load LED on and off after each minute.
4. Once enough statistics are collected, find the difference between the mean pulse integral for LED pulses with the load LED on and the load LED off. Calculate α from these integrals.
5. Repeat the process with the load LED brightness reduced. Continue dimming the load LED to measure enough brightnesses in the detector response range to fit.

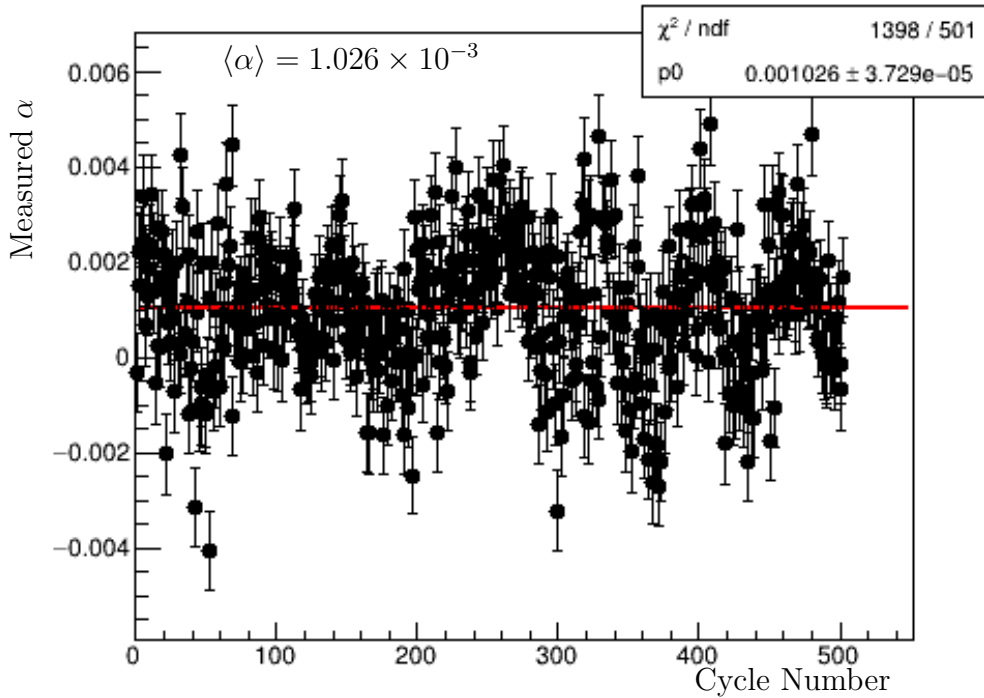


Figure 5.17: Compton PMT data with ≈ 500 load LED cycles. Plotted is the difference in delta LED pulse size between load LED states. The particular data shown here was taken with $Y_{ON} - Y_{OFF}$ approximately equal to the PREX-II average, so $\langle \alpha \rangle$ is close to the overall correction for the entire experimental run.

Once all measurements are taken, values of α are plotted as a function of $Y_{ON} - Y_{OFF}$ and fit. A linear fit function is sufficient to characterize α for all signal sizes. In principle, the intercept of this linear fit should be zero as there cannot be any gain shift without a change in background signal. However, for PREX-II gain shift tests this is not required as the gain shift measurement do not need a comparison with beam off data.

An example of the data from one gain shift run can be seen in Fig. 5.17. The data shown has ≈ 500 cycles in which the delta LED PMT response is compared between load on and load off intervals. The average α measured is compared with other runs at different load LED intensities and fit. The

fit parameters are then included to calculate α dynamically in the photon analysis to correct the photon asymmetry per laser cycle. For PREX-II the average relative correction to the asymmetry is 0.22%.

We were unable to directly measure the CREX tube for gain shift due to a malfunction in the pulser system. So instead, the gain shift calculation is determined from pulser running that was taken during the CREX experimental run. As for PREX-II the gain shift data are taken from the delta LED pulse size, however for CREX the laser cycling system is used instead of the load LED. A full fit of α as a function of $Y_{ON} - Y_{OFF}$ is not possible as the LED system cannot be used at different Compton signal size. In lieu of a full cycle-to-cycle correction, the decision was made to instead limit the uncertainty from gain shift by scaling α to the highest value of $Y_{ON} - Y_{OFF}$ seen during the CREX experiment, and use the size of the potential correction as the uncertainty from gain shift.

During running the highest scaled value of gain shift is $\alpha = 0.01246$. This corresponds to a 0.15% correction on the asymmetry. The correction on the asymmetry is smaller for CREX than it was for PREX-II despite the fact that the measured gain shift is larger. This is due to the fact that CREX has a much higher signal-to-noise ratio, meaning that the uncertainty due to background subtraction is much less sensitive to a mismeasurement than it would have been in PREX-II.

5.6.4 Beam Kinematics

Because the calculation of analyzing power $\langle \mathcal{A}_l \rangle$ is dependent on the beam energy E the precision of the measurement of beam energy will add to the uncertainty on the analyzing power. The beam energy is measured by observing the beam position along the arc on the beamline heading into Hall A after the steering dipoles, from which the beam kinematics can be extracted. For PREX-II beam energy is $E = 953.4 \pm 1.0$ MeV while for CREX the beam energy is was $E = 2182.2 \pm 1.1$ MeV. For PREX-II this is a relative uncertainty on the analyzing power (and directly on the measured asymmetries) of 0.1% while for CREX the uncertainty contribution from beam energy is 0.05%.

The beam energy is also used to correct the analyzing power as the simulations to determine the analyzing power were performed before experimental running using the assumed beam energy. The difference between the assumed beam energy and the actual measurement is on the order of $\tilde{1}$ MeV indicating

the correction is small enough to be calculated using a numerical calculation of Eqn. 4.25.

Radiative corrections defined in Sec. 4.2 are also applied to asymmetries in both experiments. However, because the kinematics to the corrections are well-defined and understood the systematic uncertainty contribution from these corrections is negligible.

5.7 CREX Compton Result

Once Compton photon asymmetries are calculated for each laser cycle, cycles are grouped together into snails each with the same IHWP state. Snail polarizations are taken from the statistically-weighted average of cycle polarization. During the experimental run, the snail polarization averages revealed that the magnitude of beam polarization was slowly decreasing. This decrease was highly correlated with the decreasing quantum efficiency of the polarized source. This effect had been observed in polarized beam experiments at JLab before. To mitigate the decreasing polarization accelerator operators first moved the laser spot location on the polarized source. This recovered the magnitude of beam polarization but as the quantum efficiency decreased again so did the beam polarization keep decreasing. After the restart from the summer shutdown the decreasing polarization was no longer observed during the final phase of the CREX run. The measured snail polarizations can be seen in Fig. 5.18.

To find the polarization averaged over the experiment the time-dependence is accounted for in the choice of averaging method. In addition, when averaging the data for the entire CREX Compton run, the snail polarizations is weighted by the statistical precision of the main experiment data taken during, or around the same time as each Compton data point. This presents a challenge as the main experiment data is aggregated in periods that do not always line up neatly with the Compton snails. To solve this three methods to calculate the CREX Compton polarization average are used and their consistency evaluated:

Escargatoire Average

Snails are grouped together into periods called “escargatoires.” Escargatoires are constructed such that each escargatoire:

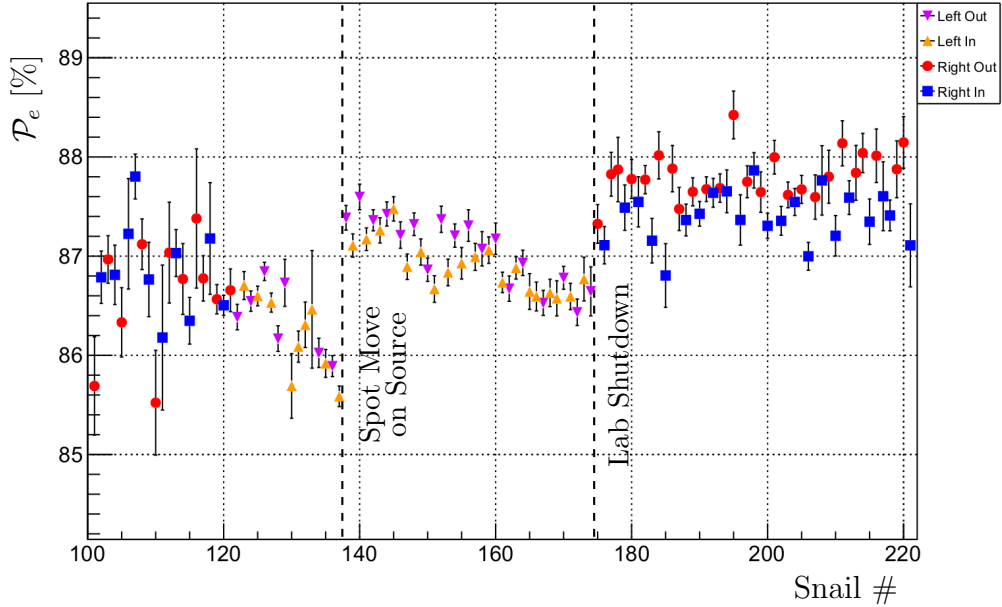


Figure 5.18: Polarization measurement for each of the CREX snails, corrected for laser DOCP, and separated by wien angle state and IHWP state. The time dependence of the polarization can be seen most prominently between snails 120 and 180. Two major changes in beam configuration are marked: first, the laser spot move on the polarized source in the injector and second, the lab shutdown for most of spring and summer 2020.

- should have approximately equal statistical precision as every other
- must have a start time and an end time such that the periods from the main experiment data and the Compton data can be matched exactly without data needing to be split further
- must only have data from each IHWP and wien state, and the data must be taken within three days of each other

The entire CREX Compton run (consisting of 121 snails) is grouped into 43 escargatoires. The polarization average is calculated internally in each escargatoire using a statistically weighted average of cycle polarizations with the same procedure discussed in Sec. 5.2.3.

However, the average polarization of the entire run is computed with a slightly different weighting which used the parity-violating asymmetry uncertainty for the run period matching the escargatoire by

$$w_i = \frac{1}{(\delta\mathcal{A}_{PV})_i^2}. \quad (5.30)$$

This is done because the primary driver of the changing beam polarization is the dropping quantum efficiency on the source, which is itself driven by the beam current draw from the source. Since the main experiment ran even more reliably than the Compton, the main experiment periodic statistical precision serves as a proxy for current draw on the source. With this weighting any losses of Compton statistical precision (due possibly to beam instability leading to cuts, or technical issues preventing Compton running) do not de-weight any parts of the Compton measurement more heavily than others, and do not affect the overall run average.

Once grouped together the escargatoire average yields a CREX Compton polarization of 87.118% with 0.021% relative statistical uncertainty. The statistical precision for each laser cycle is calculated from Eqn. 5.11, and aggregated for each escargatoire and over the run period with Eqn. 5.30.

Piecewise Fit Average

In order to characterize the time-dependence of the polarization, the CREX Compton data is divided up into five “pieces” which are fit linearly. Piece 1 comprises the first right wien period. Piece 2 is the left wien period from when it started up to the laser spot move on the source. Piece 3 is the remainder of the left wien period until the lab shutdown. Piece 4 includes just two snails that were taken just after the accelerator began running again but had not yet reached a steady state. Piece 5 was the remainder of the last right wien period. Once the pieces are fit, the average polarization is calculated by evaluating the fit for each piece at the time each escargatoire is taken, and then taking a weighted average of each piece. Different IHWP states are fit separately, as the PREX-II polarization data demonstrates that the IHWP state can affect the magnitude of polarization if the vacuum window in the injector is birefringent.

The challenge in applying a linear fit to the pieces with observable time-dependence of polarization is that without adjustment, the two fit parameters (intercept and slope) are correlated. The sensitivity of the determination

of the intercept parameter to the determination of the slope parameter is dependent on the mean position of the escargatoire data in the piece on the x-axis. To remove this correlation entirely fits are done on piece 2 and piece 3 with the entire CREX Compton data shifted on the x-axis such that the fit is taken around the mean time of each piece. This fit yields a slope parameter for each piece that is completely uncorrelated from intercept. In addition when fitting for slope, the data is not separated by IHWP state because the IHWP cannot affect the rate of change of polarization.

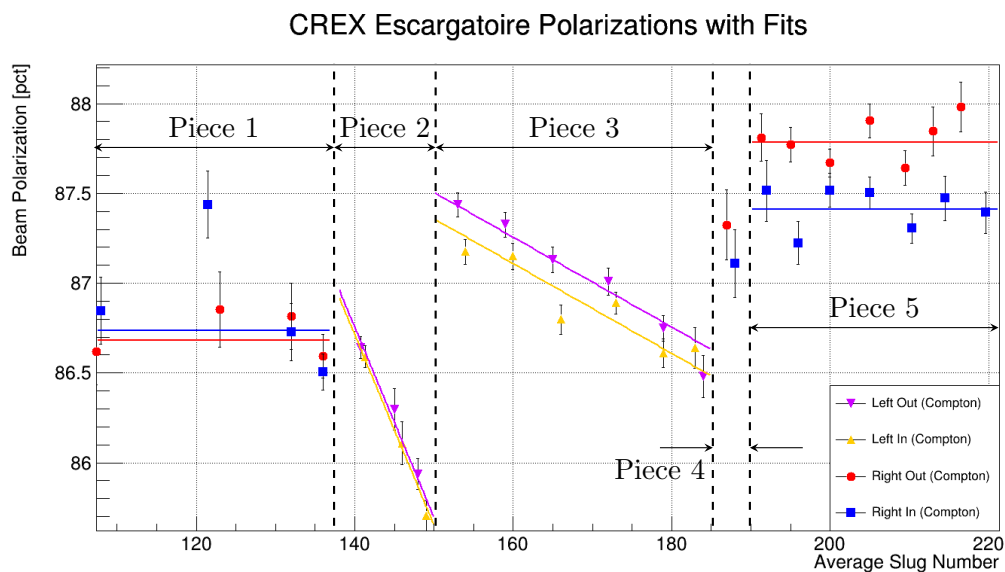


Figure 5.19: CREX polarization averages grouped by escargatoire. The run is divided up into 5 pieces which are linearly fit except for piece 4 which is short. The x-axis is proportional to current draw off the polarized source, the primary cause of the decaying quantum efficiency.

With the slope parameters obtained the escargatoire polarization averages are subtracted by the slope parameter times the average slug number to get data from each piece distributed around the intercept with no time-dependence. The mean of this data (again separated by IHWP state) is the intercept.

The fits to the Compton escargatoire polarizations can be seen in Fig. 5.19. There are five pieces, of which four are fit. There are eight fits in total plus the two snail polarizations in piece 4. The time-dependent fits in

piece 2 and piece 3 were each evaluated at the weighted mean slug number of the escargatoires in the piece. The result is two polarization averages per piece which are used to calculate the average for the entire CREX run. The weights for the average are, like before, the statistical precision of the main experiment asymmetry measured during each piece. The result is a polarization mean of 87.119% with 0.018% relative statistical uncertainty.

Mini-Escargatoire Average

In order to understand if there are other time-dependent effects on the polarization besides the decreasing quantum efficiency of the source, the CREX Compton data is grouped into “mini-escargatoires.” Mini-escargatoires differed from regular escargatoires in that no requirement of polarization statistics is imposed. In short, mini-escargatoires are constructed by using the minimum necessary grouping of CREX Compton data: grouping snails together only if it is necessary to match the start and stop times of slugs taken at the same time.

This results in 95 mini-escargatoires being formed. The average polarization and uncertainty is obtained with the same calculation used to get the escargatoire polarization average. The average polarization by this method is 87.104% with 0.022% relative statistical uncertainty.

CREX Compton Averages

The three different models of CREX polarization time dependence are compared and found to agree with each other to a high degree of accuracy. The mean polarization and statistical uncertainty for each model can be seen summarized in table 5.6. The weighted mean of the three models comes out to 87.115% polarization. The statistical uncertainty on each model calculation is on the order of 0.02%, so an overall statistical uncertainty of 0.02% is applied to the mean.

The uncertainties for the CREX measurement can be seen summarized in table 5.7. The only corrections that are applied to the CREX asymmetries are laser polarization (in that \mathcal{P}_γ normalized all experiment asymmetries), the beam energy correction to the analyzing power, and the radiative corrections to the measured asymmetries. The data is not corrected for gain shift and photon cone offset, as the precise value of the correction could not be obtained for either effect. Instead the uncertainty is taken from the maximum possible

| Method | Polarization Mean | Rel. Uncert. |
|---------------------------|--------------------------|---------------------|
| Escargatoire Average | 87.118% | 0.021% |
| Piecewise Fits | 87.119% | 0.018% |
| Mini-Escargatoire Average | 87.104% | 0.022% |
| Total Average | 87.115% | 0.020% |

Table 5.6: Average and uncertainty of the CREX polarization for all three different methods. All three averages are within uncertainty of each other and therefore the uncertainty from the choice of model for time-dependence is negligible.

magnitude of the effect from the Compton data. The plots of Compton asymmetries for each snail, as well as additional information about the CREX running conditions can be found in Appendix B.

| Source | Rel. Correction | Uncertainty Contribution |
|----------------------|------------------------|---------------------------------|
| Laser DOCP | 0.29% | 0.45% |
| Photon Cone Offset | - | 0.20% |
| Gain Shift | - | 0.15% |
| Beam Energy | 0.103% | 0.05% |
| Nonlinearity | - | 0.02% |
| Model | - | 0.02% |
| Radiative Correction | 0.3% | - |
| <i>Statistics</i> | - | <i>0.02%</i> |
| Total | - | 0.52% |

Table 5.7: Uncertainty table for CREX Compton measurement. All uncertainties quoted here are relative.

For CREX the Compton polarimeter measurement found that $\mathcal{P}_e^{Compton} = (87.115 \pm 0.453)\%$ which is 0.52% relative uncertainty. This is remarkable because this stands as one of the most accurate Compton polarimetry measurements of an electron beam ever made. Other Compton beam polarimetry measurements can be seen in table 5.8. The CREX precision ties the reported precision of the 1997-98 run period at SLAC's SLD program. The JLab Hall A polarimeter used for PREX-II and CREX had been used before for multiple experiments with only HAPPEX-III reporting a polarization uncertainty below 1%.

| Year | Facility | Experiment | $\delta\mathcal{P}_e/\mathcal{P}_e$ | Citation |
|-------------|--------------------|-------------------|-------------------------------------|-----------------|
| 1997/98 | SLAC | SLD | 0.52% | [96] |
| 2008 | MAMI | A4 | 2.4%* | [97, 98] |
| 2009 | JLab Hall A | HAPPEX-III | 0.96% | [35] |
| 2010 | JLab Hall A | PREX-I | 1.13% | [36] |
| 2013/14 | JLab Hall C | QWeak | 0.59% | [87] |
| 2016 | JLab Hall A | DVCS | 2.78% | [99] |
| <i>2020</i> | <i>JLab Hall A</i> | <i>CREX</i> | <i>0.52%</i> | |

Table 5.8: Comparison of the overall uncertainty precision on recent Compton polarimetry reported results.

*Statistical uncertainty only

The increase in precision observed during CREX compared to other Hall A experiments is due in part to the improvements to beam and apparatus control during experimental running. The HAPPEX-III Compton polarization measurement systematics is dominated by contribution from the laser DOCP determination [80]. For CREX this is significantly less of a factor because of the upgrades to the Compton laser system which introduced the QWP/HWP entrance function reducing uncertainty due to vacuum window birefringence. The uncertainty contribution due to PMT nonlinearity and from gain shift is lower in part due to the selection of PMT but also due to CREX’s general insensitivity to pedestal uncertainty. Additionally, the CREX Compton signal-to-background ratio is high enough, and the CREX Compton runs precise enough to enable deeper investigations of systematic uncertainty sources than had been done before on this device.

5.7.1 CREX Møller Result

The Møller polarimeter is used in concert with the Compton to measure the beam polarization. Because the Møller polarimeter runs are invasive, special times during the experimental run are allocated for Møller runs. A single Møller run for polarization takes ≈ 8 hours including the time for the accelerator operators to engage the Møller configuration and to return to the experimental configuration.

The Møller polarization measurements can be seen in Fig. 5.20. There are nine measurements in total. A single Møller measurement consists of two

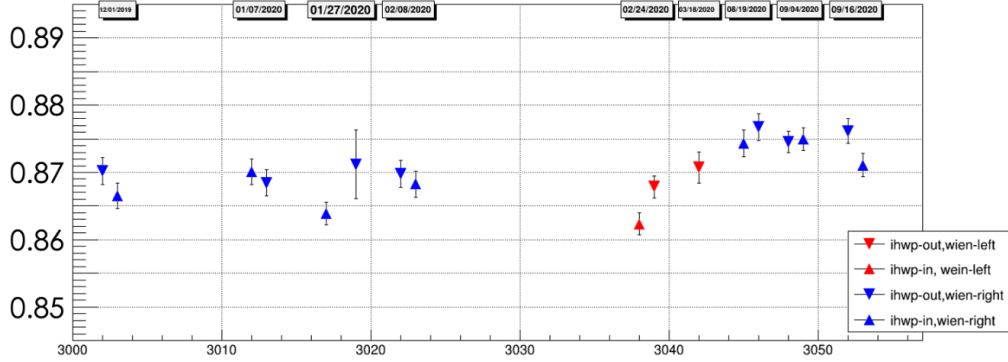


Figure 5.20: Plot of the Moller polarization measurements separated by wien and IHWP state, and marked by date taken.

reported values: the reported polarization in each IHWP state. This is the case for every Møller measurement except the one taken on March 18th. Due to technical issues with one of the Møller magnets, several polarization measurements were aborted before any polarimetry data could be obtained. The magnet issue affects Møller measurements mostly taken during the wien left period in CREX running, hence the low number of wien left measurements in Fig. 5.20.

| Source | Uncertainty Contribution |
|----------------------------|--------------------------|
| Foil Polarization | 0.57% |
| High Current Extrapolation | 0.50% |
| Null Asymmetry (Cu Foil) | 0.22% |
| Beam Bleedthrough | 0.18% |
| Analyzing Power A_{zz} | 0.16% |
| Dead Time Correction | 0.15% |
| Others | 0.13% |
| Total | 0.85% |

Table 5.9: Møller polarimetry systematic uncertainties for CREX running.

The Møller polarimetry systematic uncertainties are listed in table 5.9. The limiting uncertainty for the Møller is the Fe target foil polarization. The magnetization is a function of target temperature and B-field from the Møller magnets [64]. Ultimately, the Møller polarimeter measures $\mathcal{P}_e^{Moller} = (87.06 \pm$

0.74)% which comes out to 0.85% relative uncertainty. This measurement is then used in addition to the Compton result to further increase the precision on the CREX beam polarization measurement.

5.7.2 CREX Combined Polarimetry Result

While the Compton and Møller polarization means for the entire CREX experiment are in very good agreement with each other, the possibility of the agreement between the two systems being time-dependent is still present, due to the time-dependence of polarization. Of the Compton polarization average methods used, the piecewise fits provide a time-dependent model of polarization that can also be evaluated for data that with no contemporary Compton running (like the Møller had). The Møller measurements are then compared with each matching Compton fit evaluated at approximately⁸ the

⁸While the Møller polarimeter measurement time is “approximate” for these calculations, all CREX Møller measurements were close enough in time to Compton measure-

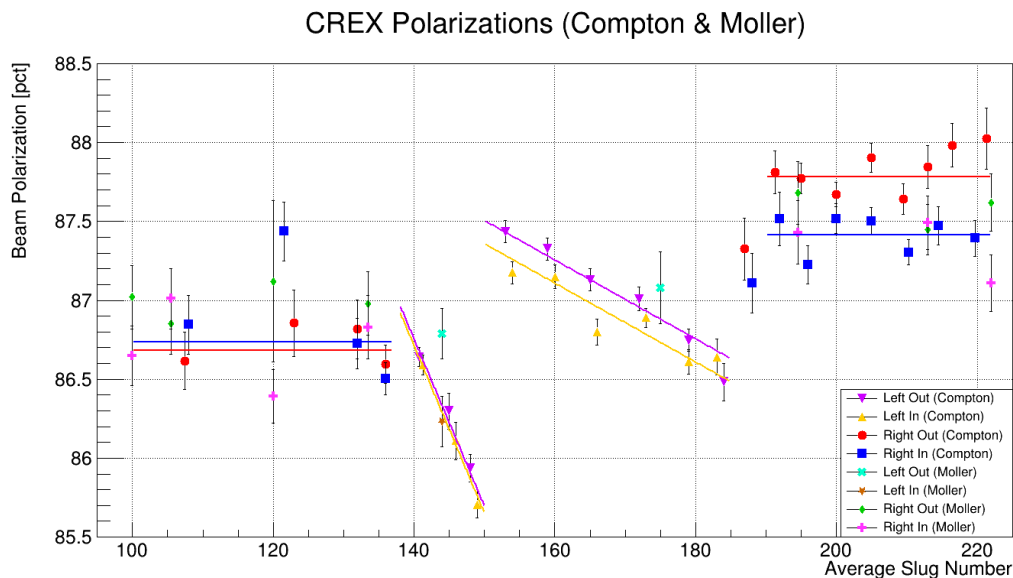


Figure 5.21: Compton escargatoire polarization averages and Møller polarization measurements plotted by time of measurement. Møller measurement times are approximate. The fits used for Compton polarization averaging are also drawn, and do not include Møller data points.

same time each Møller measurement was made. The Møller data points are shown added to the Compton fits in Fig. 5.21.

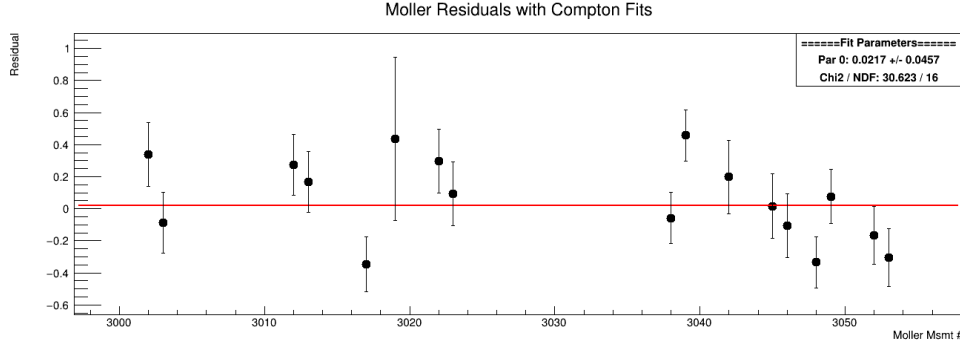


Figure 5.22: Residuals between the Compton piecewise fits and measured Møller polarizations for each Møller measurement plotted chronologically. The reported Møller polarizations are subtracted from the Compton piecewise fits, with the exact fit used determined by the IHWP state of the measurement and the approximate time of the measurement. The overall mean of the residuals is zero, showing strong agreement between the Møller and Compton measurements.

The average difference between the Møller measurements and the Compton fits is 0.0217 ± 0.0457 out of a mean of 87.1% polarization. The agreement between Compton and Møller measurements is then well within the overall uncertainty of both measurements, and is also statistically consistent between polarimeters. There is no indication that the agreement between Compton and Møller is time-dependent either, meaning that no uncertainty between Compton and Møller polarimeters needs to be added in order to use the average of the two. The residuals between the Møller measurements and the Compton piecewise fits can be seen in Fig. 5.22.

Because the sources of Møller systematic uncertainty are not correlated to the sources of Compton systematic uncertainty, the average polarizations of both Møller and Compton polarimetry are together using an inverse-variance weighted mean. With $\mathcal{P}_e^{Compton} = (87.115 \pm 0.453)\%$ and $\mathcal{P}_e^{Moller} = (87.06 \pm 0.74)\%$ the overall beam polarization is $\mathcal{P}_e = (87.10 \pm 0.386)\%$ with 0.44% relative uncertainty. This is certainly the most accurate beam polarization measurement ever taken for an experiment at JLab, and represents significant

ments that the approximation made no difference.

progress towards extremely high-precision polarimetry required by future polarized beam experiments.

5.8 PREX-II Compton Result

Though the main process of the analysis is the same for both PREX-II and CREX Compton data, the differences between the data quality of the two experiments means that different considerations are taken into account for the PREX-II analysis. Firstly, no time-dependence is observed in the PREX-II polarization data, therefore time-dependent weighting for calculating the polarization average is not necessary. Additionally polarimetry data from both Compton & Møller during PREX-II revealed that the magnitude of polarization is lower for IHWP in data than it was for IHWP out data. The cause was determined after the PREX-II experimental running to be from the high voltage setpoints used on the Pockels cell in the polarized source, which induced a birefringent effect on the vacuum window causing the laser in the polarized source to have a significant linear polarization component before it hit the GaAs photocathode. It was eventually determined however that the average polarization of both IHWP states would be sufficient to normalize the parity violating asymmetry.

Additionally, the approach to systematic uncertainties taken in the PREX-II Compton analysis have some differences compared with that done for CREX. While for CREX the photon cone offset is calculated using the simulation described in Sec. 5.6.1, for PREX-II the beam position is more tightly controlled allowing for a point-to-point photon cone offset correction. Additionally a correction is applied for the PREX-II gain shift, as direct measurements had been completed for the PREX-II PMT before the full PREX-II Compton analysis.

The PREX-II Compton measurements can be seen in Fig. 5.23. Additionally the Møller polarization measurements for each IHWP state can be found overlaid in the same figure. Both Compton and Møller data agreed that the difference between polarization magnitude for each IHWP state is ≈ 1.2 percentage points. Across both IHWP states the Møller reports $\mathcal{P}_e = (89.7 \pm 0.8)\%$ while the Compton reports an average of $\mathcal{P}_e = 89.68\%$ with 0.15% statistical uncertainty. Additional PREX-II Compton plots for snailwise variables can be found in Appendix A.

While the statistical agreement between Compton and Møller data is

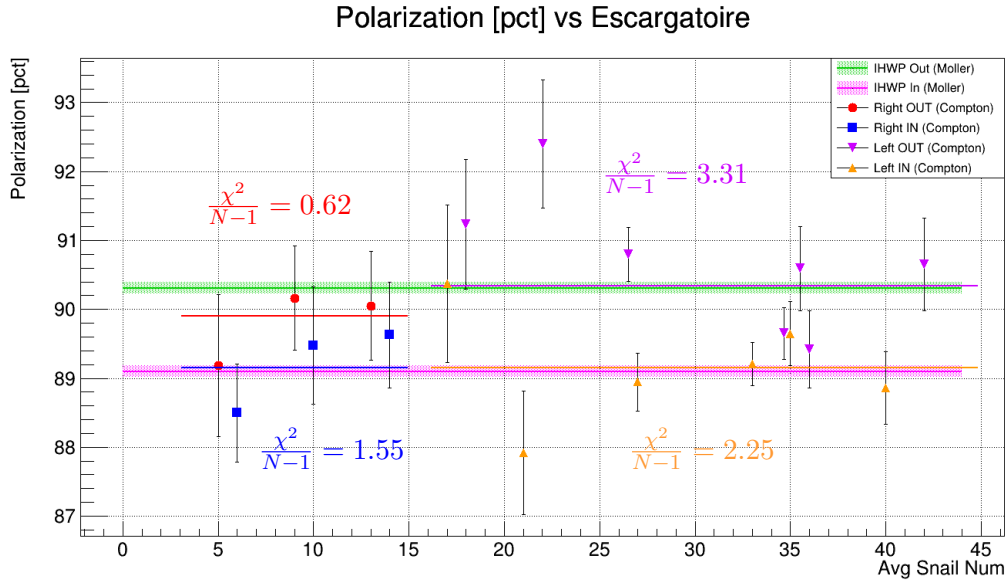


Figure 5.23: Comparison between PREX-II Compton and Møller results. Because PREX-II did not observe a polarization time-dependence, the Møller data is drawn as an overall average of all Møller measurements. Only statistical errors are shown for each polarimeter.

again, remarkable, indications of non-statistical behavior in the measured polarization in the Compton data set prompted deeper investigations of possible sources of systematics. Specifically, run periods taken within a few hours of each other show a degree of variation in the asymmetry and polarization measurements which cannot be confirmed by the Møller nor can they be correlated with any known variables in the Compton system. Investigations into new potential sources of systematic uncertainty (such as the dependence on helicity-correlated beam position differences) yield null results. Ultimately, the decision was made to only use the Møller polarimetry data for PREX-II in hopes that the analysis of the CREX Compton data (which was carried out after the PREX-II Compton analysis) would shed light on any further systematic uncertainty sources. Indeed, the CREX Compton data, due to its remarkable precision necessitates the development of new methods of quantifying systematic uncertainty. This leaves the possibility of a reanalysis of the PREX-II Compton data open for future study with new improvements to the analysis process that the CREX Compton data helped us develop.

Chapter 6

PREX-II/CREX Analysis

Over the entire 85-day PREX-II run period 126.98 C of beam charge usable for asymmetry measurements was deposited on target. Of that, 113.98 C of charge passed a series of cuts defined for analysis during running. At an average of 70 μA , this is the equivalent of 18.8 days of continuous beam deposited on target. For CREX the run period was 120 days and 382.56 C of cuts-passing charge was deposited on target which is the equivalent of 29.5 days of continuous beam. Data from two experimental periods are first organized into CODA runs where the DAQ is continuously recording data, which are subsequently grouped into slugs as described in Sec. 5.2.1. Analysis of both runs and slugs was conducted continuously during experimental running to monitor changes in data quality. This analysis informs the calibration and cut parameters used by the analyzer at different points during running.

The fundamental unit of time of the analysis is the MPS, a single helicity period. The fundamental unit of asymmetry measurements is the multiplets. Multiplets can either be quartets (consisting of four MPSs) or octets (consisting of eight MPSs) depending on the run configuration. Multiplets are grouped into “miniruns” containing five minutes worth of accepted multiplets. Miniruns are divided up within a CODA run, with a typical CODA run containing 3-10 miniruns. Runs are grouped into slugs with the same IHWP state as described in Sec. 5.2.1. Slugs are grouped into “Pitts” which consist of four neighboring slugs with approximately equal statistics in each IHWP state.

6.1 Cuts

Individual MPS windows and multiplets are subject to being cut if they are found to be unsuitable for asymmetry calculations. The cuts used for PREX-II and CREX running can be divided up into two categories. The first cut category is for any cuts relating to hardware failures in either DAQ electronics or beam monitors. The analyzer cuts events based on a series of hardware checksums. Events that saturate the ADCs are also cut. BCMs, BPMs, beam modulation and fast feedback are also monitored for hardware failures and are included in cuts by the analyzer.

The second category of cuts are applied based on the beam configuration. If either the beam position or energy experiences a rapid change (referred to as a “burp”) a short period around the burp is cut to enforce stability. If either the beam position or energy are outside of their ideal range, these events are also cut. The same cuts are applied to beam current, with an additional cut on beam current to remove any events where the beam is off.

It is important to note that none of the cut criteria are applied directly to detector data, or asymmetries, or other helicity-correlated values.

6.2 Asymmetries

As shown in Eqn. 2.3, the asymmetry that is read directly off the detector is contaminated by sources of “false” experimental asymmetry which need to be corrected during the analysis. To get the physics asymmetry \mathcal{A}_{phys} corrections are applied both during and after experimental running. The sources of false asymmetry are obtained through the data in the analyzer which gathers information from the main detectors, the \mathcal{A}_T detectors and the beamline monitors. \mathcal{A}_{corr} — the measured asymmetry over all multiplets after correction for these false asymmetries — can be written as

$$\mathcal{A}_{corr} = \mathcal{A}_{det} - \mathcal{A}_Q - \mathcal{A}_{pos} - \mathcal{A}_T - \mathcal{A}_{nonlin} - \mathcal{A}_{blind}, \quad (6.1)$$

where \mathcal{A}_{det} is the uncorrected asymmetry directly from the main detectors, \mathcal{A}_Q is the asymmetry in beam charge, \mathcal{A}_{pos} is the asymmetry resulting from helicity-correlated beam position and energy, \mathcal{A}_T is the transverse asymmetry, \mathcal{A}_{nonlin} is the false asymmetry arising from detector nonlinearity, and \mathcal{A}_{blind} is a blinding term.

\mathcal{A}_{blind} in particular is chosen by an arbitrary seed string which is hashed to a numerical offset before each experiment began. The asymmetry range from which \mathcal{A}_{blind} is chosen (referred to as the “blinding box”) is selected to be about $10\times$ the expected statistical precision of each experiment. For PREX-II: $-150 \text{ ppb} < \mathcal{A}_{blind}^{PREX} < 150 \text{ ppb}$ while for CREX: $-900 \text{ ppb} < \mathcal{A}_{blind}^{CREX} < 900 \text{ ppb}$. \mathcal{A}_{blind} , as its name implies, is unknown to experimenters during experimental running, and is only revealed to experimenters after the full analysis of all other subsystems is completed.

The physics asymmetry can be expressed using another set of corrections with

$$\mathcal{A}_{phys} = R_{radcorr} R_{Q^2} R_{acc} \frac{\mathcal{A}_{corr} - \mathcal{P}_e \sum_i f_i \mathcal{A}_{back,i}}{\mathcal{P}_e (1 - \sum_i f_i)}, \quad (6.2)$$

where R_{Q^2} is a correction factor obtained from the Q^2 measurement, R_{acc} is the correction from the acceptance function, $R_{radcorr}$ is from radiative corrections, $\mathcal{P}_e \sum_i f_i \mathcal{A}_{back,i}$ is the total false asymmetry from detected backgrounds, and $\frac{1}{1 - \sum_i f_i}$ is the background dilution factor.

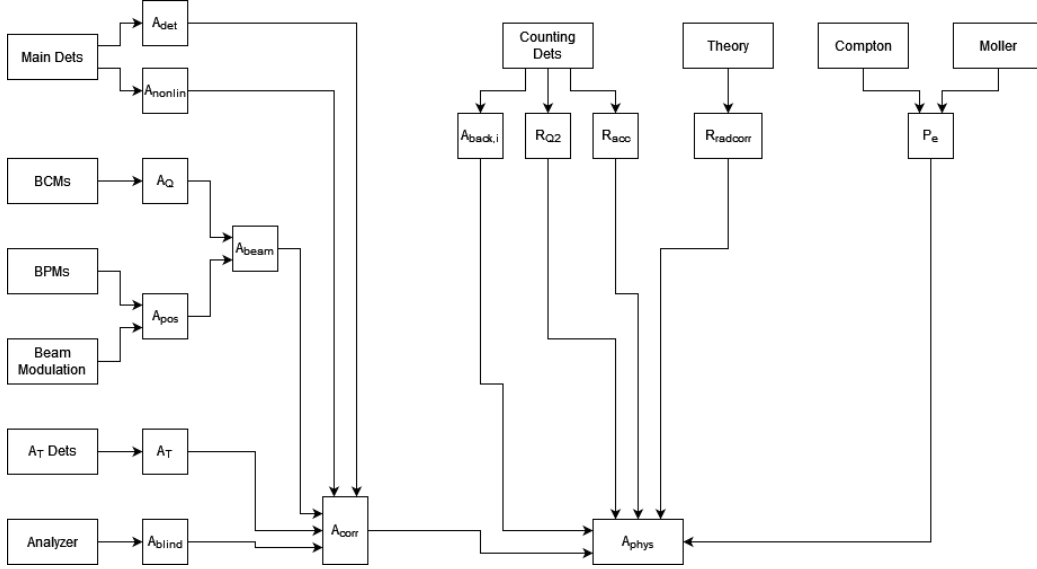


Figure 6.1: The various PREX-II/CREX subsystems and their contribution to the physics asymmetry calculation. It should be noted that this diagram is not comprehensive of the analysis process.

A visualization of the analysis process to compute \mathcal{A}_{phys} as described by Eqn. 6.1 and 6.2 can be seen in Fig. 6.1. Some corrections such as charge

asymmetry are applied in analysis during experimental running whereas others such as beam polarization and Q^2 corrections are dependent on measurements which are not fully analyzed until after the experimental run period.

| Experiment | \mathcal{A}_{raw} [ppb] | | $\delta\mathcal{A}_{raw}$ [ppb] |
|-------------------|---------------------------|-------|---------------------------------|
| PREX-II | 431.64 | \pm | 44.01 |
| CREX | 2026.81 | \pm | 189.88 |

Table 6.1: PREX-II/CREX detector asymmetries with only the charge asymmetry correction applied: $\mathcal{A}_{raw} = \mathcal{A}_{det} - \mathcal{A}_Q$.

The so-called ‘‘raw’’ asymmetries ($\mathcal{A}_{raw} = \mathcal{A}_{det} - \mathcal{A}_Q$) from the detectors for both PREX-II and CREX before any corrections are applied can be found in Tab. 6.1.

6.2.1 Helicity-Correlated Beam Properties

The false asymmetries from the beam arise from helicity-dependent effects of the beam at the target. The first of these to consider is charge asymmetry \mathcal{A}_Q . The calculation of \mathcal{A}_Q depends on the hall BCMs and because \mathcal{A}_Q is typically the largest and best-measured correction, it is corrected first. The experimental charge asymmetries can be seen in table 6.2.

| Experiment | \mathcal{A}_Q [ppb] | | $\delta\mathcal{A}_Q$ [ppb] |
|-------------------|-----------------------|-------|-----------------------------|
| PREX-II | 20.68 | \pm | 25.80 |
| CREX | -88.8 | \pm | 26.20 |

Table 6.2: PREX-II/CREX BCM asymmetries.

Correcting asymmetries due to helicity-correlated position, angle and energy differences is more complicated. Firstly, there is no direct monitor of position and angle differences at the target therefore it must be extrapolated from other position monitors. The space of beam motion at the target has five components: helicity-correlated position differences at the target in the two transverse directions, the differences in angle at the target in the two transverse dimensions, and beam energy: $\vec{B} = (x, y, \theta_x, \theta_y, E_{bpm})$.

These corrections are applied together to form the asymmetry correction

\mathcal{A}_{pos} from Eqn. 6.1 [100] as

$$\mathcal{A}_{pos} = \sum_{i=1}^5 C_i \Delta B_i, \quad (6.3)$$

where ΔB_i is the helicity-correlated difference in beam parameter B_i

$$\Delta B_i = \frac{B_i^+ - B_i^-}{2}, \quad (6.4)$$

and C_i is the asymmetry sensitivity to beam parameter B_i

$$C_i = \frac{\partial \mathcal{A}_{raw}}{\partial \Delta B_i}. \quad (6.5)$$

Because there is no direct measurement of helicity-correlated position, angle and energy differences at the target, the BPMs are used to measure position-differences along the beamline and extrapolate those differences at the target. For this, PREX-II and CREX uses six BPMs which each measure in two transverse dimensions totalling twelve position monitors along the beamline. These six BPMs included three BPMs in Hall A itself, and three BPMs on the arc leading into Hall A. The BPMs on the arc are especially sensitive to beam energy fluctuations as they exist in a dispersive region, while the other monitors are primarily used to project the position and angle changes at the target.

The next section describes how the sensitivities C_i can be determined.

6.2.2 Regression & Dithering

Regression

The goal of the linear regression technique is to measure the correction slopes C_i between measured detector asymmetries and helicity-correlated beam properties measured by beamline monitors. Using the naturally-occurring beam motion and position differences, the correlations are extracted directly. A visualization of position and energy correlations can be seen in Fig. 6.2.

While the correlation slopes C_i represent the effect of helicity-correlated beam properties at the target, the measurement of correlation slopes is taken at each position monitor. All twelve position monitors are used to calculate a

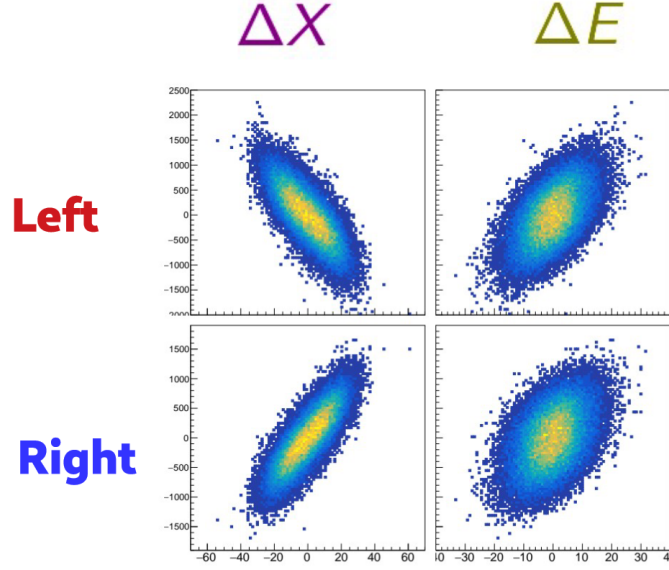


Figure 6.2: Plots showing the correlation between left HRS (*top row*) and right HRS (*bottom row*) asymmetries and beam position differences (*left column*) and energy differences (*right column*). Note that due to the symmetry of the spectrometers the position correlations are opposite sign in each side, but for energy the sign of the correlations are the same.

simultaneous correction for all degrees of freedom. This can be accomplished through a linear transformation

$$\Delta\vec{B} = \mathcal{R}\Delta\vec{M}, \quad (6.6)$$

where $\Delta\vec{M}$ are the beam monitor differences [100]. The transformation \mathcal{R} must then be diagonalized to get the correction for each individual beam monitor. Then denoting the beam monitor correlation slopes as β_i the asymmetry correction is reparameterized as

$$\mathcal{A}_{raw} - \mathcal{A}_{pos} = \mathcal{A}_{raw} - \sum_i \beta_i \Delta M_i. \quad (6.7)$$

The correction slopes then minimize the value of χ^2 as

$$\chi^2 = \sum_j \left[\mathcal{A}_{raw,j} - \sum_i \beta_i \Delta(M_i)_j \right]^2, \quad (6.8)$$

for j measurements of asymmetry. The minimization condition is

$$\frac{\partial \chi^2}{\partial \beta_i} = 0. \quad (6.9)$$

This equation is then solved for β_i by applying an inverse linear transform.

Dithering

The beam modulation system, also called “dithering,” is designed to artificially induce small trajectory excursions at the target. The position and operation of the coils needed to induce this motion is described in Sec. 3.2.3. After every dithering cycle the response in both the beam monitors and the detectors are calculated.

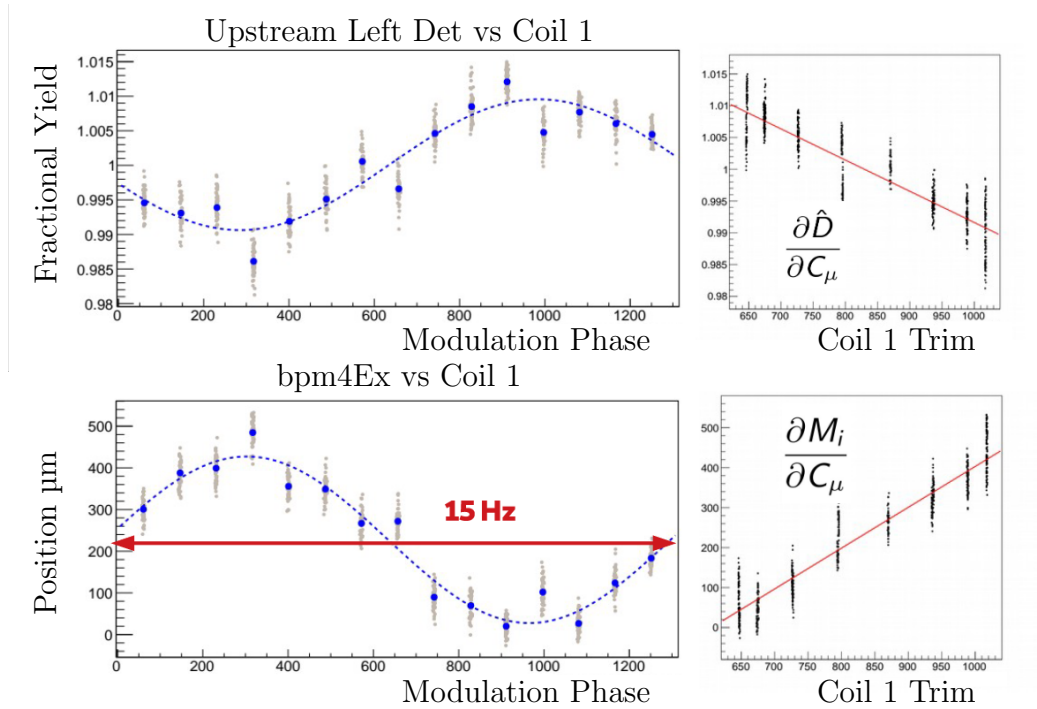


Figure 6.3: Response of both the main detectors (specifically the upstream left arm detector) and BPMs (specifically bpm4Ex) to a dithering cycle. Slopes are extracted from each cycle and plotted on the right.

We then calculate the sensitivity to each beam monitor M_i as $\frac{\partial D}{\partial M_i}$. Beam modulation directly measures the sensitivity of the detector to each coil C_k ,

$\frac{\partial \hat{D}}{\partial C_k}$ and the sensitivity of the beam monitors to the coils $\frac{\partial M_i}{\partial C_k}$ for any monitor i . Analogous to Eqn. 6.7, the sensitivity to each coil can be written as

$$\frac{\partial \hat{D}}{\partial C_k} = \sum_i \frac{\partial D}{\partial M_i} \frac{\partial M_i}{\partial C_k}, \quad (6.10)$$

where \hat{D} is the relative change in the detector signal over the modulation $\hat{D} = \frac{D}{\langle D \rangle}$, and the monitor sensitivity $\frac{\partial D}{\partial M_i}$ is analogous to β_i . The coil sensitivities can be seen for a single beam modulation cycle in Fig. 6.3. The equation then can be rewritten in matrix form, which is inverted to solve for $\frac{\partial D}{\partial M_i}$.

Lagrange Multipliers

The method of Lagrange multipliers can be used to allow the sensitivities from beam modulation to constrain regression and dithering, as well as the sensitivities from regression. This is especially helpful if the parameter space of natural beam motion needed for regression isn't large enough relative to electronics noise to resolve correlation slopes accurately. The Lagrangian function can be written as

$$\mathcal{L} = \chi^2 + \sum_k \lambda_k \left(\frac{\partial \hat{D}}{\partial C_k} - \sum_i \frac{\partial D}{\partial M_i} \frac{\partial M_i}{\partial C_k} \right), \quad (6.11)$$

where λ_k is the Lagrange multiplier for modulation coil k . The constraints on the Lagrangian function are:

$$\frac{\partial \mathcal{L}}{\partial \lambda_k} = 0, \quad \frac{\partial \mathcal{L}}{\partial \beta_i} = 0, \quad (6.12)$$

where $\beta_i = \frac{\partial D}{\partial M_i}$. This can be solved by matrix inversion, and uncertainties can be assigned to the size of the correction based on the statistical uncertainty of regression and the eigenvectors of the modulation covariance matrix [100].

6.2.3 Asymmetry Corrections

The size of the asymmetry correction due to helicity-correlated beam properties is listed in Tab. 6.3.

| Experiment | \mathcal{A}_{pos} [ppb] | | $\delta\mathcal{A}_{pos}$ [ppb] |
|-------------------|---------------------------|-------|---------------------------------|
| PREX-II | -60.4 | \pm | 2.50 |
| CREX | 53.45 | \pm | 5.44 |

Table 6.3: Asymmetry corrections from Lagrange multipliers

All 12 monitors are used by the correction to better limit the contribution of the electronics noise. The uncertainty on the correction then comes from the dominant five monitors (for the five degrees of freedom of the beam trajectory.) The central value of the correction is the same as the correction without dithering constraints to within 3%. Thus, an overall uncertainty of 3% is assigned to the correction.

6.3 Spectrometer Optics & Acceptance

Because the asymmetry, and the sensitivity to R_n is a sensitive function of scattering angle θ , understanding the spectrometer acceptance over the scattering angle distribution becomes essential for normalizing the asymmetry. Additionally, by calibrating the spectrometer optics measurements of detector alignment, and inelastic contamination are possible. Optics calibration for both PREX-II and CREX took place at the start of experimental running as part of the experimental commissioning processes.

For PREX-II and CREX five scattering kinematic parameters are calibrated: x and y the displacement with respect to the central ray in the dispersive and transverse directions respectively, θ and ϕ the angles with the central ray in the dispersive and transverse planes respectively, and δ the fractional change in momentum from the central ray [70]. The transport of the trajectories through the spectrometer magnets is modeled as a series of matrix transformations on these optical parameters from the target to the detector planes [101]. This transport is made simpler by applying the constraints of the HRS design.

To aid in the explicit identification of accepted particles, two sieve slit collimators are installed on either side of the primary beamline collimator. the sieves have a unique pattern of holes that certain segments of the acceptance can pass through. The accepted electrons in the tracking detectors then only shows the electrons which pass the sieve pattern. A picture of the sieve collimators can be seen in Fig. 6.4.

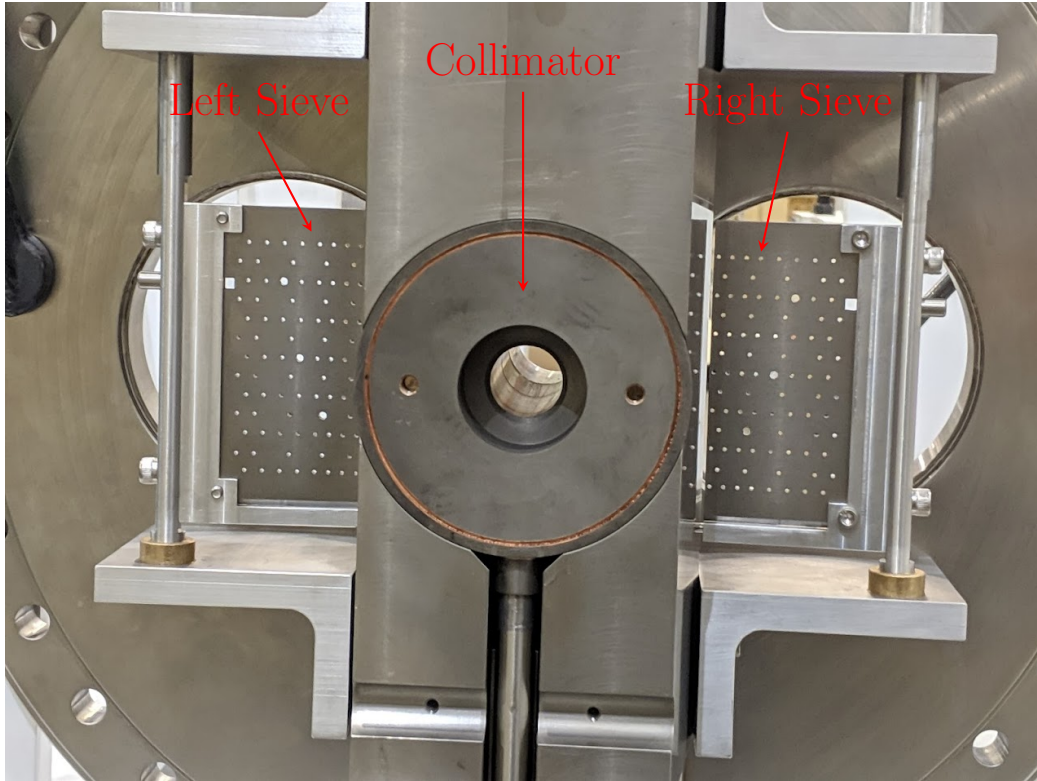


Figure 6.4: Photo of the main collimator assembly with the sieves inserted into the path of the acceptance.

These sieves are aligned such that the “central ray” of the acceptance passes through the central sieve hole of each sieve. Also, the sieves are able to be retracted during non-optics running such that they will not impact the experimental data.

The end of the optics calibration gives a reconstruction of scattering geometry at the target. This, in tandem with simulation, produces an acceptance function which details the likelihood of a scattered electron being in the acceptance as a function of scattering position and angle. The acceptance function for CREX as a function of θ specifically can be seen in Fig. 6.5. The acceptance function is then weighted by asymmetry and cross section (using the functions shown in Fig. 2.3) to quantify the measured asymmetry expectation value as a function of θ .

The effect of the uncertainty on the acceptance function and the physics

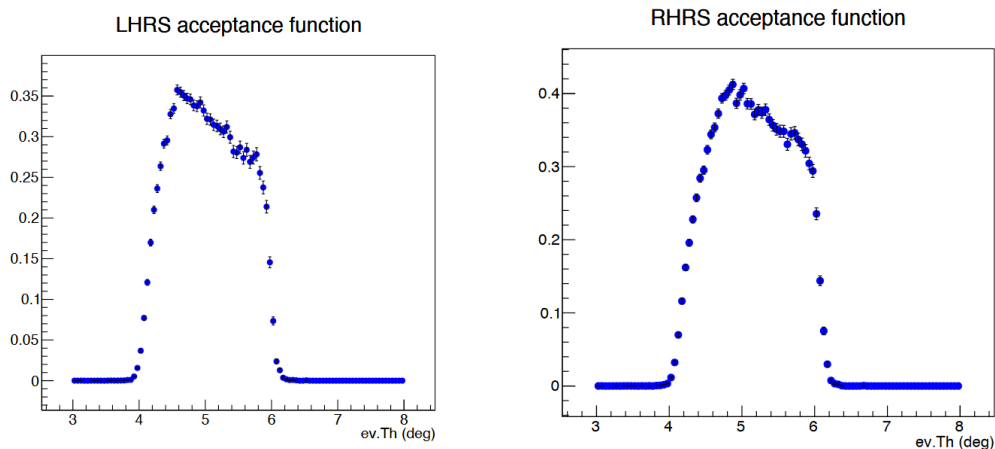


Figure 6.5: The acceptance function for both HRS’s in dispersive scattering angle θ . The PREX-II acceptance function derivation follows approximately the same procedure.

extraction is then dependent on physics model, in addition to kinematic factors (such as the consistency of Q^2 or beam energy). Thus the optics calibration is used for counting measurements during both PREX-II and CREX while the full acceptance function is only normalized after the experimental run periods¹.

6.4 Counting Mode Measurements

6.4.1 Detector Alignment & Inelastic Backgrounds

Detector alignment checks need to be done during the running of both PREX-II and CREX in order to keep the center of elastic scatters (the “elastic peak”) focused on the main detectors. This accounts for small slow drifts in the spectrometer optics configurations. Detector alignment is also important in order to prevent inelastic scatters from nuclear excitations from adding to the false asymmetry. The design of the spectrometers (as discussed in 3.6) allows for separation between elastic scatters and lower-momentum inelastic scatters.

¹The analysis of the spectrometer optics and the acceptance function was done primarily by Ryan Richards, Kent Paschke, and Siyu Jian.

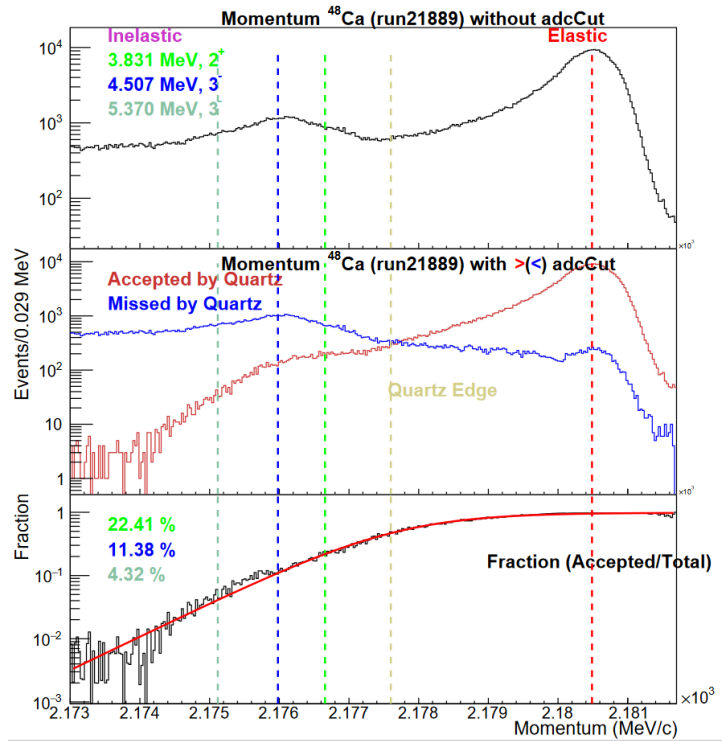


Figure 6.6: Inelastic background peaks as seen in the RHRS in one alignment run during CREX. Three primary inelastic states are shown: 2^+ and two 3^- states. The top plot shows the momentum spectrum with the three excited states plotted. The bottom plot shows the probability of acceptance as a function of momentum.

The inelastic contribution is a more significant issue for CREX, which has more pronounced inelastic peaks at a close distance to the edge of the main detectors. The primary excited states of ^{48}Ca contributing to the CREX \mathcal{A}_{PV} measurement are the $J^p = 2^+$ and two $J^p = 3^-$ states. These are identified by a small peak in the momentum spectra of the main detectors with lower momentum than the elastic peak (as seen in Fig. 6.6.) Fits of expected contributing states are used to bound the possible magnitude of the contribution from each. Theoretical estimates of \mathcal{A}_{PV} from each contributing state along with uncertainty estimates are used to estimate the total correction and uncertainty.

That quantification can be seen in Tab. 6.4. Inelastics produce an overall

| State | Δp [MeV] | f_i [%] | $\mathcal{A}_{PV} \pm \delta\mathcal{A}_{PV}$ [ppb] | $\delta\mathcal{A}_{PV}$ [%] |
|----------------|------------------|-----------|---|------------------------------|
| 2 ⁺ | 3.831 | 0.59 | 8100 \pm 2700 | 0.71 |
| 3 ⁻ | 4.507 | 0.66 | 2700 \pm 1400 | 0.38 |
| 3 ⁻ | 5.370 | 0.12 | 3800 \pm 2700 | 0.13 |
| Total | | | | 0.82 |

Table 6.4: CREX inelastic uncertainty contribution on \mathcal{A}_{PV} . Here $\mathcal{A}_{PV} \pm \delta\mathcal{A}_{PV}$ is the theoretical asymmetry contribution from each inelastic state. [19]

relative uncertainty of 0.82% on CREX \mathcal{A}_{PV} . For PREX-II the same process is used but due to the inelastic peaks being much further from the elastic peak the overall contribution is 0.02%².

6.4.2 Q^2 Measurements

The average four-momentum transfer squared Q^2 was also needed to normalize the asymmetry measurement. Kinematically Q^2 can be expressed as

$$Q^2 = (p_e - p'_e)^2 \simeq 2EE'(1 - \cos\theta), \quad (6.13)$$

in the limit that $E \gg m_e$ and $E' \gg m_e$ [102]. this can be parameterized in terms of either E or E' exclusively as

$$Q^2 = \frac{2E^2(1 - \cos\theta)}{1 + \frac{E}{m_e}(1 - \cos\theta)} = \frac{2E'^2(1 - \cos\theta)}{1 - \frac{E'}{m_e}(1 - \cos\theta)} \approx 4EE' \sin^2\left(\frac{\theta}{2}\right). \quad (6.14)$$

Thus a Q^2 measurement can be made with just the beam energy E and the average scattering angle θ . Beam energy is measured on the beamline arc leading into Hall A. This is accomplished by scanning the field of one of the arc dipoles and extracting the field integral. This is then compared with the beam profile scans along the arc and in Hall A which give the beam bending angle, and thus an estimate of energy. This is done once for each experiment as the energy would vary little over the course of the run [59].

To deduce the scattering angle θ we decompose it into a function depend-

²The inelastic background was examined primarily by Devi Adhikari.

ing on target scattering angles θ_{tg} ϕ_{tg} as

$$\theta = \frac{\cos \theta_0 - \phi_{tg} \sin \theta_0}{\sqrt{1 + \theta_{tg}^2 + \phi_{tg}^2}}, \quad (6.15)$$

where θ_0 is the scattering angle of the central ray. Measuring θ_0 involves doing a pointing measurement, which uses the water cell target. With the water cell the targets showed two elastic peaks, one for scattering off of hydrogen and one for oxygen³. The energy difference between the two peaks is used to identify θ_0 , which is used in conjunction with the detector optics to get a function for θ , and subsequently Q^2 .

With a pointing measurement for each HRS in each experiment, Q^2 measurements are taken regularly by measuring the Q^2 distribution in the VDCs. These measurements are taken at low beam current so as to not overwhelm the detectors.

| Quantity | PREX-II | CREX |
|---|-----------------------|---------------------|
| $\langle Q^2 \rangle$ [GeV ²] | 0.00616 \pm 0.00004 | 0.0297 \pm 0.0002 |
| LHRS θ_0 | 4.765° \pm 0.016° | 4.765° \pm 0.016° |
| RHRS θ_0 | 4.747° \pm 0.018° | 4.747° \pm 0.018° |

Table 6.5: Average Q^2 measurements for both spectrometer arms from PREX-II/CREX. Note that because the pointing angle was defined by the spectrometer configuration the pointing angles are equal for both experiments. Uncertainties on Q^2 take into account time-dependence.

The results of the Q^2 measurements for both PREX-II and CREX can be seen in Tab. 6.5. The Q^2 measurements also provide one of the key parameters for measuring the weak neutral form factor as seen in Eqn. 1.25.

6.5 Transverse Asymmetry Measurements

As part of the PREX-II and CREX experimental run plan, several days of transverse running were allocated. During this time the beam polarization is oriented transverse to the beam and the transverse asymmetry \mathcal{A}_T is measured on ²⁰⁸Pb, ⁴⁰Ca, ⁴⁸Ca, and ¹²C. These measurement periods not only

³Hydrogen is a much lighter nucleus than oxygen meaning nuclear recoils of hydrogen give greater energy losses than for oxygen.

provided novel transverse asymmetry data on these nuclei, they could also be used to constrain the \mathcal{A}_T correction on \mathcal{A}_{PV} .

Notably, \mathcal{A}_T from the ^{208}Pb target was found to be zero so no asymmetry correction is applied for PREX-II [103].

For ^{48}Ca the \mathcal{A}_T correction is applied in two parts: A_{TH} representing the asymmetry from the horizontal transverse component of beam polarization and A_{TV} for the vertical component of beam polarization. The vertical polarization component creates an asymmetry in the horizontal detector direction and therefore is measured from the main detectors by weighting the asymmetry by target scattering angle ϕ_{tg} . Here the weighting is done in the form of a “double difference” or finding the difference between measured asymmetries in the left and right detectors⁴. The form of the corrected measured asymmetry is

$$A_{m,corr,dd}^V \approx \mathcal{P}_V \mathcal{A}_n \frac{\langle \phi_{tg} \rangle_{left} - \langle \phi_{tg} \rangle_{right}}{2}, \quad (6.16)$$

where \mathcal{P}_V is the vertical beam polarization and \mathcal{A}_n is the corrected asymmetry measured during transverse running [70]. Also in this convention $\langle \phi_{tg} \rangle_{left}$ and $\langle \phi_{tg} \rangle_{right}$ have opposite signs to reflect the fact that the angles are on opposite sides of the central beam axis. Then the vertical asymmetry correction during longitudinal running is proportional to the transverse running asymmetry as⁵

$$A_{TV} = A_{m,corr,dd}^V \xi, \quad (6.17)$$

where ξ is the left-right vertical scattering asymmetry:

$$\xi = \frac{\langle \phi_{tg} \rangle_{left} + \langle \phi_{tg} \rangle_{right}}{\langle \phi_{tg} \rangle_{left} - \langle \phi_{tg} \rangle_{right}}. \quad (6.18)$$

\mathcal{A}_{TH} cannot be measured by the difference between the HRSs but instead must be bound by the possible \mathcal{P}_H and difference in vertical angle acceptance on each HRS. PREX-II and CREX use specialized detectors positioned to have increased sensitivity to vertical scattering angle. These “ \mathcal{A}_T ” detectors are placed vertically above and below the main detectors. This positioning allows the top-bottom detector asymmetry to exploit a greater degree of θ_{tg} variation than the main detector acceptance.

⁴During CREX only the upstream detectors were used so double-differences were only calculated with those detectors.

⁵This model is made with the assumption that $\mathcal{A}_n \propto \phi_{tg}$

| Quantity | A_{TV} [ppb] | \pm | δA_{TV} [ppb] | A_{TH} [ppb] | \pm | δA_{TH} [ppb] |
|----------------|----------------|-------|-----------------------|----------------|-------|-----------------------|
| CREX Part 1, 2 | -7.68 | \pm | 3.56 | 1.2 | \pm | 28.8 |
| CREX Part 3 | -6.10 | \pm | 6.04 | 37.6 | \pm | 34.2 |

Table 6.6: CREX transverse asymmetry corrections for both horizontal and vertical components. The run is divided up in part 1 and 2 (from December 2019 to March 2020) and part 3 (August and September 2020) to reflect the different beam configuration upon returning from the shutdown. [70]

This method produced the asymmetries quoted in Tab. 6.7. It should be noted that the uncertainty range for the \mathcal{A}_{TV} correction is less than that of the \mathcal{A}_{TH} correction, implying that the \mathcal{A}_{TH} measurement is a larger contributor to systematic uncertainty on \mathcal{A}_{PV} . This reflects the fact that the \mathcal{A}_{TV} measurement is done using the left and right HRSs, of which the geometry is well known and measured and can be used as part of the analysis.

Additionally, a “spin dance” was performed during which the electron spins in the accelerator are rotated while simultaneously polarimeters are run to measure the beam polarization in each hall. This is done to identify the effect of spin precession in the accelerator to make it easier to adjust the injector configuration. The data from the spin dance from before CREX suggest that the correction from \mathcal{A}_{TH} would be limited to 13 ppb. Because both beam energy is stable and the Wien configuration is recoverable after changes 13 ppb could be taken as the overall size of the correction as it was reliable and a tighter bound than those from the \mathcal{A}_T detector measurements.

6.6 PREX-II/CREX Physics Asymmetry

At the end of the analysis for both experiments, the asymmetry corrections are applied to find the experimental physics asymmetry. These include dominant sources of uncertainty such as beam polarization, the acceptance normalization, and also the backgrounds from the diamond foils on the PREX-II targets and the ^{40}Ca impurity in the CREX targets. In addition, uncertainty for acceptance rescattering inside the spectrometers is studied but is deemed to be small for both experiments. The uncertainties can be seen in Tab. 6.7.

The precision of both experiments relied on accurate determination of the corrections for each run period. Two of the largest of these corrections are for \mathcal{A}_Q and \mathcal{A}_{pos} . The measurement of these two asymmetries during

| | PREX-II | | CREX | |
|-----------------------------------|--|--|--|--|
| | \mathcal{A}_{PV} Uncertainty Contribution [ppb] | \mathcal{A}_{PV} Uncertainty Contribution [%] | \mathcal{A}_{PV} Uncertainty Contribution [ppb] | \mathcal{A}_{PV} Uncertainty Contribution [%] |
| Polarization | 5.23 | 0.95% | 13.1 | 0.49% |
| Transverse Asymmetry | 0.00 | <0.01% | 12.7 | 0.48% |
| Acceptance Normalization | 4.56 | 0.83% | 23.9 | 0.90% |
| Beam Correc- tion | 2.98 | 0.54% | 6.9 | 0.26% |
| Nonlinearity | 2.69 | 0.49% | 6.7 | 0.25% |
| Carbon Back- ground | 1.45 | 0.26% | - | - |
| ⁴⁰ Ca Back- ground | - | - | 8.8 | 0.33% |
| Charge Cor- rection | 0.25 | 0.04% | 1.1 | 0.04% |
| Inelastic Back- ground | 0.04 | <0.01% | 21.8 | 0.82% |
| Rescattering | <0.01 | <0.01% | 0.5 | 0.02% |
| Systematic Uncertainty | 8.16 | 1.48% | 39.4 | 1.48% |

Table 6.7: Sources of systematic uncertainty for both PREX-II and CREX.

experimental running thankfully keeps the \mathcal{A}_{PV} uncertainty contribution of both controlled.

The experimental asymmetries with all corrections applied can be seen in Tab. 6.8. The asymmetry blinding factor \mathcal{A}_{blind} is only revealed after all other analysis work is completed. Removal of the blinding factor does not affect the absolute statistical uncertainty but it does affect the absolute systematic uncertainties which are calculated from the relative uncertainties in Tab. 6.7. In both experiments the total uncertainty is dominated by statistics. For PREX-II $\mathcal{A}_{PV} = 550 \pm 16$ (stat) ± 8 (syst) ppb (3.3% overall precision) [104]. For CREX, $\mathcal{A}_{PV} = 2658 \pm 106$ (stat) ± 39 ppb (4.2% overall precision).

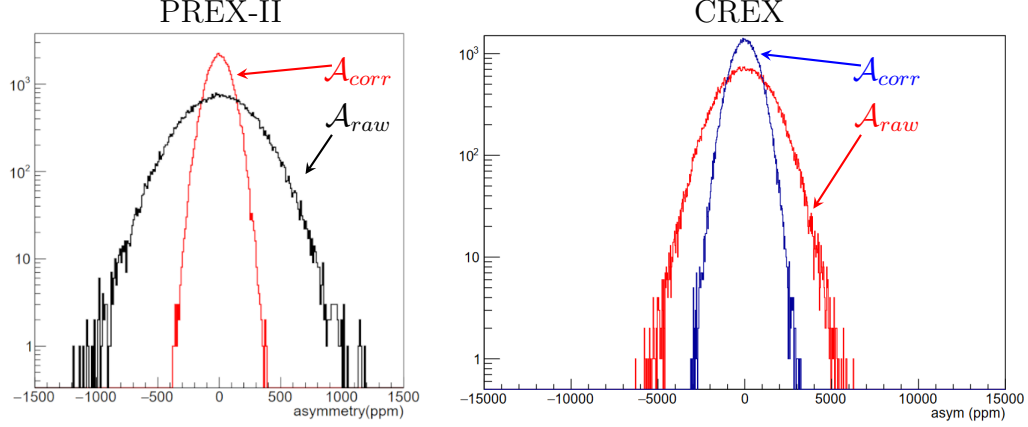


Figure 6.7: The \mathcal{A}_{raw} and \mathcal{A}_{corr} distributions plotted for all multiplets passing cuts in and example run for both PREX-II and CREX.

All figures in parts-per-billion

| Asymmetry | PREX-II | CREX |
|--|--|---|
| \mathcal{A}_{raw} | 431.64 ± 44.01 (stat) | 2026.81 ± 189.88 (stat) |
| \mathcal{A}_Q | 20.68 ± 0.25 (syst) | -112.4 ± 1.1 (syst) |
| \mathcal{A}_{pos} | -60.38 ± 2.50 (syst) | 53.45 ± 5.44 (syst) |
| \mathcal{A}_{corr} | 492.02 ± 13.52 (stat) | 2080.3 ± 83.8 (stat) |
| \mathcal{A}_{phys} | 549.4 ± 16.1 (stat) ± 8.1 (syst) | 2334.8 ± 106.1 (stat) ± 37.3 (syst) |
| \mathcal{A}_{blind} | 0.5 | -255.7 |
| Unblinded \mathcal{A}_{phys} | 550.0 ± 18.0 | 2658.6 ± 113.2 |

Table 6.8: Selected experimental asymmetry results from both PREX-II and CREX including the final unblinded asymmetry. Uncertainties on asymmetries are both statistical and systematic unless otherwise noted.

Chapter 7

Results & Discussion

The PREX-II and CREX experimental results have significant implications for the theory of nuclear structure as laid out in Ch. 1. The PREX-II result sheds new light on neutron star physics as well as the direct properties of ^{208}Pb nuclei. The CREX result can be shown to resolve tensions between different theoretical nuclear modelling methods. This chapter will discuss the nuclear properties revealed by the \mathcal{A}_{PV} measurements from PREX-II and CREX.

7.1 Form Factors & Skin Thickness

7.1.1 PREX-II

As discussed in Sec. 1.2.3 and explicitly demonstrated in Eqn. 1.33, a measurement of \mathcal{A}_{PV} can be used to find the weak form factor F_W if the Coulomb form factor F_{ch} is known [105]. With a measurement of F_W then F_n can be extracted because the weak charge is dominated by the neutron. At the particular kinematics selected for these experiments the form factor is highly sensitive to the mean neutron radius squared $\langle r_n^2 \rangle$, which can be extracted.

With the assumption of a uniform interior density, the size of the distribution implies the neutron density ρ_n . The sum of both proton and neutron densities gives the total interior baryon density of nuclei as

$$\rho_b = \rho_n + \rho_p. \tag{7.1}$$

The nuclear charge density is modeled as a two-parameter Fermi distribution of the form

$$\rho_W^{(r)} = \rho_W^0 \frac{\sinh(c/a)}{\cosh(r/a) + \sinh(c/a)}, \quad (7.2)$$

where r is the radial coordinate, c is the radius parameter, a is the surface thickness parameter, and ρ_W^0 is the weak charge density at $r = 0$ [44]. The density parameter ρ_W^0 is fixed by requiring that the distribution integrates to the nuclear weak charge. The mean weak radius squared is calculated as [106]

$$\langle R_W^2 \rangle = \frac{3}{5}c^2 + \frac{7}{5}(\pi a)^2. \quad (7.3)$$

Matching the radius parameter c to the weak charge radius determined by PREX-II or CREX gives R_W on ^{208}Pb and ^{48}Ca respectively. The surface parameter a relies on input from different theoretical models, which introduces a theoretical uncertainty to the measured nuclear properties.

A plot of weak charge density can be seen in Fig. 7.1. Indeed the weak charge radius can be seen to extend beyond the charge radius in the Fermi distribution.

| ^{208}Pb parameter | Value & Uncertainty |
|-------------------------------|--|
| $F_W(\langle Q^2 \rangle)$ | 0.368 ± 0.013 (exp.) ± 0.001 (theo.) |
| R_W [fm] | 5.795 ± 0.082 (exp.) ± 0.013 (theo.) |
| ρ_W [fm^{-3}] | -0.0798 ± 0.0038 (exp.) ± 0.0013 (theo.) |
| ρ_b [fm^{-3}] | 0.1480 ± 0.0040 |
| Δr_{np}^{208} [fm] | 0.278 ± 0.078 (exp.) ± 0.012 (theo.) |

Table 7.1: Physical measurements of ^{208}Pb as measured from the PREX-II asymmetry and reported in Adhikari et al. [104].

The physical measurements of ^{208}Pb from the measured \mathcal{A}_{PV} of PREX-II can be seen in table 7.1. It should be noted that the earlier PREX-I reported value of $\delta r_{np}^{208} = 0.33_{-0.18}^{+0.16}$ fm [36] can be combined with the PREX-II result to produce an overall measurement of

$$\Delta r_{np}^{208} = 0.283 \pm 0.071 \text{fm}. \quad (7.4)$$

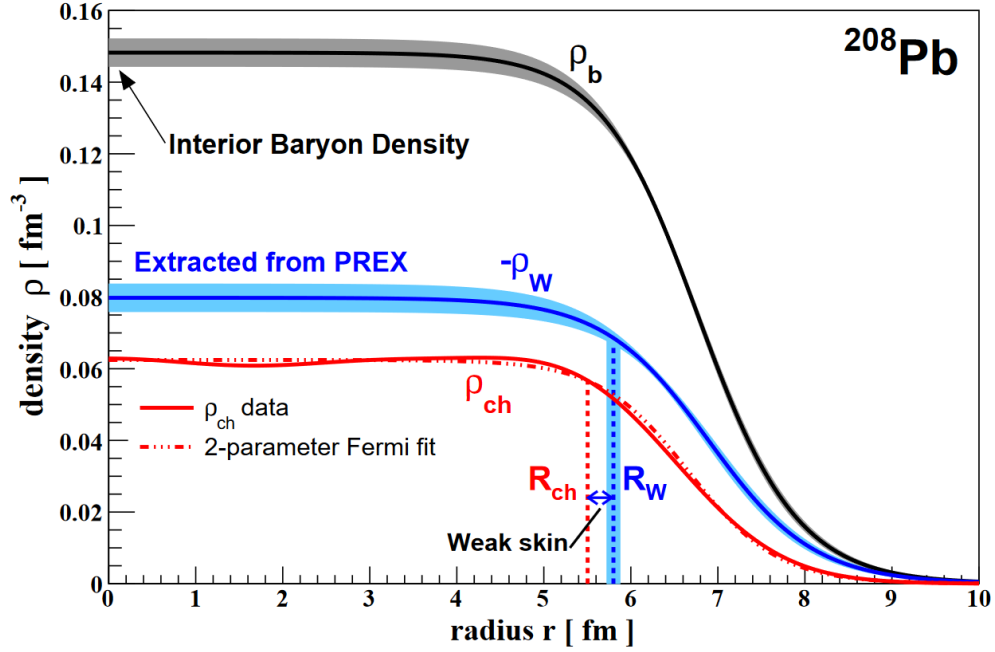


Figure 7.1: ρ_{ch} and ρ_W for ^{208}Pb plotted vs. nuclear radius. From these we can extract ρ_p and ρ_n from which we can show the interior baryon density ρ_b . Compare this with Fig. 1.1. Reproduced from [104].

7.1.2 CREX

The same analysis procedure can then be applied for the CREX data to derive the physical properties of ^{48}Ca . It should be noted that as of the publication of this dissertation these reported properties are still preliminary.

The CREX form factor was found to be [107]

$$F_W(\langle Q^2 \rangle) = 0.1297 \pm 0.0055. \quad (7.5)$$

Previous predictions made with the FSUGold nuclear structure model (and others) had predicted the CREX asymmetry at the CREX $\langle Q^2 \rangle$ at ≈ 2480 ppb which is slightly less than the actual CREX measurement, indicating F_W was slightly larger than these models had predicted [107, 108]. The difference of form factors from CREX was then $F_{ch} - F_W = 0.0283$, which can be seen plotted alongside a number of structure models in Fig. 7.2.

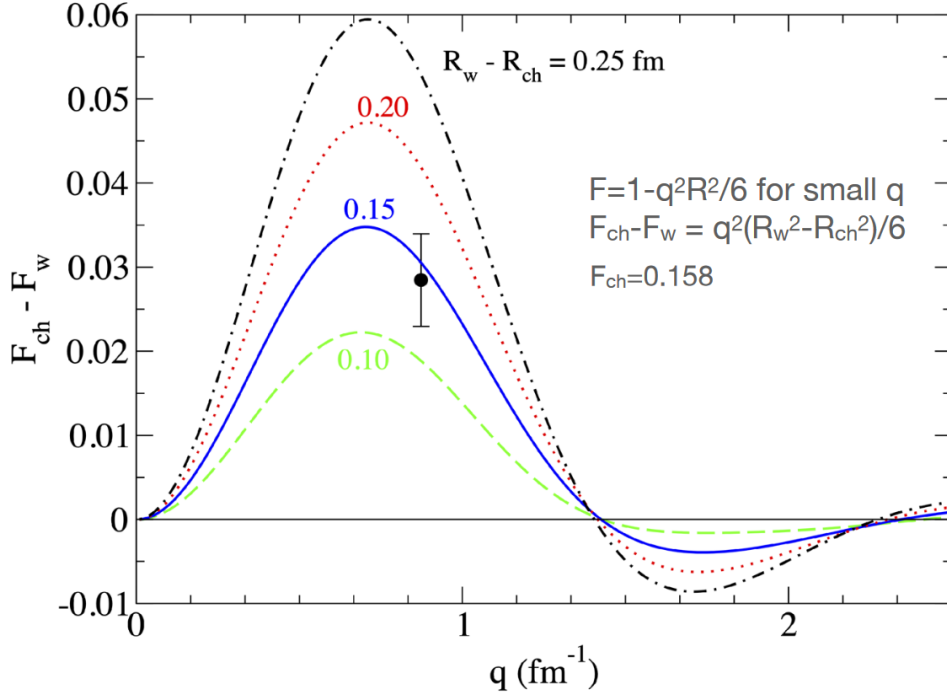


Figure 7.2: Form factor difference $F_{ch} - F_W$ in ^{48}Ca . The value extracted from CREX \mathcal{A}_{PV} and error bars is shown in black. The curves shown correspond to the form factor calculations for different nuclear structure models, and are shown contoured by the model's predicted weak charge skin (from 0.10 fm to 0.25 fm). [107]

No neutron skin thickness is reported here because as of the publication of this dissertation the CREX analysis is still ongoing.

7.2 Implications

7.2.1 PREX-II & Symmetry Energy

The nuclear symmetry energy term L (from Eqn. 1.40) is dependent on nuclear pressure, which is itself dependent on baryon density. Thus the PREX results can be used to constrain this value. L can be determined from a fit of the strong correlation between L and Δr_{np} . This correlation can be

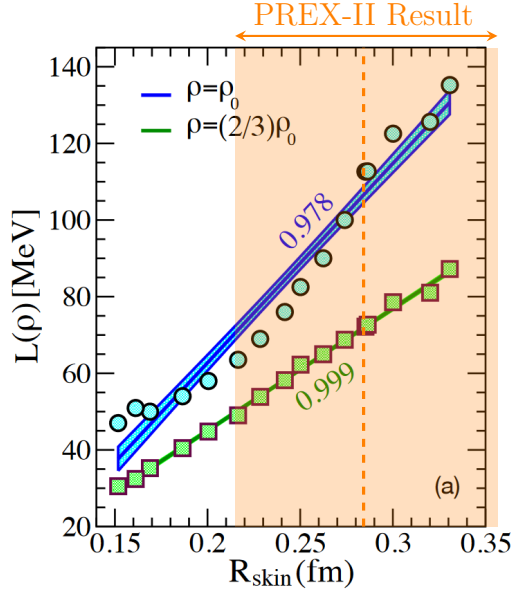


Figure 7.3: Symmetry energy term L plotted for saturation density ρ_0 and $\frac{2}{3}\rho_0$. The PREX-I and II mean and uncertainty on Δr_{np} are also drawn. Adapted from [109].

seen in Fig. 7.3.

The results of PREX-I and II find that at nuclear saturation density $L = (106 \pm 37)$ MeV [109]. And at $\frac{2}{3}$ saturation density (approximately the average of saturation and surface density) $L = (71.5 \pm 22.6)$ MeV. This result is striking because it is in tension with predictions made using different empirical and calculated constraints [110].

7.2.2 PREX-II & Neutron Stars

As discussed in Sec. 1.3.2, because the equation of state for a neutron star and a single nucleus of ^{208}Pb can be parameterized similarly, the measurement of Δr_{np} can be used to set bounds on the astrophysical properties of neutron stars. One important astrophysical parameter is the neutron star deformability Λ from Eqn. 1.42.

The NICER telescope on the International Space Station found that for a neutron star of 1.4 solar masses $11.96 \text{ km} \leq R_{NS} \leq 14.26 \text{ km}$ [111].

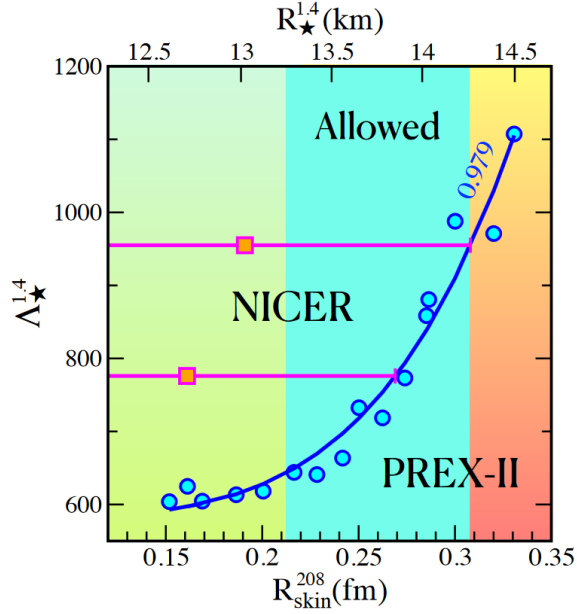


Figure 7.4: Deformability parameter $\Lambda_{1.4}$ for a neutron star of 1.4 solar masses plotted against Δr_{np}^{208} . Predictions by a set of energy density functionals appear in blue points. The PREX-II result can be seen along with the results from the NICER astronomical survey. There is good agreement between the two. Figure reproduced from [109].

This overlaps the bounds on R_{NS} set by the PREX-II result as seen in Fig. 7.4. The combination of NICER and PREX-II then limits deformability as: $642 \leq \Lambda_{1.4} \leq 955$. The binary neutron star merger event observed by LIGO (GW170817) initially put an upper bound on deformability as $\Lambda_{1.4} \leq 800$ [26]. A later review of the event set the bound as $\Lambda_{1.4} \leq 580$ [112] which conflicts the with PREX-II result. Whether this conflict is real or whether it can be resolved can be determined through future measurements on both neutron stars and ^{208}Pb .

7.2.3 CREX Implications for DOM Theories

Different approaches towards nuclear structure calculations yield different measurements of Δr_{np}^{48} as discussed in Sec. 1.3.3. While the neutron skin analysis for CREX is not yet complete at the time of this dissertation's publication, the high asymmetry measured clearly suggests a thin neutron

skin on ^{48}Ca . This appears to favor the *ab initio* calculations. In particular the chiral EFT NNLO_{sat} model predicts $0.12 \text{ fm} \leq \Delta r_{np}^{48} \leq 0.15 \text{ fm}$ [113].

The result is likely in tension with the ρ_n DOM model which predicted a neutron skin of $0.249 \pm 0.023 \text{ fm}$ [29]. For DFT models, while different models and parameterizations result in a range of radii $0.12 \text{ fm} \leq \Delta r_{np}^{48} \leq 0.26 \text{ fm}$ [114], the specific FSUGold prediction of $\Delta r_{np}^{48} = 0.20 \text{ fm}$ appears to be in slight tension with the CREX result. The CREX result skin thickness then should (once it is fully calculated) help inform DFT and DOM approaches to properly converge on a model that is sufficient for both ^{208}Pb and ^{48}Ca masses [44].

7.3 What Does the Future Hold?

PVES as an experimental technique has been in development for over forty years and has seen many improvements to the technique. Further developments in the technique are still on the horizon to allow for greater precision measurements on progressively lower \mathcal{A}_{PV} . Several proposed experiments will continue this development in different regimes of electroweak physics.

7.3.1 MOLLER

While the standard model predicts the existence of the weak-mixing term $\sin^2 \theta_w$, its value must be obtained empirically. The SLC device at SLAC and the LEP collider at CERN both made measurements of θ_w at $q \approx 100 \text{ GeV}$ using electron-positron collisions [115]. θ_w has also been measured at low q with results from Cs \mathcal{A}_{PV} [116] and Møller scattering [33]. The primary constraint on θ_w at low energies comes from Qweak [37], however higher precision measurements can still be made.

The MOLLER Experiment, a PVES measurement planned for JLab's Hall A will make an ultraprecise measurement of the weak mixing angle at $q^2 = 0.0056(\text{GeV}/c)^2$. The MOLLER proposal calls for a measurement of $\mathcal{A}_{PV} \approx (35.6 \pm 0.73) \text{ ppb}$, representing over an order of magnitude increase in required statistical and systematic precision from PREX-II and CREX.

To accomplish this the MOLLER collaboration has proposed a new spectrometer and detector package for Hall A to allow for an acceptance with low Q^2 . MOLLER will employ a toroidal spectrometer structure which allows for a high degree of separation between scattered electron angle and electron en-

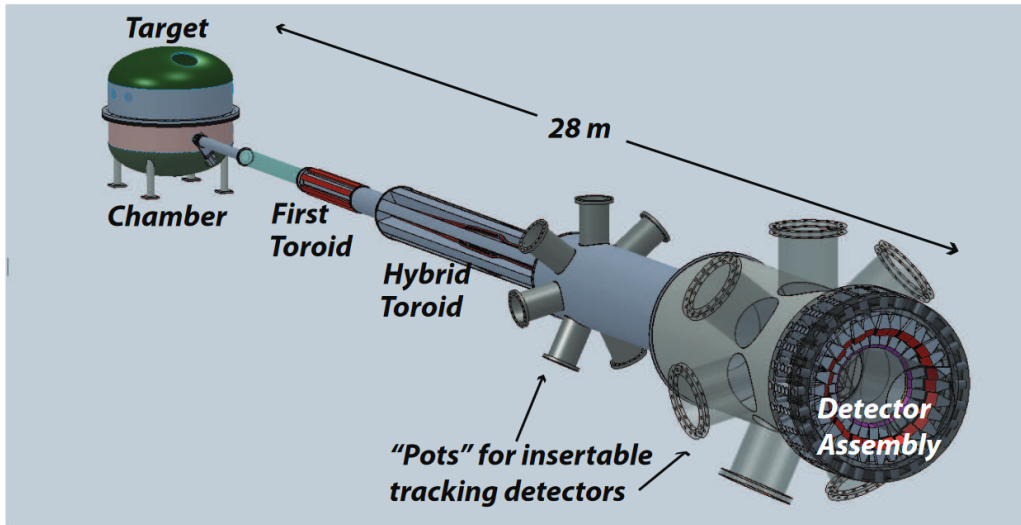


Figure 7.5: Schematic of the MOLLER target, spectrometer and detectors. Reproduced from [40].

ergy. This will allow for an acceptance with a scattering angle of $<1^\circ$ but with a high range of azimuthal angle scatters. The multi-year run plan will yield an 2.08% fractional statistical uncertainty.

The proposal also calls for a 1.0% bound on total systematic uncertainty. This would include a 0.5% bound on Q^2 uncertainty, a 0.4% bound on both beam corrections and beam polarimetry [117]. PREX-II and CREX have shown significant progress towards meeting these goals for MOLLER. In particular the 0.44% beam polarization measurement from CREX presented in this dissertation¹ has shown that 0.4% polarimetry is possible and imminently achievable at JLab. Nevertheless, development on the MOLLER experiment continues in order to achieve the experiment's precision goals.

7.3.2 SoLID

Another project coming to Hall A at JLab is the Solenoidal Large Intensity Detector (SoLID). SoLID is a high-luminosity, large-acceptance detector package which includes GEM tracking detectors, electron and hadron Čerenkov detectors, and a calorimeter for particle identification. The detec-

¹see Ch. 5 and Sec. 5.7 for more information.

tor acceptance will also be a significantly larger fraction than that used for PREX-II and CREX. The design of the SoLID detector can be seen in Fig. 7.6.

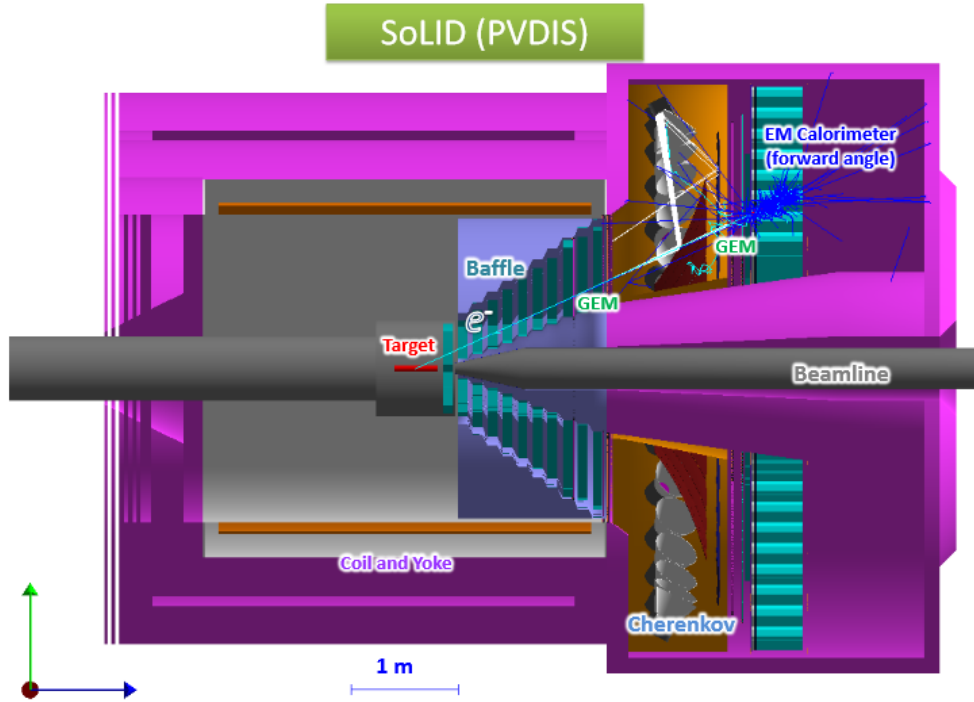


Figure 7.6: Cross-sectional simulation model of the SoLID detector in its PVDIS configuration. Reproduced from [118].

One of the experiments approved for the SoLID run program is a parity-violating deep inelastic scattering (PVDIS) measurement. The goal of this experiment is to precisely measure the weak couplings of quarks C_{2q} . This will serve as an extension to a past Hall A PVDIS experiment from before the 12 GeV accelerator upgrade [119].

This PVDIS experiment calls for a 0.6% precision measurement on \mathcal{A}_{PV} which will again require tight controls on systematic uncertainties. Like MOLLER, SoLID PVDIS also calls for a 0.4% bound on beam polarimetry which must be achieved in order to fulfill experimental goals [118].

7.3.3 P2 & MREX

In addition to the MOLLER experiment, the P2 experiment seeks to make a high-precision measurement θ_w at low q . The P2 experiment proposes to measure an \mathcal{A}_{PV} of 39.94 ppb, which would make it the smallest PVES asymmetry measured to date. P2 seeks to make this measurement to a precision of $\delta\mathcal{A}_{PV}/\mathcal{A}_{PV} = 1.4\%$. To do this P2 will take advantage of the Mainz Microtron (MAMI) accelerator in Mainz, Germany, which will produce a 155 MeV spin-polarized electron beam. This experiment will run after the construction of the Mainz Energy Recover Superconducting Accelerator (MESA) is finished.

Additionally the MESA facility will also host the MREX experiment, which measures the same \mathcal{A}_{PV} on ^{208}Pb that PREX-II did, but to an even high degree of precision (1.4% total.) [120]

7.4 Summary

PREX-II and CREX represent a substantial advancement not just for the PVES technique but also for different approaches to nuclear structure theory. The PREX-II neutron skin measurement $\Delta r_{np}^{208} = (0.283 \pm 0.071)$ fm favors a stiff equation of state for ^{208}Pb nuclei. This also indicates a similar state in the polarizability and deformability of neutron stars which motivates further studies of both heavy nuclei on Earth and neutron stars in the heavens. The PREX-II result may even prove to be useful to theoreticians using *ab initio* approaches as calculation efficiency begins to approach the level where ^{208}Pb nuclei can be modeled [121]. While the CREX measurement is not yet fully analyzed, it offers the potential to resolve differing predictions of different nuclear models.

Running both PREX-II and CREX was an important challenge to be met. Both experiments were designed to operate with high radiation-length high- Z targets, meaning radiological hazards had to be properly controlled to make these experiments possible. In addition, the data acquisition had to operate at extremely high rate to maximize statistical precision. Data quality was monitored continuously throughout running to keep the asymmetry data quality high enough to minimize the magnitude of systematic corrections.

Concerning beam polarimetry, the CREX Compton measurement in particular $\mathcal{P}_e^{\text{Compton}} = (87.115 \pm 0.453)\%$ demonstrates the capabilities of Comp-

ton polarimetry at JLab. At 0.52% fractional uncertainty the CREX measurement is the most precise polarization measurement at JLab and among the most precise measurements made with any Compton polarimeter. However, there is still work to be done to fulfill the 0.4% polarimetry uncertainty requirements for future PVES experiments.

Appendix A

PREX-II Compton Snailwise Plots

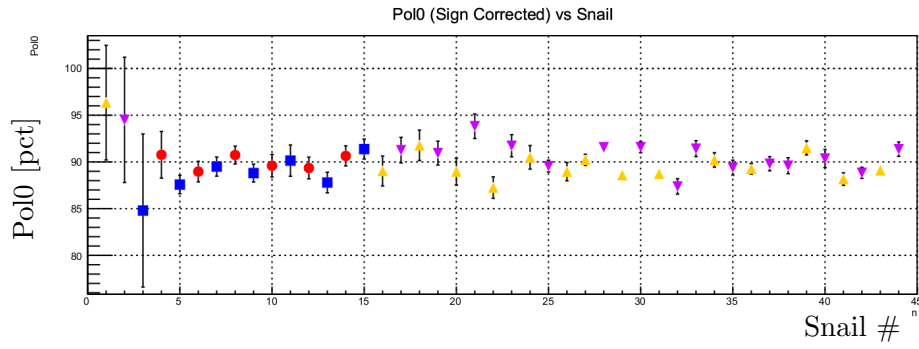
This appendix contains the plots for various quantities as tracked and plotted over snails for the entire Compton running of the PREX-II experiment. The quantities shown here are in order:

- **Pol0:** The mean beam polarization measured in each snail.
- **Asym0:** The mean asymmetry measured in each snail including gain shift correction from Eqn. 5.28 and radiative corrections.
- **Asym0NGC:** The mean asymmetry measured in each snail, not including gain shift or radiative corrections.
- **Asym0LasOn:** The mean asymmetry of the laser-on period in each laser cycle in the snail. Same asymmetry as in Eqn. 5.8.
- **Asym0LasOff:** The mean asymmetry of the two laser-off periods in each laser cycle in the snail. Same asymmetry as in Eqn. 5.9.
- **numRuns:** The number of Compton CODA runs in each snail.
- **numCycles:** The number of complete laser cycles identified in the snail.
- **numCyclesAcc:** The number of complete laser cycles which passed CycleCut (described in Sec. 5.3.2) in the snail.

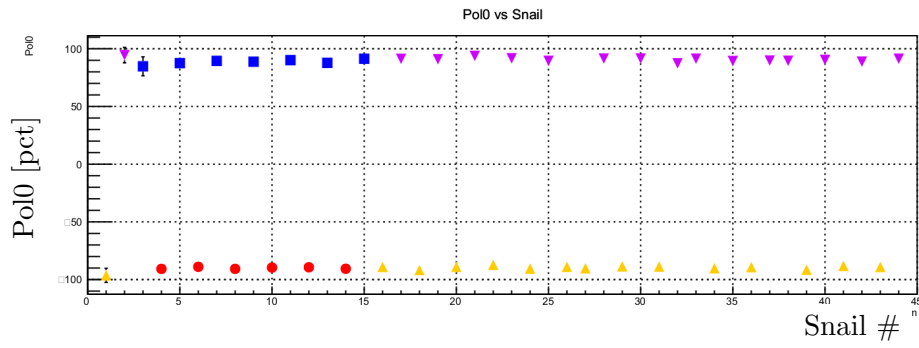
- **qw1:** QW1 angle setting, measured in encoder units.
- **hw1:** HW1 angle setting, measured in encoder units.
- **qw2:** QW2 angle setting, measured in encoder units.
- **LaserPolarization:** Laser cavity DOCP for each snail.
- **snailTime:** The total time each accepted laser cycle took in the snail, measured in seconds.

Additionally plots of asymmetry and polarization are shown in both sign-corrected and non-sign-corrected variants. The sign correction is applied for each snail depending on the Wien and IHWP configuration relative to the Pockels cell voltage. If the snail was taken in either Wien-Left and IHWP-Out or Wien-Right and IHWP-In configurations the asymmetry is multiplied by +1. Conversely, if the snail was taken in either Wien-Right and IHWP-Out or Wien-Left and IHWP-In configurations the asymmetry is multiplied by -1. This is to reflect that fact that flipping the wien or the IHWP states each reverses the direction of beam polarization relative to the Pockels cell voltage and the sign of the asymmetry measured in the Compton photon detector will be opposite for each flip.

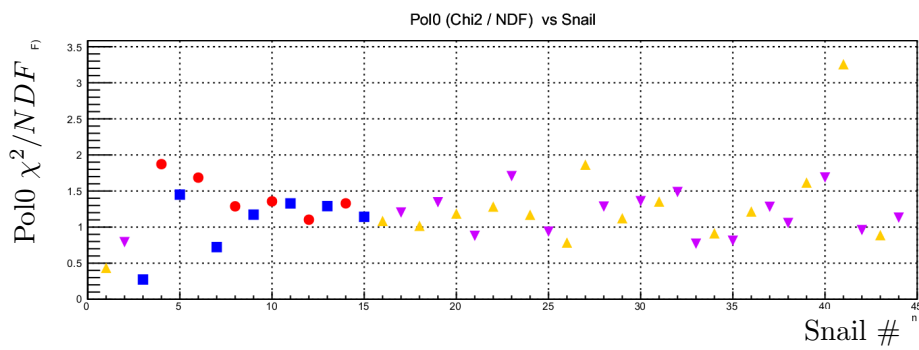
Also, snail variables that were computed as a weighted average of cycle variables (such as polarization and asymmetry) also have their relevant χ^2 per fit degree of freedom plotted.



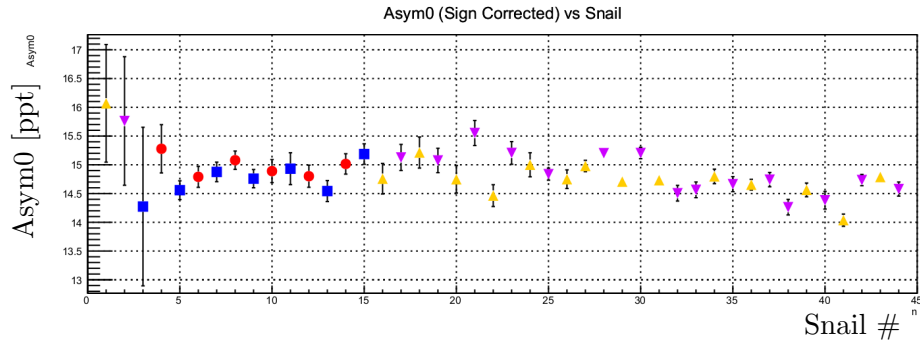
Sign-Corrected Pol0 vs. Snail Number



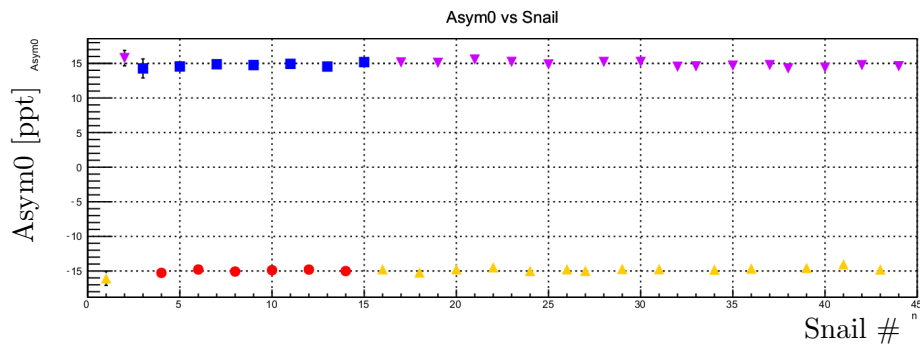
Pol0 vs. Snail Number



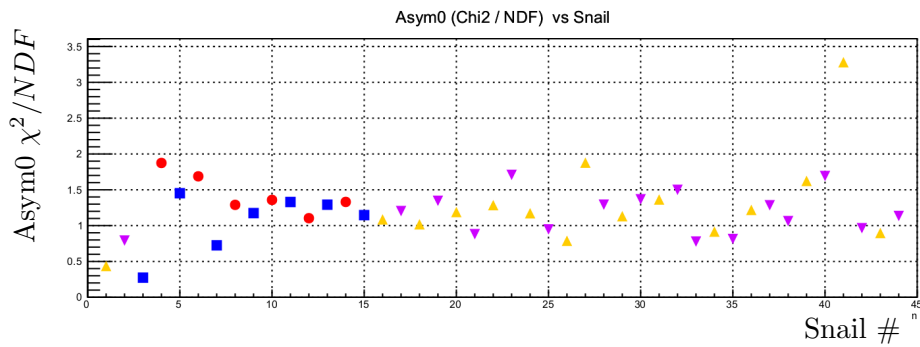
Pol0 χ^2 / NDF vs. Snail Number



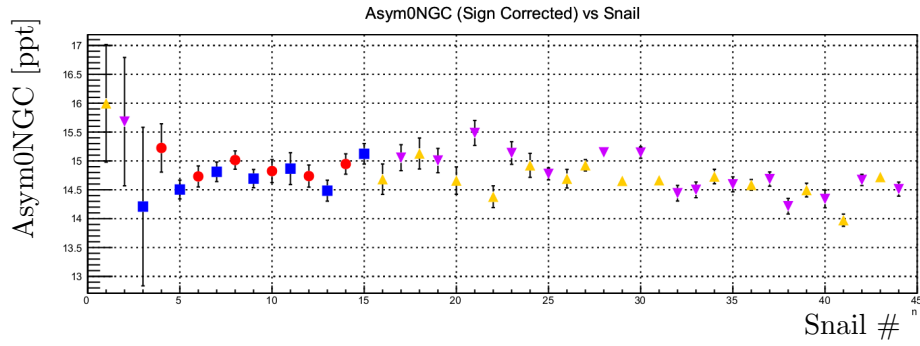
Sign-Corrected Asym0 vs. Snail Number



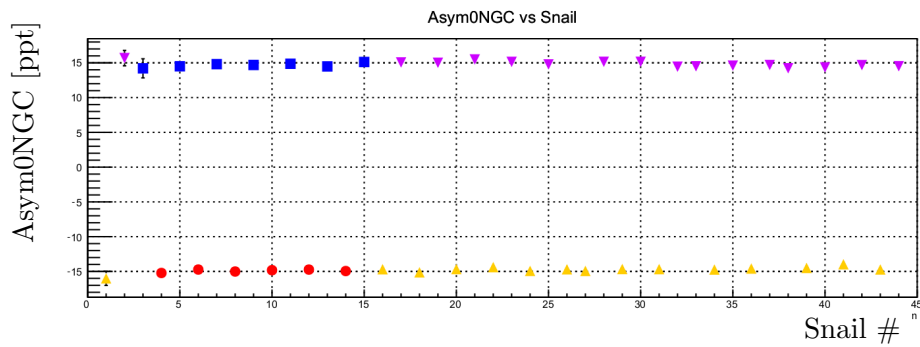
Asym0 vs. Snail Number



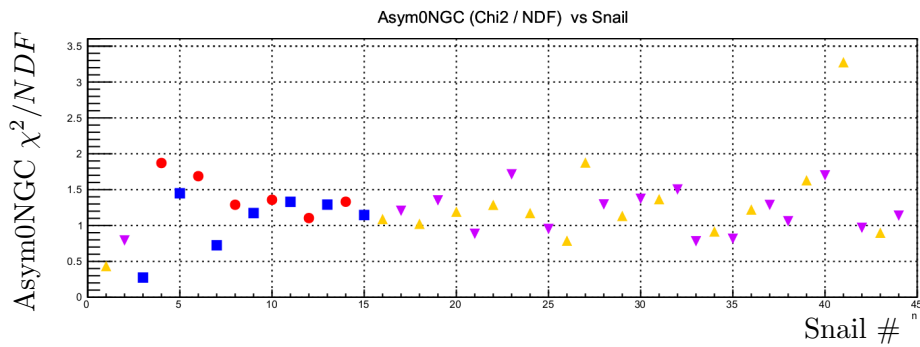
Asym0 χ^2/NDF vs. Snail Number



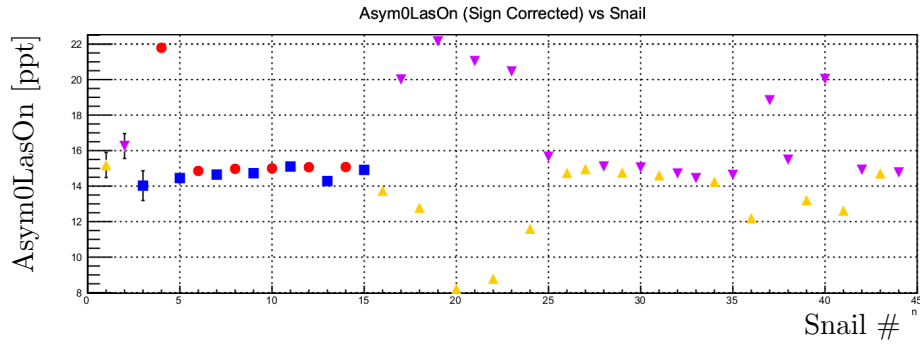
Sign-Corrected Asym0NGC vs. Snail Number



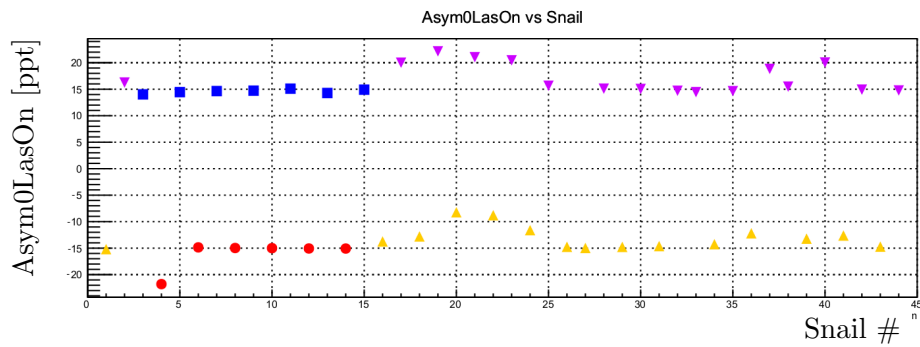
Asym0NGC vs. Snail Number



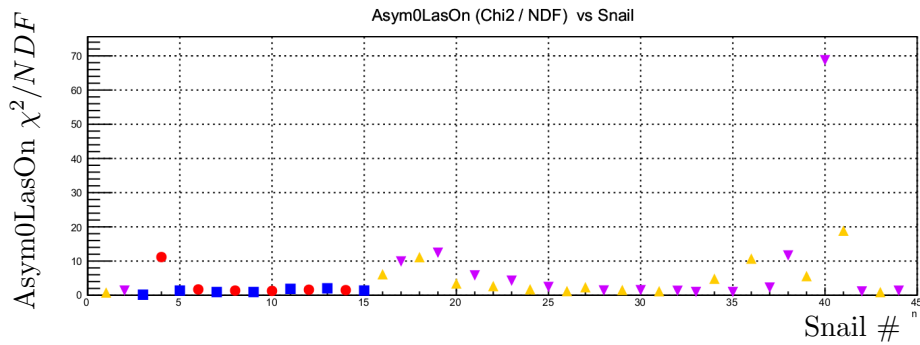
Asym0NGC χ^2/NDF vs. Snail Number



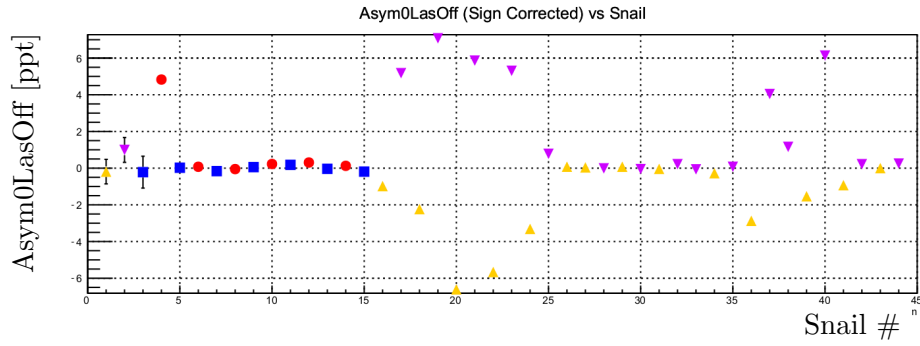
Sign-Corrected Asym0LasOn vs. Snail Number



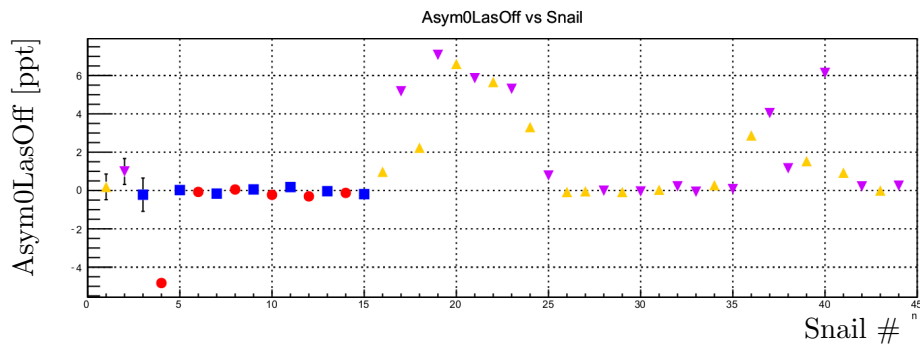
Asym0LasOn vs. Snail Number



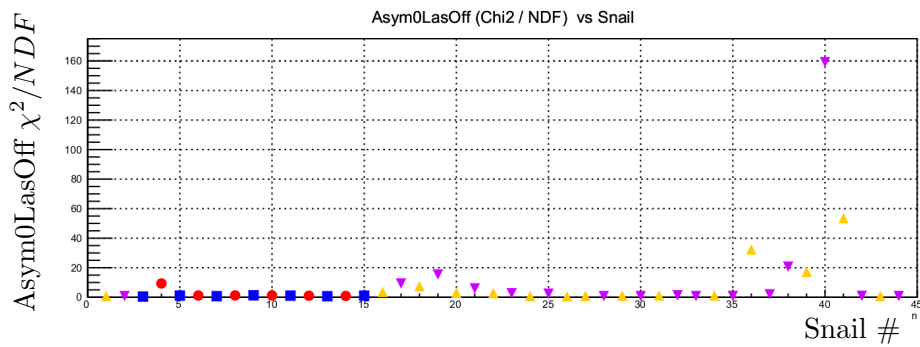
Asym0LasOn χ^2/NDF vs. Snail Number



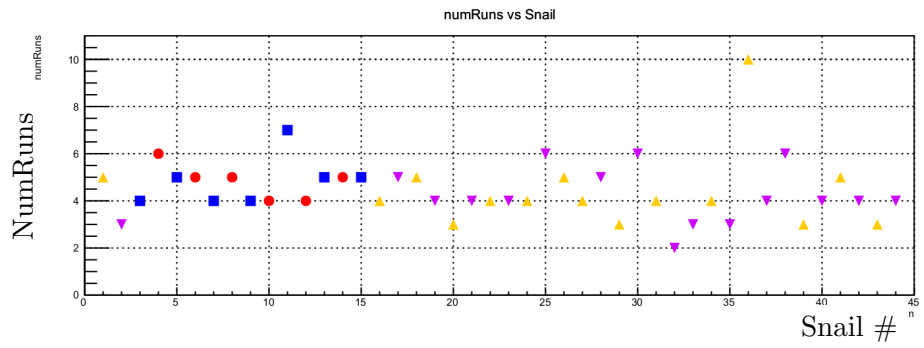
Sign-Corrected Asym0LasOff vs. Snail Number



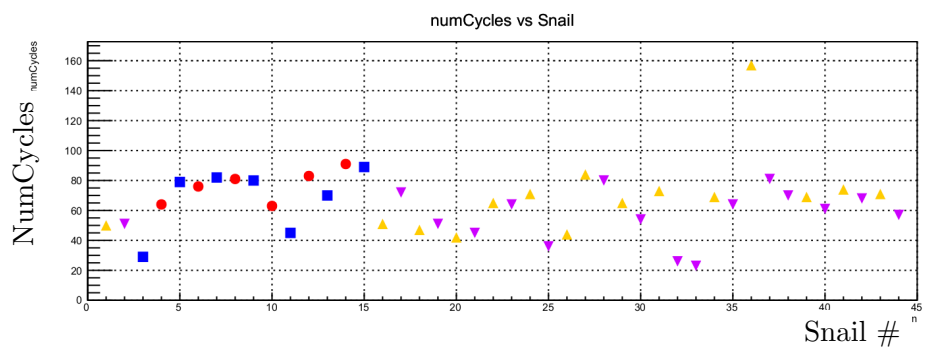
Asym0LasOff vs. Snail Number



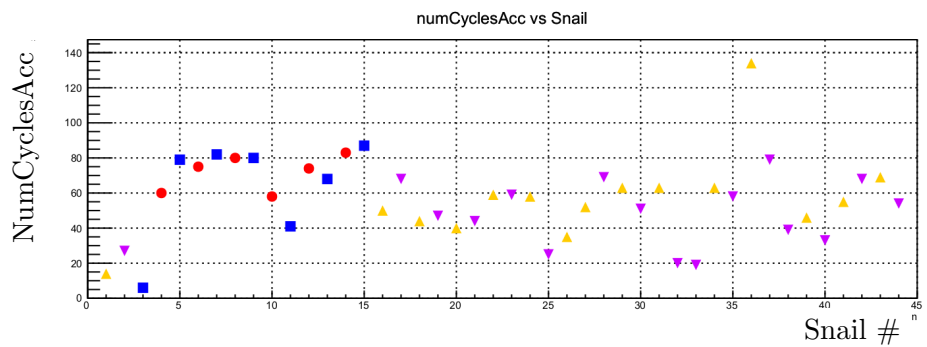
Asym0LasOff χ^2/NDF vs. Snail Number



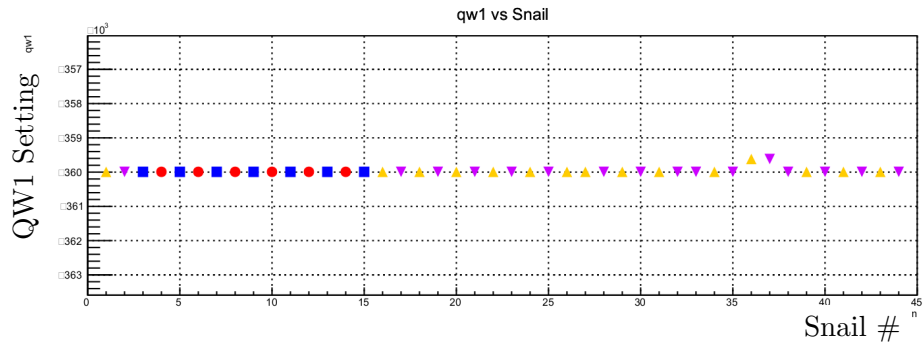
NumRuns vs. Snail Number



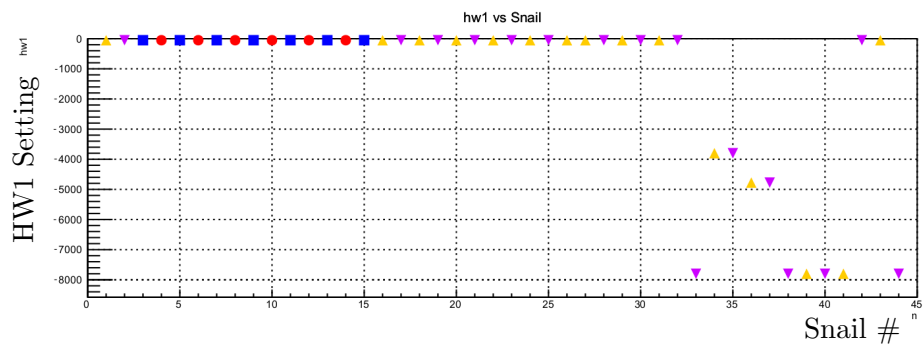
NumCycles vs. Snail Number



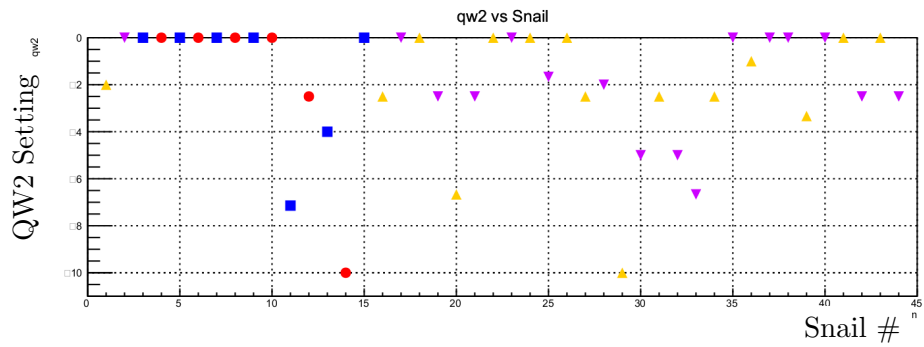
NumCyclesAcc vs. Snail Number



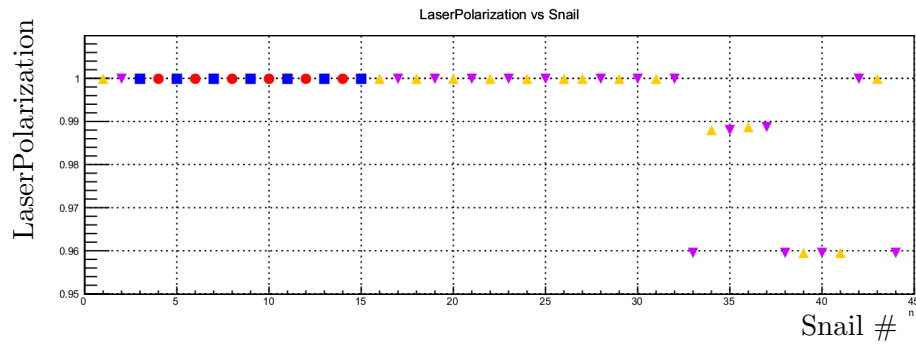
QW1 vs. Snail Number



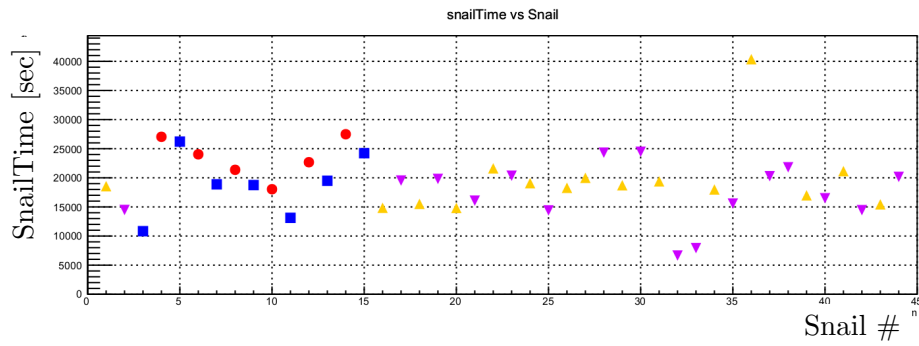
HW1 vs. Snail Number



QW2 vs. Snail Number



LaserPolarization vs. Snail Number

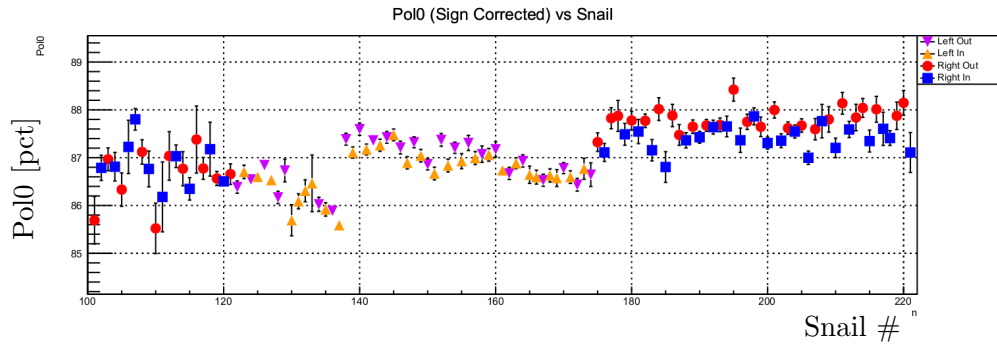


Snail Time vs. Snail Number

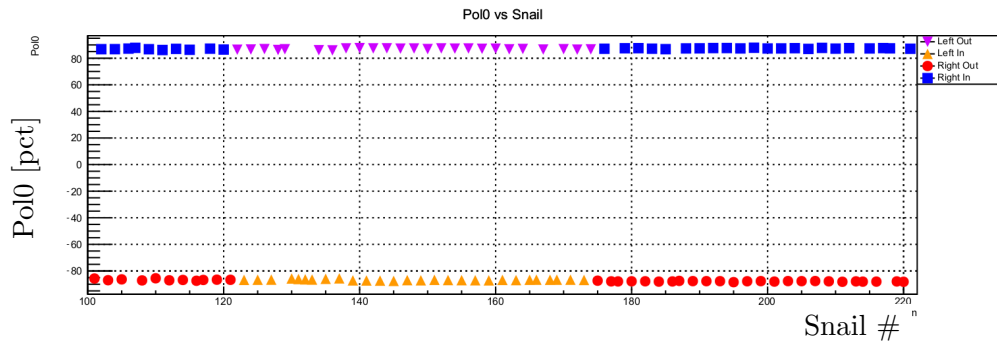
Appendix B

CREX Compton Snailwise Plots

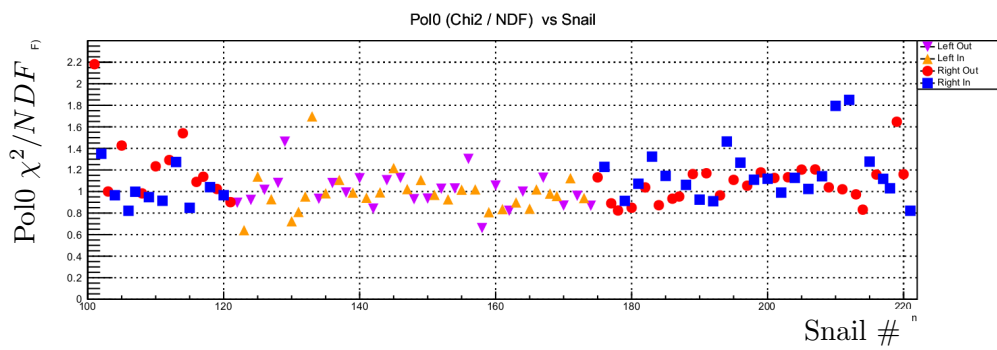
This appendix contains the plots for various quantities as tracked and plotted over snails for the entire Compton running of the CREX experiment. The plots here are in the same order and quantity as Appendix A.



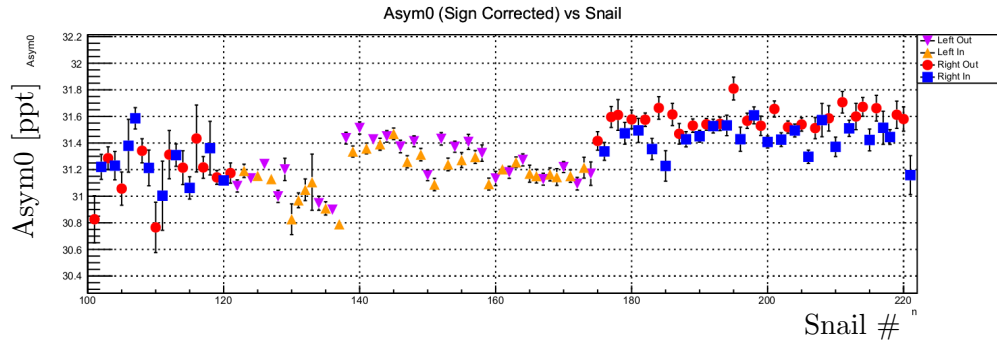
Sign-Corrected Pol0 vs. Snail Number



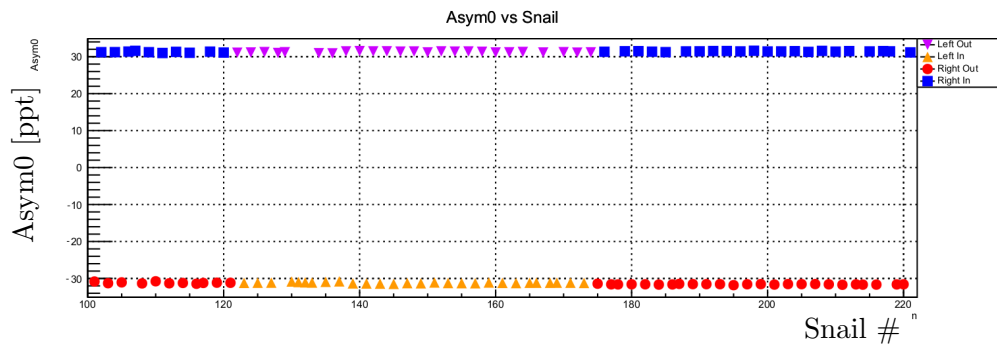
Pol0 vs. Snail Number



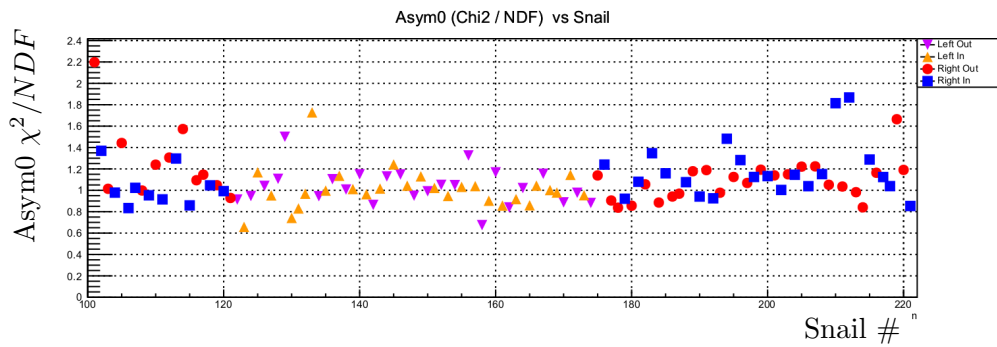
Pol0 χ^2/NDF vs. Snail Number



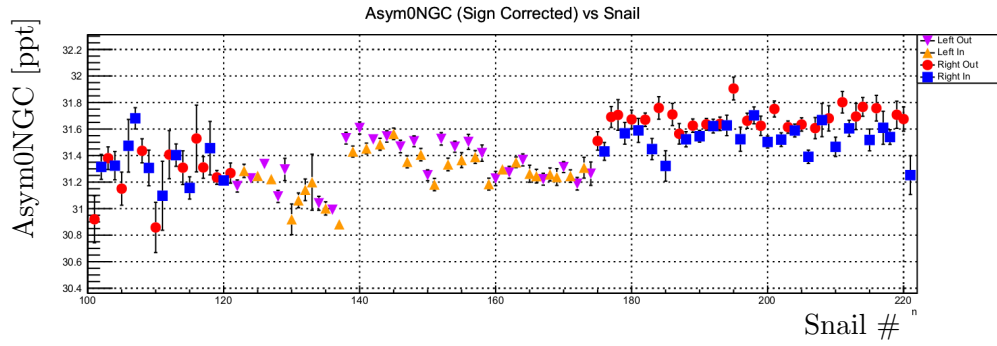
Sign-Corrected Asym0 vs. Snail Number



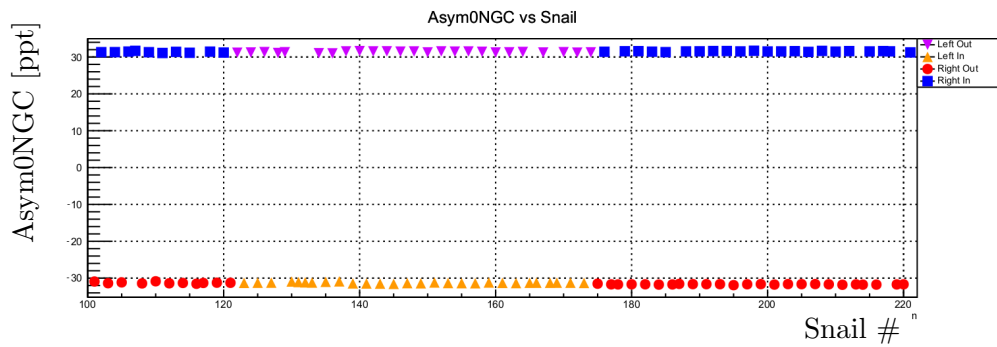
Asym0 vs. Snail Number



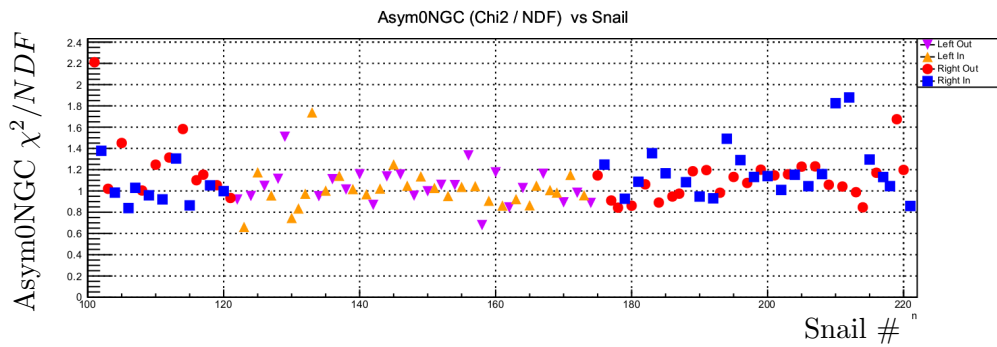
Asym0 χ^2/NDF vs. Snail Number



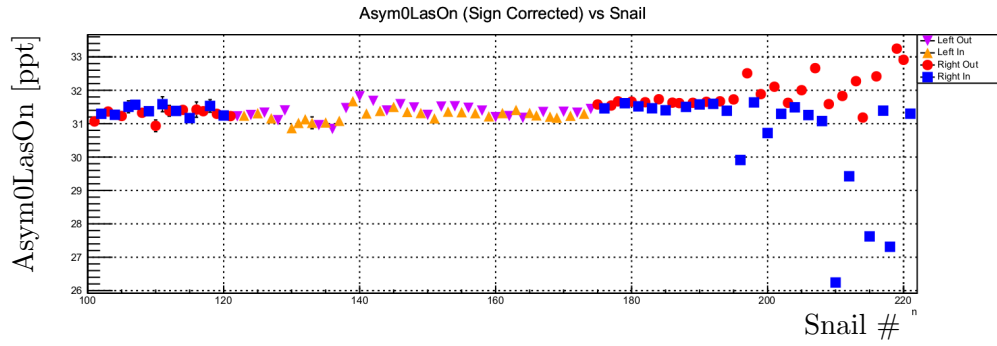
Sign-Corrected Asym0NGC vs. Snail Number



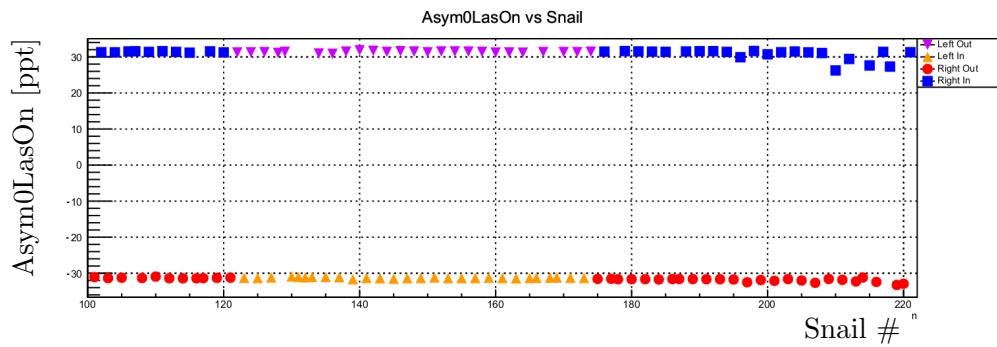
Asym0NGC vs. Snail Number



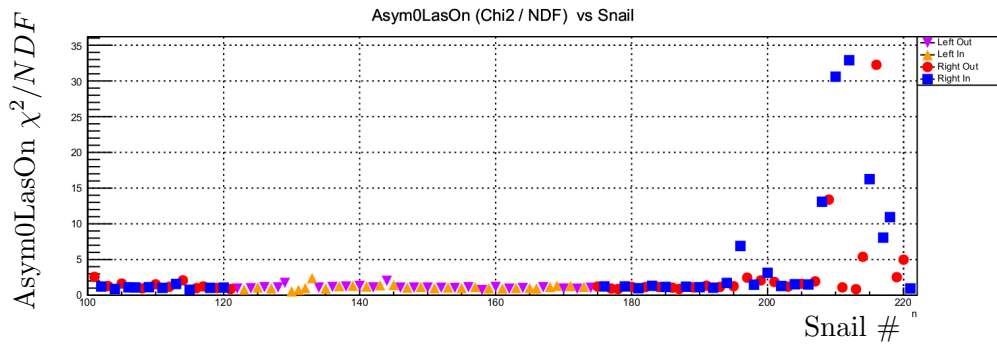
Asym0NGC χ^2 / NDF vs. Snail Number



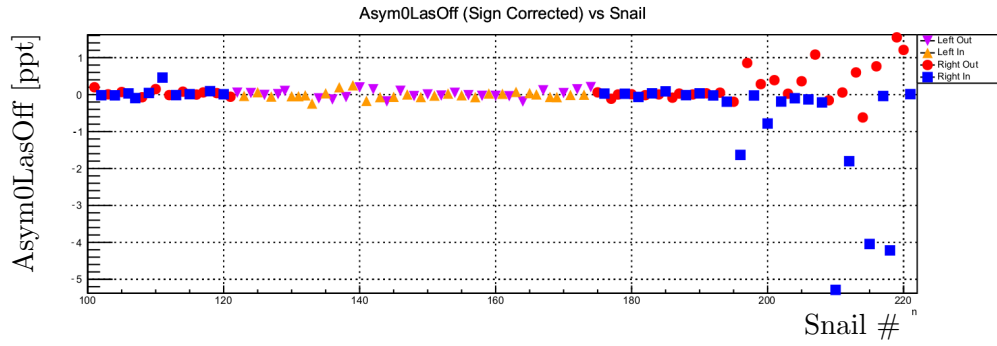
Sign-Corrected Asym0LasOn vs. Snail Number



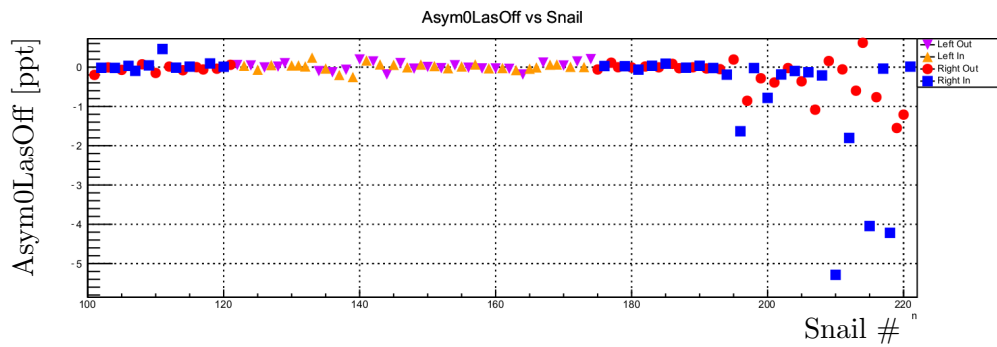
Asym0LasOn vs. Snail Number



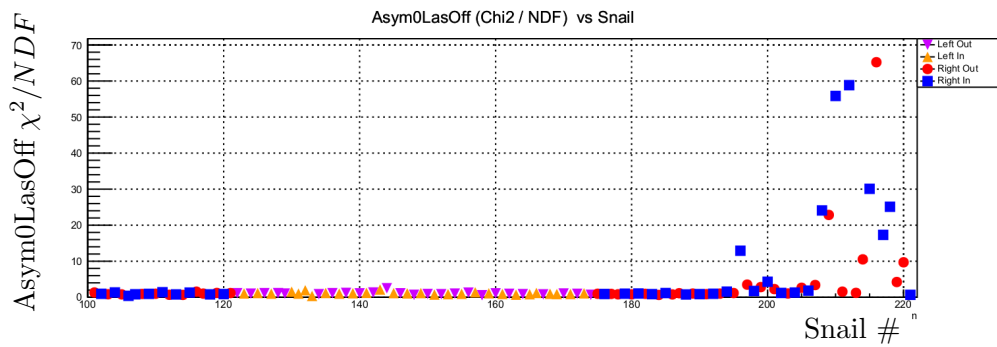
Asym0LasOn χ^2/NDF vs. Snail Number



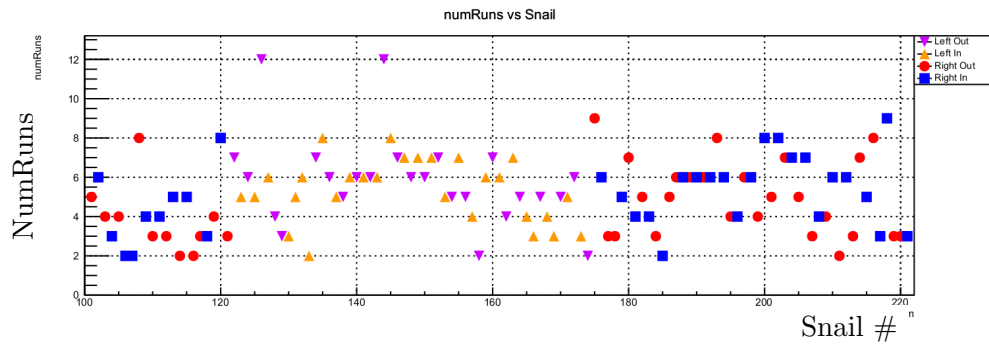
Sign-Corrected Asym0LasOff vs. Snail Number



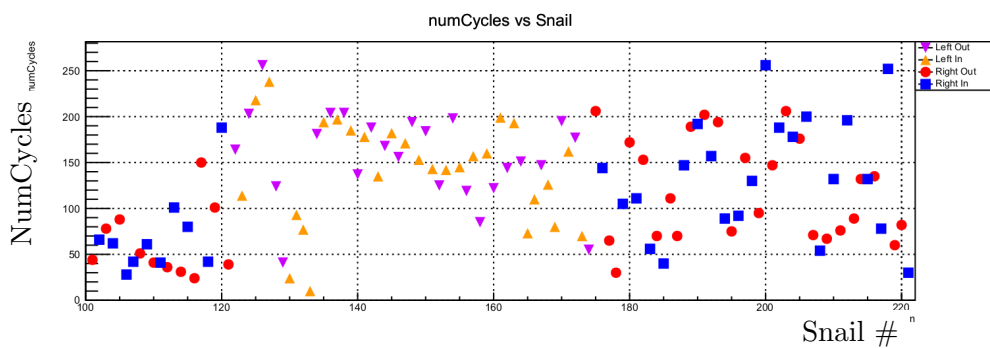
Asym0LasOff vs. Snail Number



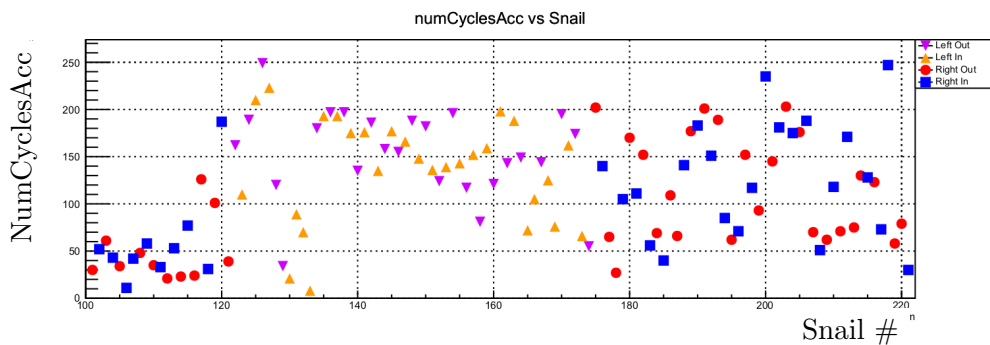
Asym0LasOff χ^2/NDF vs. Snail Number



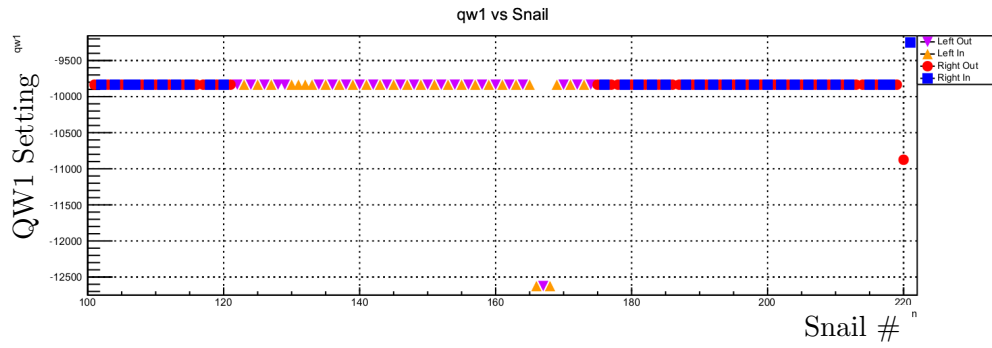
NumRuns vs. Snail Number



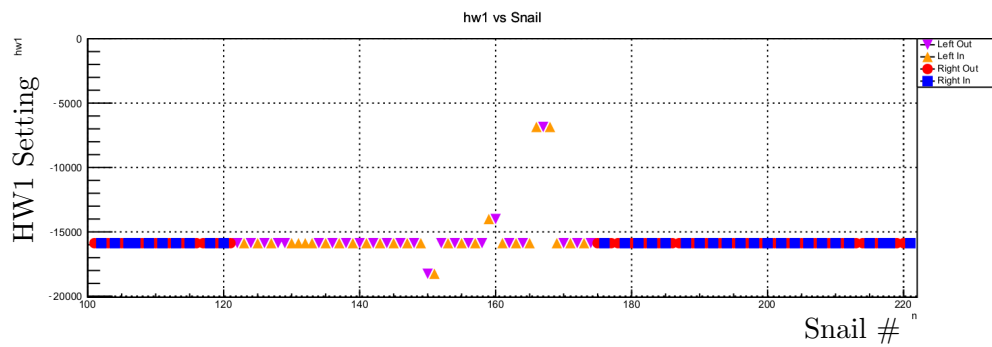
NumCycles vs. Snail Number



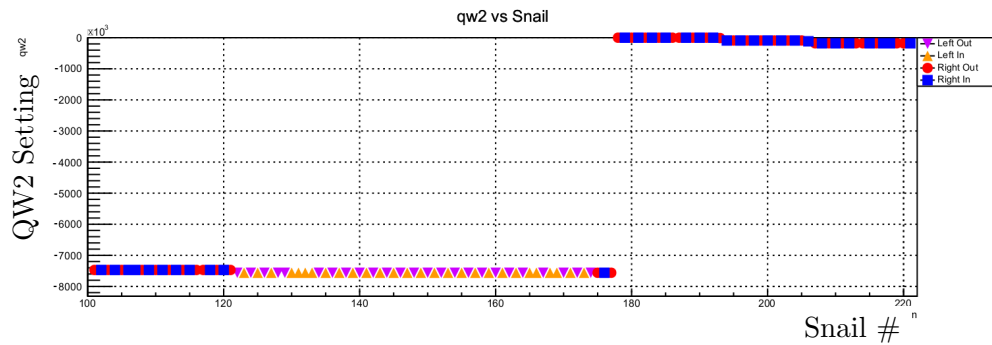
NumCyclesAcc vs. Snail Number



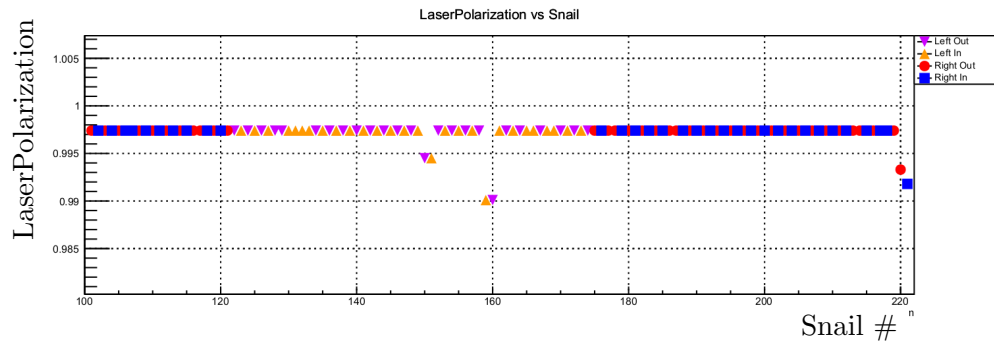
QW1 vs. Snail Number



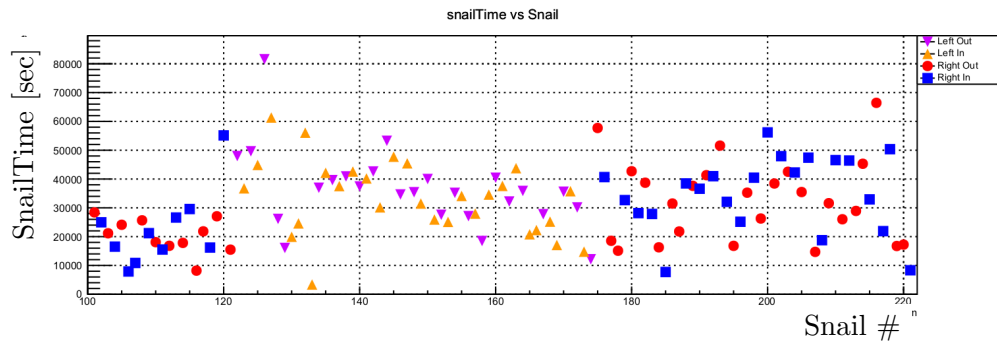
HW1 vs. Snail Number



QW2 vs. Snail Number



LaserPolarization vs. Snail Number



Snail Time vs. Snail Number

Bibliography

- [1] Professor E. Rutherford F.R.S. “LXXIX. The scattering of α and β particles by matter and the structure of the atom”. In: *The London, Edinburgh, and Dublin Philosophical Magazine and Journal of Science* 21.125 (1911), pp. 669–688. DOI: 10.1080/14786440508637080.
- [2] N. Bohr. “I. On the constitution of atoms and molecules”. In: *The London, Edinburgh, and Dublin Philosophical Magazine and Journal of Science* 26.151 (1913), pp. 1–25. DOI: 10.1080/14786441308634955.
- [3] J. Chadwick. “Possible Existence of a Neutron”. In: *Nature* 129 (1932), p. 312. DOI: 10.1038/129312a0.
- [4] W. Gerlach and O. Stern. “Der experimentelle Nachweis der Richtungsquantelung im Magnetfeld (In German) [The experimental proof of directional quantization in a magnetic field]”. In: *Zeitschrift für Physik* 9 (1922), pp. 349–352. DOI: 10.1007/BF01326983.
- [5] W. Pauli, Jr. “Zur Quantenmechanik des magnetischen Elektrons. (German) [On the quantum mechanics of the magnetic electron]”. German. In: *j-Z-PHYSIK* 43.9–10 (Sept. 1927), pp. 601–623. ISSN: 0939-7922 (print), 1431-5831 (electronic). DOI: <https://doi.org/10.1007/BF01397326>. URL: <http://link.springer.com/article/10.1007/BF01397326>; <http://www.springerlink.com/content/ww10g288m777t400/fulltext.pdf>.
- [6] Paul Adrien Maurice Dirac. “The quantum theory of the electron”. In: *Proc. R. Soc. Lond. A* 117 (1928), pp. 610–624. DOI: 10.1098/rspa.1928.0023.
- [7] T. D. Lee and C. N. Yang. “Question of Parity Conservation in Weak Interactions”. In: *Phys. Rev.* 104 (1 Oct. 1956), pp. 254–258. DOI: 10.1103/PhysRev.104.254. URL: <https://link.aps.org/doi/10.1103/PhysRev.104.254>.

- [8] C. S. Wu et al. “Experimental Test of Parity Conservation in Beta Decay”. In: *Phys. Rev.* 105 (4 Feb. 1957), pp. 1413–1415. DOI: 10.1103/PhysRev.105.1413. URL: <https://link.aps.org/doi/10.1103/PhysRev.105.1413>.
- [9] B Foris and C N Papanicolas. “Electron Scattering and Nuclear Structure”. In: *Annual Review of Nuclear and Particle Science* 37.1 (1987), pp. 133–176. DOI: 10.1146/annurev.ns.37.120187.001025.
- [10] H. De Vries, C.W. De Jager, and C. De Vries. “Nuclear charge-density-distribution parameters from elastic electron scattering”. In: *Atomic Data and Nuclear Data Tables* 36.3 (1987), pp. 495–536. ISSN: 0092-640X. DOI: [https://doi.org/10.1016/0092-640X\(87\)90013-1](https://doi.org/10.1016/0092-640X(87)90013-1). URL: <https://www.sciencedirect.com/science/article/pii/0092640X87900131>.
- [11] G. W. Hoffmann et al. “0.8 GeV $p+^{208}\text{Pb}$ elastic scattering and the quantity Δr_{np} ”. In: *Phys. Rev. C* 21 (4 Apr. 1980), pp. 1488–1494. DOI: 10.1103/PhysRevC.21.1488. URL: <https://link.aps.org/doi/10.1103/PhysRevC.21.1488>.
- [12] A. Krasznahorkay et al. “Neutron-skin thickness in neutron-rich isotopes”. In: *Nuclear Physics A* 731 (2004), pp. 224–234. ISSN: 0375-9474. DOI: <https://doi.org/10.1016/j.nuclphysa.2003.11.034>. URL: <https://www.sciencedirect.com/science/article/pii/S0375947403018712>.
- [13] C.Y. Prescott et al. “Parity non-conservation in inelastic electron scattering”. In: *Physics Letters B* 77.3 (1978), pp. 347–352. ISSN: 0370-2693. DOI: [https://doi.org/10.1016/0370-2693\(78\)90722-0](https://doi.org/10.1016/0370-2693(78)90722-0). URL: <https://www.sciencedirect.com/science/article/pii/0370269378907220>.
- [14] David Griffiths. “Introduction to Elementary Particles”. In: 1st. John Wiley & Sons Inc., 1987, pp. 198–201. ISBN: 0-471-60386-4.
- [15] R. P. Feynman. “Space-Time Approach to Quantum Electrodynamics”. In: *Phys. Rev.* 76 (6 Sept. 1949), pp. 769–789. DOI: 10.1103/PhysRev.76.769. URL: <https://link.aps.org/doi/10.1103/PhysRev.76.769>.

- [16] E. Fermi. “Versuch einer Theorie der β -Strahlen [An Attempt at a Theory of β -Rays]”. In: *Z. Physik* 88 (Mar. 1934), pp. 161–177. DOI: 10.1007/BF01351864.
- [17] Steven Weinberg. “A Model of Leptons”. In: *Phys. Rev. Lett.* 19 (21 Nov. 1967), pp. 1264–1266. DOI: 10.1103/PhysRevLett.19.1264. URL: <https://link.aps.org/doi/10.1103/PhysRevLett.19.1264>.
- [18] C. J. Horowitz et al. “Parity violating measurements of neutron densities”. In: *Phys. Rev. C* 63 (2 Jan. 2001), p. 025501. DOI: 10.1103/PhysRevC.63.025501. URL: <https://link.aps.org/doi/10.1103/PhysRevC.63.025501>.
- [19] Devi Lal Adhikari. “Neutron Skin Measurement of ^{208}Pb Using Parity-Violating Electron Scattering”. PhD thesis. Pocatello, ID, USA 83201: Idaho State University, May 2021.
- [20] X. Roca-Maza et al. “Neutron Skin of ^{208}Pb , Nuclear Symmetry Energy, and the Parity Radius Experiment”. In: *Phys. Rev. Lett.* 106 (25 June 2011), p. 252501. DOI: 10.1103/PhysRevLett.106.252501. URL: <https://link.aps.org/doi/10.1103/PhysRevLett.106.252501>.
- [21] “University Physics”. In: vol. 3. 2016. Chap. 74. ISBN: 978-1-947172-22-7.
- [22] Wei-Chia Chen and J. Piekarewicz. “Building relativistic mean field models for finite nuclei and neutron stars”. In: *Phys. Rev. C* 90 (4 Oct. 2014), p. 044305. DOI: 10.1103/PhysRevC.90.044305. URL: <https://link.aps.org/doi/10.1103/PhysRevC.90.044305>.
- [23] X. Roca-Maza and N. Paar. “Nuclear equation of state from ground and collective excited state properties of nuclei”. In: *Progress in Particle and Nuclear Physics* 101 (2018), pp. 96–176. ISSN: 0146-6410. DOI: <https://doi.org/10.1016/j.ppnp.2018.04.001>. URL: <https://www.sciencedirect.com/science/article/pii/S0146641018300334>.
- [24] M Thiel et al. “Neutron skins of atomic nuclei: per aspera ad astra”. In: *Journal of Physics G: Nuclear and Particle Physics* 46.9 (Aug. 2019), p. 093003. ISSN: 1361-6471. DOI: 10.1088/1361-6471/ab2c6d.

- [25] F. J. Fattoyev, J. Piekarewicz, and C. J. Horowitz. “Neutron Skins and Neutron Stars in the Multimessenger Era”. In: *Physical Review Letters* 120.17 (Apr. 2018). ISSN: 1079-7114. DOI: 10.1103/physrevlett.120.172702.
- [26] B. P. et al. Abbott. “GW170817: Observation of Gravitational Waves from a Binary Neutron Star Inspiral”. In: *Phys. Rev. Lett.* 119 (16 Oct. 2017), p. 161101. DOI: 10.1103/PhysRevLett.119.161101. URL: <https://link.aps.org/doi/10.1103/PhysRevLett.119.161101>.
- [27] Michael Bender, Paul-Henri Heenen, and Paul-Gerhard Reinhard. “Self-consistent mean-field models for nuclear structure”. In: *Rev. Mod. Phys.* 75 (1 Jan. 2003), pp. 121–180. DOI: 10.1103/RevModPhys.75.121. URL: <https://link.aps.org/doi/10.1103/RevModPhys.75.121>.
- [28] C Forssén et al. “Living on the edge of stability, the limits of the nuclear landscape”. In: *Physica Scripta* T152 (Jan. 2013), p. 014022. DOI: 10.1088/0031-8949/2013/t152/014022.
- [29] M. H. Mahzoon et al. “Neutron Skin Thickness of ^{48}Ca from a Nonlocal Dispersive Optical-Model Analysis”. In: *Phys. Rev. Lett.* 119 (22 Nov. 2017), p. 222503. DOI: 10.1103/PhysRevLett.119.222503. URL: <https://link.aps.org/doi/10.1103/PhysRevLett.119.222503>.
- [30] R. F. Garcia Ruiz et al. “Unexpectedly large charge radii of neutron-rich calcium isotopes”. In: *Nature Physics* 12.6 (Feb. 2016), pp. 594–598. ISSN: 1745-2481. DOI: 10.1038/nphys3645. URL: <http://dx.doi.org/10.1038/nphys3645>.
- [31] T. M. Ito et al. “Parity-Violating Electron Deuteron Scattering and the Proton’s Neutral Weak Axial Vector Form Factor”. In: *Physical Review Letters* 92.10 (Mar. 2004). ISSN: 1079-7114. DOI: 10.1103/physrevlett.92.102003.
- [32] F. E. Maas et al. “Measurement of Strange-Quark Contributions to the Nucleon’s Form Factors at $Q^2=0.230\text{ (GeV/c)}^2$ ”. In: *Physical Review Letters* 93.2 (July 2004). ISSN: 1079-7114. DOI: 10.1103/physrevlett.93.022002.

- [33] P. L. Anthony et al. “Precision Measurement of the Weak Mixing Angle in Møller Scattering”. In: *Phys. Rev. Lett.* 95 (8 Aug. 2005), p. 081601. DOI: 10.1103/PhysRevLett.95.081601. URL: <https://link.aps.org/doi/10.1103/PhysRevLett.95.081601>.
- [34] K. A. Aniol et al. “Parity-Violating Electron Scattering from ^4He and the Strange Electric Form Factor of the Nucleon”. In: *Phys. Rev. Lett.* 96 (2 Jan. 2006), p. 022003. DOI: 10.1103/PhysRevLett.96.022003. URL: <https://link.aps.org/doi/10.1103/PhysRevLett.96.022003>.
- [35] Z. Ahmed et al. “New Precision Limit on the Strange Vector Form Factors of the Proton”. In: *Phys. Rev. Lett.* 108 (10 Mar. 2012), p. 102001. DOI: 10.1103/PhysRevLett.108.102001. URL: <https://link.aps.org/doi/10.1103/PhysRevLett.108.102001>.
- [36] S. Abrahamyan et al. “Measurement of the Neutron Radius of ^{208}Pb Through Parity-Violation in Electron Scattering”. In: *Phys. Rev. Lett.* 108 (2012), p. 112502. DOI: 10.1103/PhysRevLett.108.112502. arXiv: 1201.2568 [nucl-ex].
- [37] The Jefferson Lab Qweak Collaboration. “Precision measurement of the weak charge of the proton”. In: *Nature* 557 (2018), pp. 207–211. DOI: <https://doi.org/10.1038/s41586-018-0096-0>.
- [38] K. Paschke et al. “PREX-II: Precision Parity-Violating Measurement of the Neutron Skin of Lead”. PREX-II Proposal. 2011.
- [39] J. Mammei et al. “CREX: Parity Violating Measurement of the Weak Charge Distribution of ^{48}Ca to 0.02 fm Accuracy”. CREX Proposal. 2013.
- [40] The MOLLER Collaboration. “The MOLLER Experiment (Measurement Of Lepton Lepton Elastic Reactions): An Ultra-precise Measurement of the Weak Mixing Angle using Møller Scattering”. MOLLER Proposal Update, URL: Link. Dec. 2010.
- [41] Shufang Ban, C J Horowitz, and R Michaels. “Parity violating electron scattering measurements of neutron densities”. In: *Journal of Physics G: Nuclear and Particle Physics* 39.1 (Nov. 2011), p. 015104. ISSN: 1361-6471. DOI: 10.1088/0954-3899/39/1/015104.

- [42] Brendan T. Reed et al. “Measuring the surface thickness of the weak charge density of nuclei”. In: *Physical Review C* 102.6 (Dec. 2020). ISSN: 2469-9993. DOI: 10.1103/physrevc.102.064308.
- [43] CREX Collaboration. “An Alternative PREX/CREX Combined Design”. Proposal to run PREX-II and CREX from the same target position. Aug. 2016.
- [44] Cameron Clarke. “Measurement of Parity-Violating Asymmetry in Elastic Electron Scattering off ^{48}Ca ”. PhD thesis. Stony Brook University, Dec. 2021.
- [45] Jonathan W. Wexler. “Measurement of the Parity Violating Asymmetry in Elastic Electron Scattering off ^{208}Pb ”. PhD thesis. University of Massachusetts Amherst, Oct. 2014.
- [46] C. J. Horowitz et al. “Weak charge form factor and radius of ^{208}Pb through parity violation in electron scattering”. In: *Phys. Rev. C* 85 (3 Mar. 2012), p. 032501. DOI: 10.1103/PhysRevC.85.032501. URL: <https://link.aps.org/doi/10.1103/PhysRevC.85.032501>.
- [47] W. Xiong et al. “A small proton charge radius from an electron–proton scattering experiment”. In: *Nature* 575 (Nov. 2019), pp. 147–150. DOI: 10.1038/s41586-019-1721-2.
- [48] H. Atac, Constantinou, and ZE. et al. M. Meziani. “Measurement of the neutron charge radius and the role of its constituents”. In: *Nat Commun* 12 (Mar. 2021), p. 1759. DOI: 10.1038/s41467-021-22028-z.
- [49] C. J. Horowitz and J. Piekarewicz. “Impact of spin-orbit currents on the electroweak skin of neutron-rich nuclei”. In: *Physical Review C* 86.4 (Oct. 2012). ISSN: 1089-490X. DOI: 10.1103/physrevc.86.045503.
- [50] Robert. D. McKeown. “Jefferson Lab 12 GeV Program”. In: *JPS Conf. Proc.* 26 (2019). Ed. by Akinobu Dote et al., p. 011017. DOI: 10.7566/JPSCP.26.011017.
- [51] Robert Rimmer et al. “JLab CW Cryomodules for 4th Generation Light Sources”. In: (Jan. 2008). URL: <https://www.osti.gov/biblio/922273>.
- [52] M. Battaglieri et al. *Dark matter search in a Beam-Dump eXperiment (BDX) at Jefferson Lab*. 2016. arXiv: 1607.01390 [hep-ex].

- [53] Caryn A. Palatchi. “Laser and Electron Beam Technology for Parity Violating Electron Scattering Measurements”. PhD thesis. Hamilton, OH: University of Virginia, May 2019.
- [54] Rupesh Silwal. “Probing the Strangeness Content of the Proton and the Neutron Radius of ^{208}Pb using Parity-Violating Electron Scattering”. PhD thesis. Sanepa, Lalitpur-2, Nepal: University of Virginia, May 2012.
- [55] Caryn Palatchi and Kent Paschke. *RTP Pockels Cell with Nanometer-Level Position Control*. 2021. arXiv: 2106.09546 [physics.ins-det].
- [56] *High current polarized electron source*. Vol. 1970. AIP. AIP Conference Proceedings, May 2018.
- [57] J. Grames et al., eds. *TWO WIEN FILTER SPIN FLIPPER*. Vol. 25. Proceedings of 2011 Particle Accelerator Conference. New York City, NY, USA, 2011.
- [58] J.-C. Denard and A. Saha, eds. *HIGH ACCURACY BEAM CURRENT MONITOR SYSTEM FOR CEBAF’S EXPERIMENTAL HALL A*. 2001 Particle Accelerator Conference. Chicago, IL, USA, 2001.
- [59] The Hall A Collaboration. *2017 Version: Jefferson Lab Hall A Standard Equipment Manual*. Ed. by Higginbotham D. and T. Keppel. JLab Hall A Operations Manual. Thomas Jefferson National Accelerator Facility. Newport News, VA 23606, U.S.A., June 2019.
- [60] Anna Boehle, Robert Michaels, and John Musson. *Low Current Cavity Monitor Tests*. Tech. rep. Newport News, VA 23606: Thomas Jefferson National Accelerator Facility, July 2008.
- [61] Victoria Owen. *Correcting for Helicity Correlated Beam Parameters in the Parity-Violating Electron Scattering Experiment of CREX at Jefferson Lab*. Access requires authentication. The College of William and Mary. Oct. 13, 2021. URL: https://prex.jlab.org/DocDB/0005/000527/001/Owen_SessionMG.pdf (visited on 10/13/2021).
- [62] M. Steigerwald, ed. *MeV Mott Polarimetry at Jefferson Lab*. Vol. 570. AIP Conference Proceedings, 2001. DOI: 10.1063/1.1384229.

- [63] Eric King. *Challenges to Reaching High-Precision 0.4% Møller Polarimetry in Hall-A at Jefferson Lab for 12 GeV Experimentation*. Presentation Slides, URL: https://prex.jlab.org/DocDB/0005/000526/001/2021-Oct-DNP__Eric-King.pdf. Access requires authentication. Oct. 2021.
- [64] William Henry. “Precision Møller Polarimetry and Applications at Jefferson Laboratory”. PhD thesis. Temple University, May 2019.
- [65] R. Dickson and V. Lebedev, eds. *FAST FEEDBACK SYSTEM FOR ENERGY AND BEAM STABILIZATION*. Trieste, Italy: International Conference on Accelerator and Large Experimental Physics Control Systems, 1999.
- [66] C. Gal, A. Zec, and C. Clarke. *prexSim*. <https://github.com/cipriangal/prexSim>. 2019.
- [67] Mark M. Pickrell et al. “The IAEA Workshop on Requirements and Potential Technologies for Replacement of ^3He Detectors in IAEA Safeguards Applications”. In: Journal of the Institute of Nuclear Materials Management (Mar. 2013).
- [68] S. V. Effendi and X. Vilhjálmsón. *SWX-201 & 201HD Neutron Shielding*. Tech. rep. Rio Rancho, NM, USA 87124: Shieldwerx LLC, 2018. URL: <https://www.shieldwerx.com/assets/SWX-201HD%5C%202018.2.pdf>.
- [69] Siyu Jian. *Update On PRex/CRex GEM detector analysis*. Presentation Slides, URL: <https://prex.jlab.org/DocDB/0004/000487/002/PRex%20Experiment%20GEM%20analysis.pdf>. Version 2. Access requires authentication. Jan. 2021.
- [70] Ryan Richards. “Measurements of the Beam Normal Asymmetry using Polarized Elastic Electron Scattering off Various Spin-0 Nuclei at 1 GeV”. PhD thesis. Stony Brook, NY: Stony Brook University, Sept. 2021.
- [71] R. Suleiman et al. *Helicity Signal Generation at Jefferson Lab*. JLab helicity technical manual. Thomas Jefferson National Accelerator Facility. Newport News, VA 23606, U.S.A., June 2014.

- [72] Juan Carlos Cornejo. “Compton Scattering Polarimetry for the Determination of the Proton’s Weak Charge Through Measurements of the Parity-Violating Asymmetry of $^1\text{H}(e, e')\text{p}$ ”. PhD thesis. Williamsburg, VA: College of William and Mary, Aug. 2016.
- [73] *Specification of HAPPEX II ADC Timing Board*. Revision 1. Jefferson Lab Electronics Group.
- [74] Arthur H. Compton. “A Quantum Theory of the Scattering of X-rays by Light Elements”. In: *Phys. Rev.* 21 (5 May 1923), pp. 483–502. DOI: 10.1103/PhysRev.21.483. URL: <https://link.aps.org/doi/10.1103/PhysRev.21.483>.
- [75] Robert Percuoco. “Chapter 1 - Plain Radiographic Imaging”. In: *Clinical Imaging (Third Edition)*. Ed. by Dennis M. Marchiori. Third Edition. Saint Louis: Mosby, 2014, pp. 1–43. ISBN: 978-0-323-08495-6. DOI: <https://doi.org/10.1016/B978-0-323-08495-6.00001-4>. URL: <https://www.sciencedirect.com/science/article/pii/B9780323084956000014>.
- [76] Junichiro Katsuta et al. “Study of the polarimetric performance of a Si/CdTe semiconductor Compton camera for the Hitomi satellite”. In: *Nuclear Instruments and Methods in Physics Research Section A: Accelerators, Spectrometers, Detectors and Associated Equipment* 840 (2016), pp. 51–58. ISSN: 0168-9002. DOI: <https://doi.org/10.1016/j.nima.2016.09.057>. URL: <https://www.sciencedirect.com/science/article/pii/S0168900216310129>.
- [77] Lukasz Swiderski et al. “Response of doped alkali iodides measured with gamma-ray absorption and Compton electrons”. In: *Nuclear Instruments and Methods in Physics Research Section A: Accelerators, Spectrometers, Detectors and Associated Equipment* 705 (2013), pp. 42–46. ISSN: 0168-9002. DOI: <https://doi.org/10.1016/j.nima.2012.11.188>. URL: <https://www.sciencedirect.com/science/article/pii/S0168900212015987>.
- [78] G. Bardin et al. “Conceptual Design Report of a Compton Polarimeter for Cebaf Hall A”. Original Compton polarimeter conceptual design report. May 1996.
- [79] C. Y. Prescott. “Spin Dependent Compton Scattering for use in Analyzing Electron Beam Polarizations”. SLAC-TN-73-001. Jan. 1973.

- [80] Megan Lynn Friend. “A Precision Measurement of the Proton Strange-Quark Form Factors at $Q^2 = 0.624 \text{ GeV}^2$ ”. PhD thesis. Pittsburgh, PA: Carnegie Mellon University, Jan. 2012.
- [81] A. Denner and S. Dittmaier. “Complete $O(\alpha)$ QED corrections to polarized Compton scattering”. In: *Nuclear Physics B* 540.1 (1999), pp. 58–86. ISSN: 0550-3213. DOI: [https://doi.org/10.1016/S0550-3213\(98\)00767-6](https://doi.org/10.1016/S0550-3213(98)00767-6). URL: <https://www.sciencedirect.com/science/article/pii/S0550321398007676>.
- [82] Abdurahim Rakhman. “The Design and Construction of a Green Laser and Fabry-Pérot Cavity System for Jefferson Lab’s Hall A Compton Polarimeter”. PhD thesis. Syracuse, NY, USA: Syracuse University, Dec. 2011.
- [83] A. Rakhman et al. “A high-finesse Fabry-Pérot cavity with a frequency-doubled green laser for precision Compton polarimetry at Jefferson Lab”. In: *Nuclear Instruments and Methods in Physics Research Section A: Accelerators, Spectrometers, Detectors and Associated Equipment* 822 (2016), pp. 82–96. ISSN: 0168-9002. DOI: <https://doi.org/10.1016/j.nima.2016.03.085>. URL: <https://www.sciencedirect.com/science/article/pii/S016890021630119X>.
- [84] Dennis R. Goldstein. *Polarized Light, Third Edition*. CRC Press, 2011. ISBN: 978-1-4398-3041-3.
- [85] R. Clark Jones. “A New Calculus for the Treatment of Optical Systems I. Description and Discussion of the Calculus”. In: *J. Opt. Soc. Am.* 31.7 (July 1941), pp. 488–493. DOI: 10.1364/JOSA.31.000488. URL: <http://www.osapublishing.org/abstract.cfm?URI=josa-31-7-488>.
- [86] N. Vansteenkiste, P. Vignolo, and A. Aspect. “Optical reversibility theorems for polarization: application to remote control of polarization”. In: *J. Opt. Soc. Am. A* 10.10 (Oct. 1993), pp. 2240–2245. DOI: 10.1364/JOSAA.10.002240. URL: <http://www.osapublishing.org/josaa/abstract.cfm?URI=josaa-10-10-2240>.
- [87] A. Narayan et al. “Precision Electron-Beam Polarimetry at 1 GeV Using Diamond Microstrip Detectors”. In: *Phys. Rev. X* 6 (1 Feb. 2016), p. 011013. DOI: 10.1103/PhysRevX.6.011013. URL: <https://link.aps.org/doi/10.1103/PhysRevX.6.011013>.

- [88] S.I. Ziegler et al. “Characteristics of the new YAlO/sub 3/:Ce compared with BGO and GSO”. In: *IEEE Transactions on Nuclear Science* 40.2 (1993), pp. 194–197. DOI: 10.1109/23.212340.
- [89] C.L. Melcher et al. “Scintillation properties of GSO”. In: *IEEE Transactions on Nuclear Science* 37.2 (1990), pp. 161–164. DOI: 10.1109/23.106611.
- [90] M. Friend et al. “Upgraded photon calorimeter with integrating read-out for the Hall A Compton polarimeter at Jefferson Lab”. In: *Nuclear Instruments and Methods in Physics Research Section A: Accelerators, Spectrometers, Detectors and Associated Equipment* 676 (2012), pp. 96–105. ISSN: 0168-9002. DOI: <https://doi.org/10.1016/j.nima.2012.02.041>. URL: <https://www.sciencedirect.com/science/article/pii/S0168900212002392>.
- [91] Takatomi Yano. “Measurement of gamma-ray production from thermal neutron capture on gadolinium for neutrino experiments”. In: *Nuclear Instruments and Methods in Physics Research Section A: Accelerators, Spectrometers, Detectors and Associated Equipment* 845 (2017). Proceedings of the Vienna Conference on Instrumentation 2016, pp. 425–428. ISSN: 0168-9002. DOI: <https://doi.org/10.1016/j.nima.2016.06.084>. URL: <https://www.sciencedirect.com/science/article/pii/S0168900216306477>.
- [92] M. Friend, G.B. Franklin, and B. Quinn. “An LED pulser for measuring photomultiplier linearity”. In: *Nuclear Instruments and Methods in Physics Research Section A: Accelerators, Spectrometers, Detectors and Associated Equipment* 676 (2012), pp. 66–69. ISSN: 0168-9002. DOI: <https://doi.org/10.1016/j.nima.2012.02.015>. URL: <https://www.sciencedirect.com/science/article/pii/S0168900212001738>.
- [93] ROOT Development Team. *ROOT 6*. GitHub repository: <https://github.com/root-project/root>, CERN: <https://root.cern/>. 2021.
- [94] Cornejo J. C. et al. *Halla_ComptonG4*. https://github.com/JeffersonLab/Halla_ComptonG4/tree/prex2. 2018.

- [95] Stéphanie Escoffier. “Precision measurement of the polarization of the TJNAF electron beam via Compton polarimetry”. [in French]. PhD thesis. 5 Rue Thomas Mann 75013 Paris, France: Université Paris 7-Denis Diderot, Oct. 2001.
- [96] D. V. Onoprienko. “Precise Measurement of the Left-Right Asymmetry in Z0 Boson Production by e+ e- Collisions. Electron Beam Polarization Measurement with the Quartz Fiber Calorimeter.”. SLAC Report 556. PhD thesis. Stanford, CA 94309: Stanford Linear Accelerator Center, Stanford University, Aug. 2000.
- [97] Yoshio Imai. “Measurement and optimization of the light polarization of the A4 Compton backscatter polarimeter”. In German. PhD thesis. Mainz U., 2019. DOI: 10.25358/openscience-1992.
- [98] S. Baunack. “The A4 experiment”. In: *Nuovo Cim. C* 035N04 (2012), pp. 11–15. DOI: 10.1393/ncc/i2012-11262-1.
- [99] M. Defurne et al. “A glimpse of gluons through deeply virtual Compton scattering on the proton”. In: *Nature Communications* 8.1 (Nov. 2017). ISSN: 2041-1723. DOI: 10.1038/s41467-017-01819-3.
- [100] Tao Ye. “Precision Measurement of the Parity Violating Asymmetry in Elastic Electron Scattering of ^{208}Pb ”. PhD thesis. Stony Brook, NY: Stony Brook University, Aug. 2021.
- [101] K L Brown. “FIRST- AND SECOND-ORDER MATRIX THEORY FOR THE DESIGN OF BEAM TRANSPORT SYSTEMS AND CHARGED PARTICLE SPECTROMETERS.” In: (Jan. 1971). DOI: 10.2172/4742148. URL: <https://www.osti.gov/biblio/4742148>.
- [102] Kiadtisak Saenboonraung. “Measurement of the Neutron Radius of ^{208}Pb Through Parity Violation in Electron Scattering”. PhD thesis. Charlottesville, VA, USA 22904: University of Virginia, May 2013.
- [103] PREX et al. *New Measurements of the Beam-Normal Single Spin Asymmetry in Elastic Electron Scattering Over a Range of Spin-0 Nuclei*. 2021. arXiv: 2111.04250 [nucl-ex].
- [104] D. Adhikari et al. “Accurate Determination of the Neutron Skin Thickness of ^{208}Pb through Parity-Violation in Electron Scattering”. In: *Physical Review Letters* 126.17 (Apr. 2021). ISSN: 1079-7114. DOI: 10.1103/physrevlett.126.172502. URL: <http://dx.doi.org/10.1103/PhysRevLett.126.172502>.

- [105] T. de Forest Jr. and J.D. Walecka. “Electron scattering and nuclear structure”. In: *Advances in Physics* 15.57 (1966), pp. 1–109. DOI: 10.1080/00018736600101254. eprint: <https://doi.org/10.1080/00018736600101254>. URL: <https://doi.org/10.1080/00018736600101254>.
- [106] Junjie Yang, Jesse A. Hernandez, and J. Piekarewicz. “Electroweak probes of ground state densities”. In: *Physical Review C* 100.5 (Nov. 2019). ISSN: 2469-9993. DOI: 10.1103/physrevc.100.054301. URL: <http://dx.doi.org/10.1103/PhysRevC.100.054301>.
- [107] C. J. Horowitz. Private communication. Dec. 2021.
- [108] Z. Lin and C. J. Horowitz. “Full weak-charge density distribution of Ca48 from parity-violating electron scattering”. In: *Physical Review C* 92.1 (July 2015). ISSN: 1089-490X. DOI: 10.1103/physrevc.92.014313. URL: <http://dx.doi.org/10.1103/PhysRevC.92.014313>.
- [109] Brendan T. Reed et al. “Implications of PREX-2 on the Equation of State of Neutron-Rich Matter”. In: *Physical Review Letters* 126.17 (Apr. 2021). ISSN: 1079-7114. DOI: 10.1103/physrevlett.126.172503.
- [110] C. Drischler et al. “How Well Do We Know the Neutron-Matter Equation of State at the Densities Inside Neutron Stars? A Bayesian Approach with Correlated Uncertainties”. In: *Physical Review Letters* 125.20 (Nov. 2020). ISSN: 1079-7114. DOI: 10.1103/physrevlett.125.202702. URL: <http://dx.doi.org/10.1103/PhysRevLett.125.202702>.
- [111] M. C. Miller et al. “PSR J0030+0451 Mass and Radius from NICER Data and Implications for the Properties of Neutron Star Matter”. In: *The Astrophysical Journal* 887.1 (Dec. 2019), p. L24. DOI: 10.3847/2041-8213/ab50c5. URL: <https://doi.org/10.3847/2041-8213/ab50c5>.
- [112] B. P. Abbott et al. “GW170817: Measurements of Neutron Star Radii and Equation of State”. In: *Phys. Rev. Lett.* 121 (16 Oct. 2018), p. 161101. DOI: 10.1103/PhysRevLett.121.161101. URL: <https://link.aps.org/doi/10.1103/PhysRevLett.121.161101>.

- [113] G. Hagen et al. “Neutron and weak-charge distributions of the ^{48}Ca nucleus”. In: *Nature Phys* 12 (Feb. 2016), pp. 186–190. DOI: 10.1038/nphys3529.
- [114] J. Piekarewicz et al. “Electric dipole polarizability and the neutron skin”. In: *Physical Review C* 85.4 (Apr. 2012). ISSN: 1089-490X. DOI: 10.1103/physrevc.85.041302. URL: <http://dx.doi.org/10.1103/PhysRevC.85.041302>.
- [115] M. Woods. “REVIEW OF WEAK MIXING ANGLE RESULTS AT SLC AND LEP”. SLAC-PUB-95-7037. Oct. 1995.
- [116] M. Cadeddu and F. Dordei. “Reinterpreting the weak mixing angle from atomic parity violation in view of the Cs neutron rms radius measurement from COHERENT”. In: *Physical Review D* 99.3 (Feb. 2019). ISSN: 2470-0029. DOI: 10.1103/physrevd.99.033010. URL: <http://dx.doi.org/10.1103/PhysRevD.99.033010>.
- [117] K. Kumar et. al. (MOLLER collaboration). “An Ultra-precise Measurement of the Weak Mixing Angle using Moller Scattering”. MOLLER Experiment Proposal, URL: Link. Dec. 2008.
- [118] The SoLID Collaboration. “SoLID (Solenoidal Large Intensity Device) Updated Preliminary Conceptual Design Report”. SoLID 2019 Design Report, URL: Link. Nov. 2019.
- [119] D. Wang et al. “Measurement of parity violation in electron-quark scattering”. In: *Nature* 506.7486 (2014), pp. 67–70. DOI: 10.1038/nature12964.
- [120] Dominik Becker et al. “The P2 experiment”. In: *The European Physical Journal A* 54.11 (Nov. 2018). ISSN: 1434-601X. DOI: 10.1140/epja/i2018-12611-6. URL: <http://dx.doi.org/10.1140/epja/i2018-12611-6>.
- [121] Baishan Hu et al. *Ab initio predictions link the neutron skin of ^{208}Pb to nuclear forces*. 2021. arXiv: 2112.01125 [nucl-th].